

# Detection of aeroacoustic sound sources on aircraft and wind turbines

Stefan Oerlemans

Detection of aeroacoustic sound sources on aircraft and wind turbines  
S. Oerlemans

Thesis University of Twente, Enschede - With ref. - With summary in Dutch.  
ISBN 978-90-806343-9-8

Copyright © 2009 by S. Oerlemans, Zwolle, The Netherlands  
Cover photograph: Anna van Nistelrooij  
Cover design: Iris Koene

# DETECTION OF AEROACOUSTIC SOUND SOURCES ON AIRCRAFT AND WIND TURBINES

## PROEFSCHRIFT

ter verkrijging van  
de graad van doctor aan de Universiteit Twente,  
op gezag van de rector magnificus,  
prof. dr. H. Brinksma,  
volgens besluit van het College voor Promoties  
in het openbaar te verdedigen  
op vrijdag 4 september 2009 om 16.45 uur

door

Stefan Oerlemans  
geboren op 24 maart 1974  
te Geffen

Dit proefschrift is goedgekeurd door de promotor:

Prof. dr. ir. A. Hirschberg

en de assistent-promotor:

Dr. ir. P. Sijtsma

Do not believe in anything simply because you have heard it.  
Do not believe in anything simply because it is spoken and rumored by many.  
Do not believe in anything simply because it is found written in your religious books.  
Do not believe in anything merely on the authority of your teachers and elders.  
Do not believe in traditions because they have been handed down for many generations.  
But after observation and analysis, when you find that anything agrees with reason and is conducive to the good and benefit of one and all, then accept it and live up to it.

(Buddha, around 500 BC)



The research described in this thesis was supported by the National Aerospace Laboratory NLR.

## Summary

This thesis deals with the detection of aeroacoustic sound sources on aircraft and wind turbines using phased microphone arrays. The characteristics of flow-induced sound from aircraft wings and wind turbine blades are derived and summarized. The phased array technique is described in detail, and several aspects of the method are discussed, for example how to account for the effects of flow and moving sources, and how to quantify array results using a source power integration method.

The reliability of the integration method is assessed using airframe noise measurements in an open and a closed wind tunnel. It is shown that, although the *absolute* sound level in the open jet can be too low due to coherence loss, the *relative* levels are accurate within 1 dB for both test sections. Thus, phased arrays enable quantitative aeroacoustic measurements in closed wind tunnels.

Next, the array technique is applied to characterize the noise sources on two modern large wind turbines. It is demonstrated that practically all noise emitted to the ground is produced by the outer part of the blades during their downward movement. This asymmetric source pattern, which causes the typical swishing noise during the passage of the blades, can be explained by trailing edge noise directivity and convective amplification. The test results convincingly show that broadband trailing edge noise is the dominant sound source for both turbines.

On the basis of this information, a semi-empirical prediction method is developed for the noise from large wind turbines. The prediction code, which only needs the blade geometry and the turbine operating conditions as input, is successfully validated against the experimental results for both turbines. Good agreement is found between predictions and measurements, not only with regard to sound levels and spectra, but also with regard to the noise source distribution in the rotor plane and the temporal *variation* in sound level (swish). Moreover, the dependence on wind speed and observer position (directivity) is well predicted. The absolute sound levels are accurate within 1-2 dB and the swish amplitude within 1 dB. The validated prediction method is then applied to calculate wind turbine noise footprints, which show that swish amplitudes up to 5 dB can be expected for cross-wind directions, even at large distance.

The influence of airfoil shape on blade noise is investigated through acoustic wind tunnel tests on a series of wind turbine airfoils. In quiescent inflow, trailing edge noise is dominant for all airfoils. At low Reynolds numbers (below 1 million), several airfoils exhibit pure tones due to laminar boundary layer vortex shedding, which can be eliminated by proper boundary layer tripping. In the presence of severe upstream turbulence, leading edge noise is dominant, and the sound level increases with decreasing airfoil thickness.

Finally, two noise reduction concepts are tested on a large wind turbine: acoustically optimized airfoils and trailing edge serrations. Both blade modifications yield a significant trailing edge noise reduction at low frequencies, which is more prominent for the serrated blade. However, the modified blades also exhibit increased tip noise at high frequencies, which is mainly radiated during the upward part of the revolution, and which is most important at low wind speeds due to high tip loading. Nevertheless, average overall noise reductions of 0.5 dB and 3.2 dB are obtained for the optimized blade and for the serrated blade, respectively. This demonstrates that wind turbine noise can be halved without adverse effects on the aerodynamic performance.





## Samenvatting

Dit proefschrift gaat over de detectie van aeroakoestische geluidsbronnen op vliegtuigen en windturbines door middel van akoestische antennes. De eigenschappen van het stromingsgeluid van vliegtuigvleugels en windturbinebladen worden afgeleid en samengevat. De akoestische antennetechniek wordt in detail beschreven, en diverse aspecten van de methode worden behandeld, bijvoorbeeld hoe effecten van stroming en bewegende bronnen kunnen worden verdisconteerd, en hoe antenneresultaten kunnen worden gekwantificeerd door middel van een integratiemethode.

De betrouwbaarheid van de integratiemethode wordt bepaald aan de hand van metingen aan het stromingsgeluid van een vliegtuigmodel in een open en een gesloten windtunnel. Aangevoerd wordt dat, hoewel het *absolute* geluidsniveau bij de open straal door coherentieverlies te laag kan zijn, de *relatieve* geluidsniveaus binnen 1 dB nauwkeurig zijn voor beide testsecties. Dit betekent dat akoestische antennes kwantitatieve aeroakoestische metingen in gesloten windtunnels mogelijk maken.

Vervolgens wordt de antennetechniek toegepast om de geluidsbronnen van twee moderne grote windturbines in kaart te brengen. Gedemonstreerd wordt dat vrijwel al het naar de grond afgestraalde geluid wordt geproduceerd door het buitenste deel van de bladen, tijdens de neergaande beweging. Deze asymmetrische bronverdeling, die het typisch zovende geluid tijdens het passeren van de bladen veroorzaakt, kan worden verklaard door richtingsafhankelijkheid en convectieve versterking van achterrangeluid. De testresultaten tonen overtuigend aan dat breedband achterrangeluid voor beide turbines de belangrijkste geluidsbron is.

Op basis van dit gegeven wordt een semi-empirische voorspellingsmethode voor het geluid van grote windturbines ontwikkeld. De voorspellingsmethode, die als invoer alleen de bladgeometrie en de bedrijfscondities van de turbine nodig heeft, wordt met succes gevalideerd aan de hand van de experimentele resultaten voor beide turbines. De voorspellingen komen goed overeen met de metingen, niet alleen qua geluidsniveaus en -spectra, maar ook wat betreft de verdeling van de geluidsbronnen in het rotorvlak en de temporele *variatie* in geluidsniveau (het zoeven). Bovendien wordt de afhankelijkheid van windsnelheid en waarnemerspositie (richtingsafhankelijkheid) goed voorspeld. De absolute geluidsniveaus zijn nauwkeurig binnen 1-2 dB, en de variatie in geluidsniveau binnen 1 dB. De gevalideerde voorspellingsmethode wordt vervolgens toegepast voor het berekenen van de geluidscontouren van een windturbine. Deze laten zien dat in de dwarsrichting (loodrecht op de windrichting) temporele variaties in geluidsniveau tot 5 dB kunnen worden verwacht, zelfs op grote afstand.

De invloed van de profielvorm op het geluid van een blad wordt onderzocht door middel van akoestische windtunnelmetingen aan een serie windturbineprofielen. In een ongestoorde aanstroming is achterrangeluid dominant voor alle profielen. Bij lage Reynoldsgetalen (minder dan 1 miljoen) vertonen diverse profielen pure tonen door wervelafschudding van een laminaire grenslaag. Deze kunnen worden voorkomen door het aanbrengen van een grenslaagstrip. Bij sterke turbulentie in de aanstroming is voorrangeluid dominant, en neemt het geluidsniveau toe met afnemende profieldikte.

Tenslotte worden twee geluidsreductieconcepten getest op een grote windturbine: akoestisch geoptimaliseerde bladprofielen en zaagtanden op de achterrand van het blad. Beide aanpassingen van het blad geven bij lage frequenties een significante reductie van het achterrangeluid, die het sterkst is voor de zaagtanden. De gemodificeerde bladen vertonen echter ook een toename van hoogfrequent tipgeluid, dat vooral ontstaat tijdens de opwaartse beweging van de bladen, en dat het belangrijkste is bij lage windsnelheden vanwege de hoge tipbelasting. Desondanks is de gemiddelde totale geluidsreductie 0.5 dB voor het geoptimaliseerde bladprofiel en 3.2 dB voor de zaagtanden. Dit toont aan dat windurbinegeluid kan worden gehalveerd zonder nadelige effecten op de aerodynamische prestaties.



# Contents

<b>1 Introduction</b>	<b>1</b>
<b>2 Characteristics of flow-induced sound</b>	<b>5</b>
2.1 Introduction	5
2.2 Wave equation	6
2.3 Refraction of sound at an interface between two fluids	9
2.4 Sources of sound	12
2.5 Sound generation by flow	16
2.6 The sound of compact bodies in a flow	19
2.7 Scattering of aerodynamic sound by an edge	20
2.8 Moving sources	23
2.9 Airfoil noise characteristics	25
<b>3 Detection of sound sources with a phased microphone array</b>	<b>31</b>
3.1 Delay-and-sum beamforming in the time domain	31
3.2 From time domain to frequency domain	34
3.3 Conventional beamforming	35
3.4 Beamforming in a flow	37
3.5 Special techniques	40
3.6 Quantification of array results	44
3.7 Moving sources	46
<b>4 Quantification of airframe noise using microphone arrays in open and closed wind tunnels</b>	<b>51</b>
<i>(published in International Journal of Aeroacoustics Vol. 6, Nr. 4, 2007)</i>	
4.1 Introduction	52
4.2 Test set-up	54
4.3 Data acquisition and processing	57
4.4 Absolute sound levels	59
4.5 Relative sound levels	66
4.6 Conclusions	70
<b>5 Location and quantification of noise sources on a wind turbine</b>	<b>73</b>
<i>(published in Journal of Sound and Vibration Vol. 299, Nr. 4-5, 2007)</i>	
5.1 Introduction	74
5.2 Experimental method	75
5.3 Results and discussion	79
5.4 Conclusions	88

<b>6 Prediction of wind turbine noise and validation against experiment</b>	<b>91</b>
<i>(accepted for publication in International Journal of Aeroacoustics)</i>	
6.1 Introduction	92
6.2 Experimental method	93
6.3 Prediction method	97
6.4 Comparison between prediction and experiment	105
6.5 Application: prediction of noise and swish footprints	113
6.6 Conclusions	114
<b>7 Aeroacoustic wind tunnel tests of wind turbine airfoils</b>	<b>117</b>
<i>(published in Journal of Solar Energy Engineering Vol. 126, Nr. 4, 2004)</i>	
7.1 Introduction	118
7.2 Sources of wind turbine blade noise	119
7.3 Airfoil models	119
7.4 Measurements and data analyses	121
7.5 Results	126
7.6 Summary	135
<b>8 Reduction of wind turbine noise using optimized airfoils and trailing edge serrations</b>	<b>137</b>
<i>(published in AIAA Journal Vol. 47, Nr. 6, 2009)</i>	
8.1 Introduction	138
8.2 Experimental Method	142
8.3 Results and discussion	149
8.4 Conclusions	161
<b>9 Conclusions</b>	<b>165</b>
<b>Appendix Signal processing</b>	<b>167</b>
<b>Acknowledgements</b>	<b>171</b>
<b>Curriculum Vitae</b>	<b>173</b>

# Chapter 1

## Introduction

Sound can evoke emotions ranging from pleasure to terror. While for many people music is the shortest way to the heart, long-term exposure to noise may cause serious health problems, such as sleep disturbance, reduced concentration, stress or fatigue. In today's society, noise pollution is an important problem which affects a large part of the population. The work described in this thesis was carried out at the Dutch National Aerospace Laboratory NLR and concerns the sound of aircraft and wind turbines (Figure 1-1). Although most people appreciate the advantages of air transport and wind energy, the accompanying noise often causes public concern. It should be noted that the perception of sound is significantly influenced by psychological factors: while for some people the sound of church bells or playing children is a source of joy, for others it represents an unacceptable disruption of their peace. For aircraft sound, it has been shown [1] that the annoyance can be reduced substantially by giving people the *impression* that their preferences with regard to noise are taken into account (without changing the actual noise exposure). Hindrance from wind turbine noise reduces significantly when people have an economic benefit from the turbines [2]. Besides psychological factors, the *nature* of the sound also plays an important role. For example, the swishing character of wind turbine noise (i.e. the variation in sound level at the blade passing frequency) makes it more disturbing than other environmental noise sources [2]. However, probably the most important parameter affecting noise nuisance, and one which can be objectively measured, is the sound *level*. In order to protect public health, sound levels in residential areas have to comply with legal regulations. However, these noise limits often constitute a major obstacle for economic activities like air traffic and wind energy. For example, many wind turbines have to operate at reduced power during the night, and in some cases even complete wind farms are canceled due to noise regulations. Thus, in order to remove these obstacles and reduce noise annoyance, it is essential to reduce the sound of aircraft and wind turbines.



Figure 1-1: Wind turbines in Spain.

This thesis focuses on *aeroacoustic*, or flow-induced, sound sources. One of the most important components of external aircraft noise, especially during approach and landing, is the broadband sound generated by the turbulent flow around the airframe. This *airframe noise* originates mainly from the landing gears, flaps, and slats (Figure 1-2). For modern large wind turbines, aerodynamic noise from the rotating blades is usually the dominant source of sound. This *airfoil noise* is also important in other applications, such as helicopters and fans. The flow mechanisms for aircraft wings and wind turbine blades are similar. Both are designed to produce *lift*, which is used to keep the aircraft in the air or to make the rotor blades turn. A wind turbine blade is particularly suitable for basic studies, because it has no engines, slats or flaps, and as such represents a 'clean' case. The velocity of the flow around a wind turbine blade is determined by its rotational speed and the wind speed. Wind turbine noise is mainly an issue at relatively low wind speeds, because then the background noise from other wind-induced sources is low. For the wind turbines considered in this thesis, the rotational speed at the blade tip is typically about 75 m/s, while the wind speed at rotor height is on the order of 10 m/s. Thus, the magnitude of the flow velocity in the tip region (where most of the sound is produced) is about 75 m/s, which is similar to the speed of an aircraft during approach. This means that the *Reynolds number* (referenced to the blade- or wing chord) is typically a few millions or more, so that the flow is turbulent and viscous forces are small with respect to inertial forces. At the same time the Mach number is only on the order of 0.2, which implies that compressibility effects are small. The characteristics of the sound generated by this type of flow are derived and discussed in **Chapter 2**. We will see that most aerodynamic noise originates from the interaction between the turbulent flow and a solid surface. Furthermore, the sound power scales with at least the 5<sup>th</sup> power of the flow speed, and the radiation pattern or *directivity* is generally not uniform.

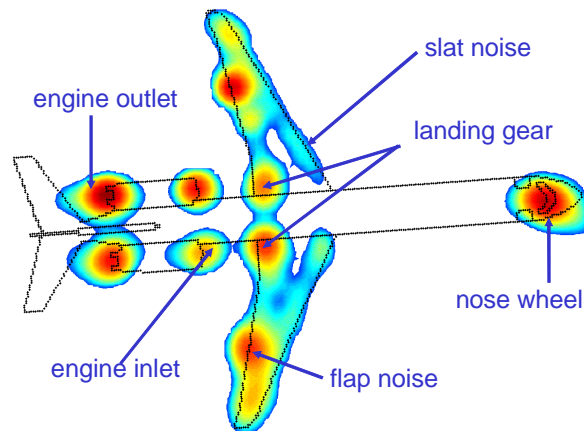


Figure 1-2: Noise sources on a landing aircraft, as measured with a microphone array.

In order to reduce sound, we first have to identify the sources. With a single microphone we can only measure the *overall* sound level, which makes it impossible to distinguish different sources. **Chapter 3** describes how sound sources can be detected using an *array* of microphones. This technique is called *beamforming*, and combines the acoustic signals on different microphones to determine from which direction the sound is coming. Several aspects of the method are discussed, for example how to account for the effects of flow and moving sources, and how array results can be quantified using a source power integration method.

While *location* of sound sources with an acoustic array has become a standard technique, the *quantification* of array results is still far from straightforward. Therefore, in **Chapter 4** the source power integration method is assessed using airframe noise measurements in a wind tunnel. The accuracy of the quantified array results is investigated in detail, not only for a quiet open jet wind tunnel, but also for a closed test section, which is traditionally only used for aerodynamic testing.

In **Chapter 5** the array method is applied to characterize the noise sources on a large modern wind turbine. The experimental results are used to explain the swishing character of wind turbine noise. Moreover, on the basis of a comparison with theoretical relations for airfoil noise, the dominant source mechanism is found to be the interaction of boundary layer turbulence with the blade trailing edge. This source, which usually defines the lower bound of wind turbine noise, is denoted as *trailing edge noise* in the following.

Once we know the source mechanism, we can try to *predict* the sound of a wind turbine. Fast and reliable prediction methods are essential for the design of quiet wind turbines and for the planning of wind farms. **Chapter 6** describes the application of a trailing edge noise prediction method to calculate the noise from two modern large wind turbines. The predictions are validated against experimental results, not only in terms of source spectra and overall sound levels, but also in terms of the noise source distribution in the rotor plane. Moreover, the turbine noise directivity and swish amplitude are predicted and compared to the measured data. It is also shown that wind turbine noise measurements can be used to determine the trailing edge noise directivity function.

Airfoil noise is determined by the flow characteristics, which in turn depend on the *airfoil shape*. **Chapter 7** describes aeroacoustic wind tunnel tests on a series of wind turbine airfoils. Measurements are carried out at various wind speeds and angles of attack, with and without upstream turbulence and boundary layer tripping. The speed dependence, directivity, and tonal behaviour are determined for both trailing edge noise and inflow turbulence noise.

**Chapter 8** describes the assessment of two noise *reduction* concepts on a large wind turbine: a modified airfoil shape and trailing edge serrations. In order to compare the blade performance for identical weather and turbine conditions, the rotor has one baseline blade, one blade with an acoustically optimized airfoil, and one blade with serrations. The acoustic behaviour of the three blades is investigated as a function of wind speed, azimuthal blade position, observer position, and blade roughness.

In summary, the main questions addressed in this thesis are the following. How accurately can we quantify aeroacoustic sound sources with a phased microphone array? What is the dominant noise source on a modern wind turbine? Can we predict wind turbine noise, including swish and directivity, using a trailing edge noise prediction method? How is airfoil noise affected by airfoil shape? Can we reduce wind turbine noise by optimized airfoils or trailing edge serrations? The main conclusions of this thesis are summarized in **Chapter 9**.

## References

- [1] E. Maris, P.J.M. Stallen, R. Vermunt, and H. Steensma, Noise within the social context: Annoyance reduction through fair procedures, *Journal of the Acoustical Society of America*, 121(4), pp 2000-2010, 2007.
- [2] F. van den Berg, E. Pedersen, J. Bouma, R. Bakker, WINDFARM perception: Visual and acoustic impact of wind turbine farms on residents - Final report, 2008.





## Chapter 2

### Characteristics of flow-induced sound

This chapter describes a number of basic acoustic concepts which are needed to understand subsequent chapters. After the introduction in Section 2.1, the propagation and refraction of sound waves are discussed in Sections 2.2 and 2.3. The relations derived in these sections will be used for the source location method described in Chapter 3. Next, Sections 2.4 to 2.7 deal with the generation of sound by a flow, and the influence of boundaries. These concepts are necessary for the interpretation of the experiments and predictions in Chapters 4 to 8. The effect of source motion on the acoustic behaviour is considered in Section 2.8. Finally, Section 2.9 gives an overview of airfoil noise mechanisms and characteristics. More details about the subjects discussed in this chapter can be found in Refs. [1-6], which have been used for the preparation of this chapter.

#### 2.1 Introduction

Sound is a weak pressure disturbance which travels through a fluid as a wave. As it passes, the perturbation causes small variations in the density and velocity of the fluid. Although acoustic pressure fluctuations are small with respect to the mean (atmospheric) pressure, the *range* in amplitudes is very large: the acoustic pressure at the threshold of pain is about ten million times higher than that at the threshold of hearing. This makes it convenient to express the pressure amplitude  $p$  on the numerically more compact logarithmic scale:

$$\text{SPL (dB)} = 20 \cdot \log \frac{P_{rms}}{P_{ref}}, \quad (2.1)$$

where SPL is the *sound pressure level* in decibels, *rms* indicates the root-mean-square value, and  $P_{ref}$  is the reference pressure of  $2 \cdot 10^{-5}$  Pa. This reference pressure corresponds to the hearing threshold (0 dB) for a typical human ear in air (at 1 kHz). To illustrate the order of magnitude of acoustic disturbances, consider a 1 kHz sound wave at the threshold of pain (140 dB). The corresponding acoustic pressure is 200 Pa, which is only a fraction of the atmospheric pressure of  $10^5$  Pa. The velocity at which the fluid particles vibrate is 0.5 m/s, which is much smaller than the wave propagation speed of about 340 m/s. Note that this *particle velocity* indicates the speed of a small amount of fluid, and *not* the velocity of individual air molecules: we assume that we can define a 'fluid particle' or 'material element' which is large compared to molecular scales but small compared to the other length scales in our problem, so that we can regard the fluid as a *continuum*. Since the particle motions are parallel to the propagation direction, sound waves are *longitudinal* waves. At 140 dB and 1 kHz, the particle *displacement* is about  $10^{-4}$  m, which is small compared to the acoustic wavelength of 0.34 m. Since the disturbances are small, the flow variables satisfy the

*linearized* equations of fluid motion. This means that each flow variable is linearly related to any other. Furthermore, multiple acoustic waves can propagate without distorting one another, because the sound fields add linearly. For sound propagation over practical distances, inertial forces are usually much larger than viscous forces. This means that for acoustic wave propagation we can neglect the effects of viscosity, i.e. we may assume the flow is frictionless or *inviscid*.

## 2.2 Wave equation

Consider a fluid with velocity  $\vec{u}_t$ , pressure  $p_t$ , and density  $\rho_t$ . From conservation of mass it follows that

$$\frac{\partial \rho_t}{\partial t} + \nabla \cdot (\rho_t \vec{u}_t) = 0, \quad (2.2)$$

and conservation of momentum gives

$$\frac{\partial (\rho_t \vec{u}_t)}{\partial t} + \nabla \cdot (\rho_t \vec{u}_t \vec{u}_t) + \nabla \cdot \mathbf{P}_t = \vec{f}, \quad (2.3)$$

where  $\nabla$  is the operator  $(\partial/\partial x, \partial/\partial y, \partial/\partial z)$ ,  $\vec{f}$  is the density of an external force field acting on the fluid (such as the gravitational force), and  $\mathbf{P}_t = p_t \mathbf{I} - \boldsymbol{\tau}$  is the fluid stress tensor with unit tensor  $\mathbf{I}$  and viscous stress tensor  $\boldsymbol{\tau}$ . By neglecting viscosity and using Eq. (2.2), we can write Eqs. (2.3) as the Euler equations

$$\rho_t \left( \frac{\partial \vec{u}_t}{\partial t} + \vec{u}_t \cdot \nabla \vec{u}_t \right) + \nabla p_t = \vec{f}. \quad (2.4)$$

We can linearize Eqs. (2.2) and (2.4) by considering small perturbations of velocity, pressure, and density. For this purpose we write  $\vec{u}_t = \vec{u}_0 + \vec{u}$ ,  $p_t = p_0 + p$ , and  $\rho_t = \rho_0 + \rho$ , where the subscript '0' indicates the uniform mean value, the quantities without subscript correspond to the fluctuations, and the subscript 't' indicates the sum. Assuming  $\vec{f} = 0$  and a constant mean velocity  $\vec{u}_0 = \vec{U}$ , the *linearized* equations for conservation of mass and momentum can be written as

$$\frac{\partial \rho}{\partial t} + \vec{U} \cdot \nabla \rho + \rho_0 \nabla \cdot \vec{u} = 0 \quad (2.5)$$

$$\rho_0 \left( \frac{\partial \vec{u}}{\partial t} + \vec{U} \cdot \nabla \vec{u} \right) + \nabla p = 0. \quad (2.6)$$

Even if the uniform quantities  $p_0$ ,  $\rho_0$ , and  $\vec{U}$  are known, Eqs. (2.5) and (2.6) only provide four equations for five unknowns  $(p, \rho, \vec{u})$ . The additional information needed is provided by the constitutional equations, i.e. empirical relationships between variables. We assume the

fluid to be in a state of local thermodynamic equilibrium. This means we can write the pressure  $p_t$  as a function of density  $\rho_t$  and entropy  $s_t$ , so that

$$dp_t = \left( \frac{\partial p_t}{\partial \rho_t} \right)_s d\rho_t + \left( \frac{\partial p_t}{\partial s_t} \right)_\rho ds_t. \quad (2.7)$$

For ideal gases momentum and heat transfer are controlled by the same molecular collisional processes. Thus, if we neglect viscosity, we should also neglect heat transfer, and therefore the flow is *isentropic*. This means that the entropy of a fluid particle remains constant. In our uniform mean fluid we therefore have a constant value of the entropy. Thus, the flow is *homotropic* and  $ds_t = 0$ . By defining the speed of sound as  $c^2 = (\partial p_t / \partial \rho_t)_s$ , Eq. (2.7) then becomes

$$p = c_0^2 \rho, \quad (2.8)$$

where we use  $c_0 = c(p_0, \rho_0)$  to approximate  $c$ . Since  $p_0$  and  $\rho_0$  are uniform,  $c_0$  is also uniform throughout the fluid. The value of the speed of sound can be calculated as follows. Air at atmospheric pressure behaves like an ideal gas so that  $p_t = \rho_t RT$ , with  $R$  the specific ideal gas constant (287 J/KgK) and  $T$  the temperature. For an isentropic ideal gas it can be derived that  $c^2 = \gamma p_t / \rho_t = \gamma RT$ , with  $\gamma = c_p / c_v$  the ratio of the specific heats at constant pressure and volume, respectively. For air  $\gamma = 1.4$ , so that  $c$  only depends on temperature, and  $c_0^2 = \gamma p_0 / \rho_0$ .

Using Eq. (2.8) we can write  $\rho$  in terms of  $p$ . By applying the operation  $(\partial / \partial t + \vec{U} \cdot \nabla)$  to Eq. (2.5), and subtracting the divergence of Eq. (2.6) from it, we eliminate  $\vec{u}$  and obtain the *convective wave equation*

$$\frac{1}{c_0^2} \left( \frac{\partial}{\partial t} + \vec{U} \cdot \nabla \right)^2 p - \nabla^2 p = 0, \quad (2.9)$$

where in cartesian coordinates  $\nabla^2 p = \partial^2 p / \partial x^2 + \partial^2 p / \partial y^2 + \partial^2 p / \partial z^2$ . For many relevant applications we can simplify Eq. (2.9) by assuming zero mean flow, so that we obtain the *wave equation* of d'Alembert

$$\frac{1}{c_0^2} \frac{\partial^2 p}{\partial t^2} - \nabla^2 p = 0. \quad (2.10)$$

This equation describes waves travelling at speed  $c_0$ . A general solution of Eq. (2.10) for a free field plane wave is  $p(\vec{x}, t) = F(\vec{n} \cdot \vec{x} - c_0 t)$ , where the unit vector  $\vec{n}$  indicates the direction of propagation, and  $F$  is a function determined by initial and boundary conditions. In fact, any sum of plane waves travelling in arbitrary directions satisfies Eq. (2.10). From Eq. (2.6) it follows that the acoustic particle velocity  $\vec{u}$  in the plane wave has magnitude

$p/\rho_0 c_0$  and direction  $\vec{n}$ . Thus, the particle motions are parallel to the propagation direction. The energy flux per unit area of a plane normal to  $\vec{n}$  is given by the acoustic intensity  $\vec{I} = p \vec{u}$ .

Using Fourier analysis (see Appendix), any smooth periodic pressure signal can be represented as the superposition of harmonic functions, each with angular frequency  $\omega = 2\pi f$  (with  $f$  the frequency in Hz). Therefore we can consider harmonic solutions to Eq. (2.10) without loss of generality. The general solution for a harmonic plane wave has the form

$$p(\vec{x}, t) = A e^{i\omega \left( t - \frac{\vec{n} \cdot \vec{x}}{c_0} \right)} = A e^{i(\omega t - \vec{k} \cdot \vec{x})}, \quad (2.11)$$

where the pressure  $p$  is actually the real part of the (complex) right-hand side. The plane wave travels at phase speed  $c_0$  in the direction of the *wave number vector*  $\vec{k} = k\vec{n} = (k_1, k_2, k_3)$ , which has length  $k = \omega/c_0$ . The *wavelength*, i.e. the distance between two adjacent crests, is given by  $\lambda = c_0/f$ . The harmonic plane wave solution of the *convective* wave equation, Eq. (2.9), is

$$p(\vec{x}, t) = A e^{i\omega \left( t - \frac{\vec{n} \cdot \vec{x}}{c_0 + \vec{n} \cdot \vec{U}} \right)} = A e^{i(\omega t - \vec{k} \cdot \vec{x})} \quad \text{with} \quad \vec{k} = \frac{\omega \vec{n}}{c_0 + \vec{n} \cdot \vec{U}} = (k_1, k_2, k_3). \quad (2.12)$$

Note that the phase speed of convected wave is equal to the sum of the propagation speed with respect to the medium,  $c_0$ , and the component of the convection velocity in the direction of propagation. This is illustrated in Figure 2-1, where  $U = \|\vec{U}\|$ . The frequency domain version of the (convective) wave equation is called the (convective) *Helmholtz equation*.

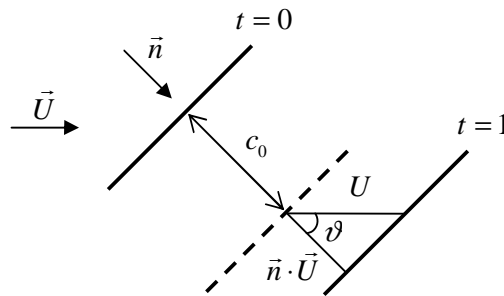


Figure 2-1: Propagation of plane wave front in uniform flow.

Besides plane waves we often consider a *radially* symmetric pressure field. From conservation of mass and momentum in a spherical shell at distance  $r$  from the origin, it follows that the product  $rp$  satisfies the one-dimensional wave equation

$$\frac{1}{c_0^2} \frac{\partial^2 rp}{\partial t^2} - \frac{\partial^2 rp}{\partial r^2} = 0. \quad (2.13)$$

Using Eq. (2.11), this leads to the following expression for an outward propagating (harmonic) spherical wave:

$$p(r,t) = \frac{A e^{i\omega(t-r/c_0)}}{r}. \quad (2.14)$$

Thus, the wave travels outward at speed  $c_0$  and its amplitude is inversely proportional to the distance. Note that at large distance the spherical wave behaves locally like a plane wave. The absence of incoming waves converging to the origin corresponds to the so-called 'free field' conditions.

### 2.3 Refraction of sound at an interface between two fluids

Sound waves often propagate in media with varying density, sound speed, or mean flow speed, for example in open jet wind tunnels or in the atmospheric boundary layer. For the open jet wind tunnels considered in this thesis (see for example Figure 4-1, pg. 55), the sound travels from a region with a Mach number of  $M = U/c_0 \sim 0.2$  through the *shear layer* to a region with still air. To see what happens at the interface consider a plane harmonic wave impinging obliquely on the boundary between two uniform fluids (Figure 2-2).

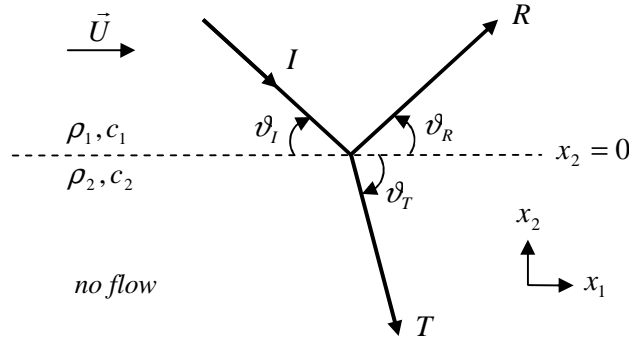


Figure 2-2: Sound refraction at an interface.

We assume an infinitely thin shear layer between two infinitely extended uniform regions 1 and 2. The fluids have different mean density and speed of sound. Fluid 1 has mean velocity  $U$  in the  $x_1$ -direction, while the unperturbed fluid in region 2 is stagnant. The amplitudes of the incident, reflected, and transmitted waves can be written as

$$\begin{aligned} P_I &= I \cdot e^{-i\vec{k}^I \cdot \vec{x}}, \quad \text{with} \quad \|\vec{k}^I\| = \omega/c_I = \omega/(c_1 + U \cos \vartheta_I) \\ P_R &= R \cdot e^{-i\vec{k}^R \cdot \vec{x}}, \quad \text{with} \quad \|\vec{k}^R\| = \omega/c_R = \omega/(c_1 + U \cos \vartheta_R) \\ P_T &= T \cdot e^{-i\vec{k}^T \cdot \vec{x}}, \quad \text{with} \quad \|\vec{k}^T\| = \omega/c_2. \end{aligned} \quad (2.15)$$

The time dependence  $e^{i\omega t}$  is omitted because the frequency is not affected by the interface. The phase speeds  $c_I$  and  $c_R$  are equal to the sum of the propagation speed with respect to the medium and the component of the convection velocity in the direction of propagation (see Figure 2-1).

For integral momentum conservation at the interface  $x_2 = 0$ , the pressure must be equal on the two sides of the boundary. This pressure continuity at  $x_2 = 0$  implies that

$$I \cdot e^{-ik_1^I \cdot x_1} + R \cdot e^{-ik_1^R \cdot x_1} = T \cdot e^{-ik_1^T \cdot x_1}, \quad (2.16)$$

where  $k_1^I = \|\vec{k}^I\| \cos \vartheta_I$  is the  $x_1$ -component of the wave number vector  $\vec{k}^I$  (and similar relations hold for  $k_1^R$  and  $k_1^T$ ). Eq. (2.16) can only be satisfied for all  $x_1$  if  $k_1^I = k_1^R = k_1^T$  and  $I + R = T$ . From the equality of the  $k_1$  wave numbers it follows that

$$\frac{c_1}{\cos \vartheta_I} + U = \frac{c_1}{\cos \vartheta_R} + U = \frac{c_2}{\cos \vartheta_T} \equiv c_w, \quad (2.17)$$

which basically says that the *surface wave speeds* should be the same: the sound wave induces a surface wave which propagates along the interface at speed  $c_w$ . The first equality shows that  $\vartheta_I = \vartheta_R$ , i.e. the angle of the reflected wave is equal to the angle of incidence. For zero mean flow, Eq. (2.17) simplifies to

$$\frac{c_1}{\cos \vartheta_I} = \frac{c_2}{\cos \vartheta_T}, \quad (2.18)$$

which is known as *Snell's law*. Eq. (2.17) can be used to see what happens to a plane sound wave impinging on an interface across which the mean flow speed decreases from  $U$  to zero (such as the shear layer in an open jet wind tunnel). We will assume for the moment that the sound speed is the same on both sides of the interface ( $c = c_1 = c_2$ ). Eq. (2.17) then shows that all waves will be bent away from the mean flow direction when passing through the shear layer (except for normal incidence when  $\vartheta_I = \vartheta_T = \pi/2$ ). This behaviour is called *refraction*, and is illustrated in Figure 2-3.

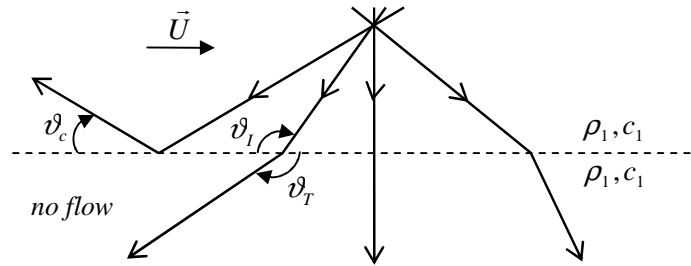


Figure 2-3: Refraction of plane waves at a shear layer.

Since downstream propagating waves are bent away from the shear layer, there is a range of transmission angles which is inaccessible to plane waves originating from the flow. This *zone of silence* is given by  $0 \leq \vartheta_r \leq \vartheta_c$ , where the critical angle  $\vartheta_c$  equals the transmission angle for grazing incidence ( $\vartheta_i = 0$ ), so that  $\cos \vartheta_c = (1 + M)^{-1}$ . For  $M = 0.2$  the critical angle is  $34^\circ$ . *Upstream* propagating waves are bent *towards* the shear layer. Thus, when the incidence angle becomes too high, there will be no propagated wave and the incident waves are totally reflected (an evanescent surface wave will also be generated but this carries no energy). The angles for which this occurs are given by  $\pi - \vartheta_c \leq \vartheta_i \leq \pi$ , where the critical angle  $\pi - \vartheta_c$  is the incidence angle corresponding to a grazing transmitted ray with  $\vartheta_r = \pi$ .

In order to calculate the amplitudes of the reflected and transmitted waves, we now restrict ourselves to the case where a transmitted wave exists ( $0 < \vartheta_i < \pi - \vartheta_c$ ), so that Eq. (2.17) is valid. Due to the surface wave induced by the incident sound wave, the interface between the fluids is perturbed by a small 'ripple'. As we ignore mixing, the particle velocity normal to the *rippled* interface must be continuous. In other words: the *displacement* of fluid particles (in the direction normal to the mean flow) must be continuous. Using this boundary condition, it can be derived [7,8] that the amplitudes of the reflected and transmitted waves are given by:

$$\frac{R}{I} = \frac{1-Z}{1+Z} \quad \text{and} \quad \frac{T}{I} = \frac{2}{1+Z}, \quad (2.19)$$

with

$$Z = \Gamma \frac{\sin(2 \vartheta_r)}{\sin(2 \vartheta_i)} \quad \text{and} \quad \Gamma = \frac{\rho_1 c_1^2}{\rho_2 c_2^2}, \quad (2.20)$$

where  $\Gamma = 1$  if the same gas is present on both sides of the interface. Note that convective effects are included through the dependence of  $\vartheta_r$  on  $U$  in Eq. (2.17). By considering a 'ray tube' impinging on the interface, and accounting for the change in cross-sectional area of the transmitted ray tube, it can be verified that the sum of the energy fluxes in the reflected and transmitted tubes is equal to the incident energy flux:

$$I^2 = R^2 + T^2 Z. \quad (2.21)$$

If we assume that the gas and the sound speed are the same on both sides of the interface, we can use Eqs. (2.17), (2.19) and (2.20) to calculate the fraction  $R^2/I^2$  of the incident energy which is reflected at the interface. It follows that for  $M < 0.25$  and  $\pi/4 \leq \vartheta_i \leq 3\pi/4$  less than 0.5% of the incident energy is reflected, and that the sound level of the transmitted wave differs less than 0.55 dB from the level of the incident wave. Therefore, in this thesis it will be assumed that all energy is transmitted through the shear layer. Although the present analysis considered plane waves impinging on a thin shear layer, it has been shown [9] that the conclusions are also largely valid for realistic open jet wind tunnel conditions, where the

sound waves may be spherical, and the shear layer thickness may be large with respect to the acoustic wavelength.

In a *closed* wind tunnel (see e.g. Figure 4-2, pg. 55), the acoustic *impedance*  $\rho_2 c_2$  of the wall is much higher than the impedance of the air  $\rho_1 c_1$ , i.e. the surface is acoustically hard. In that case  $\Gamma$  and  $Z$  approach zero, and all energy is reflected regardless of the incidence angle. The transmitted wave has  $T = 2I$  but it carries negligible energy because the particle velocity  $T/\rho_2 c_2$  is practically zero. Due to this *pressure doubling* the sound level measured by wall-mounted microphones will be 6 dB higher than the free-field value.

## 2.4 Sources of sound

Before addressing the generation of sound by flow, we first need to introduce the concept of a sound source. Up to now we have considered propagating waves whose behaviour is governed by the homogeneous wave equation, Eq. (2.10). This equation only describes the *propagation* of (1) sound generated at boundaries, (2) incoming sound fields from infinity, or (3) sound due to initial perturbations. We define deviations from the 'acoustical behaviour', given by the homogeneous wave equation, to be the *sound source*  $q(\vec{x}, t)$ :

$$\frac{1}{c_0^2} \frac{\partial^2 p}{\partial t^2} - \nabla^2 p = q. \quad (2.22)$$

Thus, the source region, where  $q$  is non-zero, is separated from the sound field, where  $q$  is zero and propagation of sound waves prevails. When the source  $q$  is known, the sound field is uniquely determined for given initial and boundary conditions. However, the converse is not true: a given sound field can be caused by different source fields. For example, an excellent audio system can create the illusion that a singer is present in the room. This has the important consequence that, in order to obtain source information from a measured sound field, we must have a physical source model. For the microphone array measurements in this thesis, we generally assume that the sources behave like so-called monopoles. This will be discussed in detail in Chapter 3. In the following sub-sections we will discuss (1) how acoustic sources can be generated, (2) how we can determine the corresponding sound field, and (3) the characteristics of basic point sources (monopole and dipole).

### 2.4.1 Source terms

In the derivation of the homogeneous wave equation several assumptions were made. In the following, a number of deviations from this 'acoustical behaviour' are not neglected but moved towards the right hand side of the conservation laws, forming so-called aeroacoustical sources. For a uniform, stagnant fluid, linearization of Eqs. (2.2) and (2.4) yields

$$\frac{\partial \rho}{\partial t} + \rho_0 \nabla \cdot \vec{u} = 0 \quad (2.23)$$

$$\rho_0 \frac{\partial \vec{u}}{\partial t} + \nabla p = \vec{f}. \quad (2.24)$$



From Eq. (2.7) it follows that

$$p = c_0^2 \rho + \left( \frac{\partial p}{\partial s} \right)_\rho s, \quad (2.25)$$

where we maintain the second term on the right-hand side (in Eq. (2.8) we discarded this term because sound propagation in a uniform flow is homentropic). By taking the time derivative of Eq. (2.23), subtracting the divergence of Eq. (2.24), and using Eq. (2.25) to eliminate  $\rho$ , we obtain the following inhomogeneous wave equation:

$$\frac{1}{c_0^2} \frac{\partial^2 p}{\partial t^2} - \nabla^2 p = -\nabla \cdot \vec{f} + \frac{1}{c_0^2} \left( \frac{\partial p}{\partial s} \right)_\rho \frac{\partial^2 s}{\partial t^2} = -\nabla \cdot \vec{f} + \frac{\partial^2}{\partial t^2} \left( \frac{p}{c_0^2} - \rho \right). \quad (2.26)$$

By defining

$$\frac{\partial m}{\partial t} \equiv \frac{1}{c_0^2} \left( \frac{\partial p}{\partial s} \right)_\rho \frac{\partial^2 s}{\partial t^2} \quad (2.27)$$

we see that the source term associated with the generation of entropy has the same effect as an (isentropic) mass source term  $m$  in the right hand side of Eq. (2.23). By writing

$$m = \frac{\partial}{\partial t} (\beta \rho_0), \quad (2.28)$$

where  $\beta$  is the volume fraction occupied by the injected mass (with density  $\rho_0$ ), the corresponding source term in the right hand side of Eq. (2.26) is  $\rho_0 \partial^2 \beta / \partial t^2$ , which shows that unsteady 'injection of volume' is a source of sound. Hence, due to thermal expansion in processes such as combustion or heat transfer, the entropy source term acts as a volume- or *monopole* source. This illustrates that, although for non-relativistic conditions mass must be conserved, a mass source term can be used to represent a complex process which we do not want to describe in detail. Besides thermal expansion, for example the sound of a pulsating sphere can also be approximated by a volume source term. The other source term in Eq. (2.26), which is associated with the force density  $\vec{f}$ , is the divergence of a vector field and therefore induces a *dipole* field (the reason for this name will become clear below). Thus, time-dependent, non-uniform force fields induce dipole sound. The force density  $\vec{f}$  can also be used to represent the reaction force of a rigid wall to unsteady hydrodynamic forces. This is actually the main source of sound in many flows.

#### 2.4.2 Green's functions

The solution of the inhomogeneous wave equation can be constructed by using the method of Green's functions. First we determine the pressure field  $G(\vec{x}, t)$  for a unit pulse which is released at position  $\vec{y}$  and time  $\tau$ , i.e.

$$\frac{1}{c_0^2} \frac{\partial^2 G}{\partial t^2} - \nabla^2 G = \delta(\bar{x} - \bar{y}) \delta(t - \tau), \quad (2.29)$$

where  $\delta$  is the Dirac delta function. The pulse response or *Green's function*  $G$  should also satisfy the causality conditions  $G = 0$  and  $\partial G / \partial t = 0$  for  $t < \tau$ , because the field pressure observed at time  $t$  must be caused by source signals that were emitted at earlier times  $\tau$ . The Green's function is further determined by the linear boundary conditions that we impose. If the boundary conditions correspond to those of the acoustical field we call it a *tailored* Green's function.

An important property of the Green's function is that it satisfies the *reciprocity* relation

$$G\langle \bar{x}, t | \bar{y}, \tau \rangle = G\langle \bar{y}, -\tau | \bar{x}, -t \rangle. \quad (2.30)$$

This relation says that the perceived pressure due to a unit pulse remains the same if we exchange source and observer position, and invert emission and observer time (for causality). The *reciprocity theorem* states that the sound field at  $\bar{x}$  due to a source at  $\bar{y}$  is equal to the sound field at  $\bar{y}$  due to the same source at  $\bar{x}$ . The reciprocity relation will be used in Section 2.7 to determine the Green's function for a source close to an edge.

Using Green's theorem the solution of the inhomogeneous wave equation Eq. (2.22) can be written in the integral form

$$p(\bar{x}, t) = \int_{-\infty}^t \int_V q(\bar{y}, \tau) G\langle \bar{x}, t | \bar{y}, \tau \rangle d^3 \bar{y} d\tau - \int_{-\infty}^t \int_S \left[ p \frac{\partial G}{\partial y_i} - G \frac{\partial p}{\partial y_i} \right] n_i d^2 \bar{y} d\tau, \quad (2.31)$$

where  $\bar{x}$  is the observer- or field coordinate,  $\bar{y}$  is the source coordinate, and  $n_i$  is the outer normal on the surface  $S$  enclosing the volume  $V$  where  $q$  is non-zero. The first term in the right hand side of Eq. (2.31) is a space and time integral of point source solutions, while the second term represents the influence of boundaries. For a tailored Green's function, which satisfies the same boundary conditions at the surface  $S$  as the pressure field  $p$ , the second term vanishes.

In free space the Green's function for a stagnant fluid is given by

$$G_0\langle \bar{x}, t | \bar{y}, \tau \rangle = \frac{\delta(t - \tau - \|\bar{x} - \bar{y}\|/c_0)}{4\pi \|\bar{x} - \bar{y}\|}. \quad (2.32)$$

This is an outward traveling impulsive wave whose amplitude is inversely proportional to the distance. Note that, since  $G_0$  only depends on  $\|\bar{x} - \bar{y}\|$ , it satisfies the symmetry property

$$\frac{\partial G_0}{\partial x_i} = -\frac{\partial G_0}{\partial y_i}, \quad (2.33)$$

i.e. moving the observer towards the source is equivalent to moving the source towards the observer. By inserting  $G_0$  in Eq. (2.31), we now obtain the following expression for the pressure field in free space due to source  $q$ :

$$p(\vec{x}, t) = \int_{\mathcal{V}} \frac{q(\vec{y}, t - \|\vec{x} - \vec{y}\|/c_0)}{4\pi\|\vec{x} - \vec{y}\|} d^3\vec{y}. \quad (2.34)$$

#### 2.4.3 Point monopole and dipole

In order to illustrate the characteristics of the pressure field induced by the mass and force terms in Eq. (2.26), we now consider the case where these sources are concentrated in one point of space. For a point volume source in  $\vec{\xi}$  with  $\beta(\vec{y}, t) = \hat{\beta}(t)\delta(\vec{y} - \vec{\xi})$ ,

$$q(\vec{y}, t) = \rho_0 \frac{\partial^2 \hat{\beta}}{\partial t^2} \delta(\vec{y} - \vec{\xi}) \equiv \sigma(t)\delta(\vec{y} - \vec{\xi}), \quad (2.35)$$

where the *source strength*  $\sigma(t)$  is the time signal generated by the source. From Eq. (2.34) the radiated pressure field is then found to be

$$p(\vec{x}, t) = \frac{\sigma(t - r/c_0)}{4\pi r}, \quad (2.36)$$

where  $r = \|\vec{x} - \vec{\xi}\|$ . This is an omnidirectional or *monopole* sound field, which we found before for the outward propagating spherical wave in Eq. (2.14). Thus, the pressure field in Eq. (2.36) satisfies the homogeneous wave equation everywhere except at the source position. A point monopole can be thought of as a pulsating sphere with vanishing radius but constant source strength.

For a point *force* in  $\vec{\xi}$ , the source term is  $q(\vec{y}, t) = -\nabla \cdot \vec{f}$ , where the strength  $\vec{f}$  has both a magnitude and a direction, and can be written as  $\vec{f}(\vec{y}, t) = \vec{F}(t)\delta(\vec{y} - \vec{\xi})$ . Since such a source can be formed by two adjacent, opposite monopole sources, a point force is called a *dipole* source. The strength  $Q$  of the monopoles and the distance  $\vec{l}$  between the two sources should be such that  $Q(t)\vec{l} = \vec{F}(t)$ , where  $\|\vec{l}\|$  goes to zero and  $Q$  is increased such that  $\vec{F}$  remains constant. A point dipole can also be thought of as a small rigid sphere oscillating in the direction of the dipole axis. From Eq. (2.34), using partial integration and the free field symmetry property in Eq. (2.33), the dipole pressure field can be written as

$$p(\vec{x}, t) = -\frac{\partial}{\partial x_i} \int_{\mathcal{V}} \frac{F_i(t - \|\vec{x} - \vec{y}\|/c_0) \delta(\vec{y} - \vec{\xi})}{4\pi\|\vec{x} - \vec{y}\|} d^3\vec{y}, \quad (2.37)$$

so that the pressure at distance  $r$  and at an angle  $\theta_d$  to the dipole axis is

$$p(r, \theta, t) = -\frac{\partial}{\partial x_i} \left\{ \frac{F_i(t-r/c_0)}{4\pi r} \right\} = \frac{\cos \theta_d}{4\pi} \left\{ \frac{1}{c_0 r} \left[ \frac{\partial F}{\partial t} \right] + \left[ \frac{F}{r^2} \right] \right\}, \quad (2.38)$$

where  $r = \|\vec{x} - \vec{\xi}\|$ ,  $F = \|\vec{F}\|$ ,  $\theta_d$  is the angle between the observer direction  $\vec{x} - \vec{\xi}$  and the force  $\vec{F}$ , and the square brackets indicate that the function should be evaluated at emission time  $t - r/c_0$ . The structure of the dipole field differs from the monopole in three respects. Firstly, the dipole pressure is composed of two terms, one falling off with  $1/r$  and one with  $1/r^2$ . The  $1/r^2$  term dominates the field close to the source and is therefore called the *near field*. At larger distances (in the *far field*) the pressure falls off with  $1/r$ , as for the monopole source in Eq. (2.36). Secondly, the dipole field has a non-uniform *directivity*. The pressure field has a  $\cos \theta_d$  dependence, with zero pressure at  $90^\circ$  to the dipole axis. This can be understood from the equal distance to the two canceling monopoles (see Figure 2-4), when the dipole is represented by two adjacent, opposite monopoles of strength  $Q$ , as described above. Thirdly, the far field pressure of the dipole (even for  $\cos \theta_d = 1$ ) is much lower than the pressure of a single monopole with the same strength  $Q$ . This can be understood from the partial cancellation of the two constituent monopoles. Thus, in free field conditions dipoles are less efficient radiators than monopoles.

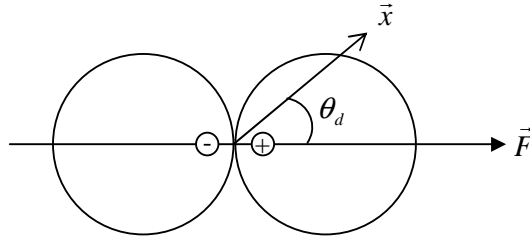


Figure 2-4: Directivity pattern of a dipole source.

## 2.5 Sound generation by flow

In the previous section we saw that deviations from the acoustical behaviour (i.e. the homogeneous wave equation) can be interpreted as sound sources. Besides the mass (entropy) and force terms discussed there, deviations from the linear inviscid behaviour of the fluid can also be considered as acoustic sources. The sound generated by a flow can be described by starting from the exact equations of motion and collecting all departures from the 'ideal' behaviour on the right hand side of an inhomogeneous wave equation. In index notation, the exact equations of mass and momentum conservation, Eqs. (2.2) and (2.3), are given by

$$\frac{\partial \rho_i}{\partial t} + \frac{\partial (\rho_i u_{ii})}{\partial x_i} = 0 \quad (2.39)$$

$$\frac{\partial (\rho_i u_{ii})}{\partial t} + \frac{\partial (\rho_i u_{ii} u_{ij})}{\partial x_j} + \frac{\partial (p_i \delta_{ij} - \tau_{ij})}{\partial x_j} = f_i. \quad (2.40)$$

where  $\delta_{ij}$  is the Kronecker  $\delta$ -function and  $\tau_{ij}$  is the viscous stress. By subtracting the divergence of Eq. (2.40) from the time derivative of Eq. (2.39), and subtracting on both sides  $c_0^2 \nabla^2 \rho_t$ , we obtain

$$\frac{\partial^2 \rho_t}{\partial t^2} - c_0^2 \frac{\partial^2 \rho_t}{\partial x_i^2} = \frac{\partial^2 (\rho_t u_{ii} u_{ij} - \tau_{ij})}{\partial x_i \partial x_j} - \frac{\partial f_i}{\partial x_i} + \frac{\partial^2 (p_t - c_0^2 \rho_t)}{\partial x_i^2}. \quad (2.41)$$

We now define deviations from the reference state  $(p_0, \rho_0)$  as  $p = p_t - p_0$  and  $\rho = \rho_t - \rho_0$ . These deviations are assumed to be linear at the observer's position, but do not need to be small in the so-called source region. This gives the famous *Lighthill equation*

$$\frac{\partial^2 \rho}{\partial t^2} - c_0^2 \frac{\partial^2 \rho}{\partial x_i^2} = \frac{\partial^2 T_{ij}}{\partial x_i \partial x_j} - \frac{\partial f_i}{\partial x_i}, \quad (2.42)$$

where Lighthill's stress tensor is defined as

$$T_{ij} = \rho_t u_{ii} u_{ij} - \tau_{ij} + (p - c_0^2 \rho) \delta_{ij}, \quad (2.43)$$

and  $c_0$  is the sound speed at the observer's position (outside the source region), where we assume a uniform stagnant fluid with  $\rho_0, p_0, c_0$ . As no approximations were made, Eq. (2.42) is exact and basically defines sound sources as the difference between the exact equations of motion and their acoustical approximations. This is called *Lighthill's analogy* which shows that we can consider all fluid motions as acoustic fields with aerodynamic source terms. The term  $-\partial f_i / \partial x_i$  represents the dipole field induced by external force fields or walls, and was already discussed in the previous section.

Lighthill's stress tensor shows that there are three other basic aeroacoustic source processes: the non-linear Reynolds stress  $\rho_t u_{ii} u_{ij}$ , the viscous forces  $\tau_{ij}$ , and deviations from the homentropic behaviour  $p = c_0^2 \rho$ . For *isentropic* flow sound is still generated by the difference between  $c$  and  $c_0$ . Note that in Eq. (2.26), where  $p$  was used as the acoustic variable, deviations from  $p = c_0^2 \rho$  appeared as a  $\partial^2 (p/c_0^2 - \rho) / \partial t^2$  source term, hence a monopole sound source. This form of the analogy is most convenient when studying combustion processes in which entropy production is the dominant sound source. The original analogy of Lighthill, which uses  $\rho$  as acoustic variable, is most suited when flows are considered with large variations in the speed of sound ( $c/c_0 \ll 1$ ), such as a bubbly source region surrounded by a pure-liquid observer's region. In such a case the entropy term has the character of a *quadrupole*:  $\partial^2 (p - c_0^2 \rho) / \partial x_i^2$ .

In the absence of external forces, the source field equals the double divergence of Lighthill's stress tensor,  $\partial^2 T_{ij} / \partial x_i \partial x_j$ , and is therefore of quadrupole type (for isentropic flows). A point quadrupole can be formed by combining two opposite point dipoles, either laterally or longitudinally. Similar to the dipole, the point quadrupole has a non-uniform directivity and a near field which is essentially different from the far field. The far field

pressure of a quadrupole is inversely proportional to the distance, and due to the double cancellation its radiation is even less efficient than a dipole.

Since Eq. (2.42) is exact, it is not easier to solve than the original equations of motion. However, if we write it in *integral* form, we can use dimensional analysis to estimate how the sound produced by free turbulence in a jet depends on the flow parameters. Assuming that there are no external forces, we insert  $q(\vec{y}, t) = \partial^2 T_{ij} / \partial y_i \partial y_j$  in Eq. (2.34), apply partial integration, and use the symmetry property in Eq. (2.33) to write the free field sound field as

$$\rho(\vec{x}, t) = \frac{\partial^2}{\partial x_i \partial x_j} \int_V \frac{T_{ij}(\vec{y}, t - \|\vec{x} - \vec{y}\|/c_0)}{4\pi c_0^2 \|\vec{x} - \vec{y}\|} d^3 \vec{y}, \quad (2.44)$$

where  $V$  is the volume in which  $T_{ij}$  is non-zero. If the jet has diameter  $D$  and flow speed  $U$ , the characteristic frequency in the flow is  $U/D$ . The far field frequency  $c/\lambda$  will be the same, so that  $D \sim M \cdot \lambda$ , with  $M = U/c$  the jet Mach number. Thus, for low Mach numbers  $D \ll \lambda$ , so that the jet is *compact* (small compared to the wavelength). This implies that variations in retarded time over the source volume  $V \sim D^3$  can be neglected. In the far field the only length scale is  $\lambda$ , so that  $\partial/\partial x \sim 1/\lambda \sim M/D$ . For the large scales in turbulent jets, which are the main sources of sound, the effects of viscosity can be neglected, and for low Mach numbers the flow is almost isentropic with  $c = c_0$ , so that we can estimate  $T_{ij} \sim \rho_0 U^2$ . Combining these approximations we obtain

$$\frac{\overline{p^2}}{(\rho_0 c_0^2)^2} \sim \left(\frac{D}{r}\right)^2 M^8 \quad (2.45)$$

for cold, low Mach number jets. This law predicts that the sound is proportional to the *eighth* power of the jet velocity, which has been confirmed by experiments. In this particular case the theory of Lighthill (1952) predicted the eighth power *before* it was observed in experiment. It should be noted that Eq. (2.45) is valid for *proportional* frequency bands (see Appendix). If narrow bands or power spectral densities are used, the sound levels will scale as  $M^7$  when measured at equal Strouhal number  $fD/U$ . This is because the number of narrow bands over which the acoustic energy is distributed is proportional to the characteristic frequency, and therefore to the jet velocity.

The eighth power dependency implies that doubling the jet Mach number increases jet noise by 24 dB. Early jet engines were designed for high speed flight and had very high jet velocities. Therefore jet noise was a dominant noise source. High-bypass turbofan engines developed in the late 1960's improved the efficiency of the engines considerably by reducing the jet flow speed. This also had the advantage that jet noise was reduced substantially, to a level comparable to that of airframe noise (during approach and landing). Eq. (2.45) also illustrates that at *low* Mach numbers turbulence in free space is a very ineffective source of sound. In the next section it will be shown that the presence of boundaries dramatically increases the acoustic efficiency of turbulence.

## 2.6 The sound of compact bodies in a flow

Lighthill's theory of aerodynamic sound, as derived in the previous section, describes the sound field emitted by a region of fluctuating flow in free space. However, for aircraft wings or wind turbine blades the presence of solid surfaces is essential. Therefore, we will now consider the sound generated by a foreign body in a flow. Consider a body which is enclosed by a control surface  $S$ , and a control volume  $V$  on the fluid side of the surface (Figure 2-5). With  $q(\vec{y}, t) = \partial^2 T_{ij} / \partial y_i \partial y_j$ , neglecting external forces and using the fact that at the observer position  $p = c_0^2 \rho$ , we can use Eq. (2.31) to write Eq. (2.42) in integral formulation

$$p(\vec{x}, t) = \int_{-\infty}^t \int_V \frac{\partial^2 T_{ij}}{\partial y_i \partial y_j} G_0(\vec{x}, t | \vec{y}, \tau) d^3 \vec{y} d\tau - \int_{-\infty}^t \int_S \left( p \frac{\partial G_0}{\partial y_i} - G_0 \frac{\partial p}{\partial y_i} \right) n_i d^2 \vec{y} d\tau. \quad (2.46)$$

Since the free field Green's function  $G_0$  is not tailored for this problem, we cannot discard the second integral on the right hand side.

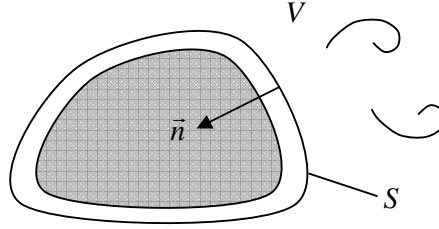


Figure 2-5: Foreign body in a flow.

Using partial integration, the symmetry in Eq. (2.33),  $\partial G / \partial t = -\partial G / \partial \tau$  ('listening later is the same as shooting earlier'), and substituting  $G_0$  from Eq. (2.32), we can rewrite Eq. (2.46) as Curle's equation

$$4\pi p(\vec{x}, t) = \frac{\partial^2}{\partial x_i \partial x_j} \int_V \left[ \frac{T_{ij}}{\|\vec{x} - \vec{y}\|} \right] d^3 \vec{y} - \frac{\partial}{\partial t} \int_S \left[ \frac{\rho_i u_{in}}{\|\vec{x} - \vec{y}\|} \right] n_i d^2 \vec{y} + \frac{\partial}{\partial x_j} \int_S \left[ \frac{P_{ij} + \rho_i u_{in} u_{ij}}{\|\vec{x} - \vec{y}\|} \right] n_i d^2 \vec{y} \quad (2.47)$$

where  $P_{ij} = p_i \delta_{ij} - \tau_{ij}$  and the square brackets indicate that the function should be evaluated at emission time  $t - \|\vec{x} - \vec{y}\| / c_0$ . The first term on the right hand side represents the sound from the turbulence in the fluid, as in Eq. (2.44). The remaining terms show that the effect of the body can be written in terms of surface monopoles and dipoles. The monopole strength is the mass flux crossing the surface, and the dipole strength represents the momentum flux through the surface and the stress applied to the surface. For a motionless, rigid body the velocity at the surface vanishes, so that the dipole sound from the body is completely determined by the  $P_{ij}$  term:

$$4\pi p(\bar{x}, t) = \frac{\partial}{\partial x_j} \int_S \left[ \frac{P_{ij}}{\|\bar{x} - \bar{y}\|} \right] n_i d^2 \bar{y}. \quad (2.48)$$

For a compact body at position  $\bar{\xi}$  and a far field observer, retarded time variations over the surface of the body are negligible. By defining the instantaneous force applied *by the fluid to the body* as

$$F_j = \int_S P_{ij} n_i d^2 \bar{y}, \quad (2.49)$$

we can write

$$4\pi p(\bar{x}, t) = \frac{\partial}{\partial x_j} \left[ \frac{F_j}{r} \right] \approx -\frac{\cos \theta_d}{c_0 r} \left[ \frac{\partial F}{\partial t} \right], \quad (2.50)$$

where  $r = \|\bar{x} - \bar{\xi}\|$  and the second equality follows from Eq. (2.38). This leads to the important conclusion that all compact rigid bodies in turbulent flow generate dipole sound due to the unsteady forces acting on them, similar to the force dipole discussed in Section 2.4. We can again use dimensional analysis to estimate how this sound depends on the flow parameters. For a characteristic surface dimension  $D$  and flow speed  $U$ , the magnitude of the forces can be estimated by  $F \sim \rho_0 U^2 D^2$ . Using  $\partial/\partial x \sim 1/\lambda \sim M/D$ , as in Eq. (2.45), we obtain

$$\frac{\overline{p^2}}{(\rho_0 c_0^2)^2} \sim \left( \frac{D}{r} \right)^2 M^6. \quad (2.51)$$

The dipole sound (in proportional frequency bands) is found to be proportional to the *sixth* power of the flow speed, which means that the body forces generate sound more effectively than the surrounding (low Mach number) free turbulence by a factor of  $M^{-2}$ . For the flows considered in this thesis, with  $M \sim 0.2$ , this corresponds to an increase in sound level of 14 dB. Thus, for low-frequency sound from a compact cylinder or airfoil dominated by unsteady lift, we expect the sixth power law and the dipole directivity pattern depicted in Figure 2-4, with maximum radiation in the cross-flow direction.

## 2.7 Scattering of aerodynamic sound by an edge

The previous section dealt with the sound radiation by a compact body in a flow. When the body is *not* compact (e.g. high-frequency airfoil noise), we have to apply a different technique to determine the characteristics of the sound. First, consider a sound source near a large rigid plane surface. A rigid plane is a reflector of sound, as we saw already at the end of Section 2.3 for plane waves impinging on an acoustically hard surface. From the boundary condition of zero normal velocity on the surface, it follows that acoustic wave reflection at a rigid surface is equivalent to the effect of a *mirror source* with the same strength. A practical example of a



mirror source will be discussed in relationship with wind tunnel walls in Section 3.5.3. The sound radiation from a turbulent flow over a rigid plane surface (e.g. the turbulent boundary layer over an airfoil) is very inefficient, because the surface at most doubles the quadrupole sources corresponding to free field turbulence. However, the presence of an *edge* can strongly enhance the radiation efficiency, as will be shown in the following.

Consider an element of turbulence near the edge of a scattering surface (Figure 2-6). This case is representative for the sound generation by a turbulent boundary layer passing the leading- or trailing edge of an airfoil. We would like to determine the far field sound produced by a turbulent eddy with volume  $l^3$ , positioned close to the edge at position  $\bar{x}_e$ . With the source term  $q(\bar{y}, t) = \partial^2 T_{ij} / \partial y_i \partial y_j$ , which is non-zero only in a limited volume  $V$ , partial integration of Eq. (2.31) gives the far field pressure at position  $\bar{x}$  as

$$p(\bar{x}, t) = \int_{-\infty}^t \int_V \frac{\partial^2 G(\bar{x}, t | \bar{y}, \tau)}{\partial y_i \partial y_j} T_{ij} d^3 \bar{y} d\tau, \quad (2.52)$$

where we assumed that the Green's function  $G$  is tailored for the present problem. In order to find the tailored Green's function, it is convenient to use the reciprocity relation Eq. (2.30), which states that  $G$  remains the same if we switch the source and observer positions (and invert emission and observer times). Thus, we have to find an expression for the pressure field  $p_e$  close to the edge, due an impulsive, far field point source. This can be done as follows.

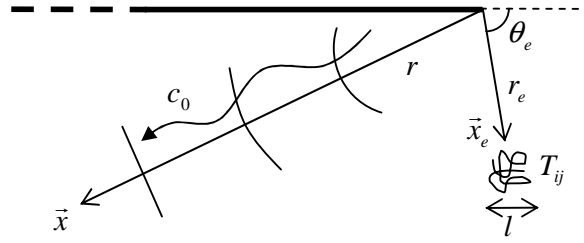


Figure 2-6: The sound of a turbulent quadrupole is scattered by the sharp edge.

Close to the edge singularity the spatial derivatives are much larger than the time derivatives (as will be confirmed below), so that locally the pressure  $p_e$  approaches a solution of the *Laplace equation* in that region:

$$\nabla^2 p_e = 0. \quad (2.53)$$

This means we have a potential flow near the edge, where the velocity is given by  $\bar{u} = \nabla \phi$ , with  $\phi$  the flow potential. The structure of this flow can be found by conformal mapping: the edge coordinates  $\bar{x} = (x_1, x_2)$  are mapped to complex space using the transformation  $Z^{\frac{1}{2}}$ , with  $Z = x_1 + ix_2$ . The edge flow field then corresponds to a uniform flow in the upper half of the complex space, above a horizontal hard wall (Figure 2-7). Since the flow potential in the complex space is proportional to the real part of the complex coordinate, it follows that in edge coordinates the potential is proportional to

$$\phi \sim r_e^{1/2} \sin(\theta_e/2). \quad (2.54)$$

This potential satisfies the Laplace equation and the boundary condition of zero normal velocity on the surface. The velocity at the edge is indeed singular, so that the use of Eq. (2.53) is justified.

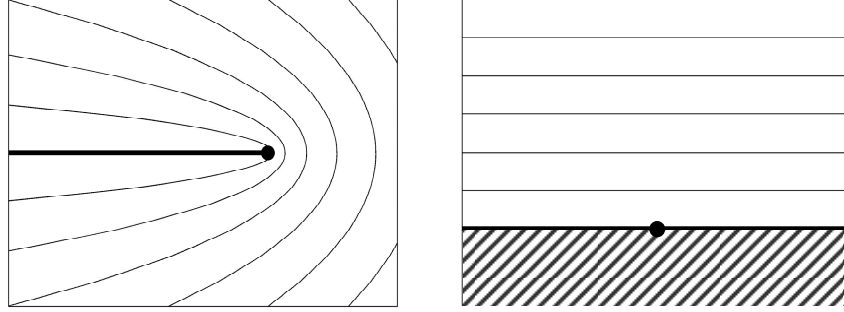


Figure 2-7: Potential flow field around edge in real space (left) and complex space (right).

Now from the momentum equation, Eq. (2.6) (without mean flow), it follows that  $p_e = -\rho_0 \partial \phi / \partial t$ , so that for harmonic pressure fluctuations  $p_e = -\rho_0 i \omega \phi$ . This means that Eq. (2.54) is also valid for  $p_e$ , and therefore also for  $G$ . Furthermore, the sound from the distant source with unit strength arrives near the edge with an amplitude proportional to  $r^{-1}$ , and to obtain the correct dimension we use the only available length scale  $\lambda \sim k^{-1}$ . This yields

$$G \sim \frac{1}{r} (kr_e)^{1/2} \sin(\theta_e/2). \quad (2.55)$$

Now we switch back from the reciprocal problem to the real problem, with the source close to the edge and the observer in the far field. Combination of Eqs. (2.52) and (2.55) then gives

$$\rho(\vec{x}, t) \sim \frac{1}{c_0^2} \int_{\mathcal{V}} T_{ij} \frac{1}{r} k^{1/2} \sin(\theta_e/2) r_e^{-3/2} \frac{\partial r_e}{\partial y_i} \frac{\partial r_e}{\partial y_j} d^3 \vec{y}. \quad (2.56)$$

Using  $k \sim M/l$  for aerodynamically generated sound, as in Eq. (2.45), and estimating the strength of one eddy as

$$\int_{\mathcal{V}} T_{ij} \frac{\partial r_e}{\partial y_i} \frac{\partial r_e}{\partial y_j} d^2 \vec{y} \sim \rho_0 U^2 l^3, \quad (2.57)$$

we obtain for the far field sound scattered by an edge in turbulent flow

$$\frac{\overline{p^2}}{(\rho_0 c_0^2)^2} \sim M^5 \left( \frac{l}{r_e} \right)^3 \left( \frac{l}{r} \right)^2 \sin^2(\theta_e/2). \quad (2.58)$$

This important result shows that the edge noise (in proportional frequency bands) scales with the *fifth* power of the flow speed. Comparison with Eq. (2.45) for free turbulence shows that the edge enhances the acoustic efficiency of the eddy by a factor of  $M^{-3}l^3/r_e^3$ , making it even more effective than the dipole radiation from the compact rigid bodies in Eq. (2.51) at low Mach numbers. The dependence of the edge noise on  $r_e^{-3}$  indicates that only eddies close to the edge contribute to the radiated sound. Since turbulence close to the plane but far from the edge radiates at most as a quadrupole, Eq. (2.58) implies that the sound from a turbulent flow over an airfoil is dominated by edge noise. This can be due to the interaction of boundary layer turbulence with the trailing edge, or due to interaction between incoming turbulence and the leading edge.

## 2.8 Moving sources

In many situations, such as flying aircraft and rotating wind turbine blades, the sound source is moving relative to the observer. In this section we will consider the effect of source motion on the perceived sound level and frequency. From Eqs. (2.31) and (2.32) it follows that in free space

$$p(\vec{x}, t) = \int_{-\infty}^t \int_V \frac{q(\vec{y}, \tau)}{4\pi\|\vec{x} - \vec{y}\|} \delta(t - \tau - \|\vec{x} - \vec{y}\|/c_0) d^3\vec{y} d\tau. \quad (2.59)$$

Now consider a moving point source at position  $\vec{\xi}(\tau)$  (Figure 2-8), with

$$q(\vec{y}, \tau) = \sigma(\tau) \delta(\vec{y} - \vec{\xi}(\tau)), \quad (2.60)$$

where  $\sigma(\tau)$  is the time signal emitted by the source.

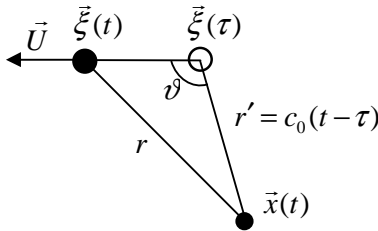


Figure 2-8: The sound arriving at  $\vec{x}(t)$  was emitted by the moving point source at  $\vec{\xi}(\tau)$ .

Substituting Eq. (2.60) into Eq. (2.59) then yields

$$p(\vec{x}, t) = \int_{-\infty}^t \frac{\sigma(\tau) \delta(t - \tau - r'/c_0)}{4\pi r'} d\tau, \quad (2.61)$$

with  $r' = \|\vec{x} - \vec{\xi}(\tau)\|$ , i.e. the distance between source and observer at emission time. Now  $\delta$ -functions have the property that for any function  $h$  and any function  $g$  which has at most simple zeros, i.e.  $(dg/d\tau)_{\tau=\tau_i} \neq 0$  if  $g(\tau_i) = 0$ ,

$$\int_{-\infty}^{\infty} h(\tau) \delta(g(\tau)) d\tau = \sum_i \frac{h(\tau_i)}{|dg/d\tau|_{\tau=\tau_i}}, \quad (2.62)$$

where the right hand side should be summed over all emission times  $\tau_i$  for which  $g(\tau_i) = 0$ . In our case  $g(\tau) = t - \tau - r'/c$  and

$$\frac{dr'}{d\tau} = -U \cos \vartheta, \quad (2.63)$$

with  $U = \|\vec{U}\|$  the absolute value of the source velocity, and  $\vartheta$  the angle between source velocity and source-observer line, both at emission time  $\tau$ . For subsonic source velocity  $U$ ,  $g$  has only one zero,  $\tau_1 = t - r'/c$ , and it follows from the above equations that

$$p(\vec{x}, t) = \frac{\sigma(\tau_1)}{4\pi r' (1 - M \cos \vartheta)}, \quad (2.64)$$

with  $M = U/c$  and  $\vartheta$  at emission time  $\tau_1$ . This important result shows that, through the factor  $(1 - M \cos \vartheta)^{-1}$ , the pressure is amplified in the forward arc, and reduced in the rear arc. This amplitude effect is called *convective- or Doppler amplification*.

The *frequency* of the perceived sound corresponds to  $f d\tau_1/dt$ , where  $f$  is the frequency of the source signal  $\sigma$ . From  $\tau_1 = t - r'/c$  and Eq. (2.63) it follows that

$$\frac{d\tau_1}{dt} = 1 - \frac{1}{c_0} \frac{dr'}{d\tau_1} \frac{d\tau_1}{dt} = 1 + M \cos \vartheta \frac{d\tau_1}{dt}, \quad (2.65)$$

so that

$$\frac{d\tau_1}{dt} = \frac{1}{1 - M \cos \vartheta}. \quad (2.66)$$

Thus, the sound radiated by the moving source of frequency  $f$  is heard by the stationary observer at the *Doppler shifted* frequency  $f/(1 - M \cos \vartheta)$ : for an approaching source ( $\cos \vartheta > 0$ ) the perceived frequency is higher than the source frequency, and for receding sources ( $\cos \vartheta < 0$ ) lower.

It is interesting to consider the effect of motion on the mass and force sources discussed earlier in Section 2.4. For a point source moving at uniform speed  $\vec{U}$ , the mass and momentum equations become

$$\frac{\partial \rho}{\partial t} + \rho_0 \nabla \cdot \bar{u} = \rho_0 \frac{\partial \hat{\beta}}{\partial t} \delta(\bar{x} - \bar{U}t) \quad (2.67)$$

$$\rho_0 \frac{\partial \bar{u}}{\partial t} + \nabla p = \bar{F} \delta(\bar{x} - \bar{U}t). \quad (2.68)$$

These equations can be combined to yield the wave equation

$$\frac{1}{c_0^2} \frac{\partial^2 p}{\partial t^2} - \nabla^2 p = \rho_0 \frac{\partial}{\partial t} \left\{ \frac{\partial \hat{\beta}}{\partial t} \delta(\bar{x} - \bar{U}t) \right\} - \frac{\partial}{\partial x_i} \{ F_i \delta(\bar{x} - \bar{U}t) \}. \quad (2.69)$$

By comparison with Eq. (2.64) we can write the solution as

$$p(\bar{x}, t) = \rho_0 \frac{\partial}{\partial t} \left[ \frac{\partial \hat{\beta} / \partial t}{4\pi r' (1 - M \cos \vartheta)} \right] - \frac{\partial}{\partial x_i} \left[ \frac{F_i}{4\pi r' (1 - M \cos \vartheta)} \right], \quad (2.70)$$

where the square brackets indicate that the term should be evaluated at emission time  $\tau_1$ . Many wavelengths from the source, the largest terms in Eq. (2.70) arise from the differentiation of the emission time  $\tau_1$ . We saw in Eq. (2.66) that  $\partial \tau_1 / \partial t = (1 - M \cos \vartheta)^{-1}$ , and we can similarly derive that  $\partial \tau_1 / \partial x_i = -r'_i / \{ c_0 r' (1 - M \cos \vartheta) \}$ , which yields

$$p(\bar{x}, t) = \frac{\rho_0 \left[ \partial^2 \hat{\beta} / \partial t^2 \right] + [\partial F_r / \partial t] / c_0}{4\pi r' (1 - M \cos \vartheta) (1 - M \cos \vartheta)}, \quad (2.71)$$

where  $\partial F_r / \partial t$  is the component of  $\partial \bar{F} / \partial t$  in the direction of the observer. We see that, while the pressure from the 'mathematical' point source in Eq. (2.64) was modified by the Doppler factor  $(1 - M \cos \vartheta)^{-1}$  due to the motion of the source, the mass and force sources in Eq. (2.71) are modified by the *square* of this factor. For dipole radiation from a rotating wind turbine blade with a tip Mach number of  $M = 0.2$ , a Doppler amplification factor of 4 dB is found for an observer in the rotor plane, which is quite significant. In practice the mass and force terms may also be coupled, which makes the situation even more complicated. For example, for a compact pulsating sphere at low Mach number it can be shown [1] that the pressure scales with the Doppler factor raised to the power 3.5. The important conclusion is that source motion will modify the amplitude by the factor  $(1 - M \cos \vartheta)$ , but the power to which this factor should be raised depends on the nature of the source.

## 2.9 Airfoil noise characteristics

Following the discussion of basic aeroacoustic source mechanisms in the previous sections, the present section will give a general overview of airfoil noise characteristics. A more comprehensive survey of previous experimental and theoretical work is given in Chapters 5-8. The airfoil noise features discussed here will be used for the interpretation of the experimental results in subsequent chapters. The flow around an airfoil is schematically depicted in

Figure 2-9. In the general case, a turbulent flow approaches the leading edge, a boundary layer develops along the surface, and turbulence from this boundary layer is convected past the trailing edge. The pressure difference between the suction and pressure side of the blade will cause a tip vortex at the side-edge. Since free turbulence is a very inefficient sound source at low Mach numbers (Section 2.5), aerodynamic noise from the airfoil will be dominated by the interaction between turbulence and the airfoil surface.

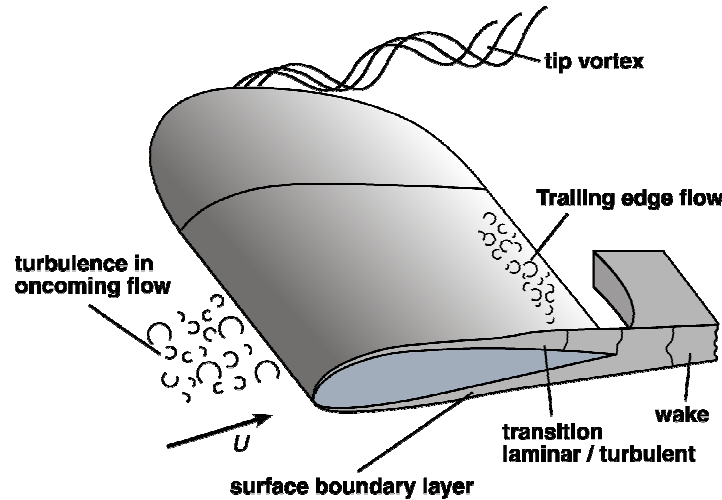


Figure 2-9: Aerodynamic noise source mechanisms on an airfoil [5].

The acoustic effect of inflow turbulence depends on the length scale  $\Lambda$  of the incident eddies. For a mean flow velocity  $U$ , the disturbances occur at a frequency  $f \approx U/\Lambda$ , which is equal to the frequency of the emitted sound  $f = c/\lambda$ . Thus, if the incident eddies are much larger than the airfoil chord  $C$ , the acoustic wavelength will also be much larger than the chord, so that the airfoil is acoustically *compact*. The eddies will cause a fluctuating force on the complete airfoil, resulting in low-frequency sound which radiates as a compact dipole and has a  $U^6$  speed dependence (Section 2.6). If the eddies are much *smaller* than the airfoil, they will induce only local pressure fluctuations which do not affect the global aerodynamic force. Turbulent eddies approaching the airfoil are distorted by the mean flow, and their sound is scattered at the leading edge, causing high-frequency noise with a  $U^5$  speed dependence (Section 2.7). The importance of inflow-turbulence noise therefore depends on the intensity and spectrum of the incident turbulence. For wind turbine blades, inflow-turbulence may be generated by the atmospheric boundary layer, by the tower wake (for downwind rotors), or by the wake from upwind turbines in a wind farm.

The sound produced by an airfoil in an *undisturbed* inflow is called *airfoil self-noise*. Depending on the flow conditions, several source mechanisms may occur. The structure of the boundary layer depends on the Reynolds number  $Re = UC/\nu$ , where  $\nu$  is the kinematic viscosity. For Reynolds numbers higher than about  $10^6$ , the initially laminar boundary layer will generally become turbulent somewhere along the chord. In our applications the Reynolds number is typically a few millions or more. As the turbulent eddies are convected past the trailing edge, their sound is scattered at the trailing edge, causing broadband noise with a  $U^5$  speed dependence. This *trailing edge noise* is an important noise source for modern large wind turbines, and its characteristics will be discussed in more detail below. If the Reynolds

number is lower than about  $10^5$ , the boundary layer on either airfoil side may remain laminar up to the trailing edge. Upstream radiating noise from the trailing edge may then trigger laminar-turbulent transition or boundary layer instabilities (Tollmien-Schlichting waves), which in turn radiate as trailing edge noise. If such a feedback loop occurs, high levels of (tonal) noise may be generated. This type of whistling noise is called *laminar-boundary-layer-vortex-shedding-noise*, and may be prevented by tripping the boundary layer, inducing transition from laminar to turbulent flow.

As the angle-of-attack increases, at some point the flow will separate from the airfoil. This corresponds to so-called *stall*. Stall causes a substantial level of unsteady flow around the airfoil, which may lead to a significant increase in noise. For mildly separated flow this *separation-stall noise* appears to be radiated from the trailing edge, whereas deep stall causes radiation from the airfoil over the entire chord.

Another source mechanism occurs if the trailing edge thickness  $h$  is increased above a critical value. This *blunt trailing edge noise* involves periodic Von Karman type vortex shedding from the trailing edge, leading to tonal noise. The frequency of the tone is determined by the Strouhal number  $St = fh/U \approx 0.1$ , and the amplitude depends strongly on the trailing edge geometry. If the trailing edge thickness is reduced to  $h/\delta^* < 0.3$ , with  $\delta^*$  the boundary layer displacement thickness, the tone disappears, but the broadband part of the spectrum remains the same as for a sharp edge.

*Tip noise*, finally, is associated with the convection of turbulence over the tip edge. Separated flow at the side-edge may cause additional tip noise.

In the following the characteristics of trailing edge noise will be discussed in more detail. The interaction of turbulence with an edge was studied theoretically by Ffowcs Williams and Hall [10]. Using the Green's function for a semi-infinite plane, the following expression was derived:

$$\frac{\overline{p^2}}{(\rho_0 c_0^2)^2} \sim M^5 \frac{L \delta^*}{r^2} \cos^3 \alpha \sin^2(\theta/2) \sin \phi, \quad (2.72)$$

where  $L$  is the spanwise length and the angles are defined in Figure 2-10. The boundary layer displacement thickness  $\delta^*$  represents a characteristic turbulence correlation scale. Eq. (2.72) illustrates a number of interesting properties of trailing edge noise. Firstly, the sound level scales with the fifth power of the flow speed, as we saw already in Section 2.7. Secondly, the pressure is proportional to  $\sin^2(\theta/2)$ , which means that maximum radiation occurs for  $\theta = \pi$  (i.e. in direction of the leading edge for trailing edge noise, and vice versa). This radiation pattern is different from the compact dipole in Section 2.6, which for an oscillating lift force has maximum intensity in the cross-flow direction. Similar to the compact dipole, the radiated trailing edge noise has reversed phase on opposite sides of the airfoil. Thirdly, Eq. (2.72) shows that the sound pressure may be reduced by yawing or sweeping the edge by an angle  $\alpha$  to the flow direction: theoretically, a yaw angle of  $\pi/4$  already gives a reduction of almost 5 dB. Extending this idea, Howe [11] calculated the theoretical noise reduction from trailing edge *serrations*. Chapter 8 of this thesis describes the results of an experimental study in which this concept is implemented on a wind turbine.

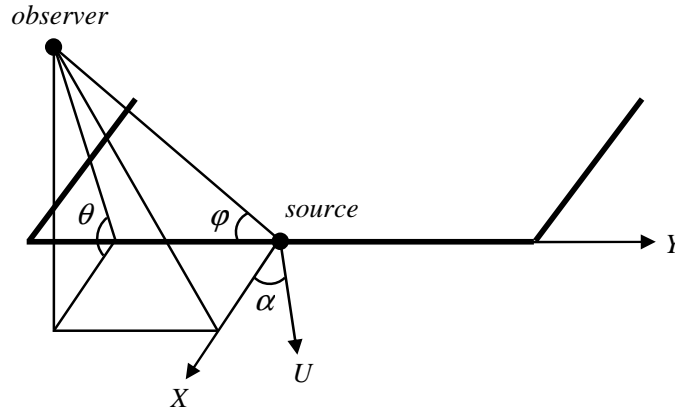


Figure 2-10: Definition of angles for trailing edge noise.

The characteristic *frequency* of trailing edge noise is determined by the Strouhal number  $St = f \delta^* / U$ . The peak of the broadband trailing edge noise spectrum occurs at a Strouhal number of order 0.1. Since  $f = c_0 / \lambda \sim U / \delta^*$ , the acoustic wavelength will be of the order of the airfoil chord  $C$  at a Mach number of  $M \sim \delta^* / C$ . Because the dependence of  $\delta^*$  on Reynolds number is weak for a turbulent boundary layer, the source behaviour will gradually change from a compact dipole to edge noise with increasing Mach number (Figure 2-11). Since usually  $\delta^* \ll C$ , the transition between the two regimes may occur at relatively low subsonic speeds.

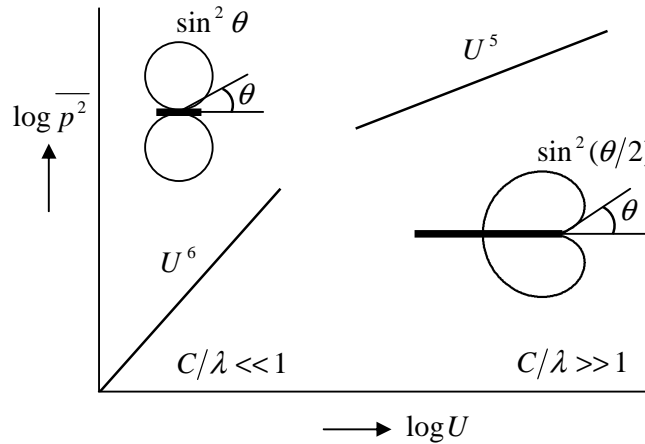


Figure 2-11: Speed dependence of trailing edge noise [4].

Amiet [12] used a different theoretical approach and analyzed trailing edge noise in terms of convecting surface pressure patterns ('gusts'). This fluctuating pressure field can be regarded as the 'footprint' of the boundary layer turbulence, and its temporal and spatial transform - the wavenumber-frequency spectrum - can be used to compute trailing edge noise. The theory considers the linear response of the flow around a semi-infinite flat plate to perturbations in the flow. Amiet included the effect of a finite chord on the radiation pattern, and found the same characteristics for the compact and edge noise limits as indicated in Figure 2-11. In the



transition region the directivity pattern was found to exhibit multiple lobes and a reduced intensity in the direction of the leading edge (see Figure 6-5, pg. 101). The different trailing edge noise theories were reviewed and unified by Howe [13]. He also studied convective effects and the implications of applying the Kutta condition (i.e. to impose a stagnation point at the trailing edge, so that the flow leaves the edge tangentially within the framework of an inviscid flow theory). Besides analytical studies, since the 1990's increasingly sophisticated *numerical* methods have been applied as well to calculate trailing edge noise [e.g. 14-18].

A comprehensive *experimental* study into trailing edge noise was performed by Brooks, Pope, and Marcolini [19]. They performed acoustic and aerodynamic wind tunnel tests on a series of NACA0012 airfoils with varying chord, at different flow speeds and angles of attack. Based on their experimental database, and using the theoretical scaling laws, they developed a semi-empirical prediction method for the above-mentioned airfoil self-noise mechanisms. By using calculated or measured aerodynamic input, their code can also be used to estimate the noise for other airfoil shapes. In Chapter 6 this method is applied to predict the trailing edge noise of rotating wind turbine blades.

## References

- [1] A.P. Dowling and J.E. Ffowcs Williams, *Sound and Sources of Sound*, Ellis Horwood Limited, 1983.
- [2] S.W. Rienstra and A. Hirschberg, *An Introduction to Acoustics*, Eindhoven University of Technology, 2001.
- [3] M.E. Goldstein, *Aeroacoustics*, McGraw-Hill, 1976.
- [4] W.K. Blake, *Mechanics of Flow-Induced Sound and Vibration*, Volumes I and II, Academic Press, 1986.
- [5] S. Wagner, R. Bareiss, and G. Guidati, *Wind Turbine Noise*, Springer, 1996.
- [6] A.D. Pierce, *Acoustics - An Introduction to Its Physical Principles and Applications*, McGraw-Hill, 1981.
- [7] H.S. Ribner, Reflection, transmission, and amplification of sound by a moving medium, *Journal of the acoustical society of America*, Vol. 29, No. 4, 1957.
- [8] P.M. Morse and K.U. Ingard, *Theoretical Acoustics*, Princeton University Press, 1968.
- [9] R.K. Amiet, Refraction of sound by a shear layer, *Journal of Sound and Vibration* 58, Vol. 4, 1978.
- [10] J.E. Ffowcs Williams and L.H. Hall, Aerodynamic sound generation by turbulent flow in the vicinity of a scattering half plane, *Journal of Fluid Mechanics*, Vol. 40, part 4, 1970.
- [11] M.S. Howe, Noise produced by a sawtooth trailing edge, *The Journal of the Acoustic Society of America* 90, 1991.
- [12] R.K. Amiet, Noise due to turbulent flow past a trailing edge, *Journal of Sound and Vibration* 47, Vol. 3, 1976.
- [13] M.S. Howe, A review of the theory of trailing edge noise, *Journal of Sound and Vibration* 61, Vol. 3, 1978.
- [14] T. Lutz, A. Herrig, W. Würz, M. Kamruzzaman, E. Krämer, Design and wind tunnel verification of low noise airfoils for wind turbines, *AIAA Journal*, Vol 45, No. 4, 2007, pp 779-792.
- [15] M. Wang and P. Moin, Computation of Trailing-Edge Flow and Noise Using Large-Eddy Simulation, *AIAA Journal* Vol. 38, No. 12, 2000.
- [16] S. Glegg, B. Morin, O. Atassi, R. Reba, Using RANS Calculations of Turbulent Kinetic Energy to Provide Predictions of Trailing Edge Noise, *AIAA Paper* 2008 2993, 2008.
- [17] R.D. Sandberg, N.D. Sandham, Direct numerical simulation of turbulent flow past a trailing edge and the associated noise generation, *Journal of Fluid Mechanics* 596, 2008.
- [18] R. Ewert and W. Schröder, On the simulation of trailing edge noise with a hybrid LES/APE method, *Journal of Sound and Vibration* 270, Vol. 3, 2004.
- [19] T.F. Brooks, D.S. Pope, and M.A. Marcolini, *Airfoil self-noise and prediction*, NASA Reference Publication 1218, 1989.



## Chapter 3

### Detection of sound sources with a phased microphone array

This chapter describes how sound sources can be located and quantified using an array of microphones. Phased arrays have a long history in astronomy, sonar, and seismology. The development of microphone arrays for aeroacoustic testing started in the 1970's [1,2], as an alternative to the acoustic mirror [3,4]. An elliptic mirror focuses the sound rays radiated from a potential source location to its focal point, where a microphone is placed. However, the mirror needs to be traversed for each potential source location, which makes the measurements time-consuming. The main advantage of a microphone array is that only a short measurement time is needed, because the scanning of possible source locations can be performed afterwards. The increasing capacity of computers and data acquisition systems, which enabled larger numbers of microphones, longer acquisition times, and higher sample frequencies, stimulated the fast development of the array technique since the 1990's [5-11]. Nowadays, microphone arrays are widely used for aeroacoustic testing on both stationary and moving sources.

In order to provide an intuitive understanding of the technique, Section 3.1 gives a qualitative description of delay-and-sum beamforming in the time domain, and introduces some relevant aspects of array results. In Section 3.2 the method is formally derived and transferred to the frequency domain. Section 3.3 then describes conventional beamforming, a variant of delay-and-sum beamforming which is generally used in this thesis. The effects of flow are addressed in Section 3.4, and some special processing techniques are discussed in Section 3.5. Section 3.6 deals with the quantification of array results using a power integration method. Finally, Section 3.7 describes the application of the array technique to moving sound sources. More details about the background of the array processing method and the implementation at NLR can be found in Refs. [12-14].

#### 3.1 Delay-and-sum beamforming in the time domain

Consider a compact sound source in a homogeneous stagnant medium with sound speed  $c$ . The sound field is measured by an array of microphones (Figure 3-1). For simplicity a linear array is shown here, but the explanation is equally valid for a two-dimensional planar array. Due to the difference in distance  $r$ , the sound will arrive slightly earlier at microphone  $m_1$  than at  $m_2$ . Furthermore, since the pressure amplitude decreases with distance, the amplitude of the acoustic pressure  $p$  will be lower on  $m_2$  than on  $m_1$ . Now suppose we know the source is located in a specific plane (e.g. the wing of an aircraft or the rotor of a wind turbine), but the position *within* this plane is unknown. Then the source location can be determined on the basis of the measured signals as follows: first, a scan grid is defined in the plane where the

source is expected. For each scan position, the microphone signals are shifted to account for the time the sound needs to travel from the scan position to the microphone. In addition, the amplitudes are adjusted to account for the distance between the scan position and the microphone. Next, the time-shifted, amplitude-adjusted signals from all microphones are summed. This procedure is called delay-and-sum.

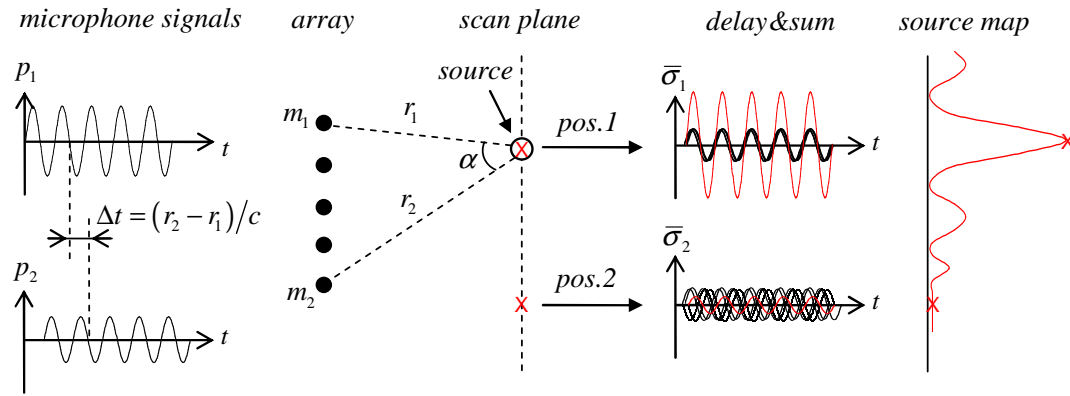


Figure 3-1: Delay-and-sum beamforming.

If a sound source is present at a given scan position (position 1 in Figure 3-1), the shifted microphone signals will be in phase and their sum will have a high amplitude. If no source is present (position 2), the shifted signals will have random phase and the amplitude of their sum will be small. Thus, the phased array essentially amplifies the sound from the scan position (or focal point) with respect to sound from other directions. By plotting the (squared) amplitude as a function of scan position, a so-called *source map* is obtained. This source map shows peaks at the source locations. The strength of a source can be determined by dividing the reconstructed peak amplitude in the source map by the number of microphones. In the case of a planar array a two-dimensional source map is obtained and the amplitudes can be indicated by colors (Figure 3-2).

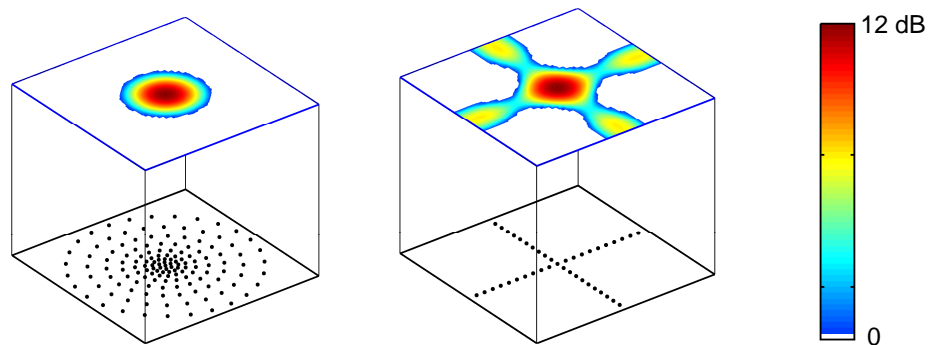


Figure 3-2: Simulated acoustic source maps of a 2 kHz point source for a random array (left) and a cross array (right). The size of the cube is  $1 \text{ m}^3$ .

The delay-and-sum technique illustrates several aspects of the beamforming methods used in this thesis. First, the main peak in the source map has a certain width, which determines the *resolution* of the array. In order to distinguish two different sources, their distance should be

larger than the peak width at 3 dB below the peak level: the narrower the peak, the higher the resolution. The non-zero peak width can be understood if we consider a scan position just next to the actual source position. The time-shifted microphone signals for this position will still be partly in phase, resulting in a non-zero reconstructed amplitude. For a given scan position next to the actual source, the phase error between the shifted signals will decrease with increasing wavelength, resulting in a higher reconstructed amplitude. Thus, the resolution of the array decreases with increasing wavelength, and therefore increases with frequency  $f$  (Figure 3-3). Similarly, it can be deduced that the resolution increases with the opening angle  $\alpha$  of the array, so that the peak width is roughly proportional to  $r/Df$ , where  $D$  is the size of the array. Note that the opening angle, and thus the effective array size, decreases when the source is not in front of the array. Thus, the array resolution decreases for oblique source directions (Figure 3-3).

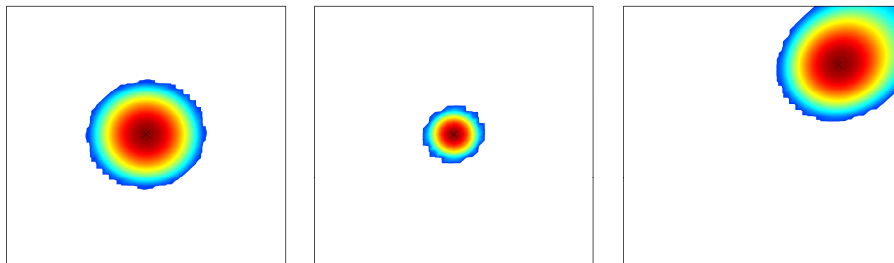


Figure 3-3: Simulated random-array source maps for 2 kHz (left), 4 kHz (middle), and for an oblique 2-kHz source (right).

Besides the main peak (or main lobe), the source map also shows *side lobes*, local maxima around the source position. These spurious sources are an inevitable consequence of the finite number of microphones in the array, and are difficult to distinguish from real secondary sources. Therefore, an important requirement of the array design is to keep the side lobe levels as low as possible. This can be achieved by the use of 'random arrays', in which the periodicity in microphone spacing is reduced (Figure 3-2).

In principle, multiple parallel scan planes (or any three-dimensional grid) can be used to estimate the distance to an unknown source. However, it should be noted that for a planar array the depth resolution (i.e. the resolution in the direction perpendicular to the array surface) is much lower than the lateral resolution. As a result, the three-dimensional main lobe of a point source has the shape of a cigar, with its long axis pointing to the array. In many cases this low depth resolution is actually an advantage, since the array results are rather insensitive to small deviations in distance (e.g. for curved wings or rotor blades).

Note that in the above explanation of the delay-and-sum technique no assumptions were made regarding the nature of the source. The method only requires that the pressure disturbance travels with the speed of sound, and that the pressure amplitude is inversely proportional to the distance. This is true for monopole-type sources in the free field, and in the acoustic far field also for dipoles and quadrupoles (see Chapter 2). If the source has a non-uniform directivity, the reconstructed source strength will be the average value over the solid angle covered by the array. Another requirement for beamforming is that the source radiates sound coherently in the direction of the array. The above explanation also shows that delay-and-sum beamforming is *not* an inverse method in the sense that a source distribution is

'sought' which matches the incoming sound field. The method simply performs an operation on the measured signals and involves no fitting or iterative procedures.

Delay-and-sum beamforming with a phased array is similar to source detection using parabolic or elliptic antennas. However, phased arrays have a number of important advantages. Whereas antennas must be physically steered to each scan position, so that many time-consuming measurements are needed to obtain a complete source map, a phased array only needs one measurement, and the scanning is done afterwards. The electronic processing also provides the flexibility to include e.g. flow effects, moving sources, or spatial weighting of the microphone signals, whereas for an antenna the time delays and weighting are fixed because they are imposed by the geometry. Furthermore, phased array processing can be performed in the frequency domain, which allows the use of several special data analysis techniques.

### 3.2 From time domain to frequency domain

In order to enable beamforming, we need to know how the sound propagates from the unknown source(s) to the microphones. We will assume the source behaves like a *monopole*, i.e. a point source with uniform directivity. From the inhomogeneous wave equation (see Section 2.4)

$$\frac{1}{c^2} \frac{\partial^2 p}{\partial t^2} - \nabla^2 p = \sigma_0(t) \delta(\vec{x} - \vec{\xi}_0), \quad (3.1)$$

where  $\sigma_0(t)$  is the source signal and  $\vec{\xi}_0$  the source position, it follows that the pressure field of the monopole is given by:

$$p(\vec{x}, t) = \frac{\sigma_0(t - \Delta t_0)}{4\pi r_0}, \quad (3.2)$$

where  $r_0 = \|\vec{x} - \vec{\xi}_0\|$  and  $\Delta t_0 = r_0 / c$ . Thus, the acoustic pressure disturbance travels at the speed of sound and its amplitude is inversely proportional to the distance.

Now consider an array of  $N$  microphones which are located in some unknown sound field at positions  $\vec{x}_n = (x_n, y_n, z_n)$ . The acoustic pressure fluctuations measured by the microphones are  $p_n(t)$ . Using time-domain delay-and-sum beamforming, as explained in the previous section, the signal from a potential source at some scan position  $\vec{\xi}$  can be estimated as follows:

$$\bar{\sigma}_{dns}(t) = \frac{1}{N} \sum_{n=1}^N 4\pi r_n p_n(t + \Delta t_n), \quad (3.3)$$

with  $r_n = \|\vec{x}_n - \vec{\xi}\|$  and  $\Delta t_n = r_n / c$ . Thus, the microphone signals are shifted in time and adjusted in amplitude, assuming that the potential source at  $\vec{\xi}$  behaves like a monopole. The factor  $4\pi$  ensures that the estimated source strength  $\bar{\sigma}_{dns}(t)$  corresponds to that of a monopole if the scan position coincides with a source position. This can be easily verified by

inserting the monopole pressure field from Eq. (3.2) into the measured pressures  $p_n(t)$  in Eq. (3.3). In that case  $\bar{\sigma}_{dns}(t) = \sigma_0(t)$  if  $\bar{\xi} = \bar{\xi}_0$ . As argued before, the assumption that the potential source behaves like a monopole does not mean the method is restricted to monopoles. In fact, if the array is located in the acoustic far field and covers only a small solid angle (so that directivity variations over the array surface are small), the radiation field of *any* stationary source can be locally approximated by the radiation field of a monopole. If directivity variations cannot be neglected, the estimated source strength will simply be the (weighted) average value over the solid angle covered by the array. Thus, for most applications the use of a multipole source model has limited added value.

Using the (discrete) Fourier transform (see Appendix), delay-and-sum beamforming can be transposed to the frequency domain without loss of generality. The pressure field of a monopole source at  $\bar{\xi}_0$  then becomes:

$$P(\bar{x}) = \frac{a_0 \cdot e^{-i\omega \Delta t_0}}{4\pi r_0}, \quad (3.4)$$

where  $P$  and  $a_0$  are the Fourier transforms of  $p$  and  $\sigma_0$ , respectively, and depend on frequency  $f$ . Delay-and-sum beamforming in the frequency domain is described by:

$$\bar{a}_{dns} = \frac{1}{N} \sum_{n=1}^N 4\pi r_n P_n e^{i\omega \Delta t_n} \equiv \frac{1}{N} \sum_{n=1}^N \frac{P_n}{g_n}, \quad (3.5)$$

where  $\bar{a}_{dns}$  and  $P_n$  are the Fourier transforms of  $\bar{\sigma}_{dns}$  and  $p_n$  respectively. Thus, Eqs. (3.4) and (3.5) are the frequency-domain equivalents of Eqs. (3.2) and (3.3), and the time shift  $\Delta t_n$  is replaced by the phase shift  $\omega \Delta t_n$ . Note that the *steering function*  $g_n = (e^{-i\omega \Delta t_n} / 4\pi r_n)$ , as defined in Eq. (3.5), corresponds to the *transfer function*  $P/a$  of the Helmholtz equation (see Section 2.2) for an assumed monopole source at scan position  $\bar{\xi}$ :

$$-\left(\frac{\omega}{c}\right)^2 P - \nabla^2 P = a\delta(\bar{x} - \bar{\xi}). \quad (3.6)$$

The transfer function describes the relation between the source amplitude  $a$  and the pressure field  $P$  of the assumed source. *Thus, delay-and-sum beamforming basically comes down to applying the inverse transfer function for an assumed monopole source at a certain scan position to the microphone signals, and summing the result.*

### 3.3 Conventional beamforming

This section describes *conventional beamforming*, a variant of delay-and-sum beamforming which is generally used in this thesis. Using the vector notation  $\mathbf{P} = (P_1 \dots P_N)^T$  and  $\mathbf{g} = (g_1 \dots g_N)^T$ , where  $T$  indicates the transpose, the error between the *measured* pressures  $\mathbf{P}$  and the *estimated* pressures  $\bar{\mathbf{a}}\mathbf{g}$  for scan position  $\bar{\xi}$  can be written as  $E = \|\mathbf{P} - \bar{\mathbf{a}}\mathbf{g}\|$ . For

delay-and-sum beamforming, substitution of the monopole pressure field from Eq. (3.4) in Eq. (3.5) shows that this error reduces to zero if the scan position  $\vec{\xi}$  coincides with the source position  $\vec{\xi}_0$ . For conventional beamforming, the optimum choice for  $\bar{a}$  is determined by minimizing  $E$  for *any* scan position. The length of vector  $E$  can be minimised by choosing  $\bar{a}$  such that  $\mathbf{P} - \bar{a}\mathbf{g}$  is perpendicular to the *steering vector*  $\mathbf{g}$  (Figure 3-4). This leads to:

$$\bar{a} = \frac{\mathbf{g}^* \mathbf{P}}{\|\mathbf{g}\|^2} = \frac{\sum_{n=1}^N g_n^* P_n}{\sum_{n=1}^N g_n^* g_n}, \quad (3.7)$$

where  $*$  indicates the complex conjugate transpose. Substitution of Eq. (3.4) in Eq. (3.7) shows that indeed the correct source pressure is recovered if the scan position  $\vec{\xi}$  coincides with the source position  $\vec{\xi}_0$  (i.e.  $\bar{a} = a_0$  and  $E = 0$  for  $\vec{\xi} = \vec{\xi}_0$ ).

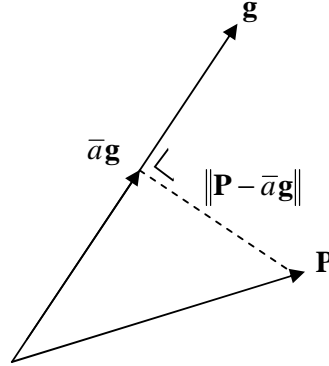


Figure 3-4:  $\|\mathbf{P} - \bar{a}\mathbf{g}\|$  is minimized by choosing  $\bar{a}$  such that  $\mathbf{P} - \bar{a}\mathbf{g}$  is perpendicular to  $\mathbf{g}$ .

When several measurements of  $\mathbf{P}$  (e.g. several blocks of samples) are used to determine an average value for  $\bar{a}$ , generally the phase of  $\bar{a}$  will be different for each measurement. Therefore, it is more meaningful to consider estimated source auto-powers:

$$\bar{A} = \frac{1}{2} |\bar{a}|^2 = \frac{1}{2} \frac{\mathbf{g}^* \mathbf{P} \mathbf{P}^* \mathbf{g}}{\|\mathbf{g}\|^4} = \frac{\mathbf{g}^* \mathbf{C} \mathbf{g}}{\|\mathbf{g}\|^4} = \frac{\sum_{m=1}^N \sum_{n=1}^N g_m^* C_{mn} g_n}{\sum_{m=1}^N \sum_{n=1}^N |g_m|^2 |g_n|^2}, \quad (3.8)$$

where  $\mathbf{C} = \frac{1}{2} \mathbf{P} \mathbf{P}^*$  is the *cross-power matrix*. Since in a stationary sound field the phase *difference* between different microphones will be constant for different measurements, the average cross-power matrix can be used to calculate the average value of  $\bar{A}$ .

The main difference between delay-and-sum beamforming and conventional beamforming is the relative weighting of the microphone signals: whereas in Eq. (3.5) the microphone signals  $P_n$  are *multiplied* by  $r_n$ , in Eq. (3.7) they are *divided* by  $r_n$  (through the



multiplication with  $\mathbf{g}^*$ , the factor  $\|\mathbf{g}\|^2$  is only for normalization). This means that with conventional beamforming, microphones close to the scan position contribute more to the array result than distant microphones. This is beneficial when the microphone signals contain noise, because the noise is not disproportionately amplified for distant microphones. When the distance between array and scan plane is large, the differences in  $r_n$  between the microphones are relatively small, so that delay-and-sum beamforming and conventional beamforming are practically equivalent. *In summary, conventional beamforming can be understood as 'weighted delay-and-sum in the frequency domain'.*

### 3.4 Beamforming in a flow

When the sound source is situated in a medium with uniform flow speed  $\vec{U}$  (e.g. in a wind tunnel), conventional beamforming according to Eq. (3.8) can still be applied. However, the steering function  $g$  should now be determined using the *convective* Helmholtz equation (Section 2.2):

$$\frac{1}{c^2} (i\omega + \vec{U} \cdot \nabla)^2 P - \nabla^2 P = a\delta(\vec{x} - \vec{\xi}). \quad (3.9)$$

Note that, except for the  $\vec{U} \cdot \nabla$  term, this equation is identical to Eq. (3.6). The transfer function  $P/a$  for Eq. (3.9) can be obtained by considering the equivalent case in the 'fly-over' reference frame, where the monopole source moves at subsonic speed  $\vec{U}$  and the fluid is stationary (Figure 3-5, left).

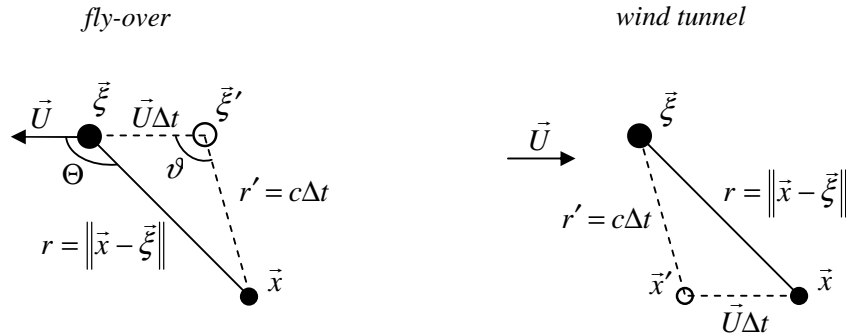


Figure 3-5: Reference frames for sound source in uniform flow.

The sound is emitted when the source is at  $\vec{\xi}'$ , and arrives  $\Delta t$  later at observer position  $\vec{x}$ . In the mean time, the source has travelled to position  $\vec{\xi}$ . For this case the transfer function can be shown to be (Section 2.8)

$$g = \frac{e^{-i\omega \Delta t}}{4\pi r' (1 - M \cos \vartheta)}, \quad (3.10)$$

where  $M$  is the absolute value of the Mach number vector  $\vec{M} = \vec{U}/c$ . Eq. (3.10) shows that  $r' = c\Delta t$  is the proper distance for calculating amplitude reduction and that the source strength is modified by the convective amplification factor  $(1 - M \cos \vartheta)$ . Note that  $r'$  is the distance the sound travels *with respect to the medium*, and that the amplification factor is determined by the speed of the source *with respect to the medium*.

In the wind tunnel reference frame (Figure 3-5, right) the situation is equivalent if the observer (i.e. the microphone) moves with the flow at speed  $\vec{U}$ . Moreover, since a stationary microphone measures the same pressure amplitudes as a moving microphone (only the reception *times* are different), Eq. (3.10) is also valid for a fixed microphone in a wind tunnel. Without flow the sound from the source at  $\vec{\xi}$  would arrive at  $\vec{x}'$  in  $\Delta t$  seconds, but due to convection by the flow the sound arrives at microphone position  $\vec{x}$  in the same time period. Again,  $r'$  is the proper distance and convective amplification occurs due to the flow. Thus, the steering function for the wind tunnel situation can be obtained by rewriting Eq. (3.10) in wind tunnel coordinates, using the following relations (which follow from the geometry):

$$\vartheta = \cos^{-1} \left( M \sin^2 \Theta + \cos \Theta \sqrt{1 - M^2 \sin^2 \Theta} \right) \quad (3.11)$$

$$r' = \frac{r}{-M \cos \Theta + \sqrt{M^2 \cos^2 \Theta - M^2 + 1}}. \quad (3.12)$$

This yields:

$$g = \frac{e^{-i\omega \Delta t}}{4\pi r \sqrt{1 - M^2 \sin^2 \Theta}} = \frac{e^{-i\omega \Delta t}}{4\pi \sqrt{\left(\vec{M} \cdot (\vec{x} - \vec{\xi})\right)^2 + \beta^2 \|\vec{x} - \vec{\xi}\|^2}}, \quad (3.13)$$

where  $\beta^2 = 1 - M^2$ . The emission time delay  $\Delta t$  can be determined from the relation

$$r' = c\Delta t = \|\vec{x} - \vec{U}\Delta t - \vec{\xi}\|, \quad (3.14)$$

which follows directly from Figure 3-5, and is found to be:

$$\Delta t = \frac{1}{c\beta^2} \left( -\vec{M} \cdot (\vec{x} - \vec{\xi}) + \sqrt{\left(\vec{M} \cdot (\vec{x} - \vec{\xi})\right)^2 + \beta^2 \|\vec{x} - \vec{\xi}\|^2} \right). \quad (3.15)$$

Note that for zero flow speed the denominator of Eq. (3.13) simplifies to  $4\pi r$  and  $\Delta t = r/c$ , so that  $g$  reduces to the steering function defined in Eq. (3.5). In this thesis, the steering function of Eq. (3.13) is used in combination with Eq. (3.8) for conventional beamforming with stationary scan planes. Note that this steering function implicitly assumes a Doppler amplification factor of  $(1 - M \cos \vartheta)$ , while in reality this factor may have to be raised to a higher exponent, depending on the nature of the source (see Section 2.8). However, for the present wind tunnel applications, with  $M \sim 0.2$  and  $\vartheta \sim \pi/2$ , generally  $M \cos \vartheta \ll 1$ , so that convective amplification effects will be small. Also note that the measured *frequency* is

not affected by the wind tunnel flow, because the source does not move with respect to the observer.

In an open jet acoustic wind tunnel the sound source is positioned *inside* the flow, but the array microphones are usually located *outside* the flow. The shear layer between the flow and the quiescent air will refract the sound, and in order to retrieve the correct source location and level the array processing algorithm should account for this. The situation is depicted in Figure 3-6, where for simplicity the source is assumed to be on the tunnel centerline. The actual sound path is indicated by the solid line, and the left and right dashed lines show the hypothetical source paths for no flow and for an infinite stream without shear layer. For a given emission angle  $\vartheta$ , the sound is convected inside the flow at propagation angle  $\Theta$ , which can be determined using Eq. (3.11). At the shear layer the sound is refracted and propagates to the observer at the external angle  $\vartheta_e$ . The refraction angle can be determined by assuming an infinitely thin sheet between the flow and the quiescent air and applying Snell's law (Section 2.3), which follows from pressure continuity at the shear layer and states that the surface wave speeds must be the same:

$$U - \frac{c}{\cos \vartheta} = \frac{-c_e}{\cos \vartheta_e}, \quad (3.16)$$

where  $U = \|\vec{U}\|$ , and  $c$  and  $c_e$  are the sound speeds inside and outside the jet respectively (note that the angle definition is inverted with respect to Section 2.3).

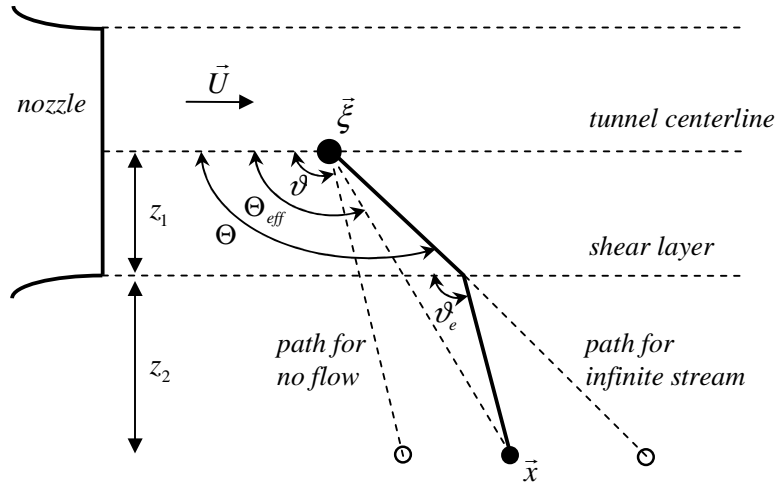


Figure 3-6: Open-jet shear layer refraction.

Eqs. (3.11) and (3.16) can be solved by iteration to yield the actual sound path for a given source and observer position. When the sound path is known, the effect of refraction on the sound *level* can be calculated by assuming conservation of acoustic energy in ray tubes passing through the shear layer. However, the calculation can be simplified significantly for many practical situations. For  $c_e \approx c$  and  $M \cos \vartheta \ll 1$ , Eq. (3.16) shows that  $\vartheta_e \approx \vartheta$ , which means that the ratio between the propagation times inside and outside the jet is equal to  $z_1/z_2$  (Figure 3-6). Thus, the observer position can be determined simply by assuming an

infinite flow with *effective* Mach number  $M_{eff} = M z_1 / (z_1 + z_2)$ . Furthermore, if  $\pi/4 < \vartheta < 3\pi/4$ , it can be assumed that all acoustic energy is transmitted through the shear layer (Section 2.3). This simplified shear layer correction method has been extensively compared [12] with the more sophisticated Amiet method [15] for an infinitely thin shear layer and with a ray acoustics method [16] incorporating the finite thickness of the shear layer. This comparison showed that the differences in array output between the three methods are negligible for  $M < 0.25$  and  $\pi/4 < \vartheta < 3\pi/4$ . Thus, for efficiency reasons the above simplification is generally used in this thesis for open jet wind tunnel tests.

### 3.5 Special techniques

A number of special techniques can be applied to improve the quality of the array results, or to obtain additional information. In this section three techniques will be discussed, namely diagonal removal, microphone weighting, and source coherence.

#### 3.5.1 Diagonal removal

The elements of the main diagonal of the cross-power matrix, i.e. the microphone auto-powers  $C_{nn} = P_n P_n^*$ , do not contain any phase information and are therefore not critical for the array performance. In fact there are many situations in which the auto-powers have an *adverse* effect on the array results. In closed test section wind tunnel measurements for instance, the microphones are usually mounted flush in the tunnel wall, so that they are exposed to the flow. Therefore the microphones will not only detect acoustic pressure disturbances, but also hydrodynamic pressure fluctuations due to the turbulent boundary layer. Since this wind noise is generally incoherent from one microphone to the other, it will only appear in the auto-powers, and not in the (averaged) cross-powers. Thus, the auto-powers have much higher levels than the cross-powers. In the beamforming process, the auto-powers contribute to the reconstructed source level at *each* scan position, because there is no phase cancellation. As a result, the wind noise in the auto-powers will cause a noise floor in the acoustic source maps, which often makes it impossible to detect the actual sound sources, as illustrated in Figure 3-7.

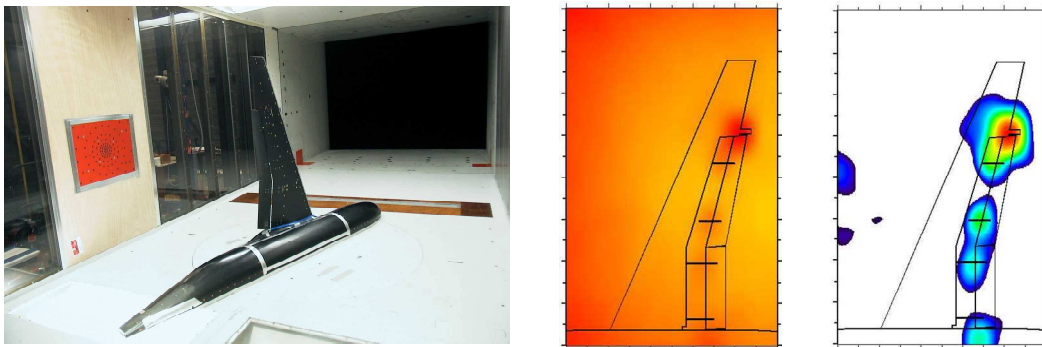


Figure 3-7: Test set-up with wall array in closed wind tunnel (left), and acoustic source maps with (middle) and without (right) auto-powers.

A similar effect occurs in open jet wind tunnel tests and acoustic field measurements. During propagation from the source to the microphone, the sound travels through a turbulent medium (the open jet shear layer or the atmospheric boundary layer), causing small time delay variations which depend on the turbulence characteristics along its path. As a result the measured acoustic signal will be deformed. Since the time delay depends on the propagation path and varies as a function of time, the phase between two microphone signals will also vary, resulting in reduced average cross-power levels. This phenomenon is called *coherence loss*, and typically increases with wind speed, distance between the microphones and frequency. The auto-powers are not affected by coherence loss because they contain no phase information. As a result the auto-powers will be higher than the cross-powers, again causing a noise floor in the acoustic source maps (see for example the right column in Figure 4-7, pg. 60).

A final example of the adverse influence of auto-powers is the presence of extraneous sound sources outside the scan plane (e.g. wind tunnel noise or wind noise in the field). Although these sources are also present in the cross-powers, they are in principle eliminated by the beamforming algorithm (depending on array resolution and side lobe characteristics). However, through the auto-powers they will still contribute to the noise floor in the source maps.

To prevent the above problems, and remove uncorrelated noise from the array results, the auto-powers can be excluded from the beamforming process. In contrast to Section 3.3, where we minimized the error  $\|\mathbf{P} - \bar{\mathbf{a}}\mathbf{g}\|$  between the measured and estimated *pressures*, we now determine the optimum choice for the estimated source amplitude  $\bar{A}$  by minimizing the error  $\|\mathbf{C} - \bar{A}\mathbf{g}\mathbf{g}^*\|$  between the measured and estimated *cross-powers*, for any scan position:

$$E^2 = \sum_{(m,n) \in S}^N |C_{mn} - A g_m g_n^*|^2, \quad (3.17)$$

where for generality  $S$  can be any subset of possible  $(m, n)$ -combinations. For auto-power elimination or *diagonal removal*,  $S$  contains all  $(m, n)$ -combinations except those for which  $m = n$ . The solution of minimizing Eq. (3.17) is:

$$\bar{A} = \frac{\sum_{(m,n) \in S}^N g_m^* C_{mn} g_n}{\sum_{(m,n) \in S}^N |g_m|^2 |g_n|^2}, \quad (3.18)$$

which is equivalent to Eq. (3.8) if  $S$  includes all  $(m, n)$ -combinations. Thus, the previously found expression for conventional beamforming turns out to be optimum for any subset  $S$ . This is not only useful for diagonal removal, but also e.g. for cross-shaped arrays, where the cross-powers between microphones in the same arm can be excluded from the processing in order to suppress side lobes. Note that the denominator of Eq. (3.18) ensures that the correct source pressure is recovered if the scan position coincides with a source position. It should also be noted that, as a result of the exclusion of certain  $(m, n)$ -combinations from the sum in Eq. (3.18), the direct relation with the time signals is lost, i.e. the beamforming no longer

corresponds to 'weighted delay-and-sum in the frequency domain'. This may result in negative values for the estimated source auto-power  $\bar{A}$ . Since negative auto-powers are not physical, these values should be discarded when the array results are quantified (Section 3.6). The beneficial effect of diagonal removal is clearly illustrated in Figure 4-7, pg. 60.

### 3.5.2 Microphone weighting

In order to improve the array results, two types of spatial shading can be applied to the microphone signals. The first weighting method is the frequency-dependent *aperture correction*. As explained in the previous section, array measurements in open jet wind tunnels or in the field often suffer from coherence loss. Since coherence loss increases with frequency and with the distance between the microphones, for higher frequencies the signals on the outer array microphones may have less or no correlation with the inner microphone signals. As a result the outer microphones do not contribute to the reconstructed source level and only add noise to the source map (see for example the right column in Figure 4-11, pg. 64). Since the estimated source amplitude is normalized using the steering functions for *all* microphone pairs included in  $S$ , see Eq. (3.18), this will lead to an underestimation of the source level.

To overcome these drawbacks, the effective array size or *aperture* can be reduced for increasing frequency. This is done by discarding the signals from all microphones whose distance  $d_n$  to the array center (i.e. the average of all microphone positions) is larger than the frequency-dependent 'aperture radius'  $R = B/f$ , where  $B$  is a constant. Thus, microphones inside the aperture radius have weight one and microphones outside this radius have a weight of zero, while the transition between  $d_n/R \approx 0.8$  and  $d_n/R \approx 1.2$  is smoothed using the Error Function. Since the main lobe width is roughly proportional to  $(Rf)^{-1}$ , application of this aperture correction leads to a more or less constant spatial array resolution as a function of frequency (until  $R$  becomes larger than the physical array dimensions). Note that for the wind turbine noise measurements (Chapters 5, 6, and 8) an *elliptical* array was used, to correct for the oblique view angle. In these cases the (frequency-dependent) effective array aperture should also have an elliptical shape.

The second weighting method is the *density correction*. As explained above, at high frequencies effectively only the inner part of the array contributes to the results. In order to maintain a low side lobe level at these high frequencies, the central part of the array usually has a higher microphone density than the outer part. However, at low frequencies this has the unwanted effect that the inner array part is more heavily weighted than the outer part, resulting in a lower array resolution. To prevent this, weight factors can be applied such that the weight per unit area is more or less constant over the surface of the array. Thus, sparsely spaced microphones in the periphery of the array will have a higher weight than the densely spaced microphones at the center. Obviously, this correction only depends on the array layout and is not a function of frequency. The effects of microphone weighting are clearly illustrated in Figure 4-11, pg. 64.

### 3.5.3 Source coherence

When multiple sources are present in a source map, the beamforming method can be readily extended to calculate the coherence between sources or source regions [17]. If  $\bar{a}_1$  and  $\bar{a}_2$  are the estimated complex source amplitudes at scan positions  $\bar{\xi}_1$  and  $\bar{\xi}_2$ , as defined in Eq. (3.7), the *source cross-power* is calculated as follows:

$$\bar{A}_{1,2} = \frac{1}{2} \bar{a}_1 \bar{a}_2^* = \frac{\mathbf{g}_1^* \mathbf{C} \mathbf{g}_2}{\|\mathbf{g}_1\|^2 \|\mathbf{g}_2\|^2}. \quad (3.19)$$

The source cross-power provides the phase difference between the two sources. Moreover, the *coherence* between the two sources can be calculated as follows:

$$\overline{CH}_{1,2} = \frac{\|\bar{a}_1 \bar{a}_2^*\|^2}{\|\bar{a}_1\|^2 \|\bar{a}_2\|^2} = \frac{\|\bar{A}_{1,2}\|^2}{\bar{A}_1 \bar{A}_2} = \frac{\|\mathbf{g}_1^* \mathbf{C} \mathbf{g}_2\|^2}{(\mathbf{g}_1^* \mathbf{C} \mathbf{g}_1)(\mathbf{g}_2^* \mathbf{C} \mathbf{g}_2)}. \quad (3.20)$$

Note that calculation of source coherence is only meaningful when the *average* cross-power matrix is used: without averaging the source coherence is equal to one by definition. Using Eq. (3.20), so-called *coherence maps* can be produced, showing the coherence of all scan positions with respect to one reference source position. In this way mirror sources, which may occur for example in closed wind tunnel sections, can be identified (Figure 3-8).

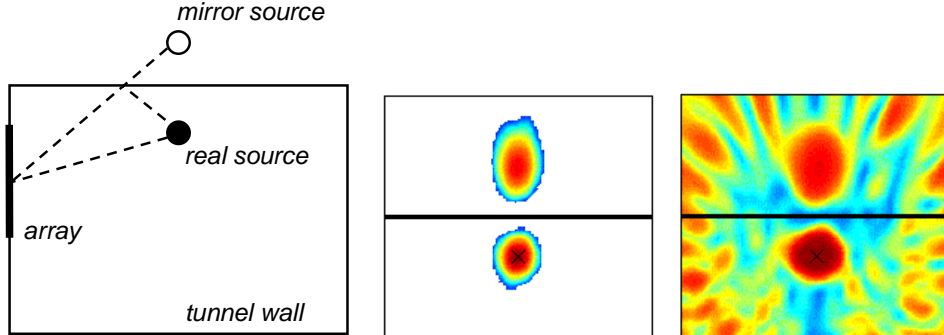


Figure 3-8: Left: test set-up with calibration source in closed wind tunnel. Middle: source map with real source and mirror source. The horizontal black line indicates the height of the tunnel ceiling. Right: coherence map with respect to the real source position, indicating the coherent mirror source and side lobes.

Furthermore, spurious side lobes can be distinguished from real secondary sources, because side lobes are coherent with their main lobe. This feature can be used to eliminate side lobes from source maps [18]. Finally, in the case of spatially extended sources, such as trailing edge noise, the spatial coherence length can be estimated, which is important for the quantification of array results. Analogous to Section 3.5.1, the source coherence method can be generalized to exclude certain elements from the cross-power matrix (e.g. the main diagonal). However, this can lead to unphysical source coherence values (i.e. negative or larger than one), because the direct relation with the time signals is lost.

### 3.6 Quantification of array results

In general we are not only interested in the source *locations*, but also in their *levels*. For well-resolved monopole sources the source level simply corresponds to the peak level in the acoustic source map. However, in practice this situation seldom occurs. Firstly, the main lobes from different sources may overlap or the source may be spatially extended (e.g. trailing edge noise). As a consequence, the peak levels in the source map depend on the extent of the source and on the (frequency-dependent) resolution of the array. Secondly, as explained in Section 3.5.1, the array signals may suffer from coherence loss, which typically results in broader main lobes with a reduced level. Thirdly, the levels in the source map may be influenced by side lobes from other sources.

To overcome these complications, a *power integration method* [19,20] can be used. This technique sums the source powers in (part of) the measured source map, and corrects the result with a scaling factor obtained by performing a simulation for a monopole source at the center of the integration region:

$$P_{exp} = \sum_{h=1}^H \bar{A}_{h,exp} \times \frac{P_{sim}}{\sum_{h=1}^H \bar{A}_{h,sim}}. \quad (3.21)$$

In this equation,  $P_{exp}$  is the integrated source power,  $P_{sim}$  is the source power of the simulated source,  $H$  is the number of scan positions, and  $\bar{A}_{h,exp}$  and  $\bar{A}_{h,sim}$  are the experimental and simulated beamforming results. The method is schematically explained in Figure 3-9. An integration contour is defined around the distributed source in the measured source map, and the integrated level is corrected using a (frequency-dependent) calibration function which is determined from a monopole simulation.

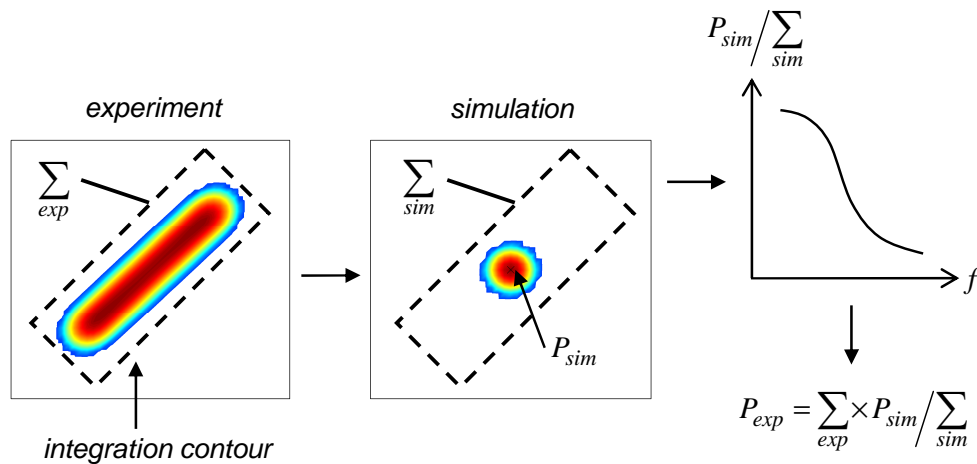


Figure 3-9: Source power integration method.

The integration technique has been applied to several wind tunnel test cases and yields accurate source levels, even in the presence of coherence loss, provided that the complete cross-power matrix is used (Figure 3-10).



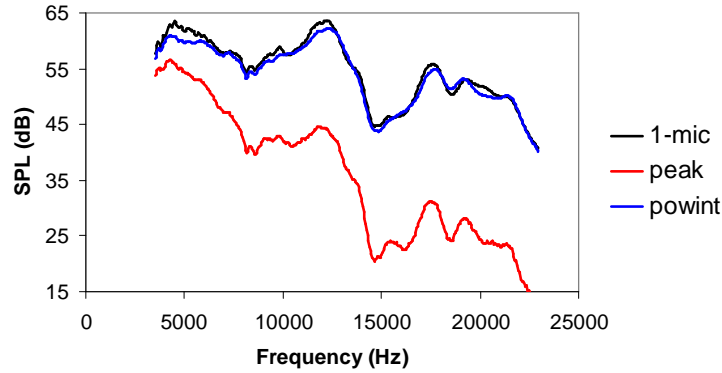


Figure 3-10: Validation of the power integration method (without Diagonal Removal) using a calibration source in the DNW-LLF open jet, at a wind speed of 50 m/s. While the peak levels in the acoustic source plot are much too low due to coherence loss, the integrated levels show good agreement with the single-microphone level.

In case of diagonal removal (Section 3.5.1) the method becomes unstable due to the contribution of unphysical negative 'source powers'  $\bar{A}_h$  to the integrated level. This can be prevented by excluding all negative source power estimates from the summations in Eq. (3.21). A more general method is to exclude all power estimates which are more than  $Z$  dB below the peak level in the source map, where  $Z$  is typically 10 or 12 dB. In this way accurate source levels can be retrieved also in case of diagonal removal (Figure 3-11).

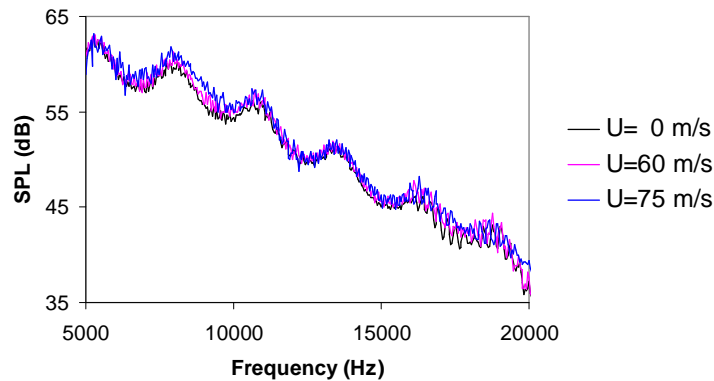


Figure 3-11: Application of the power integration method (with Diagonal Removal) to a calibration source in the DNW-LST closed test section. The good agreement between the integrated levels at the different wind speeds suggests that coherence loss is not important.

However, even with the use of a threshold  $Z$ , the absolute integrated levels can become too low when diagonal removal is applied in the presence of coherence loss (Figure 3-12). In such cases the integration technique can still be very useful for quantifying sound level differences between different source regions or model configurations. The accuracy of absolute and relative integrated airframe noise levels is investigated in detail in Chapter 4.

There are a number of considerations with regard to the choice of the integration area. Firstly, the integration method is only valid if the variation in array resolution over the integration region is small, because the scaling factor in Eq. (3.21) is determined using a

single monopole source at the center of the integration contour. Variations in array resolution can be accounted for by using multiple reference sources or multiple smaller integration regions. Another argument for a small integration region is that it suppresses large contributions from side lobes and/or the noise floor in the source map. On the other hand, the integration region should contain the complete source and should be large enough to capture main lobe broadening due to coherence loss. When sources are quantified using multiple adjacent integration regions, each region should be large enough to avoid 'double counting'. Furthermore, the source(s) should preferably be close to the center of the integration region, so that the number of contributing sidelobes is similar to that for the simulated reference source. Sometimes the source of interest cannot be completely included in the integration region due to the presence of extraneous sources, for example model-endplate sources in trailing edge noise measurements (Chapter 7). In such cases a smaller integration region can be used in combination with a dedicated integration method which incorporates the shape of the source.

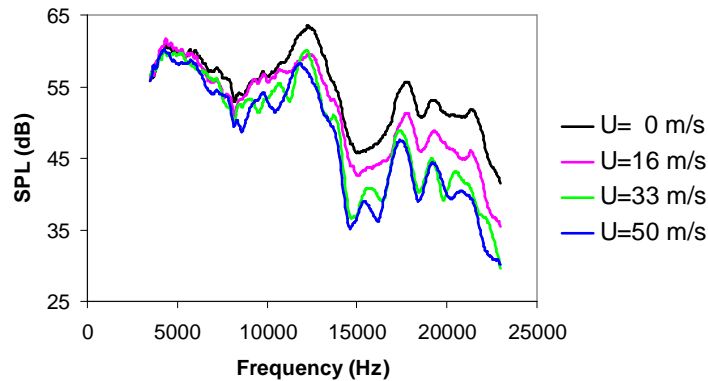


Figure 3-12: Application of the power integration method (with Diagonal Removal) to a calibration source in the DNW-LLF open jet, at several wind speeds. The combination of Diagonal Removal with coherence loss leads to significantly reduced integrated levels at higher wind speeds.

For extended sources, the integration method should in principle also account for source coherence [17]. The coherence length of a source can be estimated on the basis of the array results, using the method described in Section 3.5.3. However, usually the coherence length is much smaller than the main lobe width, so that a distribution of uncorrelated monopoles can be assumed, which means that Eq. (3.21) can be straightforwardly applied. When a source is close to a reflecting wall (e.g. in a closed wind tunnel section), the integrated source level will be disturbed by the nearby mirror source, which is coherent with the original source [21]. An example of a mirror source was shown in Figure 3-8. Using special processing techniques the influence of these mirror sources can be suppressed. However, when the source is not too close to the wall, as is usually the case in a wind tunnel, such corrections are not necessary.

### 3.7 Moving sources

When a sound source moves with respect to the microphone array (for example a flying aircraft or rotating wind turbine blades), application of a stationary scan plane results in a time-averaged, spread-out source map. This is illustrated in Figure 5-1 (pg. 75), which shows

the average sound source distribution in the rotor plane of a wind turbine. These maps provide very useful information, for example that practically all noise is produced by the outer part of the blades during their downward movement. However, it is impossible to distinguish the sound from the three individual blades. In order to obtain a clearer picture of the sources, we would therefore like to apply *moving* scan planes, which are 'attached' to the rotating blades. In this way the individual blade sources can be located and quantified, using the same measurement data (see Figure 5-10, pg. 85). How this is achieved will be described in the following.

For moving sources the acoustic transfer function depends on time, and the measured pressure signals are affected by the Doppler frequency shift. Thus, to retrieve the correct, dedopplerized source signal, beamforming must be done in the time domain. While for stationary sources the fixed steering function can be applied to the *average* cross-power matrix, for moving sources *each* individual sample must receive a time shift and amplitude correction which depends on the source position (and speed) at emission time. This makes time-domain beamforming much more time-consuming than frequency-domain beamforming.

In order to determine the transfer function between the source signal  $\sigma(t)$  and the pressure field  $p$ , we have to consider the wave equation for a moving monopole source in a uniform flow  $\vec{U}$ :

$$\frac{1}{c^2} \left( \frac{\partial}{\partial t} + \vec{U} \cdot \nabla \right)^2 p - \nabla^2 p = \sigma(t) \delta(\vec{x} - \vec{\xi}(t)). \quad (3.22)$$

This equation is the time-domain equivalent of Eq. (3.9), except that the source position  $\vec{\xi}$  is now a function of time. The transfer function  $p / \sigma$  for Eq. (3.22) can be found by combining the two cases depicted in Figure 3-5, as shown in Figure 3-13.

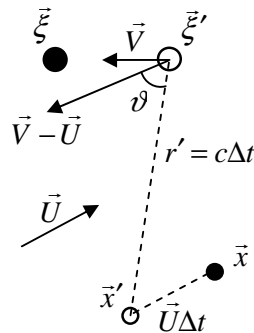


Figure 3-13: Moving sound source in uniform flow.

Without flow, the sound emitted from source position  $\vec{\xi}'$  would arrive at  $\vec{x}'$  in  $\Delta t$  seconds, but due to convection by the subsonic flow  $\vec{U}$  the sound arrives at microphone position  $\vec{x}$  in the same time period. In the mean time the source has travelled to position  $\vec{\xi}$ . Therefore,  $r' = c\Delta t$ , the distance the sound travels with respect to the medium, is the proper distance for calculating amplitude reduction. Furthermore, the speed of the source with respect to the

medium, which determines the amplification factor, is now  $\vec{V} - \vec{U}$ , where  $\vec{V}$  is the subsonic source velocity *at emission time* (i.e. at position  $\vec{\xi}'$ ). Thus, from Eq. (3.10) it follows that

$$\begin{aligned} p(\vec{x}, t + \Delta t) &= \frac{\sigma(t)}{4\pi r' \left(1 - \frac{1}{c} \|\vec{U} - \vec{V}\| \cos \vartheta\right)} \\ &= \frac{\sigma(t)}{4\pi \left\{c\Delta t + \frac{1}{c} (\vec{U} - \vec{V}) \cdot (\vec{x} - \vec{U}\Delta t - \vec{\xi}')\right\}} \end{aligned} \quad (3.23)$$

Note that this equation implicitly assumes a Doppler factor of  $(1 - M_{tot} \cos \vartheta)$ , with  $M_{tot} = \|\vec{U} - \vec{V}\|/c$ , while in reality this factor may have to be raised to a higher exponent, depending on the nature of the source. The emission time delay  $\Delta t$  can be determined from the relation

$$r' = c\Delta t = \|\vec{x} - \vec{U}\Delta t - \vec{\xi}'\|, \quad (3.24)$$

which follows directly from Figure 3-13. As long as the source moves subsonically, the solution to this equation is unique, and is found to be:

$$\Delta t = \frac{1}{c\beta^2} \left( -\vec{M} \cdot (\vec{x} - \vec{\xi}') + \sqrt{(\vec{M} \cdot (\vec{x} - \vec{\xi}'))^2 + \beta^2 \|\vec{x} - \vec{\xi}'\|^2} \right). \quad (3.25)$$

Note that this equation is identical to Eq. (3.15) for a stationary source in a flow, except that  $\vec{\xi}$  is replaced by  $\vec{\xi}'$ , since the source is now moving in the flow. From Eq. (3.23) it follows that the transfer function, which relates the source amplitude to the pressure field, is given by:

$$F(\vec{x}, \vec{\xi}', \vec{V}) = \frac{p(\vec{x}, t + \Delta t)}{\sigma(t)} = \frac{1}{4\pi \left\{c\Delta t + \frac{1}{c} (\vec{U} - \vec{V}) \cdot (\vec{x} - \vec{U}\Delta t - \vec{\xi}')\right\}}. \quad (3.26)$$

By using this transfer function as steering function, we can estimate the strength of a moving sound source from the measured microphone signals  $p_n$ . For a given, moving scan point with position  $\vec{\xi}'$  and velocity  $\vec{V}$  at *emission time*  $t$ , the reconstructed source amplitude  $\bar{\sigma}(t)$  can be found using delay-and-sum beamforming:

$$\bar{\sigma}(t) = \frac{1}{N} \sum_{n=1}^N \frac{p_n(t + \Delta t_n)}{F(\vec{x}_n, \vec{\xi}', \vec{V})} \equiv \frac{1}{N} \sum_{n=1}^N \bar{\sigma}_n(t), \quad (3.27)$$

where  $\Delta t_n$  is found by evaluating Eq. (3.25) for  $\vec{x} = \vec{x}_n$ . Note that Eq. (3.27) reduces to Eq. (3.3) if  $\vec{U}$  and  $\vec{V}$  are zero. By choosing a series of equally spaced emission times  $t$ , the dedopplerized source signal is obtained. Note that the times  $(t + \Delta t_n)$  at which the microphone signals should be evaluated generally do not coincide with the measurement

times  $w\Delta t_s$  (with  $w$  an integer and  $\Delta t_s$  the sample interval, see Appendix). Thus, in order to obtain the microphone pressure at the desired times, the measured signals are linearly interpolated. For equally spaced emission times  $t$ , the evaluation times  $(t + \Delta t_n)$  at a certain microphone will *not* be equally spaced if the source is moving. This has consequences for the required sample frequency and low-pass filter.

The dedopplerized source spectrum can be obtained by applying the Fourier transform to the reconstructed source signal  $\bar{\sigma}(t)$ , resulting in the frequency-dependent source amplitude  $\bar{a}(\bar{\sigma})$ . However, since  $\bar{\sigma}(t)$  is the sum of the time-shifted and amplitude-adjusted microphone signals  $\bar{\sigma}_n(t)$ , as defined in Eq. (3.27), any incoherent noise in the measurements will also contribute to the reconstructed source amplitude  $\bar{a}$ . To remove this incoherent noise from the array result, we can apply a method which is analogous to the diagonal removal technique described in Section 3.5.1. First, we write the reconstructed source amplitude as:

$$\bar{a}(\bar{\sigma}) = \frac{1}{N} \sum_{n=1}^N \bar{a}_n(\bar{\sigma}_n). \quad (3.28)$$

Then the estimated source auto-power can be calculated as:

$$\bar{A} = \frac{1}{2} |\bar{a}(\bar{\sigma})|^2 = \frac{1}{2N^2} \left| \sum_{n=1}^N \bar{a}_n(\bar{\sigma}_n) \right|^2 = \frac{1}{2N^2} \sum_{m=1}^N \sum_{n=1}^N \bar{a}_m(\bar{\sigma}_m) \bar{a}_n^*(\bar{\sigma}_n). \quad (3.29)$$

By removing the  $n = m$  terms from the double sum, and replacing  $N^2$  by  $(N^2 - N)$ , we obtain the equivalent of diagonal removal. As mentioned before, the exclusion of certain  $(m, n)$ -combinations may result in unphysical negative values for the estimated source auto-powers, which should be discarded. Using the frequency-domain expression from Eq. (3.29), the other special techniques described in previous sections, such as microphone weighting and power integration, can be readily applied to moving sources.

## References

- [1] M.J. Fisher, M. Harper Bourne, Source location in jet flows, Aeronautical Research Council Report ARC 35/383/N910, 1974.
- [2] J. Billingsley, R. Kinns, The acoustic telescope, Journal of Sound and Vibration, Vol. 48 (4), 1976.
- [3] F.R. Grosche, H. Stiewitt, B. Binder, Acoustic wind tunnel measurements with a highly directional microphone, AIAA Journal Vol. 15 (11), 1977.
- [4] R.H. Schlinker, Airfoil trailing edge noise measurements with a directional microphone, AIAA paper 77-1269, 1977.
- [5] J.R. Underbrink, R.P. Dougherty, Array design for non-intrusive measurement of noise sources, Noise-Con 96, Seattle, 1996.
- [6] M. Mosher, Phased arrays for aeroacoustic testing - Theoretical development, AIAA paper 96-1713, 1996.
- [7] J.F. Piet, G. Elias, Airframe noise source localization using a microphone array, AIAA paper 97-1643, 1997.

- [8] P. Sijtsma, H. Holthusen, Source location by phased array measurements in closed wind tunnel test sections, AIAA paper 99-1814, 1999.
- [9] U. Michel, B. Barsikow, J. Helbig, M. Hellmig, M. Schüttpelz, Flyover noise measurements on landing aircraft with a microphone array, AIAA paper 98-2336, 1998.
- [10] T.C. van den Dool, M.M. Boone, Microphone T-array technology for moving noise source measurements, Internoise, Nice, France, 2000.
- [11] T.F. Brooks, W.M. Humphreys, A deconvolution approach for the mapping of acoustic sources (DAMAS) determined from phased microphone arrays, AIAA paper 2004-2954, 2004.
- [12] P. Sijtsma, Experimental techniques for identification and characterisation of noise sources, Von Karman Institute Lecture Notes, 2004.
- [13] D.H. Johnson and D. E. Dudgeon, Array Signal Processing, Prentice Hall, 1993.
- [14] T.J. Mueller (Ed.), Aeroacoustic Measurements, Springer, 2002.
- [15] R.K. Amiet, Refraction of sound by a shear layer, Journal of Sound and Vibration 58, Vol. 4, pp. 467-482, 1978.
- [16] J.B.H.M. Schulten, Computation of aircraft noise propagation through the atmospheric boundary layer, Proceedings of the 5th International Congress on Sound and Vibration, Adelaide, Australia, 1997.
- [17] S. Oerlemans and P. Sijtsma, Determination Of Absolute Levels From Phased Array Measurements Using Spatial Source Coherence, AIAA paper 2002-2464, 2002.
- [18] P. Sijtsma, CLEAN Based on Spatial Source Coherence, AIAA paper 2007-3436, 2007.
- [19] T.F. Brooks and W.M. Humphreys, Effect of directional array size on the measurement of airframe noise components, AIAA paper 99-1958, 1999.
- [20] S. Oerlemans and P. Sijtsma, Acoustic Array Measurements of a 1:10.6 Scaled Airbus A340 Model, AIAA paper 2004-2924, 2004.
- [21] P. Sijtsma, H.H. Holthusen, Corrections for mirror sources in phased array processing techniques, AIAA paper 2002-2462, 2002.

## Chapter 4

### Quantification of airframe noise using microphone arrays in open and closed wind tunnels

*Published as: S. Oerlemans, L. Broersma, and P. Sijtsma, Quantification of airframe noise using microphone arrays in open and closed wind tunnels, International Journal of Aeroacoustics Vol. 6, Nr. 4, 2007 (reprinted with permission).*

#### **Abstract**

The reliability of the phased array technique for quantifying airframe noise was assessed in the DNW-LLF open and closed wind tunnel sections. Acoustic measurements were performed on wing noise from a 1:10.6 scaled Airbus A340 model, using a 4-m diameter out-of-flow microphone array in the open jet and a 1-m diameter wall array in the closed test section. Apart from the differences in array resolution, the source characteristics are generally similar for both test sections. The open jet results show that, although the absolute integrated array level can be too low due to e.g. coherence loss, the relative sound levels determined with the array (i.e. differences between configurations) are accurate within 0.5 dB. The difference between the absolute array levels in the closed test section and the far field levels in the open jet is smaller than 3 dB for all frequencies. The relative array levels in the closed test section agree with the open jet within 1 dB, provided that the flow conditions - and therefore the noise source characteristics - are similar.

## Nomenclature

$A$	Reconstructed source auto-power
AAAP	Average Array Auto-Powers (open jet)
$B$	Array size parameter: $r=B/f$ (with $f$ in kHz)
$C$	Cross-Spectral Matrix
CTS	Closed Test Section
DNW-LLF	German-Dutch Wind Tunnels - Large Low-speed Facility
DR	Diagonal Removal
$f$	Frequency
$\mathbf{g}$	Steering vector
$h$	Scan grid index
$H$	Number of scan locations
$L$	Length scale for $St$ normalization
$m$	Microphone index
$n$	Microphone index
$N$	Number of microphones
OJ	Open Jet
$p$	Complex pressure amplitude
$P_{exp}$	Integrated source power
$P_{sim}$	Simulated source power
PI	Power Integration
QCMB	Quarter-Circle Microphone Boom
$r$	Array radius
SNR	Signal-To-Noise ratio
SPL	Sound Pressure Level
$St$	Strouhal number
$U$	Wind speed
$x$	Speed exponent for wing noise
$\alpha$	Aircraft angle of attack
$\delta_F$	Flap angle
$\theta$	Array opening angle

### 4.1 Introduction

Phased microphone arrays have become an important tool in aeroacoustic testing for their ability to localize and quantify different noise sources. Arrays are used in wind tunnels and in the field, and can be applied to stationary and moving objects. However, while source location has become a standard technique, the *quantification* of array results is still far from straightforward. For incoherent, separate monopole sources the absolute sound level corresponds to the peak level in the acoustic source map. However, in practice this situation seldom occurs. First, aeroacoustic noise sources are often spatially extended (e.g. slat noise, trailing edge noise). As a consequence, the peak levels in the source map depend on the extent and coherence of the source region and on the (frequency-dependent) resolution of the array. Second, the levels may be influenced by coherence loss between the microphones. Coherence loss can occur when sound is scattered by turbulence (e.g. in the shear layer of an open jet wind tunnel), and typically results in broader lobes with a reduced level in the source map. The effects of coherence loss increase with frequency, wind speed, and the distance between the array microphones. Apart from scattering by turbulence, coherence loss may also occur when the noise source does not radiate coherently in all directions. This effect increases with



the opening angle of the array. Finally, the levels in the acoustic source map may be influenced by side lobes from other sources.

To overcome these complications, Dougherty and Mosher [1] employed a method for the quantification of array results. They defined an integration area around the source region and calculated a frequency-dependent array calibration function, assuming a source distribution of uncorrelated monopoles. Brooks *et al.* [2] extended this method, and applied it to simulations of a line source and to measurements of a calibrator source and flap side-edge noise. It was found that absolute spectra of different sources could well be recovered from the phased array results, and that coherence loss did not reduce the quality of the results significantly. However, the results were less reliable when the integration method was applied in combination with diagonal removal (DR). Diagonal removal [1] involves the removal of the main diagonal (i.e. the auto-powers) from the cross-spectral matrix, and is often inevitable in situations with low signal-to-noise ratio (e.g. a closed wind tunnel). An alternative method for reducing extraneous noise sources may involve the eigenvalue decomposition of the cross-spectral matrix, and removing the eigenvector(s) corresponding to unwanted noise [3].

An integration method similar to that of Brooks *et al.* [2] was used by Soderman *et al.* [4] to determine the relative importance of different airframe noise sources in a closed wind tunnel. However, the reliability of the absolute and relative sound levels was not investigated, probably because single-microphone levels of the wall-mounted array were contaminated by flow noise. Blacodon *et al.* [5] applied a quantification method to airframe noise in an open jet wind tunnel, and found good agreement of overall integrated levels with single-microphone spectra. However, their results may have been limited to low frequencies, where coherence loss effects are small. Furthermore, no source maps were shown for higher frequencies, where a high noise floor may have artificially increased the quantified array levels since no DR was applied [11].

Sijtsma *et al.* [6] extended the integration method to moving sound sources, and found that absolute levels can be accurately determined when auto-correlations (the time-domain equivalent of auto-powers) are included in the beamforming process. When auto-correlations were discarded, the integrated levels were too low, presumably due to suppression of secondary sources. Alternative array quantification methods, for linear noise sources such as trailing edge noise and slat noise, were presented in [7-10]. Acoustic source maps were translated to absolute source levels using an array calibration function determined from simulations of an uncorrelated line source. In [10] good agreement between integrated array levels and single-microphone values was found for the frequency range where trailing edge noise was dominant (up to about 4 kHz). A drawback of these methods is that they are only suitable for line sources.

Oerlemans *et al.* [11] performed acoustic array measurements on wing noise from a 1:10.6 scaled Airbus A340 model in the open and closed test sections of the DNW-LLF wind tunnel. They used a modified version of the integration method from [2], which in case of DR discards negative 'source powers' in both the simulated and measured source plots. It was shown that in both test sections DR should be applied to obtain meaningful local source spectra, because without DR the results were obscured by uncorrelated noise in the main diagonal of the cross-spectral matrix. For the open jet the absolute integrated levels were found to be too low due to coherence loss, but relative levels (differences between configurations) could be determined accurately. Although the effective array size was reduced with increasing frequency to reduce coherence loss effects, the dependence of integrated

levels on array size was not systematically investigated. In the closed test section coherence loss effects seemed to be small, but the reliability of absolute and relative levels could not be assessed because of flow noise on the wall-mounted array microphones. The array results for both test sections were not compared to each other because of changes to the model and wing devices.

It is worth noting that in the last years new deconvolution methods have been developed to increase the spatial resolution of phased microphone arrays [12-17]. Although these methods in principle account for resolution and side lobe effects, the calculated levels will still be affected by coherence loss. So even if fast and reliable algorithms are found, it is important to understand the different parameters influencing the reconstructed source levels.

The objective of the present study is to assess the reliability of absolute and relative array levels for open and closed wind tunnel sections. Acoustic array measurements were performed on wing noise from a 1:10.6 scaled Airbus A340 model in the open and closed test sections of the DNW-LLF wind tunnel. The purpose of these tests was to determine the acoustic effect of several wing devices that were intended to enhance the aerodynamic performance of the wing. The acoustic tests were done using a 4-m diameter out-of-flow microphone array in the open jet and a 1-m diameter wall array in the closed test section. The open jet results were used to systematically investigate the effect of DR and array size on the integrated sound levels. Moreover, since the same aircraft model was used in both test sections, the combined data base provided a unique opportunity to compare the array results for the open jet and closed test section quantitatively. Although in the end the array technique is intended for localization and quantification of different noise sources, in this study the integration method will be applied only to the complete model (or wing), in order to allow comparison to far field microphone levels.

The structure of this article is as follows. In Section 4.2 the test set-up is described, followed by the data acquisition and processing procedures in Section 4.3. In Section 4.4 the integrated array spectra for both test sections are assessed in terms of absolute levels. Section 4.5 discusses the accuracy of relative sound levels, i.e. differences between configurations. The conclusions of this study are summarized in Section 4.6.

## **4.2 Test set-up**

The test campaigns in the open and closed test sections of the DNW-LLF were both performed using the 8x6 m<sup>2</sup> tunnel nozzle (Figure 4-1 and Figure 4-2). The same 1:10.6 scaled Airbus A340 model was used for both test campaigns. It had through-flow engine nacelles, winglets, and a vertical tail plane, but no horizontal tail plane and no landing gears. The wing span was 5.5 m and the length of the model was 5.9 m. The only model difference between the two test campaigns was related to the tripping of the slats. During the closed section tests (November 2003), where generally no tripping was applied, sometimes a narrowband tone occurred at the outer slat. This tone was considered to be due to the low Reynolds number and therefore not representative for the real aircraft. By tripping the slat the tone could be removed without affecting the aerodynamic performance of the wing or the broadband wing noise levels. Therefore in the subsequent open jet tests (January 2004) all slats were tripped.

The model was tested in take-off, landing, and approach configuration, and, as a background noise reference, also in the clean ('cruise') configuration. Measurements were

done at wind speeds of 50, 60, and 70 m/s and angles of attack of about  $3^\circ$ ,  $5^\circ$ , and  $7^\circ$ . The geometrical angles of attack were slightly lower in the closed section and slightly higher in the open jet, in order to compensate for the open jet effect and obtain the same lift. The model was tested in the baseline configuration and with several wing devices.

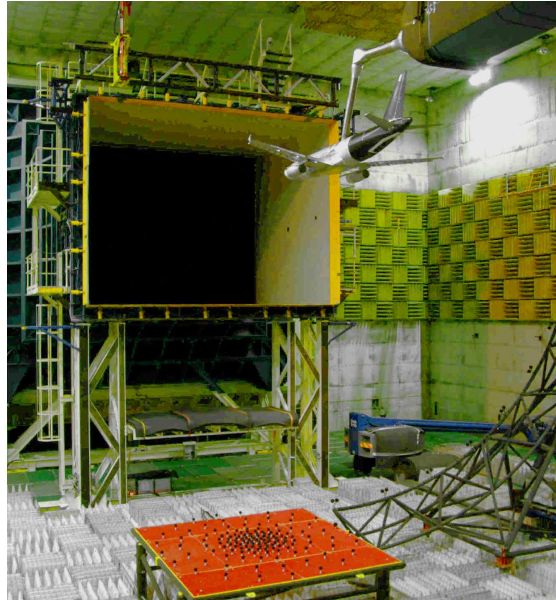


Figure 4-1: Test set-up in DNW open jet, with out-of-flow microphone array (in red) and far field quarter-circle microphone boom.



Figure 4-2: Test set-up in DNW closed test section, with wall arrays on the tunnel floor.

Acoustic measurements were done using a 4-m diameter out-of-flow microphone array in the open jet and a 1-m diameter wall array in the closed test section (Figure 4-3). The open jet array consisted of 140 LinearX M51  $\frac{1}{2}$ -inch microphones mounted in an acoustically open metal grid and was positioned below the left wing of the model, at a vertical distance of 7.6 m. The closed section array consisted of 128 LinearX M51 microphones flush-mounted in a plate on top of the tunnel floor (plate thickness a few centimetres), and was positioned below the right wing of the model, at a vertical distance of 3 m. Note that although three

arrays were used in the closed section (to investigate directivity effects), in the present study only the central array is considered. Due to the different array diameters and distances, the (maximum) opening angle was  $\theta_{OJ}=29^\circ$  for the open jet array and  $\theta_{CTS}=19^\circ$  for the closed section array (Figure 4-4).

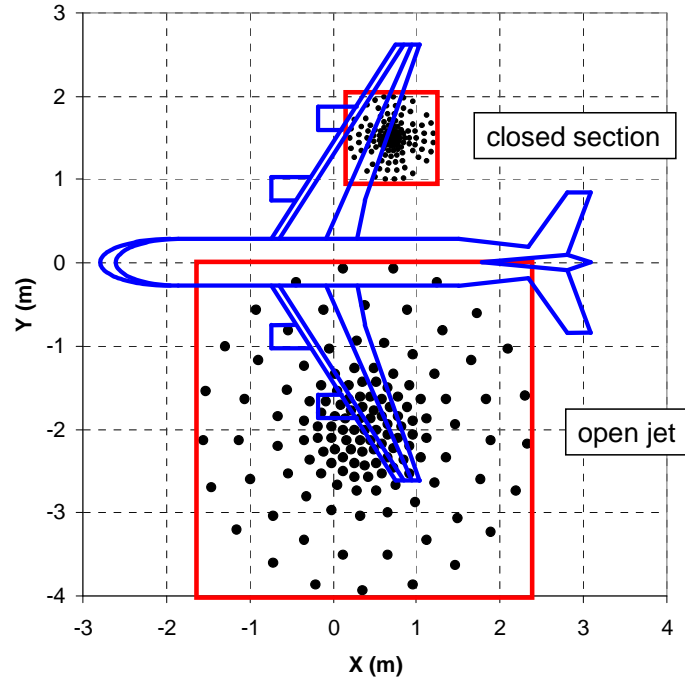


Figure 4-3: Top view of array positions for closed test section and open jet.

In order to measure the far field directivity of the aircraft noise, a quarter-circle microphone boom (QCMB) with a radius of 7.3 m was used in the open jet, which could be traversed in flow direction (Figure 4-1). Although these far field data are not analyzed in detail here, they will be used as a reference for the out-of-flow array levels.

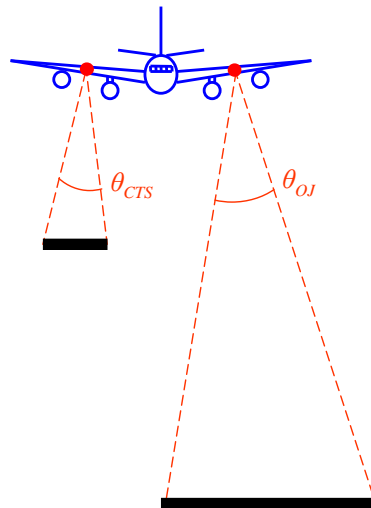


Figure 4-4: Front view of array positions for closed test section and open jet.

### 4.3 Data acquisition and processing

In both test campaigns data were acquired using the VIPER multi-channel data-acquisition system [18]. In the open jet the microphone signals were measured at a sample frequency of 102.4 kHz and a measurement time of 30 s. The acoustic data were processed using an FFT block size of 2048 with a Hanning window and an overlap of 50%, yielding 3000 averages and a narrowband frequency resolution of 50 Hz. In the closed test section the sample frequency was 122.88 kHz and the measurement time 20 s, leading to 1200 averages and a narrowband frequency resolution of 30 Hz (block size 4096). High-pass filters were used to suppress high-amplitude pressure fluctuations from the wind tunnel (at low frequencies), and thus to extend the dynamic range of the AD converter to low pressure amplitudes (at high frequencies). These 2<sup>nd</sup> order filters [18] reduced the pressure amplitudes for frequencies below 500 Hz (open jet) and 6 kHz (closed section). The levels presented here are corrected for the filter response. Prior to the measurements, all array microphones were calibrated at 1 kHz using a pistonphone. The frequency response of the individual open jet microphones was taken from calibration sheets provided by the manufacturer. The frequency-response of the individual closed section microphones (installed in the wall array) was taken from calibration measurements in an anechoic chamber. For low frequencies this amounted to the 6 dB correction for pressure doubling, but above 5 kHz the corrections deviated significantly from 6 dB (depending on frequency), probably due to details of the installation. No corrections were applied for microphone directivity, since these effects are considered to be small for the angles under consideration here. Phase matching of the microphones was checked prior to the tests using a cross-correlation analysis with a calibration source at known positions.

The array data were processed using conventional beamforming [19] to obtain the reconstructed source auto-powers  $A$  on a grid of scan locations in the plane of the model:

$$A = \frac{\sum_{m=1}^N \sum_{n=1}^N g_m^* C_{mn} g_n}{\sum_{m=1}^N \sum_{n=1}^N |g_m|^2 |g_n|^2}. \quad (4.1)$$

In this equation,  $g$  is the steering vector for a given scan location,  $m$  and  $n$  are microphone indices,  $*$  indicates the complex conjugate, and  $C$  is the cross-spectral matrix containing the cross-powers between all pairs of microphones (for each narrowband frequency):

$$C_{mn}(f) = \frac{1}{2} p_m(f) p_n^*(f). \quad (4.2)$$

From the reconstructed source auto-powers, acoustic source maps in 1/3-octave bands were produced. The influence of uncorrelated noise was suppressed by discarding the main diagonal in the cross-spectral matrix (diagonal removal [1]), which corresponds to removing all  $m = n$  terms from the double summations in Equation (4-1). In the closed test section DR was also applied to remove pressure fluctuations from the turbulent wall boundary layer. It should be noted that DR only removes the uncorrelated part of the boundary layer noise. However, for the frequencies of interest the correlation lengths of the turbulent boundary layer noise are much smaller than the spacing between the microphones. The remaining wind tunnel noise was removed by subtracting the integrated background noise spectrum from the

integrated wing noise spectrum (see Section 4.4.2). The effect of sound refraction by the open jet shear layer was corrected using a simplified Amiet method [20]. The scan grid, with a mesh size of 3 cm in the open jet and 2.5 cm in the closed section, was placed in the plane of the wings and rotated in accordance with the angle of attack. In order to reduce coherence loss effects and to increase the array resolution, spatial shading was applied to the microphone signals in the open jet. The first shading accounted for the variation of microphone density over the surface of the array. The second shading reduced the effective array radius  $r$  for increasing frequency according to  $r=B/f$ , with frequency  $f$  in kHz and  $B$  a measure for the frequency-dependent array size. For the open jet a standard value of  $B=6$  m·kHz was used. No shading was applied to the closed section microphone signals, because array processing with variable effective array size indicated that coherence loss effects were small in this test section [11,21].

The source maps were further processed using a power integration method similar to the method described in [1], which is called the 'simplified method' in [2]. This technique sums the source powers in (part of) the measured source map, and corrects the results with a scaling factor obtained by performing a simulation for a monopole source at the centre of the integration region:

$$P_{exp} = \sum_{h=1}^H A_{h,exp} \times \frac{P_{sim}}{\sum_{h=1}^H A_{h,sim}}. \quad (4.3)$$

In this equation,  $P_{exp}$  is the integrated source power,  $P_{sim}$  is the source power of the simulated source,  $A_h$  are the simulated or experimental beamforming results, and  $h$  is the scan grid index. In order to prevent contributions from negative 'source powers' in the case of DR, the scan levels  $A_h$  that were negative or more than 12 dB below the peak level (in the simulated or measured source map) were set to zero. It should be noted that, because the scaling factor in Eq. (4.3) is determined using a single monopole source at the centre of the scan grid, the simplified integration method is only valid if the variation in array resolution (or beamwidth) over the integration region is small. For the present study this was verified by simulations of an extended line source and by using multiple integration regions with reduced size (see also Section 4.4.3). In order to suppress contributions from spurious side lobes, the integration contours for the open jet and closed section were fitted around the wings (Figure 4-5). For the open jet both wings were integrated to allow comparison of the integrated levels to absolute sound levels in the far field. For the closed test section only the right wing was integrated because of the oblique view angle to the left wing (Figure 4-4), which led to a significantly lower resolution.

To enable a good comparison between the integrated array levels and the array auto-powers, the 'Average Array Auto-Powers' (AAAP) were calculated. These were obtained by averaging the auto-powers of all array microphones, using the same (frequency-dependent) microphone weights as applied during the beamforming (see above). The AAAP were also compared to the sound levels measured at the quarter-circle far field microphone boom. In order to obtain approximately the same directivity, the average level of the far field positions opposite of the array was used (Figure 4-6). Three decibels were added to the integrated array spectra for the closed section to account for the second wing.

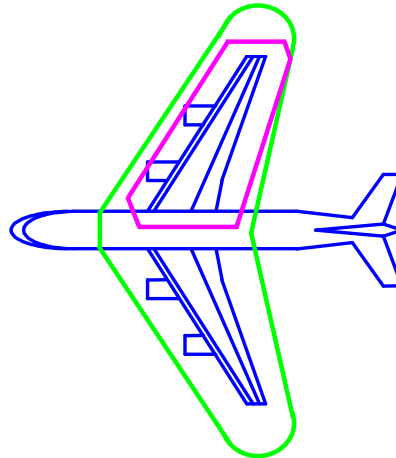


Figure 4-5: Integration contours for open jet (green) and closed test section (pink).

Finally, all far field and integrated array spectra were normalized to the same reference distance (including a correction for atmospheric absorption) to allow direct comparison of the levels. The source maps and spectra are presented in 1/3-octave bands at model scale frequencies, without A-weighting.

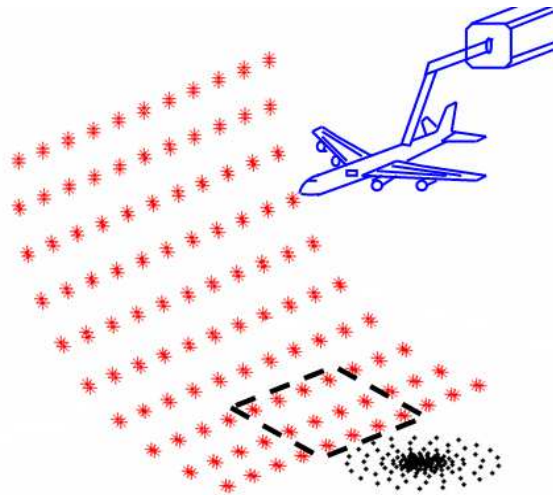


Figure 4-6: The dashed rectangle indicates the far field microphone positions that were used as a reference for the out-of-flow array levels.

#### 4.4 Absolute sound levels

In this section the integrated array spectra are assessed in terms of absolute sound levels. In Section 4.4.1 the source maps for both test sections are compared. In Section 4.4.2 the absolute integrated levels are compared to the sound level measured by the far field microphones in the open jet. In Section 4.4.3 the differences between the array spectra and far field levels are further analyzed.

#### 4.4.1 Source maps

Figure 4-7 shows the source maps for the landing configuration, for the closed test section and the open jet. The left wing source maps of the open jet are mirrored to allow easier comparison to the closed test section. For the open jet, the results with and without diagonal removal are shown. It can be seen that DR drastically improves the results by eliminating the high noise floor in the source maps. This indicates that the main diagonal of the cross-spectral matrix contains a significant amount of uncorrelated 'noise' which is not present in the off-diagonal terms. Since the signal-to-noise ratio is good in this frequency range (see below), these uncorrelated signals in the main diagonal are not due to wind tunnel background noise, but due to noise from the model which has lost its phase relationship as a result of coherence loss [11,22].

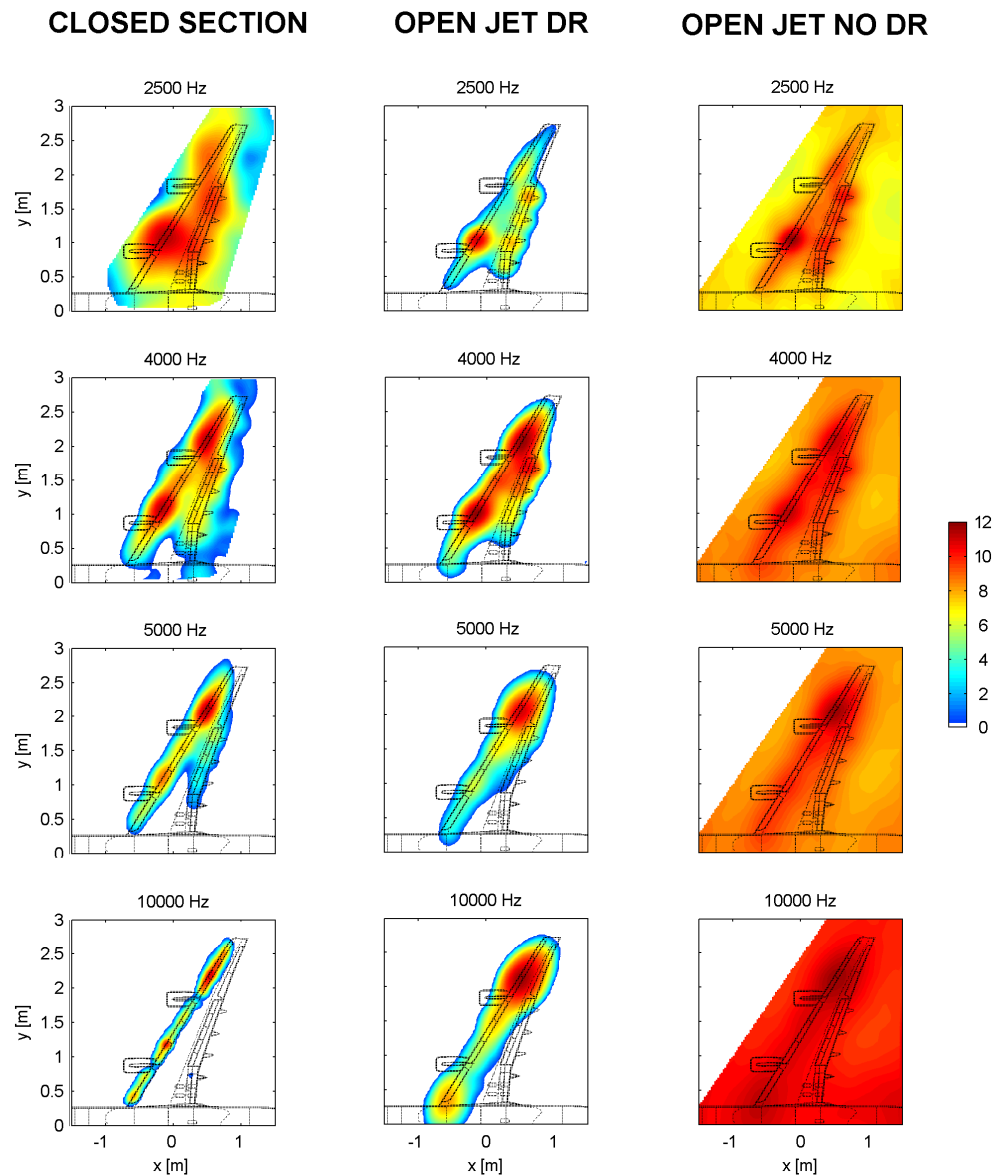


Figure 4-7: Source maps for landing configuration at  $U=60$  m/s and  $\alpha=5^\circ$ . Results are shown for the closed test section (with DR) and the open jet (with and without DR). The range of the colour scale is always 12 dB, the maximum level is adjusted for each individual plot.



For the closed test section only the results with DR are shown, since in this case the main diagonal was contaminated by tunnel wall boundary layer fluctuations, again leading to source maps with a high noise floor. Comparison between the closed section and open jet results shows that, although the array resolution is different, the source characteristics are quite consistent: at low frequencies the dominant noise sources are located close to the inner engine and at the trailing edge flaps, while for increasing frequency the outer slat becomes more important. In terms of resolution the open jet array performs better than the closed section array at low frequencies, but worse at high frequencies. Around 4-5 kHz the resolution is similar, because at that frequency the effective opening angle (Figure 4-4) is approximately the same for both arrays (note that with  $B=6$  m-kHz the effective radius of the open jet array at 4 kHz is 1.5 m).

#### 4.4.2 Integrated spectra

The source maps were quantified using the power integration method described in Section 4.3. Note that for the open jet both wings were integrated, to allow comparison to absolute sound levels in the far field (Figure 4-5). Before comparing the integrated levels to the far field spectra, it is useful to look at the signal-to-noise ratio (SNR) for the different methods (Figure 4-8).

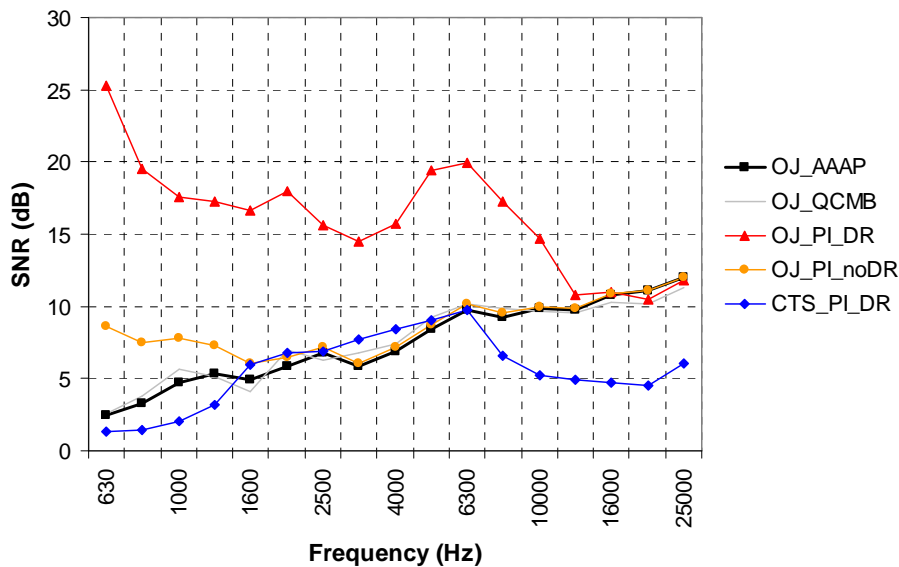


Figure 4-8: Signal-to-noise ratio at  $U=60$  m/s and  $\alpha=5^\circ$ , for different methods in open jet (OJ) and closed test section (CTS): average array auto-powers (AAAP), quarter-circle microphone boom (QCMB), and power integration (PI) with and without diagonal removal (DR).

The SNR was defined as the difference in noise level between the landing and clean (or 'cruise') configuration, which was used as a background noise reference. For the far field microphones (AAAP and QCMB, see Figure 4-6), the SNR increases from about 2 dB at low frequencies to 12 dB at high frequencies. For the integrated open jet array spectra with DR the SNR is generally much higher, because the array focuses on the wing noise and thus reduces background noise from the wind tunnel. However, when DR is *not* applied, the SNR reduces

to the AAAP level above 2.5 kHz, due to the high noise floor in the source maps. The SNR for the closed test section is significantly lower than in the open jet (with DR). At low frequencies this is due to the influence of extraneous noise sources in the wind tunnel (e.g. the sting), which influence the integrated wing noise as a result of the limited array resolution. At high frequencies the relatively low SNR is due to the fact that the (leading edge) source region occupies only a small part of the (full wing) integration region. As a result of the large integration area the low noise floor in the source map adds up to a significant level. Therefore, the SNR could be improved by using a smaller integration area around the sources or by increasing the spot size by reducing the effective array size (and thus resolution).

Figure 4-9 compares the integrated spectra for the different methods. All spectra were corrected for background noise (see SNR in Figure 4-8). The far field spectra QCMB and AAAP are quite consistent, except at the low frequencies where the SNR is relatively low. In order to obtain the most direct comparison, in the remainder of this article the AAAP will be used as a reference for the integrated array spectra. The integrated open jet spectra are cut off at 16 kHz because at higher frequencies side lobes dominate the source maps, due to the reduced array size (and thus smaller number of microphones). When DR is not applied in the open jet, the integrated levels are increased due to the high noise floor in the source maps (Figure 4-7). As mentioned before, this noise floor is due to noise from the model which has lost its phase relationship as a result of coherence loss. So even though the SNR is quite high, the integration method without DR is not suitable for quantification of different source regions on the model [11]. When DR is applied, the integrated levels are close to the AAAP at low frequencies, but significantly lower for increasing frequency. The spectrum for the closed test section is relatively close to the open jet AAAP over the whole frequency range (within 3 dB). Note that the CTS spectrum starts at 1.6 kHz because at lower frequencies the resolution is too low for reliable wing noise integration.

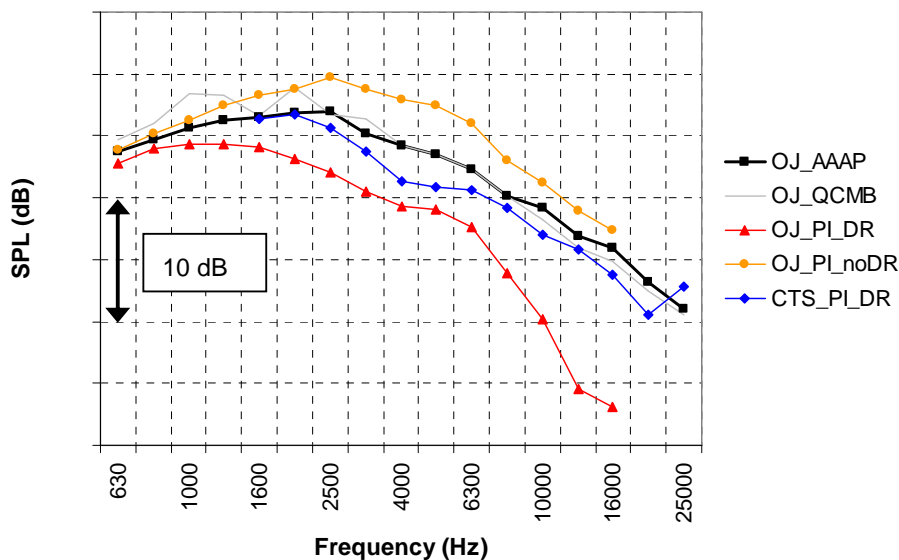


Figure 4-9: Absolute sound levels for landing configuration at  $U=60$  m/s and  $\alpha=5^\circ$ , using different methods. Same legend as in Figure 4-8.

#### 4.4.3 Difference between array spectra and far field levels

Several possible explanations for the differences between the integrated array spectra and the open jet Average Array Auto-Powers (AAAP) were examined. First, systematic errors may occur due to simplifications used in the integration method (e.g. the assumption of constant beamwidth over the integration region). Such errors were quantified by performing simulations for a line source at the wing leading edge, and comparing the experimental deviation from the open jet AAAP to the simulated deviation (Figure 4-10). For the closed test section (CTS) the simulated deviation is always smaller than 1 dB, but for the open jet a difference of almost 6 dB occurs at 16 kHz. Additional simulations (not shown here) indicated that this deviation is not caused by negative side lobes (due to DR) that reduce the level of adjacent sources on the leading edge. Possible errors due to the assumption of a constant beamwidth were investigated by using multiple integration regions with reduced size, and were also found to be small. Rather, the difference turned out to be due to side lobes which are *inside* the integration contour for the simulated point source used to calculate the scaling factors, but are *outside* the integration contour in the actual measurement. This analysis shows that systematic errors may be present when significant side lobes occur, such as in the open jet at high frequencies (these errors could be reduced by increasing the number of microphones or integrating less than 12 dB below peak level). However, for both test sections these errors do not (fully) explain the experimentally observed differences between integrated spectra and AAAP.

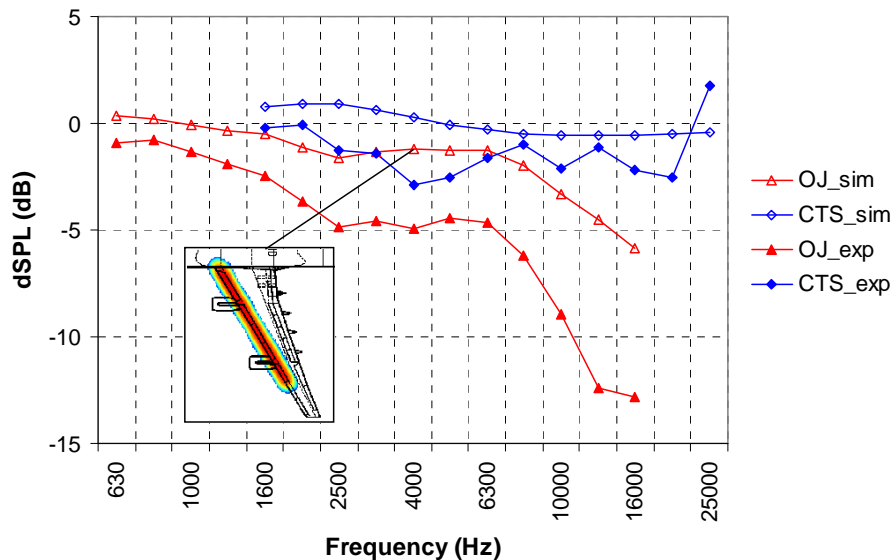


Figure 4-10: Deviation of integrated array spectra (with DR) from open jet AAAP, for measured wing noise and for simulated line source at wing leading edge.

For the open jet, a probable cause for the reduced integrated levels is coherence loss [11,22]. As mentioned in Section 4.1, coherence loss effects increase with distance between the microphones. Therefore, the effect of varying the array size parameter  $B$  was investigated for the open jet. The source maps in Figure 4-11 show that the resolution increases with increasing array size. However, at high frequencies coherence loss between distant microphones results in a high noise floor. When the array is kept smaller ( $B=3$ ) the noise floor

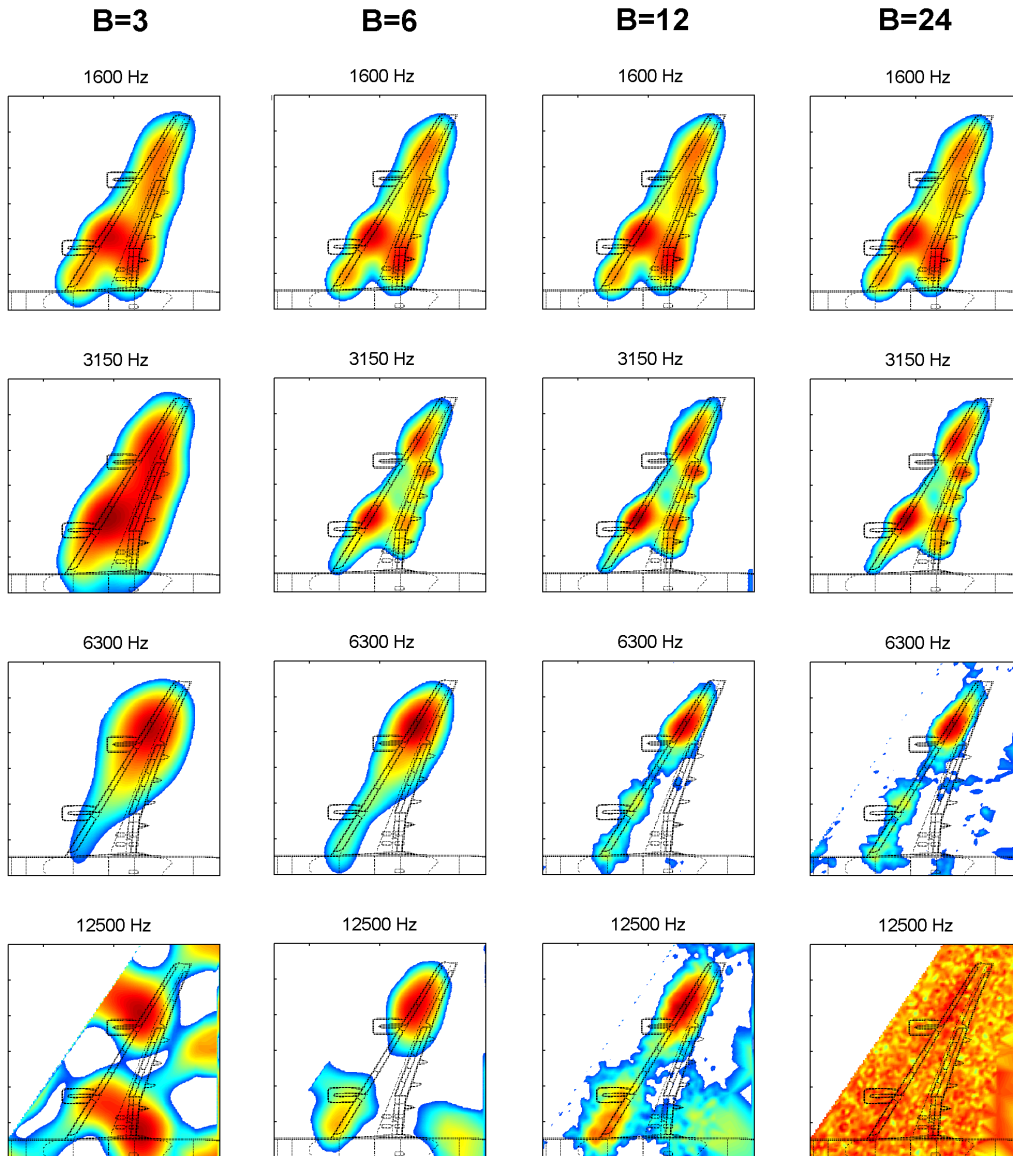


Figure 4-11: Open jet source maps for landing configuration at  $U=60$  m/s and  $\alpha=5^\circ$ , for different values of array size parameter  $B$ .

is suppressed, but at high frequencies side lobes start to dominate the source maps due to the small number of microphones.

These observations are reflected in Figure 4-12, which shows the deviation from the AAAP (the AAAP were calculated for each array size, although these showed very little variation). For low frequencies the four lines coincide because all array microphones are used in all cases. For intermediate frequencies, the integrated level decreases with increasing array size, due to coherence loss. For the highest frequencies, the integrated levels for the largest array increase due to the high noise floor. All in all the best compromise seems to be achieved at  $B=6$ , which was used as the standard value.

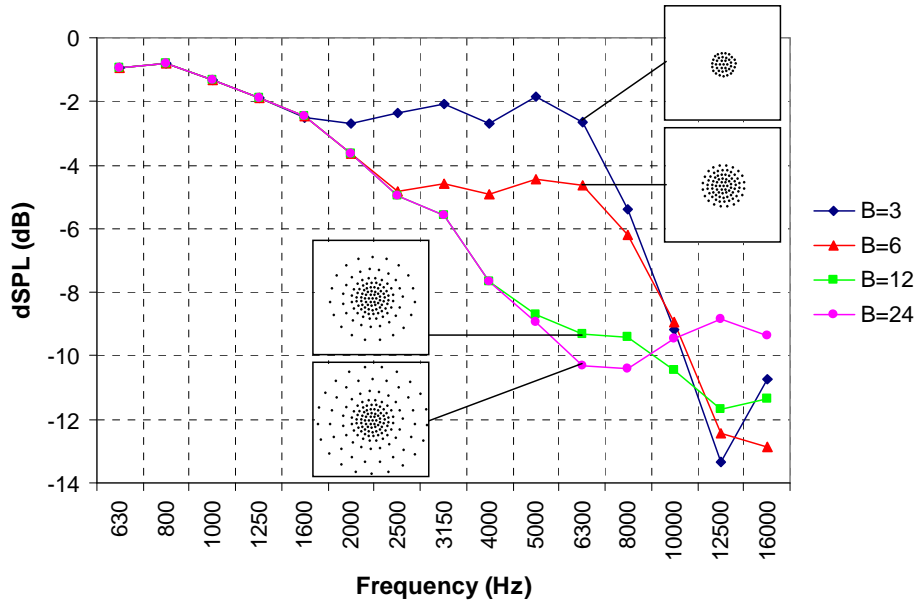


Figure 4-12: Deviation of integrated open jet array spectra (with DR) from AAAP, for different values of the array size parameter  $B$ . The array size at 6.3 kHz is indicated in the figure. Landing configuration at  $U=60$  m/s and  $\alpha=5^\circ$ :

Besides the distance between the microphones, coherence loss effects are also expected to increase with wind speed, due to the higher turbulence levels in the open jet shear layer. This is confirmed in Figure 4-13, which shows that the deviation from the AAAP increases with wind speed. Thus, for the open jet the difference between integrated array spectra and AAAP can be explained mainly by coherence loss, and to a lesser extent by systematic errors.

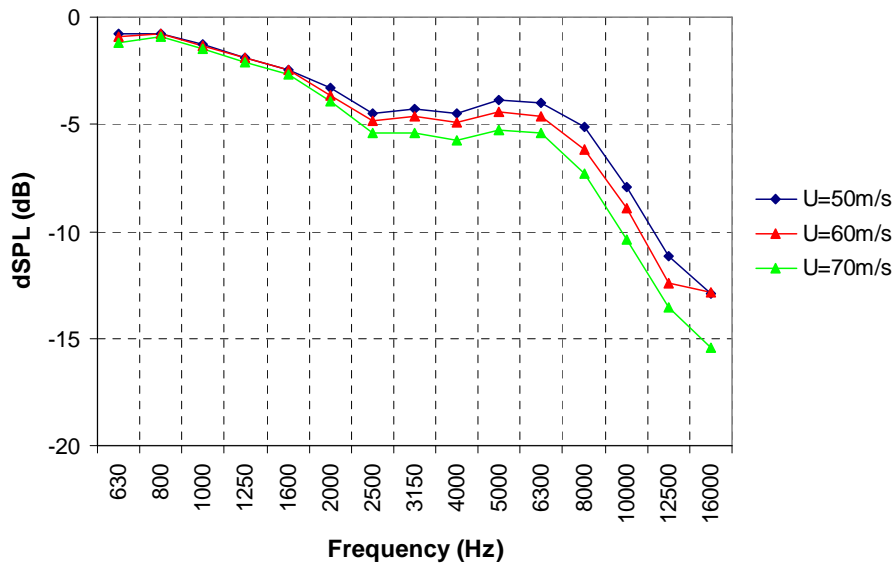


Figure 4-13: Deviation of integrated open jet array spectra (with DR) from AAAP, for different wind speeds. Landing configuration at  $\alpha=5^\circ$ :

The possible presence of coherence loss in the closed test section was investigated by reducing the array size and comparing the integrated array levels to those from the full array. If coherence loss were present, the integrated levels should increase with decreasing array size, similar to the open jet (Figure 4-12). However, when the outer one, two or three microphone rings were removed in the array processing, the integrated spectra remained practically the same (within 0.5 dB). Thus, similar to [11], coherence loss does not seem to be significant in the closed test section, and cannot explain the (relatively small) experimentally observed differences between integrated array spectra and AAAP (Figure 4-10).

Another reason for these differences could be directivity: whereas the AAAP contain noise contributions from both wings under different angles, the integrated CTS array spectrum contains the noise from one wing only (Figure 4-4). Although 3 dB was added to the CTS spectrum to account for the second wing, a strong lateral directivity (i.e. perpendicular to the flow direction) of the wing noise could cause a difference between the integrated CTS spectrum and the AAAP from the open jet. This directivity effect was quantified by calculating the left and right wing spectra separately for the open jet test. The resulting spectra differed less than 1 dB, indicating that the wing noise has no strong lateral directivity for the angles considered here. From the wing noise footprints obtained from the quarter-circle microphone boom (not shown here) it can be concluded that also the *polar* directivity (i.e. in the flow direction) is small in the direction of the arrays.

Another possible explanation for the difference between the CTS spectrum and the open jet AAAP could be microphone installation effects. The free-field microphones in the open jet array were installed in a non-reflecting, acoustically open metal grid, while the CTS microphones were flush-mounted in a wall array. As mentioned in Section 4.3, the frequency-response of the installed wall array microphones was determined in an anechoic chamber, outside the wind tunnel, and was found to deviate significantly from the 6 dB correction for pressure doubling at frequencies higher than 5 kHz. It could be that small details of the installation slightly affect the response of the array microphones. This may be checked by an *in-situ* array calibration.

Finally, the difference between integrated array levels in the CTS and the AAAP in the open jet could be due to a difference in the flow parameters. As mentioned in Section 4.2, the geometrical angle of attack in the closed test section was slightly lower than in the open jet, in order to obtain the same lift coefficient. However, equal lift does not necessarily mean that the wing flow parameters are the same. Aerodynamic measurements on wind turbine airfoils in open and closed wind tunnel sections have indicated that *for equal lift* the boundary layer transition from laminar to turbulent occurs more upstream in the open jet than in the closed test section [23]. Although the ratio of wing chord over tunnel dimension is much smaller in the present DNW tests, different transition or separation locations may significantly affect the aerodynamic noise produced by the high-lift configurations studied here. Such effects might explain the differences in source characteristics between the open jet and the closed test section (Figure 4-7). This issue will be further discussed in Section 4.5.

#### 4.5 Relative sound levels

Whereas in the previous section the accuracy of the *absolute* sound levels was assessed, the present section deals with the accuracy of *relative* sound levels. With relative sound levels the noise differences between different configurations are meant, often the most important

quantity in aeroacoustic tests. Since the tested wing devices only had a small effect on the wing noise (generally below 1 dB), they were not very suitable for assessing relative sound levels. Therefore, in this section wing noise differences due to variation in wind speed, angle-of-attack, and flap angle will be used to assess the accuracy of the relative integrated spectra for the open and closed test section, by comparison to the open jet AAAP.

In order to investigate the speed dependence of the wing noise, normalized sound levels were plotted as a function of Strouhal number  $St = fL/U$ , where  $f$  is frequency,  $U$  is wind speed, and  $L$  is a length scale for which here a constant value of 1 cm was chosen. The sound levels were normalized as  $SPL - 10x \log U$ , where  $x$  indicates the dependence of the wing noise on the flow speed ( $p^2 \sim U^x$ ). For the AAAP, which are regarded to represent the true wing noise levels, the best data collapse is obtained for  $x = 5$  (Figure 4-14).

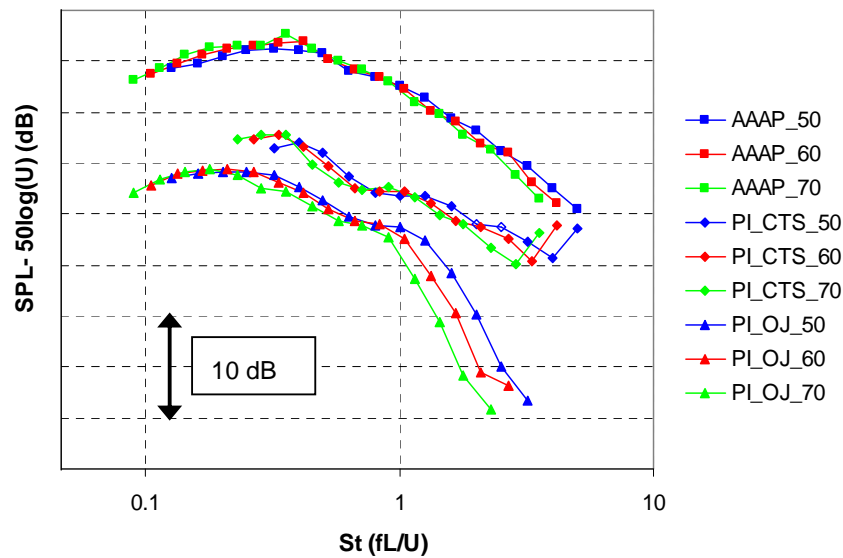


Figure 4-14: Normalized spectra at three wind speeds (50, 60, and 70 m/s) for the AAAP and for the integrated array spectra (with DR) in the open jet and the closed test section. Landing configuration at  $\alpha=5^\circ$ . The two open markers in the PI\_CTS\_50 spectrum indicate that a narrowband tone was removed from the spectrum.

However, if the same scaling is applied to the integrated array spectra for the open jet, significant scatter occurs at high  $St$ . This is due to the fact that the deviation of the integrated array levels from the AAAP (due to coherence loss) increases with wind speed (Figure 4-13). Thus, in the open jet one should be careful to compare integrated array spectra for different wind speeds, because this may lead to too low speed exponents. For example, to collapse the high frequencies of the integrated open jet spectra, a value of 1 should be used for  $x$ , which is much lower than the actual value of 5. For the integrated array spectra in the closed test section also a small amount of scatter occurs at high  $St$  (Figure 4-14), which may indicate that some coherence loss occurs here as well, although reducing the array size did not increase the integrated levels (see previous section).

Next, the effect of aircraft angle-of-attack on wing noise was examined for the open jet and the closed test section. Figure 4-15 shows the source maps at 5 kHz, where the array performance is similar for both test sections. For the lower angles of attack the source

characteristics are quite consistent: at  $3^\circ$  the middle wing is most important, whereas at  $5^\circ$  the outer wing becomes dominant. At  $7^\circ$  a dominant noise source appears in the open jet close to the outboard engine, which is not present in the closed section. As argued in the previous section, this difference in source characteristics is most probably not due to directivity effects, but due to different flow conditions caused by the different geometrical angle-of-attack.

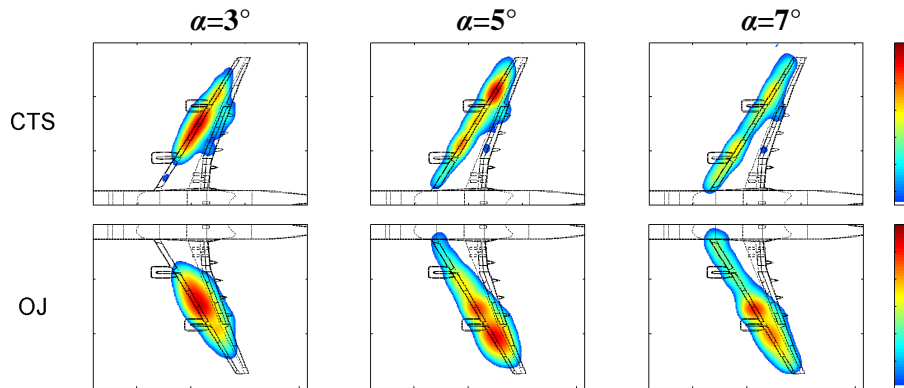


Figure 4-15: Effect of angle-of-attack on the source characteristics in the closed test section and open jet (5 kHz), for the approach configuration at  $U=60$  m/s. The maximum level of the 12 dB colour scale is the same within both rows.

The 'delta spectra' for the three angles of attack are shown in Figure 4-16 for the three different methods: the AAAP and integrated array spectra for the open jet, and the integrated array spectra for the closed test section. The CTS spectra for the highest frequencies ( $\geq 10$  kHz) were calculated using a reduced array size to improve the SNR (see Section 4.4.2). Figure 4-16 shows that the integrated array spectra for the open jet agree to the AAAP within 0.5 dB over the whole frequency range, for both changes in angle-of-attack. Thus, the power integration method is very reliable in terms of relative noise levels.

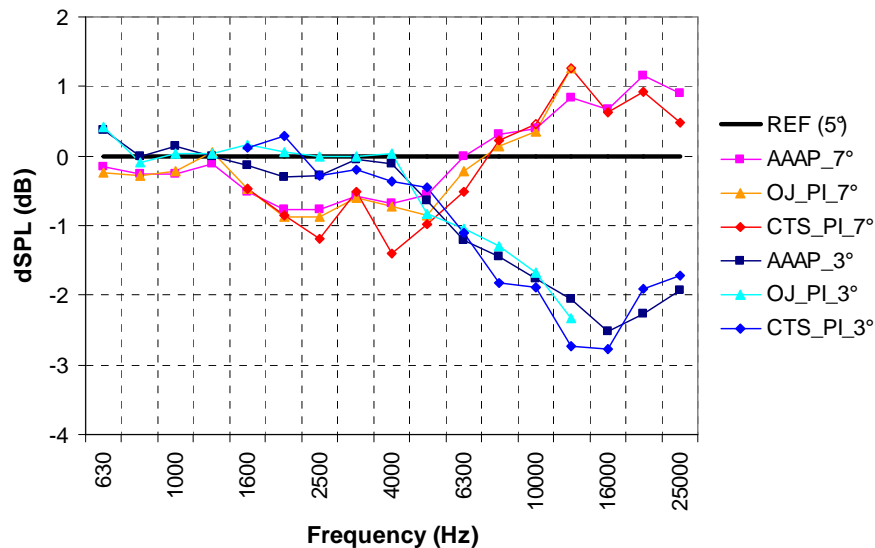


Figure 4-16: Effect of angle-of-attack on wing noise for the approach configuration at  $U=60$  m/s. Shown are the open jet AAAP and the integrated array spectra for the open jet and the closed test section. All spectra are referenced to the respective spectrum at  $5^\circ$ .



Moreover, it is seen that the delta spectra from the closed section also agree within 1 dB, despite the small differences in source characteristics mentioned above. This illustrates that when the flow conditions - and therefore the noise source characteristics - are similar, the phased array results for the open and closed section are very consistent.

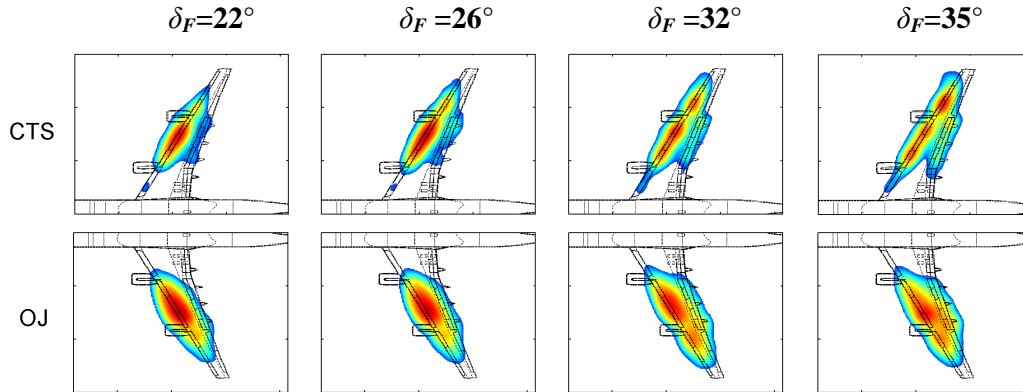


Figure 4-17: Effect of flap angle on the source characteristics in the closed test section and open jet (5 kHz) at  $U=60$  m/s and  $\alpha=3^\circ$ . The maximum level of the 12 dB colour scale is the same within both rows.

Finally, Figure 4-17 shows the effect of varying flap angle for both test sections, again in terms of 5-kHz source maps. The source characteristics seem to be fairly similar: for increasing flap angle the dominant noise source at the middle wing decreases, while the source just outside the outboard wing increases in strength. If we compare the open jet AAAP to the integrated array spectra in the open jet (Figure 4-18), the results are consistent within 0.5 dB, which confirms the reliability of the array method to determine relative noise levels (i.e. differences between configurations).

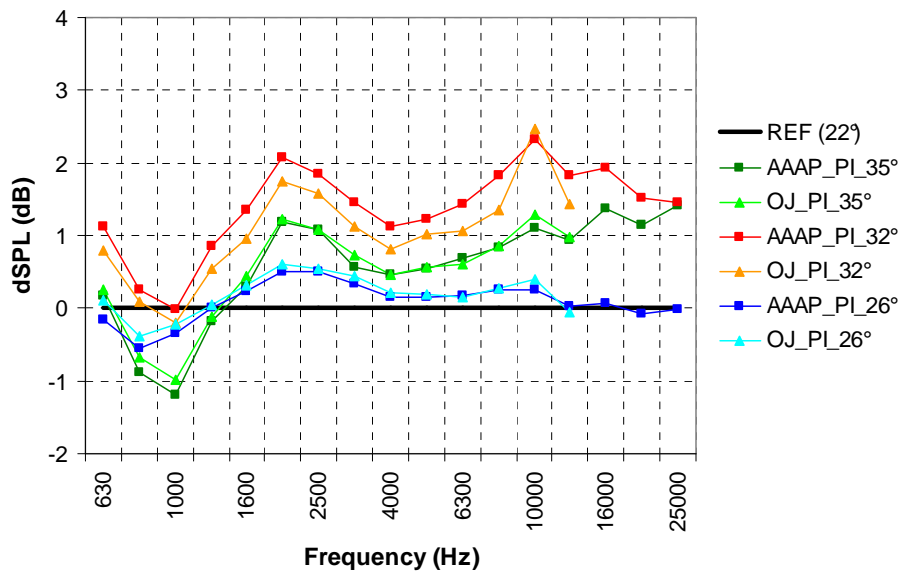


Figure 4-18: Effect of flap angle on wing noise at  $U=60$  m/s and  $\alpha=3^\circ$ . Shown are the open jet AAAP and the integrated array spectra for the open jet. All spectra are referenced to the respective spectrum at a flap angle of  $22^\circ$ .

However, if we compare relative spectra from the open jet to those from the *closed* test section (Figure 4-19), large differences occur. Whereas the CTS spectra consistently show an increase in noise each time the flap angle is increased, the open jet spectrum decreases when the flap angle changes from 32° to 35°. This difference between open and closed test section cannot be explained by an inaccuracy in the integration method, since the integrated array spectra were shown to be accurate within 0.5 dB in terms of relative noise levels. In the previous section it was already mentioned that differences in directivity due to the different array set-ups in both sections are also small. Apparently, different flow conditions in the open jet and closed test section result in relatively large differences in wing noise. It was checked if this might be caused by the fact that the slats were tripped in the open jet while they were not tripped in the closed section (see Section 4.2). However, comparison of closed section measurements with and without trips showed that these only removed tonal noise and did not affect broadband noise levels significantly. This suggests that in some cases the flow conditions in the open jet and closed test section are not identical, even though the produced lift may be the same.

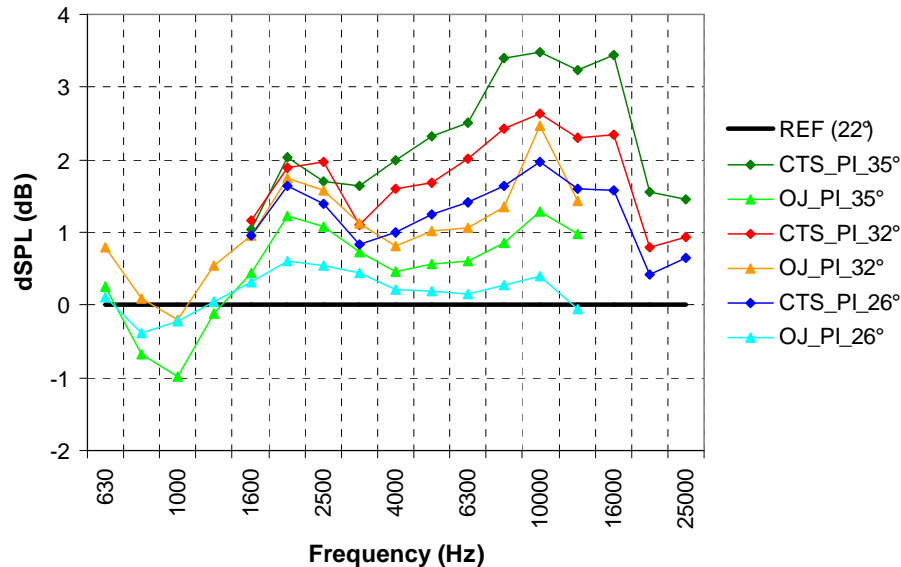


Figure 4-19: Effect of flap angle on wing noise at  $U=60$  m/s and  $\alpha=3^\circ$ . Shown are the integrated array spectra for the open jet and the closed test section. All spectra are referenced to the respective spectrum at a flap angle of  $22^\circ$ .

#### 4.6 Conclusions

The reliability of the phased array technique for quantifying airframe noise was assessed in the DNW-LLF open and closed wind tunnel sections. Acoustic measurements were performed on wing noise from a 1:10.6 scaled Airbus A340 model, using a 4-m diameter out-of-flow microphone array in the open jet and a 1-m diameter wall array in the closed test section. Since the same aircraft model was used in both test sections, the array results for the open jet and closed test section could be compared quantitatively. The spectra measured by far field microphones in the open jet were used as a reference for the absolute sound level.

In both test sections diagonal removal was applied to obtain meaningful array results. In terms of resolution the array performance was similar for both sections around 4-5 kHz. For lower frequencies the open jet array performed better, for higher frequencies the closed section array. Apart from the differences in array resolution, the source characteristics were generally similar for both test sections.

The results for the open jet show that, although the *absolute* integrated array level can be too low by more than 10 dB due to coherence loss, the *relative* sound levels determined with the array (i.e. differences between configurations) are accurate within 0.5 dB. Since the amount of coherence loss depends on wind speed, one should be careful to compare integrated spectra for different wind speeds.

The difference between the absolute array levels in the closed test section and the far field levels in the open jet is smaller than 3 dB for all frequencies. The *relative* array levels in the closed test section agree with the open jet within 1 dB, provided that the flow conditions - and therefore the noise source characteristics - are similar. In some cases larger differences between the two test sections occur, especially at high-lift conditions. These differences are most likely due to slightly different flow conditions in the open jet and closed test section, even though the angle-of-attack is adjusted such that the produced lift is the same.

### Acknowledgments

The authors would like to thank the colleagues from DLR, Airbus, and DNW for their valuable contributions to the definition of the tests and the interpretation of the results. The comments from A. Hirschberg (University of Twente) during this study are highly appreciated. For this investigation use was made of wind tunnel results from the AWIATOR project, which was sponsored by the European Commission.

### References

- [1] Mosher, M., "Phased arrays for aeroacoustic testing - Theoretical development", AIAA paper 96-1713, 1996.
- [2] Brooks, T.F., and Humphreys, W.M., "Effect of directional array size on the measurement of airframe noise components", AIAA paper 99-1958, 1999.
- [3] Dougherty, R.P., "Source Location with Sparse Acoustic Arrays; Interference Cancellation", Presented at the First CEAS-ASC Workshop: Wind Tunnel Testing in Aeroacoustics, DNW, 5-6 November 1997.
- [4] Soderman, P.T. *et al.*, "Airframe Noise Study of a CRJ-700 Aircraft Model in the NASA Ames 7-by 10-foot Wind Tunnel No. 1", AIAA paper 2002-2406, 2002.
- [5] Blacodon, D., and Elias, G., "Level estimation of extended acoustic sources using an array of microphones", AIAA paper 2003-3199, 2003.
- [6] Sijtsma, P., and Stoker, R.W., "Determination of Absolute Contributions of Aircraft Noise Components using Fly-Over Array Measurements", AIAA paper 2004-2958, 2004.
- [7] Oerlemans, S., and Sijtsma, P., "Determination of Absolute Levels from Phased Array Measurements Using Spatial Source Coherence", AIAA paper 2002-2464, 2002.
- [8] Mendoza, J.M., Brooks, T.F., and Humphreys, W.M., "An aeroacoustic study of a leading edge slat configuration", International Journal of Aeroacoustics, Vol. 1, Nr. 3, 2002.
- [9] Hutcheson, F.V., and Brooks, T.F., "Effects of Angle of Attack and Velocity on Trailing Edge Noise", AIAA paper 2004-1031, 2004.
- [10] Oerlemans, S., and Migliore, P., "Aeroacoustic Wind Tunnel Tests of Wind Turbine Airfoils", AIAA paper 2004-3042, 2004.

- [11] Oerlemans, S., and Sijtsma, P., "Acoustic array measurements of a 1:10.6 scaled Airbus A340 model", AIAA paper 2004-2924, 2004.
- [12] Brooks, T.F. and Humphreys, W.M., "A deconvolution approach for the mapping of acoustic sources (DAMAS) determined from phased microphone arrays", AIAA paper 2004-2954, 2004.
- [13] Dougherty, R.P., "Extensions of DAMAS and benefits and limitations of deconvolution in beamforming", AIAA paper 2005-2961, 2005.
- [14] Brooks, T.F. and Humphreys, W.M., "Three-dimensional application of DAMAS methodology for aeroacoustic noise source definition", AIAA paper 2005-2960, 2005.
- [15] Brooks, T.F. and Humphreys, W.M., "Extension of DAMAS phased array processing for spatial coherence determination (DAMAS-C)", AIAA paper 2006-2654, 2006.
- [16] Ravetta, P.A., Burdisso, R.A., and Ng, W.F., "Noise source localization and optimization of phased array results (LORE)", AIAA paper 2006-2713, 2006.
- [17] Ehrenfried, K. and Koop, L., "A comparison of iterative deconvolution algorithms for the mapping of acoustic sources", AIAA paper 2006-2711, 2006.
- [18] Holthusen, H. and Smit, H., "A new data-acquisition system for microphone array measurements in wind tunnels", AIAA paper 2001-2169, 2001.
- [19] Johnson, D.H., and Dudgeon, D.E., "Array Signal Processing", Prentice Hall, 1993.
- [20] Amiet, R.K., "Refraction of Sound by a Shear Layer", Journal of Sound and Vibration, Vol. 58, No. 2, pp. 467-482, 1978.
- [21] Broersma, L., "Acoustic Array Measurements - Airframe Noise and Wind Turbine Noise", Master's Thesis, Twente University, January 2006.
- [22] Dougherty, R.P., "Turbulent decorrelation of aeroacoustic phased arrays: lessons from atmospheric science and astronomy", AIAA paper 2003-3200, 2003.
- [23] Herrig, A., Würz, W., Lutz, T., Braun, K., Krämer, E., Oerlemans, S., "Trailing-edge noise measurements of wind turbine airfoils in open and closed test section wind tunnels", Proceedings of the First International Meeting on Wind Turbine Noise: Perspectives for Control, Berlin, October 2005.

## Chapter 5

### Location and quantification of noise sources on a wind turbine

*Published as: S. Oerlemans, P. Sijtsma and B. Méndez López, Location and quantification of noise sources on a wind turbine, Journal of Sound and Vibration 299, 869-883, 2007 (reprinted with permission).*

#### **Abstract**

Acoustic field measurements were carried out on a three-bladed wind turbine with a rotor diameter of 58 m, in order to characterize the noise sources and to verify whether trailing edge noise from the blades was dominant. To assess the effect of blade roughness, one blade was cleaned, one blade was tripped, and one blade remained untreated. A large horizontal microphone array, positioned about one rotor diameter upwind from the turbine, was used to measure the distribution of the noise sources in the rotor plane and on the individual blades. The operation parameters of the turbine were recorded in parallel to the acoustic tests. In total more than 100 measurements were performed at wind speeds between 6 and 10 m/s. The array results reveal that besides a minor source at the rotor hub, practically all noise (emitted to the ground) is produced during the downward movement of the blades. This strongly asymmetric source pattern can be explained by convective amplification and trailing edge noise directivity. The blade noise is produced at the outer part of the blades (but not at the very tip), and the level scales with the 5<sup>th</sup> power of the local flow speed. Comparison of the noise from the individual blades shows that the tripped blade is significantly noisier than the other two. Narrowband analysis of the dedopplerized blade noise spectra indicates that trailing edge bluntness noise is not important. All in all, the test results convincingly show that broadband trailing edge noise is the dominant noise source for this wind turbine.

## 5.1 Introduction

Wind turbine noise is one of the major hindrances for the widespread use of wind energy. In order to reduce wind turbine noise the source mechanisms must be known. For a modern large wind turbine, aerodynamic noise from the blades is generally considered to be the dominant noise source, provided that mechanical noise is adequately treated [1]. The sources of aerodynamic noise can be divided into low-frequency noise, inflow-turbulence noise, and airfoil self-noise. Low-frequency noise is caused by the aerodynamic interaction between the tower and the blades, and is considered to be of little importance for turbines with an upwind configuration (i.e. with the rotor upstream of the tower). Inflow-turbulence noise is caused by the interaction of upstream atmospheric turbulence with the leading edge of the blade, and depends on the atmospheric conditions. Airfoil self-noise is the noise produced by the blade in an undisturbed inflow, and is caused by the interaction between the turbulent boundary layer and the trailing edge of the blade. Self-noise can be tonal or broadband in character, and may be caused by several mechanisms, such as turbulent-boundary-layer-trailing-edge noise (subsequently denoted as trailing edge noise), trailing edge bluntness noise, or blade tip noise [1]. Both inflow-turbulence noise and airfoil self-noise can contribute to the overall sound level of a wind turbine, but the relative importance of the different mechanisms is not clear yet, and may depend on the specifications of the turbine [2].

Due to the large number of applications (e.g. wind turbines, airplanes, helicopters, fans), the characteristics of airfoil noise have been investigated extensively in both experimental and theoretical studies [3-13]. Both inflow-turbulence and self-noise mechanisms were considered and the dependence on parameters such as flow speed, angle-of-attack, radiation direction, and airfoil shape was characterized. These studies formed the basis of several semi-empirical wind turbine noise prediction models, which were validated by comparison to field measurements [14-20].

Since the field results only provided the overall sound level of the turbine, the relative importance of the different mechanisms was determined mainly on the basis of the predictions. In some studies inflow-turbulence noise was regarded to be the dominant source [11,14-16,18], while others considered trailing edge noise to be dominant [17]. In another case the turbine noise in different frequency ranges was attributed to mechanical noise, trailing edge noise, tip noise, and inflow-turbulence noise [19]. Only in a few studies source location measurements were performed to provide more direct information on the source mechanisms [21-23]. These measurements were done using an acoustic parabola or a linear microphone array, and focused only on the horizontal blade position.

The present study concerns acoustic field measurements that were carried out in the framework of the European SIROCCO project [24]. The objective of the project is to reduce wind turbine noise by designing new airfoils with low trailing edge noise emissions [25,26]. Although this concept has been successfully demonstrated for a model scale rotor [27], application to a full-scale wind turbine is only effective if trailing-edge noise is dominant. Therefore, the goal of the present field tests was to characterize the noise sources on the baseline turbine, and to verify whether trailing edge noise from the blades was dominant. The measurements were performed on a three-bladed GAMESA G58 wind turbine with a rotor diameter of 58 m. In order to assess the effect of blade roughness due to e.g. dirt or insects, prior to the acoustic tests one blade was cleaned, one blade was tripped, and one blade was left untreated. A large horizontal microphone array, positioned about one rotor diameter

upwind from the turbine, was used to measure the distribution of the noise sources in the rotor plane and on the individual blades.

In the present paper the array results are presented and analyzed. The characteristics of mechanical and aerodynamic noise sources are investigated, and the effect of blade roughness is examined by comparing the noise from the individual blades. From these analyses the importance of the different possible source mechanisms is assessed. Section 5.2 describes the test set-up and the array processing methods. In Section 5.3 the results are presented and discussed. The conclusions of this study are summarized in Section 5.4.

## 5.2 Experimental method

### 5.2.1 Test set-up

The measurements were carried out on a pitch-controlled, three-bladed GAMESA G58 wind turbine, which has a rotor diameter of 58 m and a tower height of 53.5 m (Figure 5-1). The turbine was located on the wind farm 'Los Monteros' in northern Spain, which has rather constant wind conditions. In order to obtain a clean inflow, a turbine on the upwind edge of the farm was chosen. About one week before the acoustic tests, one blade was cleaned, one blade was first cleaned and then tripped, and one blade remained untreated. Tripping was done using zigzag tape of 0.4 mm thickness over the complete radius, at 5% chord on the suction and pressure side of the blade. The rotor RPM was about 25, which corresponds to a tip Mach number of 0.22. The acoustic array consisted of 148 Panasonic WM-61 microphones, mounted on a horizontal wooden platform of 15x18 m<sup>2</sup>. The platform was positioned about 58 m upwind from the turbine, resulting in a 'view angle' of about 45° (Figure 5-2).



Figure 5-1: Test set-up with G58 wind turbine and microphone array platform. The noise sources in the rotor plane (averaged over several rotations) are projected on the picture.

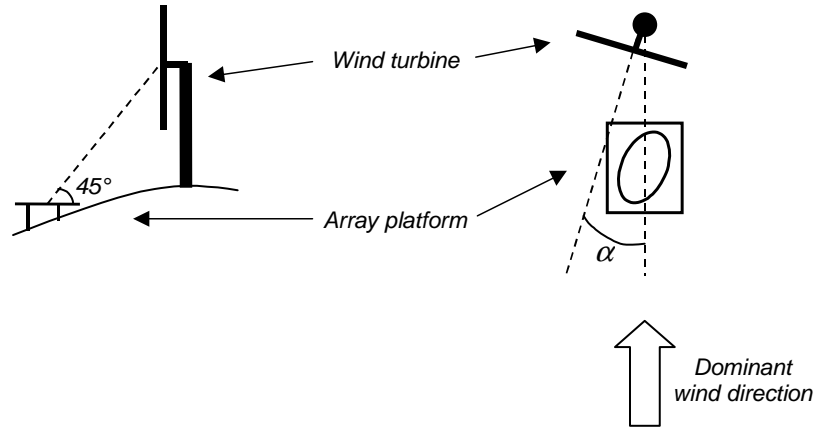


Figure 5-2: Schematic picture of test set-up: side view (left) and top view (right).

The 'misalignment angle'  $\alpha$  was the angle between the rotor axis (depending on wind direction) and the line from turbine to array. As a reference, two calibrated B&K microphones were placed on the platform as well. All microphones were mounted flush to the surface of the platform, with the membrane parallel to the platform, and without windscreens. The array had an elliptic shape (Figure 5-3) to obtain approximately the same array resolution in the horizontal and vertical direction of the rotor plane, despite the view angle of 45°. The ellipse was slightly tilted towards the right-hand side of the rotor plane, to obtain maximum resolution on the side where the blades move downward and where maximum noise radiation was expected. The array had a high microphone density in the center to ensure low side-lobe levels at high frequencies, and a low-density outer part to obtain a good resolution at low frequencies.

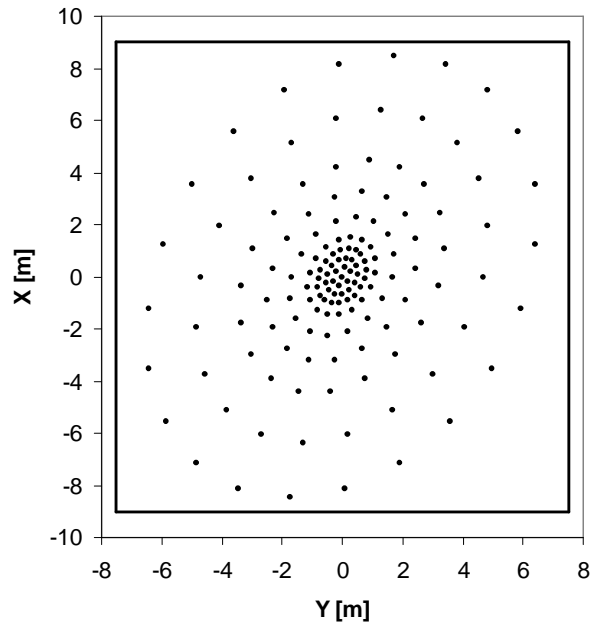


Figure 5-3: Layout of array microphones. The rectangle indicates the platform dimensions.



### 5.2.2 Data acquisition

Acoustic data from the array microphones were synchronously measured at a sample frequency of 51.2 kHz and a measurement time of 30 s. The acoustic data were processed using a block size of 2048 with a Hanning window and an overlap of 50%, yielding 1500 averages and a narrowband frequency resolution of 25 Hz. A second-order 500 Hz high-pass filter was used to suppress high-amplitude pressure fluctuations at low frequencies, and thus extend the dynamic range to low pressure amplitudes at high frequencies. The sound levels were corrected for the filter response and for pressure doubling due to the platform. Prior to the measurements, the sensitivity at 1 kHz was determined for all array microphones using a calibrated pistonphone. The frequency response of the Panasonic microphones was taken from previous calibration measurements. No corrections were applied for microphone directivity, since calibration measurements showed that these effects amounted to less than 2 dB up to 20 kHz, for angles smaller than 75° with respect to the microphone axis. Phase matching of the microphones was checked using a calibration source at known positions.

In parallel to the acoustic measurements, the following turbine operation parameters were acquired at a sample rate of 3 Hz: wind speed, power production, turbine orientation, RPM, blade pitch angle, and temperature. The measured wind speed (at the rotor hub) was translated to the wind speed at 10 m height using the standard wind profile from the IEC norm for wind turbine noise measurements [28].

### 5.2.3 Test program

During the test campaign, which lasted from 8-15 December 2003, a total number of 110 acoustic measurements was performed. By applying the following criteria, the 35 most stable measurements were selected for further processing:

- 1) Wind speed within 15% (and within 1.5 m/s) of average;
- 2) Misalignment angle  $\alpha$  (see Figure 5-2) smaller than 12° and within 2° of average;
- 3) Rotor RPM within 8% of average;
- 4) Blade pitch angle within 3° of average;
- 5) Overloads in acoustic data (e.g. due to wind gusts) less than 1%.

The above averages were calculated for the 30 s period of each acoustic measurement. The distribution of the 35 selected measurements over the different wind speed intervals is given in Table 5-1. It can be seen that all wind speeds are well represented. The rotor RPM typically varied between 22 and 26.

Table 5-1: Distribution of measurements over wind speed bins.

Wind speed at 10 m (m/s)	6	7	8	9	10
No. of measurements	6	6	12	5	6

### 5.2.4 Phased array processing

The microphone array data were processed using two different methods. With the first method, noise sources in the rotor plane were localized using conventional beamforming [29]. Thus, noise from the rotor hub can be separated from blade noise, and it can be seen where in

the rotor plane the blade noise is produced (see e.g. Figure 5-1). The method shows the integrated effect of the three blades, averaged over the complete measurement time of 30 s (i.e. several rotations). The first step of this processing involves the calculation of an averaged cross-spectral density matrix which contains the cross-powers of all microphone pairs in the array. To improve the resolution and to suppress background noise (e.g. wind-induced pressure fluctuations on the microphones), the main diagonal of the cross-power matrix (i.e. the auto-powers) was discarded. A frequency-dependent spatial window was applied to the microphone signals, in order to improve the resolution at low frequencies and to suppress coherence loss effects at high frequencies (due to propagation of the sound through the atmospheric boundary layer). The scan grid, with a mesh size of 1 m in both directions, was placed in the rotor plane of the wind turbine, and was rotated in accordance with the orientation of the turbine (depending on wind direction). The  $6^\circ$  angle between the rotor axis and the horizontal plane was also accounted for. The effect of sound convection in the atmospheric boundary layer was taken into account by assuming a constant wind speed between the scan location and the microphones. This constant wind speed was calculated as the average wind speed between the rotor hub and the array center, using the standard wind profile from the IEC norm for wind turbine noise measurements [28]. The narrowband acoustic source plots were summed to 1/3-octave bands, and the scan levels were normalized to a constant reference distance. The noise sources in the rotor plane were quantified using a source power integration method [30]. By defining one integration contour around the whole rotor plane and one only around the hub, noise levels from the hub and the blades were determined.

The second processing method employed three rotating scan planes to localize the (de-dopplerized) noise sources on the three individual blades [31]. This enabled a comparison of the noise from the clean, tripped, and untreated blade. The start position of the scan planes was determined using a trigger signal from the turbine, that was recorded synchronously with the acoustic data. The mesh size of the scan grid was 0.5 m in both directions, and the scan plane was placed around the blade, in the rotor plane. Similar to the first processing method, the narrowband acoustic source plots were summed to 1/3-octave bands, and the scan levels were normalized to a constant reference distance. Since the source plots of the rotor plane indicated that practically all noise was produced during the downward movement of the blades (Figure 5-1), and since the array resolution was highest on the right-hand side of the rotor plane, the blades were only scanned during their downward movement (for azimuthal angles from  $0^\circ$  to  $180^\circ$ , with  $0^\circ$  the upper vertical blade position). The noise from the blades was quantified using a power integration method for moving sound sources [32]. An integration contour was defined which surrounds the noise from the blade but excludes the noise from the rotor hub. In order to limit processing time, only the first two rotor revolutions after the start of each acoustic measurement were processed (one at a time). Comparison of the integrated spectra showed that the differences in average blade noise levels between the first and second rotation were smaller than 0.3 dB for all frequencies, which indicates a good repeatability.

### 5.3 Results and discussion

In this section the results of the acoustic array measurements are presented and analyzed. Section 5.3.1 describes the characteristics of the noise sources in the rotor plane, while in Section 5.3.2 the noise sources on the individual rotor blades are analyzed.

#### 5.3.1 Noise sources in the rotor plane

In this section the distribution of the noise sources in the rotor plane is examined. The noise levels from the rotor hub and the blades are compared, and an analysis is made of convective and directivity effects. Furthermore, the speed dependence of the blade noise levels is investigated.

##### 5.3.1.1 Distribution of noise sources in the rotor plane

The average source distributions in the rotor plane are shown in Figure 5-4 as a function of frequency. In order to show the general trends, these source distributions were averaged over all measurements. The source plots show the integrated effect of the three blades, averaged over the complete measurement time of 30 s (i.e. several rotations). A number of observations can be made from these plots. The most striking phenomenon is that practically all downward radiated blade noise (as measured by the array) is produced during the downward movement of the blades. Since the range of the dB scale is 12 dB, this means that the (downward radiated) noise produced during the upward movement is at least 12 dB less than during the downward movement. This effect was observed for basically all measurements and all frequencies, and is very similar to results obtained earlier on a model scale wind turbine, where it was attributed to convective amplification and directivity of trailing edge noise [27]. In Section 5.3.1.3 a detailed analysis will be given of this phenomenon.

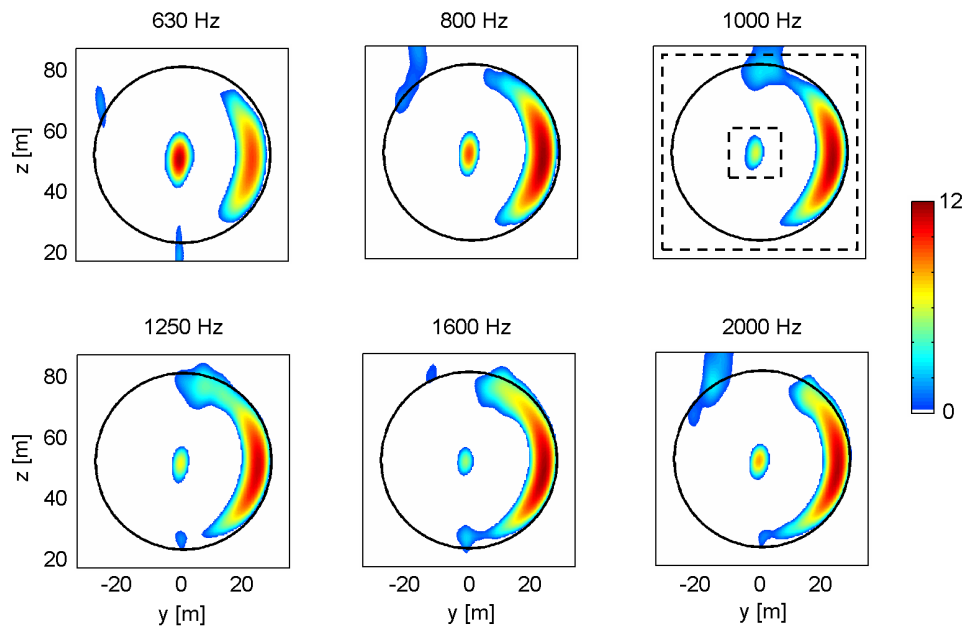


Figure 5-4: Average distribution of noise sources in the rotor plane, as a function of frequency. The black circle indicates the trajectory of the blade tips. The range of the dB scale is 12 dB. The dashed rectangles at 1 kHz indicate the integration contours for the quantification of blade and hub noise.

A second observation in Figure 5-4 is that the noise from the blades appears to dominate the noise from the rotor hub. In section 5.3.1.2 the sound levels of both sources will be quantified to confirm this observation. With regard to the blade noise, it can be seen that the sources are located at the outer part of the blades, but not at the very tip. Thus, tip noise is not important for the present turbine. The peak location of the blade sources moves outward for increasing frequency, from a radius of 21 m at 315 Hz to a radius of 26 m at 5 kHz. Assuming that trailing edge noise is the responsible mechanism, this can be explained by the higher flow speeds and the smaller chord at higher radii, resulting in a thinner trailing edge boundary layer. In Section 5.3.2.1 the source locations will be determined as a function of frequency for the individual blades. Finally, the source distributions show that blade-tower interaction effects are not significant, although above 1 kHz a slight noise increase is visible at the location of the tower.

### 5.3.1.2 Blade noise versus hub noise

The noise from the blades and the rotor hub was quantified using the source power integration method mentioned in Section 5.2.4. The integration contours are shown in Figure 5-4 (1 kHz): the small box was used for quantification of hub noise, while blade noise was defined as the difference between the integrated sound levels for the large and small box. The spectra in Figure 5-5 (averaged over all measurements) confirm the observation from the source plots, that the blade noise is significantly higher than the noise from the hub.

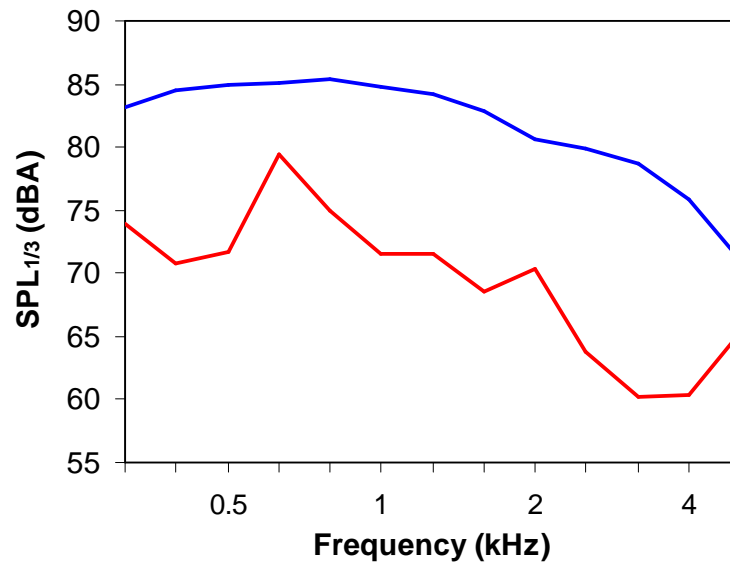


Figure 5-5: Average spectra of hub noise (—) and blade noise (—).

The hub noise shows a peak at 630 Hz, which is probably due to the gearbox. The blade noise is broadband in nature, as would be expected for trailing edge noise. The highest A-weighted levels occur around 800 Hz. Interestingly, the blade noise spectrum seems to consist of two broad 'humps': a low-frequency hump centered at 800 Hz, and a high-frequency hump starting at 2 kHz. These two humps may be caused by trailing edge noise from the suction- and pressure-side boundary layers respectively. The difference between the overall sound pressure

levels from hub and blades was found to increase with wind speed, from about 8 dB(A) at 6 m/s to about 11 dB(A) at 10 m/s. Apparently, blade noise increases faster than hub noise with increasing wind speed. In conclusion, blade noise is clearly dominant for the present wind turbine.

### 5.3.1.3 Convective amplification and directivity

Apart from a small influence from the atmospheric boundary layer and the tower, the flow conditions on the blade, and consequently the acoustic source strength, are considered to be independent of rotor azimuth. Therefore, the strong asymmetry observed in the acoustic source distributions (Figure 5-4) is expected to be caused by convective (Doppler) amplification and directivity. Similar source patterns were found for a model scale wind turbine in a wind tunnel, where no wind speed gradient was present [27]. The effect of convective amplification is illustrated by the influence of the turbine orientation on the acoustic source distribution: Figure 5-6 shows that the location of the source region shifts upward or downward when the right- or left-hand side of the rotor plane is turned towards the array respectively (the misalignment angle  $\alpha$  was defined in Figure 5-2). This effect was also observed in [27], and can be qualitatively explained by the change in the component of the blade velocity in the direction of the array, which results in a change in convective amplification.

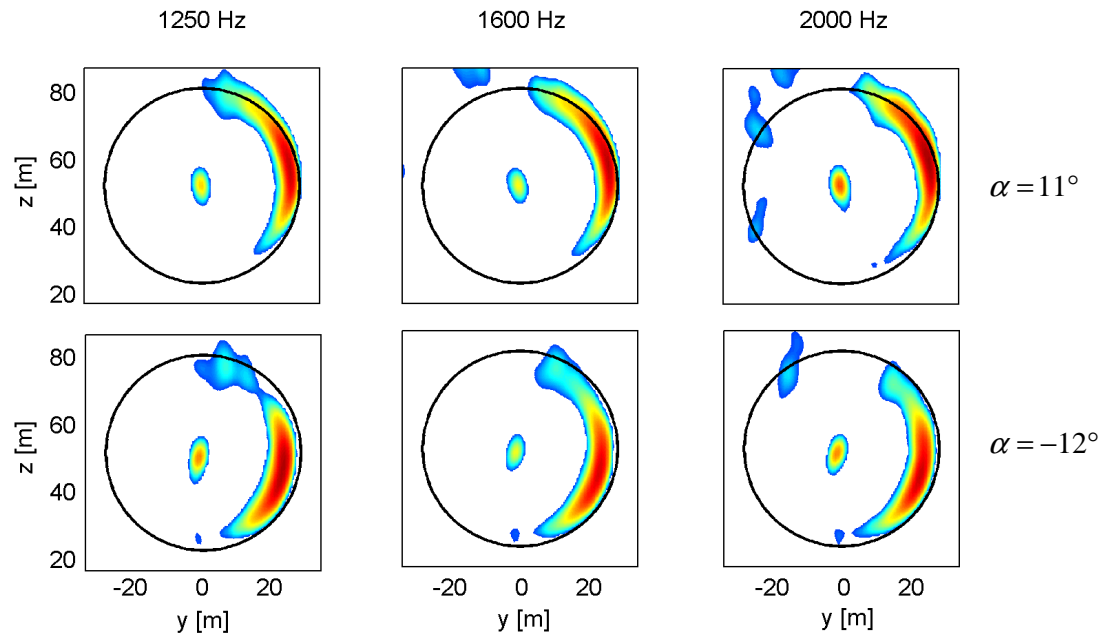


Figure 5-6: Shift of blade noise location due to difference in misalignment angle  $\alpha$ .

In order to determine if convective amplification and directivity can quantitatively explain the strong asymmetry in the measured source distribution, the expected magnitude of these effects was calculated for the present test set-up. The following directivity function for high-frequency trailing edge noise was used [33]:

$$D = \frac{2 \sin^2(\theta/2) \sin^2 \phi}{(1 - M \cos \xi)^4}, \quad (5.1)$$

where  $\theta$  is the angle between the blade chord line and the source-observer line,  $\phi$  is the angle between the plane of the blade and the plane containing the chord line and the observer,  $\xi$  is the angle between the blade flow velocity and the source-observer line, and  $M$  is the (undisturbed) blade Mach number. The numerator in Eq. (5.1) describes the directivity of high-frequency trailing edge noise. It was analytically derived for edge noise from a semi-infinite flat plate [6,34], but was also found to be valid for finite airfoils [9], provided that the angle  $\theta$  is not too close to  $180^\circ$  and the acoustic wavelength is smaller than the airfoil chord. Note that this directivity factor is slightly different from the factor derived by Howe [4], who used an alternative theoretical approach. In the limit for low-frequency dipole noise, where the acoustic wavelength is much larger than the airfoil chord, the  $\sin^2(\theta/2)$  term changes into  $\sin^2 \theta$  [5,33]. For inflow-turbulence noise radiated from the leading edge the  $\theta$ -dependence is inverted [5,11] and  $\theta$  should be replaced by  $(\pi - \theta)$ . The denominator in Eq. (5.1) represents the convective amplification factor for trailing edge noise. As mentioned by Brooks&Burley [33], different exponent power laws between 1.5 and 4.5 have been found in different theoretical approaches, while experimental validation has been very limited. Following [33], here the 4<sup>th</sup> power for compact dipole sources is used [35].

For the present calculations the observer position was taken to be the center of the microphone array. The source was assumed to be located at the trailing edge of the blade at a radius of 25 m, which is the location where we typically observed blade noise (Figure 5-4). In order to account for the convection of sound by the wind, so-called 'retarded' source coordinates were used [33]. For the RPM and wind speed typical values of 25 and 8 m/s were used respectively. Figure 5-7 shows the calculated convective amplification and directivity factors as a function of rotor azimuth (zero azimuth is the upper vertical blade position).

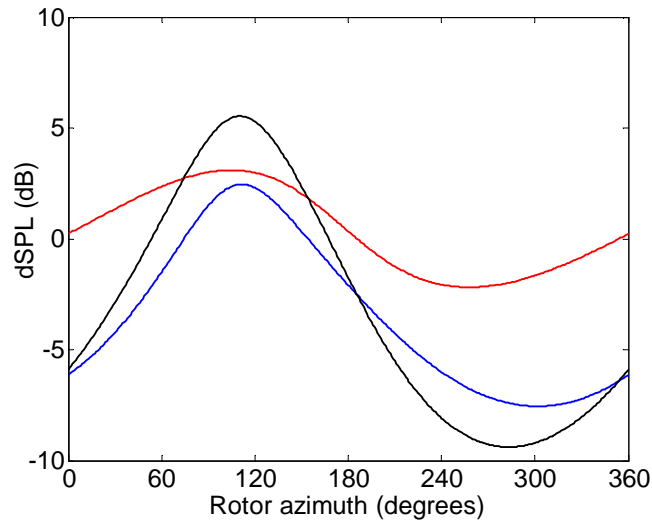


Figure 5-7: Calculated convective amplification (—) and directivity (—) factors for high-frequency trailing edge noise. The black line (—) indicates the combined effect.

It can be seen that the experimental trend is well reproduced: the calculation shows a maximum at  $110^\circ$  azimuth and the difference between the downward and upward blade movement is 14.9 dB. These values are in good agreement with the experimentally obtained average values of  $102^\circ$  azimuth and a level difference of about 15 dB between the left- and right-hand side of the rotor plane. Figure 5-7 shows that the peaks for the convective amplification and directivity factors roughly coincide, and that directivity contributes most to the asymmetry. For a misalignment angle of  $12^\circ$ , the calculated peak azimuth shifted by about  $11^\circ$ , in accordance with the experimental results in Figure 5-6.

Since for low frequencies the acoustic wavelength is of the same order as the blade chord (0.67 m at a radius of 25 m), the directivity factor was also calculated using the low-frequency approximation with a  $\sin^2 \theta$  dependence (Figure 5-8). However, these calculations show a peak azimuth of  $135^\circ$  and a level difference of only 6.9 dB (including the convective effect). Since the experimental results exhibited a peak azimuth around  $102^\circ$  and a level difference of about 15 dB for all frequencies (between 315 Hz and 5 kHz), the high-frequency approximation in Eq. (5.1) seems to be valid for the whole frequency range. Furthermore, if inflow-turbulence (leading edge) noise rather than trailing edge noise would be the responsible mechanism for the blade noise, the  $\theta$ -dependence would be inverted and the peak azimuth would occur during the upward movement of the blade (Figure 5-8). Thus, the present analysis shows that only the high-frequency trailing edge noise factors in Eq. (5.1) satisfactorily explain the experimental results. It should be realized that the asymmetry in source locations is purely an effect of observer location, i.e. for an observer on the rotor axis the source pattern would be symmetrical. For other (far field) observer locations, Eq. (5.1) can be applied to estimate convective and directivity effects.

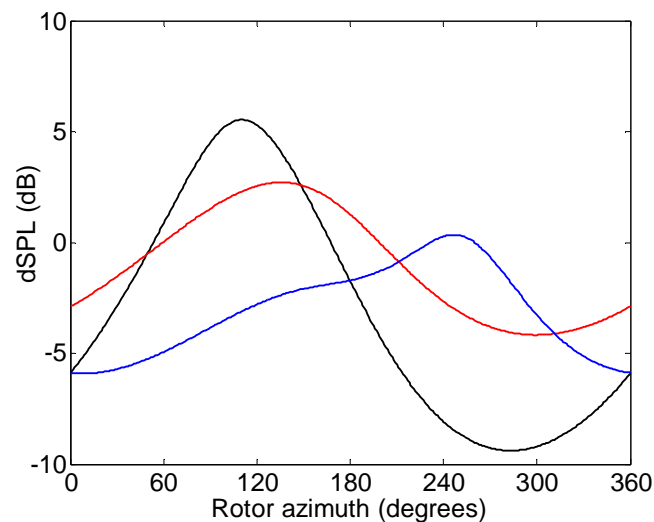


Figure 5-8: Calculated combined effect of convective amplification and directivity for high-frequency trailing edge noise (—), low-frequency dipole noise (—), and inflow-turbulence noise from the leading edge (—).

### 5.3.1.4 Speed dependence of blade noise

The speed dependence of the noise levels was investigated by calculating normalized sound levels as a function of Strouhal number  $St = fL/U$ , where  $f$  is frequency and  $L$  a typical length scale. For trailing edge noise,  $L$  is usually taken to be the boundary layer thickness at the trailing edge [5,6], although a recent study suggests that a constant reference length should be used [12]. Since in the present tests the trailing edge boundary layer thickness was not measured, a constant value of 1 cm was chosen for  $L$ . For  $U$  the undisturbed flow speed as perceived by the blade was used, defined as the vector sum of the wind speed and the rotational speed (induced velocity is neglected). The rotational speed was calculated for a radius of 25 m, which is the location where we typically observed blade noise (Figure 5-4). The noise levels were normalized as  $SPL_{norm} = SPL - 10x \log(U_{blade}/U_{ref})$ , with  $SPL$  and  $SPL_{norm}$  the measured and normalized noise levels respectively.  $U_{ref}$  is a constant reference speed, for which here a value of 50 m/s was chosen. The variable  $x$  indicates the dependence of the blade noise on the flow speed: the acoustic energy is assumed to be proportional to the flow speed to the power of  $x$  ( $p^2 \sim U^x$ ).

The measured and normalized blade noise spectra for the 35 individual measurements are shown in Figure 5-9. The normalization was done using a value of 5 for  $x$ , which gave the best data collapse. This is indicative of trailing edge noise, since normally  $x$  is around 5 for trailing edge noise, and around 6 for inflow turbulence noise [6,10]. It can be seen that without normalization the scatter in data is 5-10 dB, even when the quietest measurement is neglected. After normalization the scatter is only 2-5 dB, including the quietest measurement. The use of a frequency-dependent source radius for the calculation of  $U$  did not significantly improve the data collapse. The remaining scatter in the normalized spectra may be due to the variation in chord and angle-of-attack along the blade radius, which leads to different trailing edge boundary layer characteristics for different source positions. Furthermore, there may be differences in turbine and weather parameters between the individual measurements. It was investigated whether the remaining scatter (after correcting for the speed effect) correlated with the misalignment angle (Figure 5-2) or blade pitch angle, but no clear relation was found.

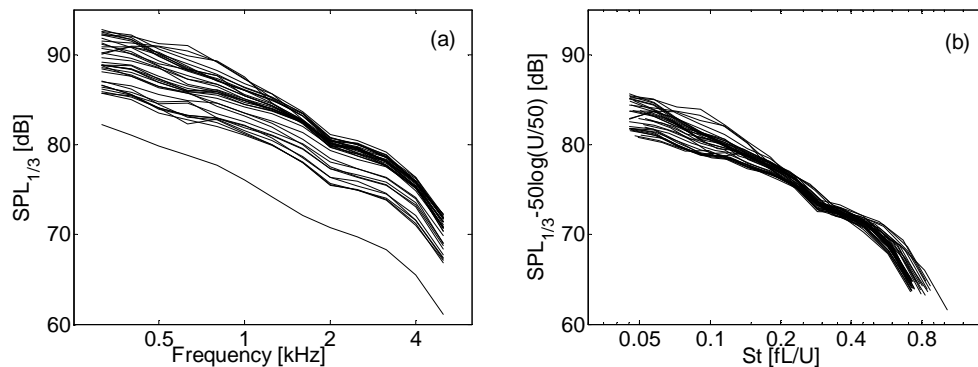


Figure 5-9: Measured (a) and normalized (b) blade noise spectra for all measurements.  $U$  is the flow speed perceived by the blade.



### 5.3.2 Noise sources on the individual blades

In this section the noise sources on the individual rotor blades are analyzed. Source levels and locations are compared for the clean, tripped, and untreated blade. The presence of trailing edge bluntness noise is examined by means of a narrowband analysis. Finally, the aerodynamic flow state on the untreated blade is assessed on the basis of the acoustic results.

#### 5.3.2.1 Source levels and locations for the individual blades

Noise source distributions on the three individual blades, integrated over azimuthal angles from  $0^\circ$  to  $180^\circ$ , are shown in Figure 5-10 for the most relevant frequency bands. The source distributions were averaged over all measurements to show the general trends. Note that the signal-to-noise ratio is very good (i.e. no spurious sources), despite the fact that only half a revolution was used (see Section 5.2.4). These plots confirm the observations from the source distributions in the rotor plane (Figure 5-4): the blades are noisier than the hub and the relative importance of the hub is largest at 630 Hz. The aerodynamic noise is produced at the outer blades and the sources move outward with increasing frequency. In addition, Figure 5-10 shows that the tripped blade is significantly noisier than the other two. This observation is a strong indication of trailing edge noise, since earlier studies have indicated that tripping does affect trailing edge noise, but has no influence on inflow turbulence (leading edge) noise [10]. Although the blade sources appear to be centered at the trailing edge, the array resolution does not seem to be sufficient to directly distinguish between leading edge and trailing edge noise. The sources for the tripped blade seem to be located at a slightly higher radius than for the clean and untreated blade.

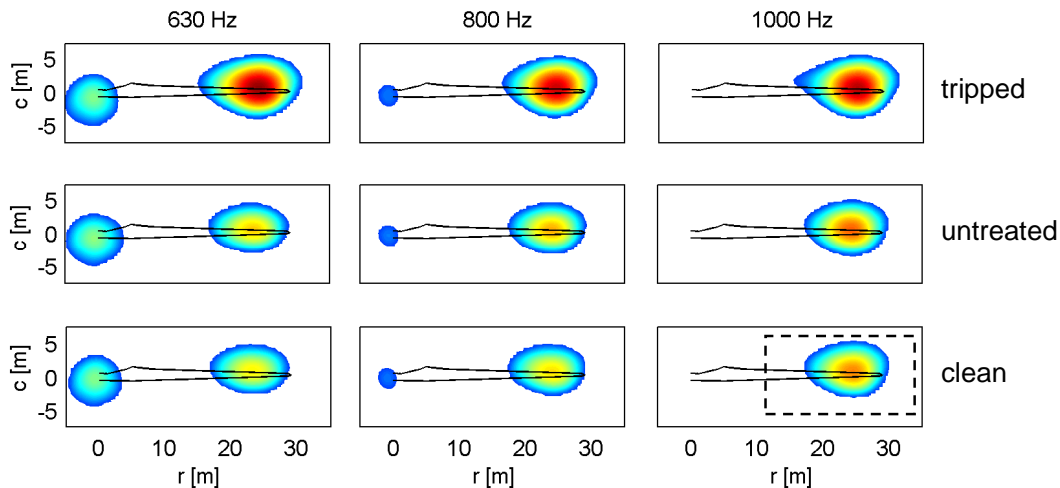


Figure 5-10: Average distribution of noise sources on the individual blades. The black line indicates the blade contour (leading edge on lower side). The range of the dB scale is 12 dB and the scale is the same for the three blades. The dashed rectangle at 1 kHz indicates the integration contours for the quantification of blade noise.

To further investigate these observations, the source levels and locations are given in Figure 5-11 for the three blades. The blade noise levels were quantified using the integration contour indicated in Figure 5-10 (1 kHz). Figure 5-11a clearly shows that the tripped blade is noisier than the other two for the important low frequencies, and that the tripped and untreated

blades are slightly noisier than the clean blade at higher frequencies. The overall A-weighted sound level for the tripped blade was 3.6 dB(A) higher than for the clean blade, while the untreated blade was only 0.1 dB(A) noisier than the clean blade. These level differences between the blades were practically independent of wind speed. The lower peak frequency for the tripped blade can be explained by the increased boundary layer thickness at the trailing edge.

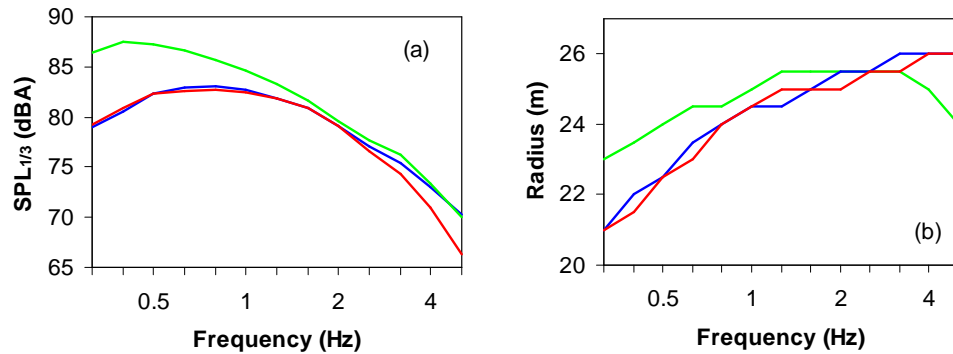


Figure 5-11: Average noise source spectra (a) and source locations (b) for the three blades: — tripped blade, — untreated blade, — clean blade.

The source radius was defined as the radius at which the maximum source level occurs in the source distributions of Figure 5-10. Since the mesh size of the scan grid was 0.5 m, these source radii are multiples of 0.5 m. Figure 5-11b shows that, except for the highest frequencies, the sources move outward with increasing frequency, and that the source radius is largest for the tripped blade. These trends can be understood from the decrease in boundary layer thickness with increasing radius, and from the thicker boundary layer for the tripped blade. No conclusive explanation was found yet for the decrease in source radius of the tripped blade at high frequencies. This effect might be connected to noise contributions from the pressure side of the blade or to the trip thickness (0.4 mm) being relatively large for the outer blade parts (see also Section 5.3.2.3).

Similar to Section 5.3.1.4 (Figure 5-9), the speed dependence of the blade noise was investigated by plotting normalized blade noise spectra as a function of Strouhal number.

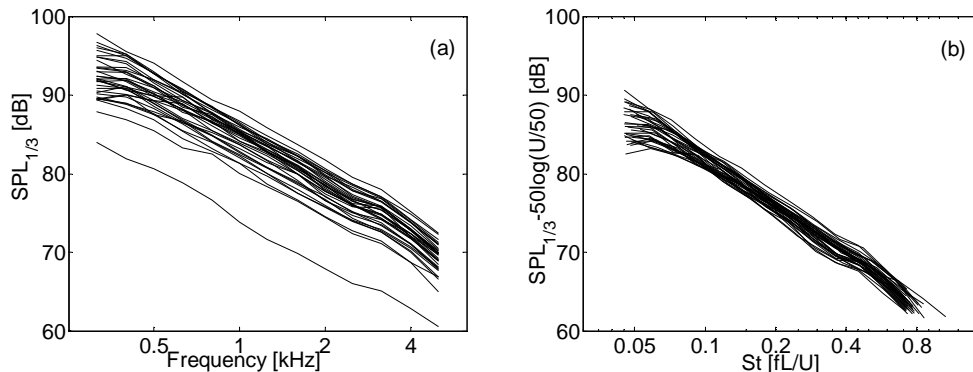


Figure 5-12: Measured (a) and normalized (b) tripped blade noise spectra for all measurements.  $U$  is the flow speed perceived by the blade.

Again, the levels and frequencies were normalized using the flow speed at a radius of 25 m. As an example, the measured and normalized spectra for the tripped blade are shown in Figure 5-12. These plots confirm that a good data collapse is obtained for  $x = 5$ , which is indicative of trailing edge noise. Similar to the results in Section 5.3.1.4, the remaining scatter in the normalized spectra may be due to the variation in chord and angle-of-attack along the blade radius, or due to differences in turbine and weather parameters between the individual measurements.

### 5.3.2.2 Trailing edge bluntness noise

When the trailing edge thickness of an airfoil is larger than about 20% of the boundary layer displacement thickness, trailing edge bluntness noise can occur [5,6,12]. Trailing edge bluntness noise is caused by periodic vortex shedding, and typically results in spectral peaks or humps, the frequency of which depends on flow speed and trailing edge (boundary layer) thickness. Bluntness noise has also been observed on wind turbines [14]. Since the blade noise spectra presented here (Figure 5-12) were in 1/3-octave bands and summed over the whole blade radius (except the hub), possible bluntness tones could be obscured. Therefore, narrowband source spectra were produced for individual radial sections, by energetically summing the chordwise scan levels in the acoustic source plots (Figure 5-10) for a given radius. Figure 5-13 shows an example of these radial source spectra for one measurement. Since the spectra are dedopplerized (see Section 5.2.4), possible bluntness tone should have been clearly visible. However, it can be seen that only small fluctuations occur, and that no narrowband tones are identified. For the other measurements no narrowband tones were observed either, for any of the blades. Therefore, it can be concluded that trailing edge bluntness noise is not important for the present turbine.

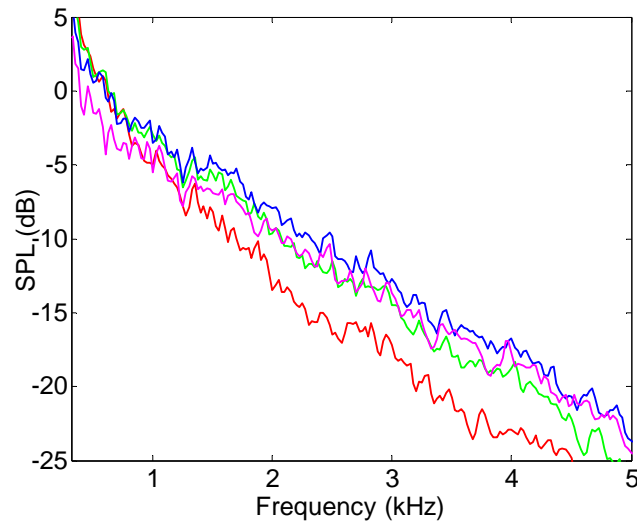


Figure 5-13: Example of narrowband spectra for individual radial sections of the clean blade, illustrating absence of trailing edge bluntness noise: —  $r=21$  m, —  $r=23$  m, —  $r=25$  m, —  $r=27$  m.

### 5.3.2.3 Aerodynamic flow state on the rotor blades

The acoustic results can also provide information about the aerodynamic flow state on the blades, which is important input for the design of low-noise airfoils [25]. Depending on the amount of contamination, a turbine blade may be aerodynamically clean (natural boundary layer transition from laminar to turbulent) or rough (premature transition close to the leading edge). Since the flow conditions vary with blade radius, the flow state may also depend on the position on the blade. Prior to the present acoustic tests, it was expected that the untreated blade, which is representative for a turbine blade during normal operation, would be rough. However, the similarity between the noise levels of the clean and untreated blade (Figure 5-11) suggests that the untreated blade was aerodynamically clean. An alternative explanation for this similarity could be that both the 'clean' and 'untreated' blades were in fact rough, because there was about one week between the cleaning of the blade and the acoustic measurements. In this case the higher levels for the tripped blade could be explained by the relatively large trip thickness (0.4 mm), which might have caused overtripping.

To get more insight in these two possibilities, two-dimensional acoustic wind tunnel tests were performed of the trailing edge noise from the GAMESA airfoil, for clean and tripped conditions [26]. These measurements showed that the trailing edge noise levels for a 0.4 mm zigzag trip (as in the field measurements) were practically identical to those for a two-dimensional turbulator strip with a thickness of 0.18 mm. This indicates that in the wind tunnel the zigzag tape did not cause overtripping. Moreover, the tripped airfoil exhibited a noise increase at low frequencies with respect to the clean airfoil, similar to the noise increase observed in the present field tests (Figure 5-11). This is a strong indication that the untreated blade was aerodynamically clean during the field tests, at least for the acoustically important frequencies. The small difference between the clean and untreated blade at high frequencies may be caused by some roughness close to the tip of the untreated blade, where the boundary layer is more easily tripped and where high frequencies are produced.

## 5.4 Conclusions

Acoustic field measurements were carried out on a three-bladed wind turbine with a rotor diameter of 58 m, in order to characterize the noise sources and to verify whether trailing edge noise from the blades was dominant. To assess the effect of blade roughness, one blade was cleaned, one blade was tripped, and one blade remained untreated. A large horizontal microphone array, positioned about one rotor diameter upwind from the turbine, was used to measure the distribution of the noise sources in the rotor plane and on the individual blades.

The array results have shown that besides a minor source at the rotor hub, practically all noise (emitted to the ground) is produced during the downward movement of the blades. This strongly asymmetric source pattern was explained by convective amplification and trailing edge noise directivity. The blade noise was produced at the outer part of the blades (but not at the very tip), and the level scaled with the 5<sup>th</sup> power of the local flow speed. Comparison of the noise from the individual blades showed that the tripped blade was significantly noisier than the other two. Narrowband analysis of the dedopplerized blade noise spectra indicated that trailing edge bluntness noise was not important. All in all, the test results have convincingly shown that broadband trailing edge noise is the dominant noise source for the present wind turbine. This conclusion is consistent with calculated results from a semi-

empirical prediction code for wind turbine noise [24]. The acoustic results indicate that the untreated blade was aerodynamically clean during the field tests.

### Acknowledgments

The authors would like to thank the colleagues from the University of Stuttgart and from the Netherlands Energy Research Foundation (ECN) for their valuable contributions to the definition of the tests and the interpretation of the results. The comments from A. Hirschberg (University of Twente) during the preparation of this paper are highly appreciated. Financial support for this research was given in part by the European Commission's Fifth Framework Programme, project reference: SIROCCO, Silent Rotors by Acoustic Optimisation (ENK5-CT-2002-00702). Financial support was also given by the Netherlands Organisation for Energy and the Environment (NOVEM).

### References

- [1] S. Wagner, R. Bareiss, G. Guidati, *Wind Turbine Noise*. Springer Verlag, 1996.
- [2] G. Guidati, J. Ostertag, S. Wagner, Prediction and reduction of wind turbine noise: an overview of research activities in Europe, AIAA paper 2000-0042, 2000.
- [3] R. Amiet, Acoustic Radiation from an Airfoil in a Turbulent Stream. *Journal of Sound and Vibration* 41 (1975) 407-420.
- [4] M.S. Howe, A review of the theory of trailing edge noise. *Journal of Sound and Vibration* 61 (1978) 437-465.
- [5] W.K. Blake, *Mechanics of Flow-Induced Sound and Vibration*, Academic Press, 1986.
- [6] T.F. Brooks, D.S. Pope, M.A. Marcolini, *Airfoil Self-Noise and Prediction*. NASA Reference Publication 1218, 1989.
- [7] T. Dassen, R. Parchen, G. Guidati, S. Wagner, S. Kang, A.E. Khodak, Comparison of measured and predicted airfoil self-noise with application to wind turbine noise reduction, *Proceedings of the European Wind Energy Conference*, Dublin, October 1997.
- [8] G. Guidati, R. Bareiss, S. Wagner, T. Dassen, R. Parchen, Simulation and measurement of inflow-turbulence noise on airfoils, AIAA paper 97-1698, 1997.
- [9] F.V. Hutcheson, T.F. Brooks, Effects of angle of attack and velocity on trailing edge noise, AIAA paper 2004-1031, 2004.
- [10] S. Oerlemans, P. Migliore, Aeroacoustic wind tunnel tests of wind turbine airfoils, AIAA paper 2004-3042, 2004.
- [11] S. Moreau, M. Roger, Competing broadband noise mechanisms in low speed axial fans, AIAA paper 2004-3039, 2004.
- [12] M. Herr, W. Dobrzynski, Experimental investigations in low noise trailing edge design, AIAA paper 2004-2804, 2004.
- [13] P.J. Moriarty, G. Guidati, P. Migliore, Prediction of turbulent inflow and trailing-edge noise for wind turbines, AIAA paper 2005-2881, 2005.
- [14] F.W. Grosveld, Prediction of broadband noise from large horizontal axis wind turbine generators, AIAA paper 84-2357, 1984.
- [15] S.A.L. Glegg, S.M. Baxter, A.G. Glendinning, *Journal of Sound and Vibration* 118 (1987) 217-239.
- [16] H.H. Hubbard, K.P. Shepherd, Aeroacoustics of large wind turbines, *Journal of the Acoustical Society of America* 89 (1991) 2495-2508.
- [17] M.V. Lowson, Theory and experiment for wind turbine noise, AIAA paper 94-0119, 1994.
- [18] P. Fuglsang, H.A. Madsen, Implementation and verification of an aeroacoustic noise prediction model for wind turbines, Risø-R-867(EN), Risø National Laboratory, 1996.
- [19] M.V. Lowson, J.V. Lowson, A.J. Bullmore, Wind turbine noise: analysis of results from a new measurement technique, AIAA paper 98-0037, 1998.
- [20] P. Moriarty, P. Migliore, Semi-empirical aeroacoustic noise prediction code for wind turbines. NREL/TP-500-34478, National Renewable Energy Laboratory, Golden, CO, 2003.

- [21] A. de Bruijn, W.J. Stam, W.B. de Wolf, Determination of the acoustic source power levels of wind turbines, Proceedings of the European Wind Energy Conference, Hamburg, October 1984.
- [22] N.J.C.M van der Borg, P.W. Vink, Acoustic noise production of wind turbines in practice, Proceedings of the European Wind Energy Conference, Thessaloniki, October 1994.
- [23] F. Hagg, G.A.M van Kuik, R. Parchen, N.J.C.M. van der Borg, Noise reduction on a 1 MW size wind turbine with a serrated trailing edge, Proceedings of the European Wind Energy Conference, Dublin, October 1997.
- [24] J.G. Schepers, A.P.W.M. Curvers, S. Oerlemans, K. Braun, T. Lutz, A. Herrig, W. Würz, B. Méndez López, SIROCCO: SIlent ROTors by aCoustiC Optimisation, Proceedings of the First International Meeting on Wind Turbine Noise: Perspectives for Control, Berlin, October 2005.
- [25] T. Lutz, A. Herrig, W. Würz, K. Braun, E. Krämer, Constrained Aerodynamic & Aeroacoustic Design of Wind-Rotor Airfoils, Proceedings of the First International Meeting on Wind Turbine Noise: Perspectives for Control, Berlin, October 2005.
- [26] A. Herrig, W. Würz, T. Lutz, K. Braun, E. Krämer, S. Oerlemans, Trailing-edge noise measurements of wind turbine airfoils in open and closed test section wind tunnels, Proceedings of the First International Meeting on Wind Turbine Noise: Perspectives for Control, Berlin, October 2005.
- [27] S. Oerlemans, J.G. Schepers, G. Guidati, S. Wagner, Experimental Demonstration of Wind Turbine Noise Reduction through Optimized Airfoil Shape and Trailing-Edge Serrations. Proceedings of the European Wind Energy Conference 2001, Copenhagen, 2001.
- [28] IEC norm 61400-11, Wind turbine generator systems – Acoustic noise measurement techniques, 2002.
- [29] D.H. Johnson, D.E. Dudgeon, Array Signal Processing, Prentice Hall, 1993.
- [30] S. Oerlemans, P. Sijtsma, Acoustic Array Measurements of a 1:10.6 Scaled Airbus A340 Model, AIAA paper 2004-2924, 2004.
- [31] P. Sijtsma, S. Oerlemans, H. Holthusen, Location of rotating sources by phased array measurements, AIAA paper 2001-2167, 2001.
- [32] P. Sijtsma, R.W. Stoker, Determination of Absolute Contributions of Aircraft Noise Components using Fly-Over Array Measurements, AIAA paper 2004-2958, 2004.
- [33] T.F. Brooks, C.L. Burley, Rotor broadband noise prediction with comparison to model data, AIAA paper 2001-2210, 2001.
- [34] R.H. Schlinker, R.K. Amiet, Helicopter rotor trailing edge noise, NASA CR-3470, 1981.
- [35] A.P. Dowling and J.E. Ffowcs Williams, Sound and sources of sound, Ellis Horwood Limited, 1983.

## Chapter 6

### Prediction of wind turbine noise and validation against experiment

*S. Oerlemans and J.G. Schepers, Prediction of wind turbine noise and validation against experiment, accepted for International Journal of Aeroacoustics (reprinted with permission).*

#### **Abstract**

A semi-empirical prediction method for trailing edge noise is applied to calculate the noise from two modern large wind turbines. The prediction code only needs the blade geometry and the turbine operating conditions as input. Using detailed acoustic array and directivity measurements, a thorough validation of the predictions is carried out. The predicted noise source distribution in the rotor plane (as a function of frequency and observer position) shows the same characteristics as in the experiments: due to trailing edge noise directivity and convective amplification, practically all noise (emitted to the ground) is produced during the downward movement of the blades, causing an amplitude modulation of broadband aerodynamic blade noise at the blade passing frequency ('swish'). Good agreement is also found between the measured and predicted spectra, in terms of levels and spectral shape. For both turbines, the deviation between predicted and measured overall sound levels (as a function of rotor power) is less than 1-2 dB, which is smaller than the scatter in the experimental data. Using a smoothed analytical trailing edge noise directivity function, the turbine noise directivity is predicted within 1-2 dB, and the swish amplitude in different directions within 1 dB. This semi-empirical directivity function shows similar characteristics as the theoretical directivity function for a flat plate, except for regions close to the plane of the blade. The validated prediction code is then applied to calculate noise footprints of the wind turbine as a function of rotor azimuth. These footprints show that for cross-wind directions the *average* level is lower than in the up- and downwind directions, but the *variation* in level is larger. Even at large distance, swish amplitudes up to 5 dB can be expected for cross-wind directions.

## 6.1 Introduction

Wind is a clean and practically inexhaustible source of energy. However, the noise of wind turbines is a major hindrance for the widespread use of wind energy. A recent survey on the perception of wind farms in the Netherlands [1] showed that sound was the most annoying aspect of wind turbines. The swishing character (amplitude modulation) of the noise was mentioned as an important factor explaining the relatively high annoyance, as compared to other sound sources of equal level (air or road traffic). For the design of quiet wind turbines, and for the planning of wind farms, the availability of fast and accurate noise prediction methods is essential. In order to have a wide range of application, prediction codes should capture the physical source mechanisms as much as possible.

For a modern large wind turbine, aerodynamic noise from the blades is generally considered to be the dominant noise source, provided that mechanical noise is adequately treated [2]. The sources of aerodynamic noise can be divided into airfoil self-noise and inflow-turbulence noise. Airfoil self-noise is the noise produced by the blade in an undisturbed inflow, and is caused by the interaction between the boundary layer and the trailing edge of the blade. Self-noise can be tonal or broadband in character, and may be caused by several mechanisms, such as turbulent boundary layer trailing edge interaction noise (subsequently denoted as trailing edge noise), laminar boundary layer vortex shedding noise, trailing edge bluntness noise, or blade tip noise. Inflow-turbulence noise is caused by the interaction of upstream atmospheric turbulence with the leading edge of the blade, and depends on the atmospheric conditions. It is an open issue to what extent inflow-turbulence noise contributes to the overall sound level of a wind turbine [3].

Due to the large number of applications (for example wind turbines, airplanes, helicopters, fans), the characteristics of airfoil noise have been investigated extensively in both experimental and theoretical studies [4-22]. Inflow-turbulence and self-noise mechanisms were considered and the dependence on parameters such as flow speed, angle-of-attack, radiation direction, and airfoil shape was characterized. These investigations formed the basis of several semi-empirical wind turbine noise prediction methods, which were assessed by comparison with field measurements [23-32]. In most cases the prediction methods included trailing edge noise and inflow turbulence noise. However, since the field results only provided the total sound level of the turbine, and sometimes part of the turbine noise was attributed to other sources, such as tip noise or mechanical noise, only an indirect validation of the prediction codes was possible. Furthermore, in none of these studies the noise directivity or swish amplitude was predicted and compared with experimental results.

A number of studies have addressed the swish phenomenon experimentally [33-39]. Swish is here defined as the amplitude modulation of broadband aerodynamic blade noise at the blade passing frequency (typically around 1 Hz). Refs. [36-38] reported detailed source localization measurements on two modern large wind turbines, using a large microphone array positioned about one rotor diameter upwind of the turbine. The array results showed that practically all noise perceived on the ground was produced by the outer part of the blades (but not the very tip), during their downward movement. This strongly asymmetric source pattern, which caused the swishing noise during the passage of the blades, was explained by trailing edge noise directivity and convective amplification. Moreover, in [36] it was shown that the source pattern could *only* be explained by trailing edge noise directivity (and not by inflow-turbulence noise or low-frequency dipole noise). Several investigations [33-35,39] reported periods of increased amplitude modulation (also referred to as 'thumping'), which could be



observed at large distance. Although various possible causes for this increased amplitude modulation have been suggested, including blade noise directivity, blade-tower interaction, variation of wind speed over the rotor, and interaction between the noise from two or more turbines, the mechanism is still not clear.

The present study describes the application of a semi-empirical prediction method for trailing edge noise to calculate the noise from two modern large wind turbines. The prediction code only needs the blade geometry and the turbine operating conditions (wind speed, RPM, blade pitch angle) as input. Previous acoustic array measurements [36-38] showed that broadband trailing edge noise is the dominant noise source for both turbines, which allows a direct validation of the trailing edge noise prediction method. Furthermore, the availability of the array results provides a unique opportunity to assess the prediction code not only in terms of source spectra and overall sound levels as a function of rotor power, but also in terms of the noise source distribution in the rotor plane. Moreover, the predicted directivity and swish amplitude is validated against acoustic measurements on a circle around the turbine, after which the noise and swish 'footprints' of the turbine are calculated.

In order to predict the turbine noise directivity and swish amplitude, the trailing edge noise directivity function must be known. This function was derived before both analytically [4-7,18] and numerically [22]. However, up to now experimental validation of the directivity function was limited to the plane normal to the trailing edge, for directions not too close to the plane of the blade [7,14]. In the present study it is shown that the acoustic measurements on a circle around the turbine in fact constitute a measurement of the *complete* trailing edge noise directivity function, including directions outside the plane normal to the trailing edge and close to the plane of the blade. This feature is used to assess the theoretical predictions of the directivity function against the experimental results.

The organization of this paper is as follows. Section 6.2 describes the experimental method employed during the field measurements, followed by a description of the prediction method in Section 6.3. In Section 6.4 the predictions are validated against the experimental results, and in Section 6.5 the prediction method is applied to calculate noise and swish footprints around the wind turbine. The conclusions of this study are summarized in Section 6.6.

## **6.2 Experimental method**

This section describes the experimental method employed during the field measurements on both turbines. The experimental results are discussed along with the predictions in Section 6.4. More detailed information about the experimental method can be found in Refs. [36-38].

### *6.2.1 Test set-up and data acquisition*

Acoustic field tests were performed for two different wind turbines. Turbine 1 was a GE 2.3 MW prototype test turbine with a rotor diameter of 94 m and a tower height of 100 m, and was located on a test site in the Wieringermeer polder (Netherlands). Turbine 2 was a GAMESA G58 850 kW turbine with a rotor diameter of 58 m and a tower height of 55 m, and was located on a wind farm in northern Spain. Both turbines were pitch-controlled and rotated in clockwise direction as seen from upwind (Figure 6-1).



Figure 6-1: Test set-up for Turbine 1 (left) and Turbine 2 (right).

The geometry of the three blades of each turbine was nominally identical. Whereas the blades of Turbine 1 were untreated, for Turbine 2 one blade was cleaned, one blade was tripped, and one blade remained untreated, to assess the effect of blade roughness due to e.g. dirt or insects.

A schematic picture of the test set-up is given in Figure 6-2. The source localization measurements were done using a 148-microphone acoustic array, mounted on a horizontal wooden platform of about  $16 \times 18 \text{ m}^2$ . The distance between the platform and the tower was roughly the same as the tower height, resulting in a 'view angle' of about  $45^\circ$ . The array microphones (Panasonic WM-61) were mounted flush to the platform and had no wind screens. The array had an elliptic shape to correct for the oblique view angle, and an increased microphone density in the center to reduce coherence loss and ensure low side-lobe levels at high frequencies. In addition to the acoustic array, for Turbine 1 eight ground microphones (LinearX M51) were placed on a 240-m diameter circle around the turbine (with  $45^\circ$  intervals), to measure the directivity of the turbine noise (Figure 6-2).

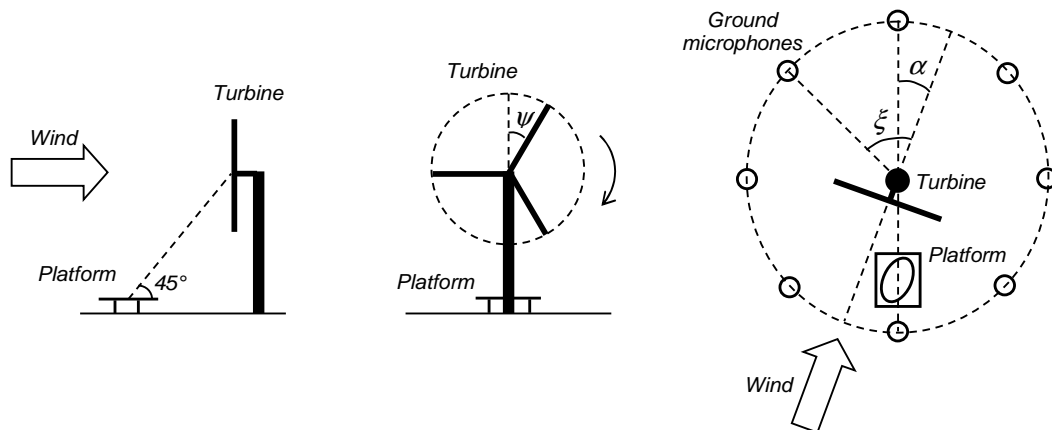


Figure 6-2: Schematic picture of test set-up: side view (left), front view (middle), and top view (right).

The ground microphones were equipped with hemisphere wind screens, and were placed horizontally on a 1-m diameter ground board, with their axes pointing to the turbine [40]. As a reference, an identical microphone, equipped with windscreen, was placed in the center of the array. In Figure 6-2,  $\psi$  indicates the azimuthal angle of the rotor,  $\alpha$  indicates the misalignment angle between turbine and array, and  $\xi$  indicates the position of a ground microphone with respect to the downwind direction.

The acoustic signals were measured using a sample frequency of 30.7 kHz (Turbine 1) or 51.2 kHz (Turbine 2) and a measurement time of 30 s. The data were processed using an FFT block size of 1024 (Turbine 1) or 2048 (Turbine 2) with a Hanning window and 50% overlap, yielding a narrowband frequency resolution of 30 Hz for Turbine 1 and 25 Hz for Turbine 2. A second-order 500 Hz high-pass filter was used to extend the dynamic range of the A/D converter. The sound levels were corrected for the filter response and for pressure doubling due to the platform or ground boards. Prior to the measurements, the sensitivity at 1 kHz was determined for all microphones using a calibrated pistonphone. The frequency response was taken from previous calibration measurements for the array microphones and from calibration sheets for the ground microphones. Phase matching of the array microphones was checked using a calibration source at known positions. A trigger signal from the turbine (one pulse per revolution) was recorded synchronously with the acoustic signals, so that the position of the rotor blades was known at all times. In parallel to the acoustic measurements, several turbine and meteo parameters were measured at a sample rate of 3 Hz or higher, including the wind speed, wind direction, turbine orientation, turbine power, RPM, and blade pitch angle. It should be noted that the measured nacelle wind speed for Turbine 2 suffers from an uncertainty. Therefore, in Section 6.4 the overall sound levels are analyzed as a function of rotor power rather than wind speed.

The test period was 1-15 November 2005 for Turbine 1, and 8-15 December 2003 for Turbine 2. Following the IEC norm for wind turbine noise measurements [40], it was attempted to obtain array measurements for wind speeds (at 10 m height) between 6 and 10 m/s. The wind speed at 10 m height was calculated from the average nacelle wind speed using the standard wind profile from the IEC norm, where the measured nacelle wind speed was assumed to be the free stream wind speed at hub height. On the basis of the turbine operational data, the most stable measurements (i.e. small misalignment angle and small variation in wind speed, RPM, and pitch angle) were selected for further analysis. An overview of the test conditions for the selected measurements is given in Table 6-1. The ground microphone measurements for Turbine 1 are mentioned separately, because these were all done on the same day.

### 6.2.2 Phased array processing

The microphone array data are processed using two different methods. The first method employs conventional beamforming [41] to localize the noise sources in the rotor plane. The resulting source maps show the integrated effect of the three blades, averaged over many revolutions (averaging of spectra was done on energy basis). The calculations are performed in narrow bands and then summed to 1/3-octave bands. The scan grid is placed in the rotor plane, accounting for the misalignment angle  $\alpha$  (see Figure 6-2) and the rotor tilt angle (i.e. the angle between the rotor axis and the horizontal plane).

Table 6–1: Overview of average test conditions (standard deviation between brackets). The first five columns indicate the number of measurements in the wind speed bins between 6 m/s and 10 m/s (wind speed at 10 m height). \*The measured nacelle wind speed for Turbine 2 suffers from an uncertainty.

	# meas. per $U_{10}$ bin					$U_{nac}$ (m/s)	RPM	pitch (°)	$P$ (MW)	$\alpha$ (°)
	6	7	8	9	10					
Turbine 1 (array)	14	14	13	5	0	10.3 (1.2)	14.7 (0.3)	0.2 (0.5)	1.6 (0.4)	-2 (3)
Turbine 1 (ground mics)	10	21	15	0	0	10.0 (1.0)	14.6 (0.4)	0.0 (0.0)	1.5 (0.3)	-11 (6)
Turbine 2 (array)	6	6	12	5	6	10.5* (1.7)	24.9 (1.9)	-0.1 (0.8)	0.47 (0.19)	-5 (7)

To improve the resolution and to suppress background noise (for example wind-induced pressure fluctuations on the microphones), the main diagonal of the cross-power matrix (i.e. the auto-powers) is discarded. A frequency-dependent spatial window is applied to the microphone signals, in order to improve the resolution at low frequencies and to suppress coherence loss effects at high frequencies (due to propagation of the sound through the atmospheric boundary layer). The effect of sound convection in the atmospheric boundary layer is taken into account by calculating the average wind speed between rotor and array from the standard wind profile in the IEC norm for wind turbine noise measurements [40]. The noise sources in the rotor plane are quantified using a source power integration method [42]. This technique sums the source powers in (part of) the measured source map, and corrects the results with a scaling factor obtained by performing a simulation for a monopole source at the centre of the integration region. The thus obtained integrated sound pressure level of the turbine is similar to the 'apparent sound power level' defined in [40]. By defining one integration contour around the whole rotor plane and one only around the nacelle, noise levels from the nacelle and the blades are determined.

The second processing method employs three rotating scan planes to produce acoustic source maps for the three individual blades, averaged over a specified azimuth range and over one or more revolutions [43]. The scan planes are placed around the blades, in the rotor plane, and their azimuthal position is determined using the trigger signal from the turbine. For each scan location and each microphone signal, the dedopplerized source signal is reconstructed by applying a time shift to each sample of the microphone signal. This time shift accounts for the travel time between the (rotating) scan location and the microphone. By summing the reconstructed source signals for all microphones, the acoustic signal emitted from a given scan location is obtained (if no source is present at the scan location the source signals from the different microphones will cancel). The de-dopplerized noise from the blades is quantified using a power integration method for moving sound sources [44], which is similar to the above-mentioned integration method for the rotor plane. An integration contour is defined which includes the noise from the blade but excludes the noise from the nacelle. The thus obtained integrated sound levels represent the contribution of the different blades to the overall sound pressure level of the turbine, as measured at the array position.

The accuracy of the source localization and quantification with the present array set-up was discussed in [38]. With regard to the spatial resolution, the location of a whistle on the

blade (at a position unknown to the acoustic test team) was determined within 0.5 m, which is considered to be accurate enough for these tests. Concerning the *relative* sound levels (i.e. differences between the blades), an accuracy of 0.1 dB was found by comparing the average overall blade noise levels for two consecutive revolutions. The accuracy in terms of *absolute* sound levels, which is most relevant for the present study, can be assessed by comparing the integrated rotor source maps to the measured sound level at the reference microphone (with wind screen) in the center of the array. If all the noise measured by the reference microphone is due to the turbine rotor (background noise measurements with stopped rotor indicated a signal-to-noise ratio of 10 dB for the reference microphone), these spectra should coincide. However, for the present measurements on Turbine 1, the average integrated level is found to be 2 dB lower than the level at the reference microphone (this difference is fairly constant as a function of wind speed). This underestimation may be caused by certain simplifications in the integration method and/or by coherence loss at the array microphones, due to the propagation of the sound through the turbulent atmospheric boundary layer. Similar effects have been observed in open jet wind tunnel tests [42] and flight measurements [44]. In Section 6.4.2 it is shown, by means of the simulated rotor noise source distribution, that the underestimation of the rotor noise level due to the integration method is about 1.4 dB, which suggests that the remaining 0.6 dB is due to coherence loss. Thus, for the assessment of the predicted overall sound levels (Section 6.4.3), 2 dB is added to the measured rotor noise levels, to account for integration and coherence loss effects.

### 6.3 Prediction method

Since the field measurements show that broadband trailing edge noise is the dominant noise source for both turbines [36-38], only this noise source is incorporated in the prediction method, which means that inflow-turbulence noise, blunt trailing edge noise, and tip noise are discarded. The calculation can be divided into three steps: blade aerodynamics (Section 6.3.1), trailing edge noise source strength (Section 6.3.2), and directivity and convective amplification (Section 6.3.3). The resulting rotor noise source distribution can then be used to calculate simulated acoustic source maps or noise footprints around the turbine (Section 6.3.4).

#### 6.3.1 Blade aerodynamics

For the aerodynamic calculations the blade is first divided into a number of radial segments (21 for both turbines in the present study). Next, for each segment the local Reynolds number and angle of attack are obtained from an aerodynamic wind turbine model, based on the blade element momentum theory [45]. Then, the RFOIL airfoil design and analysis code [46] is used to calculate the trailing edge boundary layer displacement thicknesses on the pressure and the suction side. RFOIL is an extension of XFOIL [47] and takes into account rotational effects.

As input to the aerodynamic calculations only the blade geometry and the turbine operating conditions are needed. The blade geometry (including the airfoils) for both turbines was provided by the manufacturers, and the RPM and blade pitch angle were taken according to the turbine control system, as measured during the field tests. The aerodynamic profile coefficients ( $c_l$ ,  $c_d$ , and  $c_m$  as a function of angle of attack) for Turbine 1 were supplied by

the manufacturer. For Turbine 2 they were obtained from the Aerodynamic Table Generator [48], which contains a large database of airfoil characteristics measured under 2-D conditions in the wind tunnel.

The effects of atmospheric turbulence, wind shear, and yaw are neglected in the calculations, i.e. stationary and axisymmetric conditions are assumed. Furthermore, it is assumed that the airfoils are clean (i.e. free transition), because the clean rotor is considered to be most representative for normal operation [38]. Thus, for Turbine 1 (which has untreated blades) the calculations can be directly compared to the experimental results. For Turbine 2 (which has one clean, one tripped, and one untreated blade), the measured data must be corrected to obtain the noise from a 'clean' rotor (see Sections 6.4.2 and 6.4.3). The trip option in XFOIL is not used because this may not be representative for the trips applied in the field tests.

In the present study calculations are done at wind speeds between about 5 m/s and 12 m/s, in steps of 0.5 m/s. The calculated displacement thickness as a function of radius is shown for both turbines in Figure 6-3. These results represent conditions close to the average experimental conditions, i.e. wind speeds of 9.75 and 8.75 m/s, RPM values of 14.75 and 25.8, and pitch angles of  $0.04^\circ$  and  $0.1^\circ$  for Turbine 1 and Turbine 2, respectively.

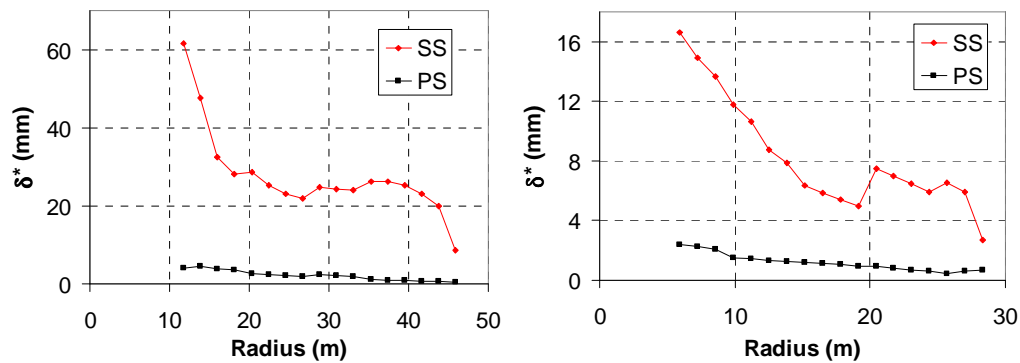


Figure 6-3: Calculated trailing edge boundary layer displacement thickness on pressure and suction side, for Turbine 1 (left) and Turbine 2 (right).

The quality of the aerodynamic modelling was verified by comparing the calculated and measured power curve for Turbine 1, and generally good agreement was found. It should be noted that this agreement does not guarantee that the calculated boundary layer thickness is correct. However, for the present field tests more detailed experimental information about the blade aerodynamics is not available. For Turbine 2 a comparison between the measured and calculated power curve is not possible, due to an uncertainty in the wind speed measurements. Thus, in order to avoid disturbing effects from uncertainties in the measured wind speed, in Section 6.4 the overall sound levels are plotted as a function of rotor power rather than wind speed.

### 6.3.2 Trailing edge noise source strength

Using the boundary layer displacement thickness and local Reynolds number from the previous section as input, the source spectrum for each radial blade segment is calculated using the 2-D semi-empirical trailing edge noise prediction code developed by Brooks, Pope,

and Marcolini [9]. In this code, the total trailing edge source strength due to the turbulent boundary layer is the sum of three contributions of the following form:

$$SPL_i = 10 \log \left( \frac{\delta_i^* M^5 L}{r^2} \right) + A_i \left( \frac{St_i}{Sr_i} \right) + K_i \quad (6.1)$$

where  $\delta^*$  is the displacement thickness,  $M$  the Mach number,  $L$  the span of the blade segment,  $r$  the distance to the observer, and  $K$  an empirical constant which depends on the Mach and Reynolds numbers. The function  $A$  describes the spectral shape as a function of the ratio between the Strouhal number  $St = f \delta^* / U$  (with  $U$  the local flow speed) and the empirical peak Strouhal number  $Sr$ . The three contributions (here denoted by the index  $i$ ) are the pressure side boundary layer, the suction side boundary layer, and an additional contribution to account for nonzero angle of attack. Eq. (6.1) is based on theoretical analyses of a turbulent, low Mach number flow over a half-plane [4], and basically states that trailing edge noise scales with the boundary layer thickness (which is a measure for the turbulence correlation scale) and the fifth power of the flow speed. The dependence on  $U^5$  was confirmed in many experimental studies, and was also found for the trailing edge noise from the present turbines [36]. Note that Eq. (6.1) only calculates the source strength for an observer at a fixed position with respect to the blade segment; directivity and convective effects are discussed in the next section.

For the trailing edge noise calculations in the present study, the original Fortran code from [9] is used with only two modifications. The first modification is that we use (for each blade segment) the trailing edge boundary layer thickness as calculated in the previous section, instead of the boundary layer thickness calculated by the program (which is an estimate for a NACA0012 airfoil). The second modification is as follows. In the original code, Eq. (6.1) takes a different form for angles of attack larger than the 'stall angle' of  $12.5^\circ$ . In the present calculations the stall angle is adjusted to the actual stall angle for the different airfoils, which is known from 2-D wind tunnel measurements. However, since these stall angles are never reached for radii larger than 30% of the tip radius, effectively only Eq. (6.1) is used for the present predictions, with all empirical constants according to [9].

### 6.3.3 Directivity and convective amplification

The calculation in the previous section yields the trailing edge source spectrum in 1/3-octave bands, for each radial blade segment. In order to obtain the *effective* source strength for a given blade azimuth angle, as perceived by an observer at a specified position, the effects of trailing edge noise directivity and convective amplification should be taken into account.

Amiet [5] derived an analytical expression for the directivity of trailing edge noise from a flat plate of arbitrary chord (see Figure 6-4 for definition of angles). Figure 6-5 shows the characteristics of this theoretical directivity function for a number of nondimensional frequencies, in the plane normal to the trailing edge (in terms of the acoustic pressure  $p$ ), and on a sphere around the trailing edge source (in dB). In these figures the flow is in the  $x$ -direction and the trailing edge runs along the  $y$ -axis.

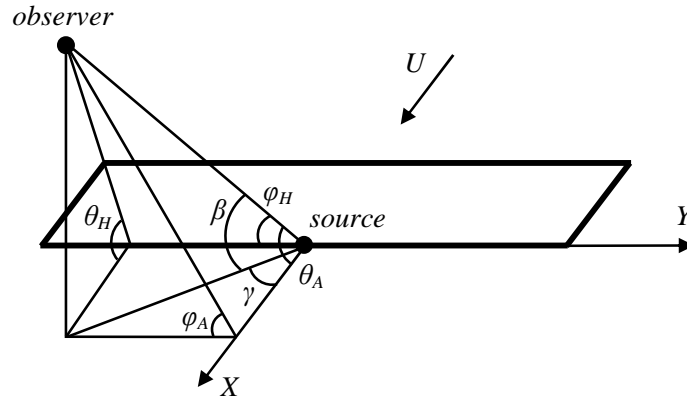


Figure 6-4: Definition of angles between observer and trailing edge source.

For low frequencies (i.e. small  $C/\lambda$ , with  $C$  the blade chord and  $\lambda$  the acoustic wavelength), the directivity shows the classical dipole pattern with  $p^2 \sim \sin^2 \theta_A \sin^2 \varphi_A$ , while for high frequencies (large  $C/\lambda$ ) the cardioid pattern  $p^2 \sim \sin^2(\theta_A/2)$  is found in the plane normal to the trailing edge. The directivity function for high frequencies is equivalent to that obtained by Ffowcs Williams and Hall [4] and Howe [6], who used an alternative theoretical approach and found  $p^2 \sim \sin^2(\theta_H/2) \sin \varphi_H$ . For intermediate frequencies more complicated patterns with multiple directivity lobes are obtained [see also 12,13]. The effect of a leading edge back-scattering correction to Amiet's formulation was investigated by Roger and Moreau [18], but they found this correction to be negligible for large wind turbine blades.

For the present turbines,  $C/\lambda$  is roughly between 0.4 and 4 for the relevant blade radii and frequencies. In order to assess the influence of the trailing edge noise directivity function on the wind turbine noise directivity and swish amplitude, it is useful to know the position of an observer on the 'directivity sphere'. For this purpose, the 'trajectories' of the eight experimental ground microphones on the directivity sphere, during one revolution of the blade, are projected on the high-frequency directivity function in Figure 6-6 (a source radius of 0.9 times the tip radius is used). It can be seen that each ground microphone follows a circle at more or less constant 'latitude'  $\beta$ , where  $\beta$  depends on the microphone angle  $\xi$  (the 'longitude'  $\gamma$  depends on the blade azimuth angle  $\psi$ ). The four lower circles represent the upwind locations, while the four upper circles correspond to the downwind locations. The asymmetry between the upper and lower trajectories is due to the rotor tilt angle, the blade pitch and twist, and the average experimental misalignment angle  $\alpha$  of  $-11^\circ$ . For a symmetrical turbine (i.e. no pitch, twist, and tilt), the latitude of an observer at large distance would be given by  $\beta = |\xi - \pi| - \pi/2$ . Figure 6-6 illustrates that the directivity measured by the far field microphones is determined by the *average* level over each trajectory, while the swish amplitude depends on the *variation* of the level along each circle (note that there are three blades on each circle, the contributions of which should be summed). Thus, the ground microphone measurements on a circle around the turbine in fact constitute a measurement of the complete trailing edge noise directivity function, and, vice versa, in order to predict the noise footprint of a wind turbine, the complete directivity function should be known.



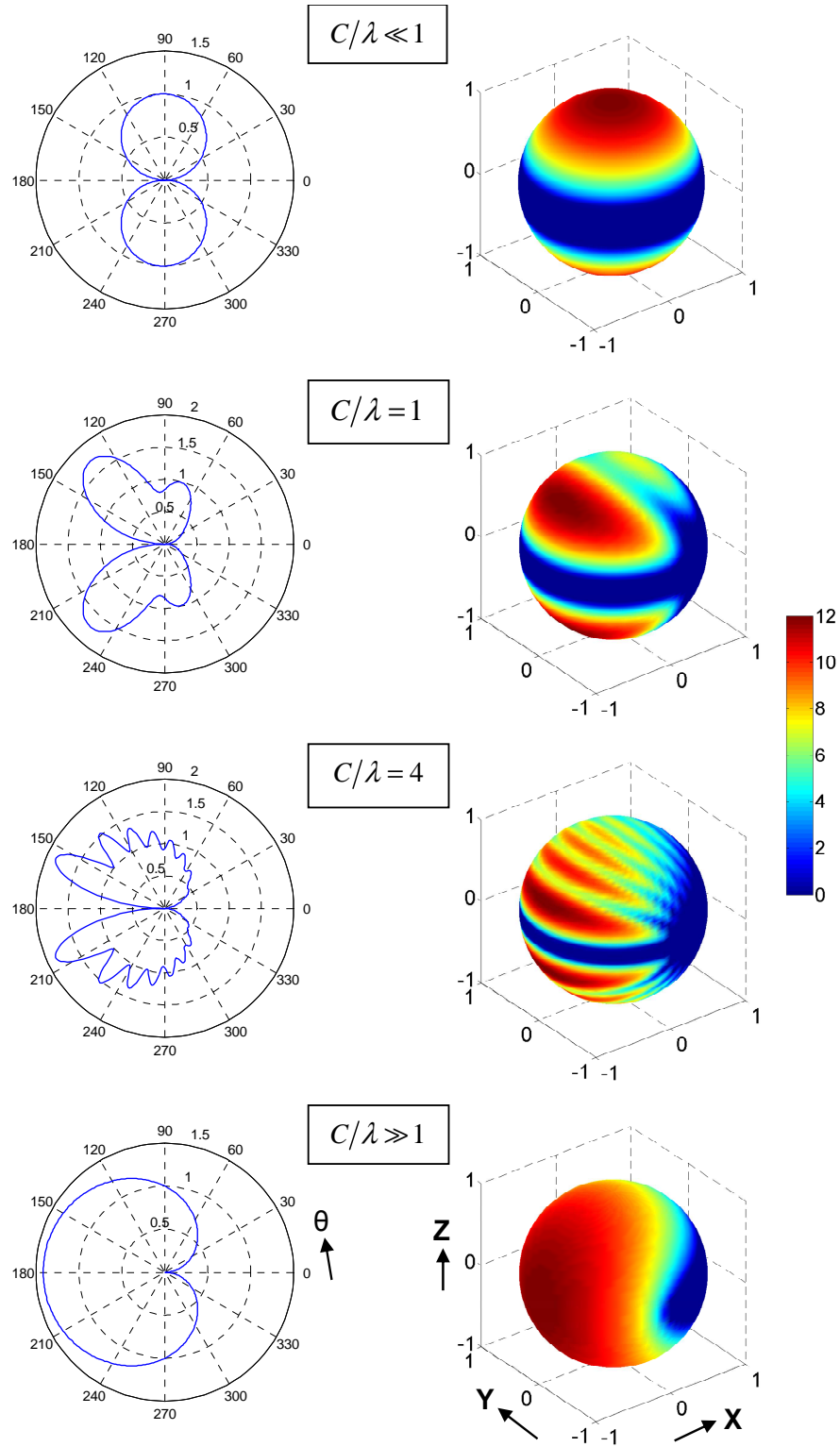


Figure 6-5: Theoretical trailing edge noise directivity function for flat plate [5].

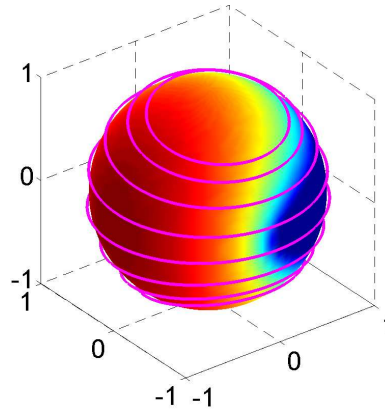


Figure 6-6: Theoretical high-frequency trailing edge noise directivity function with 'trajectories' of ground microphones:  $\xi = -11^\circ, 34^\circ, 304^\circ, 79^\circ, 259^\circ, 124^\circ, 214^\circ, 169^\circ$  (top to bottom).

The dependence of the wind turbine noise directivity and swish amplitude on the trailing edge noise directivity function can be exploited to assess the theoretical directivity function against the experimental results. First, the exact, frequency-dependent theoretical flat plate directivity function (Figure 6-5) is considered. The resulting turbine noise and swish directivity are shown in Figure 6-7 ('exact'), and show reduced levels and high swish amplitudes for positions close to the rotor plane.

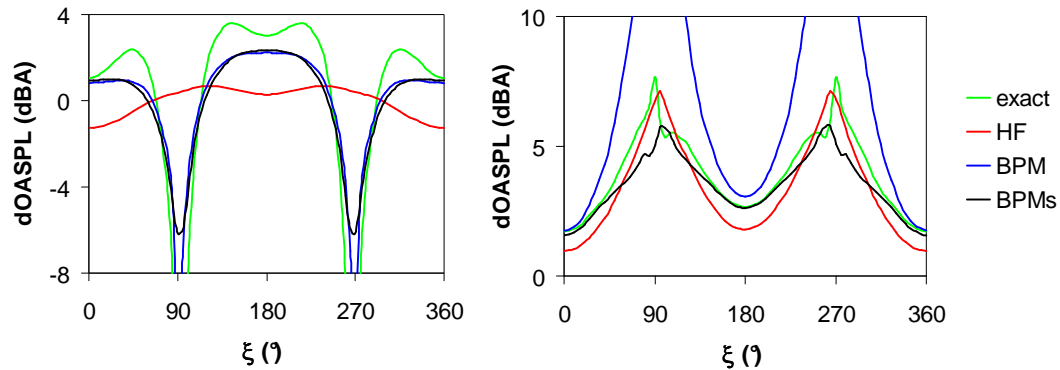


Figure 6-7: Predicted turbine noise directivity (left) and swish amplitude (right) for four different trailing edge noise directivity functions.

These trends agree well with the experimental results (to be discussed in Section 6.4.4), but due to the steep fall-off of the directivity function for small  $\beta$  (Figure 6-5), relatively large quantitative deviations are found close to the rotor plane. Next, the high-frequency directivity function  $p^2 \sim \sin^2(\theta_H/2)\sin\phi_H$  (Figure 6-6) is considered. However, although these predictions (Figure 6-7, 'HF') also show increased swish amplitudes close to the rotor plane, the experimental 'dips' in the directivity (around  $\xi=90^\circ$  and  $\xi=270^\circ$ ) are not reproduced. Therefore, a frequency-independent directivity function is defined, which shows good agreement with the measurements for all directions, and allows easy implementation in prediction codes. The basis of this directivity function is a modified version [9] of the

theoretical high-frequency trailing edge noise directivity:  $p^2 \sim \sin^2(\theta_A/2)\sin^2\phi_A$ . This function (Figure 6-8A) has the cardioid pattern in the plane normal to the trailing edge, and shows the desired fall-off to zero in the plane of the blade, by assuming that the  $\phi$ -dependence is the same as for the classical low-frequency dipole [49]. In previous studies it was used for the prediction of noise from helicopters [50] and wind turbines [24,26,30-32], and in [36,37] it was successfully applied to explain the rotor noise source distribution as perceived at an upwind observer position. However, this function has a discontinuity for  $\theta_A = \pi$ , causing unrealistically high swish amplitudes close to the rotor plane (Figure 6-7, 'BPM'). Therefore, the function is smoothed around the discontinuity by averaging it over a certain range of  $\beta$  and  $\gamma$ . On the basis of the experimental results, the averaging range  $(d\beta, d\gamma)$  is chosen to be  $(\pi/12, 2\pi/3)$  for  $\beta = 0$ , and is reduced to  $(0, 0)$  for  $\beta = \pi/2$  (using the error function). Thus, for regions away from the plane of the blade, the smoothed function is identical to the original function used in [9]. The resulting turbine noise directivity and swish amplitude (Figure 6-7, 'BPMs') correspond well to the experimental results (Section 6.4.4). Thus, this smoothed semi-empirical directivity function (Figure 6-8B) appears to be a good approximation of the true directivity function for trailing edge noise from an airfoil. It shows similar characteristics as the theoretical directivity function in Figure 6-5 ( $C/\lambda = 1, 4$ ), except for the steep fall-off close to the plane of the blade for  $\beta = 0$ .

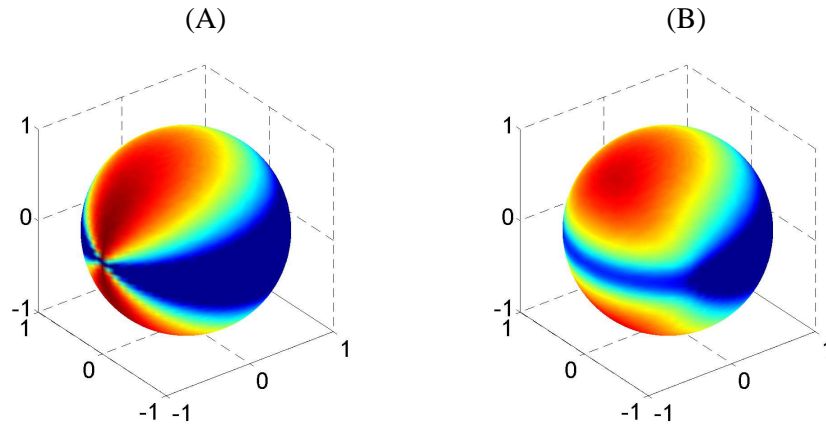


Figure 6-8: (A) Analytical trailing edge noise directivity function [9]. (B) Smoothed analytical directivity function used in present prediction code.

Thus, for the present predictions the following function is used to account for directivity and convective amplification:

$$D_s = \frac{[2\sin^2(\theta_A/2)\sin^2\phi_A]_s}{(1-M\cos\zeta)^4}, \tag{6.2}$$

where the subscript  $s$  indicates the smoothing over  $\beta$  and  $\gamma$ ,  $\zeta$  is the angle between the blade flow velocity and the source-observer line, and  $M$  is the (undisturbed) blade Mach number. The numerator in Eq. (6.2) describes the trailing edge noise directivity as discussed

above, and is the most important contributor to the asymmetrical rotor noise source pattern [36]. The denominator represents the convective amplification factor for trailing edge noise, and indicates that the source amplitude increases when the source is moving towards the observer. As mentioned by Brooks and Burley [50], different exponent power laws between 1.5 and 4.5 have been found in different theoretical approaches, while experimental validation has been very limited. Following [50], here the 4<sup>th</sup> power for compact dipole sources is used [51]. For the present low Mach numbers this convective factor is practically equivalent to that derived by Howe [6] for trailing edge noise. The Doppler *frequency* shift is accounted for by calculating for each source frequency the Doppler-shifted frequency at the observer position, and redistributing the acoustic energy over the appropriate frequency bands.

#### 6.3.4 Simulated source maps and noise footprints

From the effective radial source strength distribution (for a given blade azimuth and observer position), as determined in the previous section, acoustic source maps and turbine noise footprints are calculated as follows. For the source maps, first the average noise source distribution in the (tilted) rotor plane is predicted, for an observer position corresponding to the position of the microphone array in the experiments. This is done by dividing one complete revolution in 180 azimuthal blade positions (i.e. an azimuthal interval of 2°), and calculating for each blade position the effective radial source distribution. In order to obtain the *average* source level for each azimuthal position, the source powers are divided by the total number of azimuthal blade positions (180). Since the number of *radial* segments is 21, the resulting rotor source distribution is composed of 3780 incoherent sources, each with a Doppler-shifted 1/3-octave band spectrum which includes directivity and convective effects. Using this source distribution, the acoustic signals (complex amplitude as function of narrowband frequency) are calculated for all microphone positions in the array, from which a simulated cross-power matrix is constructed. This cross-power matrix is further processed using the same procedure that is used for the measured data (see Section 6.2.2), allowing direct comparison to the experimental results.

For the noise footprints, three blades are modeled at 120° from each other. The radial source distribution for each blade is calculated as described in the previous section. Thus, for a given rotor position, the total number of sources is 63. The revolution is divided in 72 azimuthal rotor positions (i.e. an interval of 5°), and for each rotor azimuth the contribution of each blade segment to the sound level at a certain observer position is calculated. For a given *emission* time (i.e. emission azimuth), the *arrival* time is generally different for the 63 blade elements. Thus, in order to calculate the perceived sound level at a fixed arrival- or *observer* time, the contribution of each blade segment is determined by interpolation between two emission azimuths. By plotting the total sound level at different observer positions for a fixed observer time, the instantaneous noise footprint is obtained. The observer time can also be expressed in terms of the rotor azimuth at observer time. By calculating noise footprints for a complete revolution (in steps of 5° azimuth), a 'time history' is obtained for each observer position. The swish amplitude for a given observer position is calculated as the difference between the minimum and maximum perceived sound level during one revolution. In the predictions a uniform wind speed is incorporated to account for convection of sound, but refraction due to wind shear is not included.

### 6.4 Comparison between prediction and experiment

In this section the predictions are compared to the experimental results. This assessment is made in terms of the noise source distribution in the rotor plane (Section 6.4.1), the rotor noise spectra (Section 6.4.2), the overall sound level as a function of rotor power (Section 6.4.3), and the directivity and swish (Section 6.4.4).

#### 6.4.1 Noise source distribution in rotor plane

The measured and predicted source maps for both turbines are shown in Figures 6-9 to 6-12. Details of the simulations are provided in Section 6.3.4. Note that these source maps correspond to the upwind measurement position on the ground. The range of the colour scale is always 12 dB, and the maximum is adjusted for each individual frequency band.

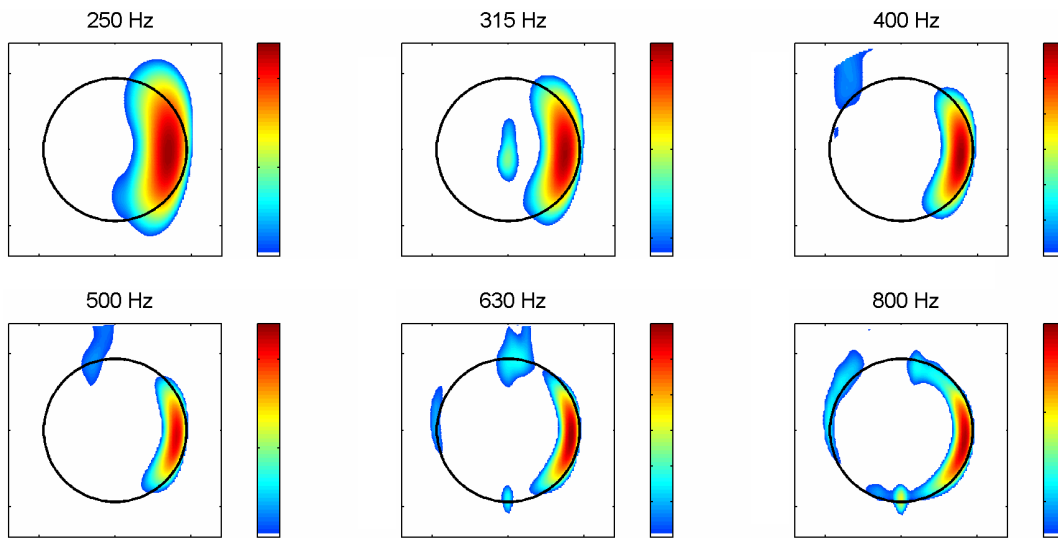


Figure 6-9: Measured source maps for Turbine 1.

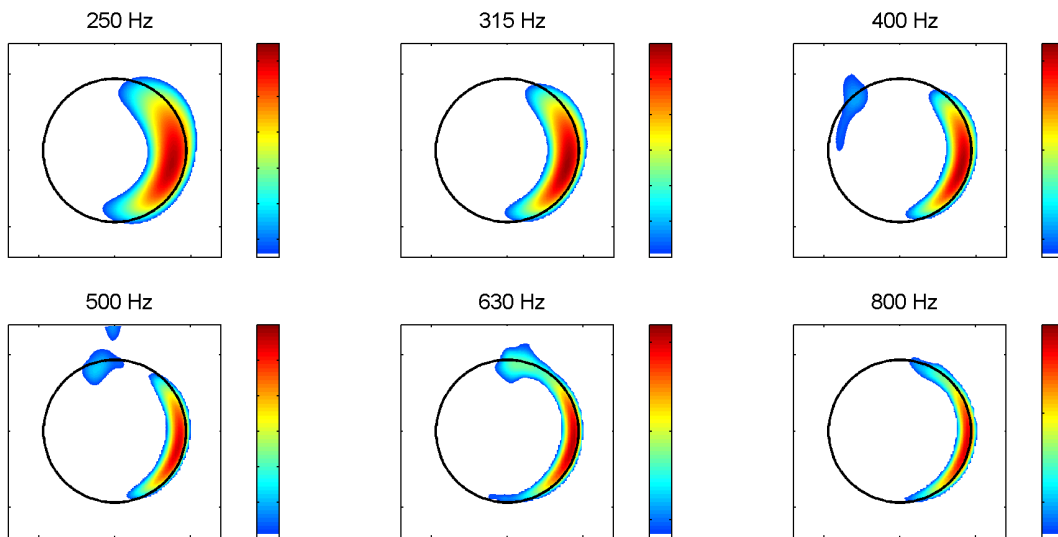


Figure 6-10: Predicted source maps for Turbine 1.

The turbines rotate in clockwise direction and the black circle indicates the trajectory of the blade tips. The experimental source maps are averaged over all measurements, the simulations are done for a misalignment angle of  $0^\circ$  and turbine conditions close to the average experimental conditions (see Section 6.3.1).

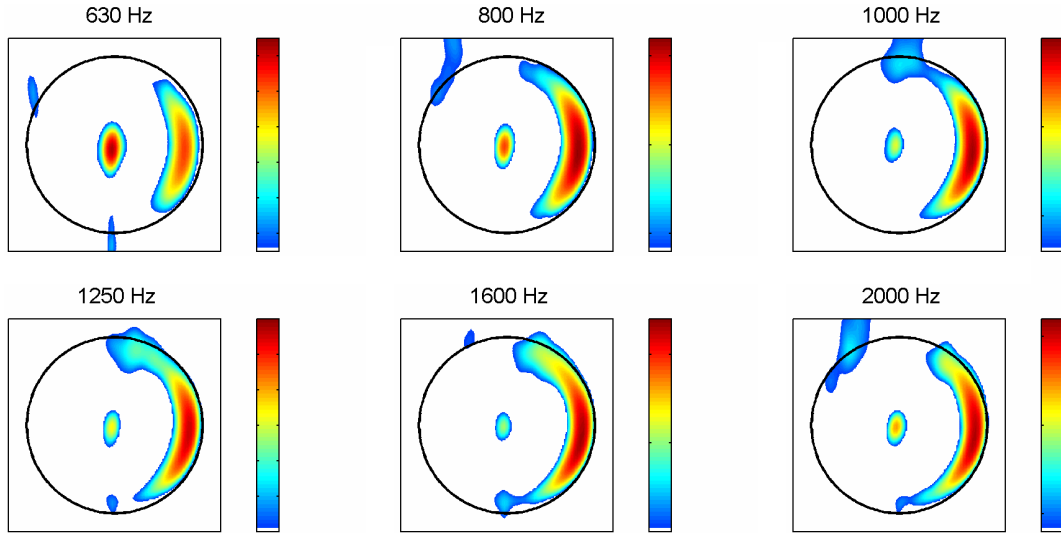


Figure 6-11: Measured source maps for Turbine 2.

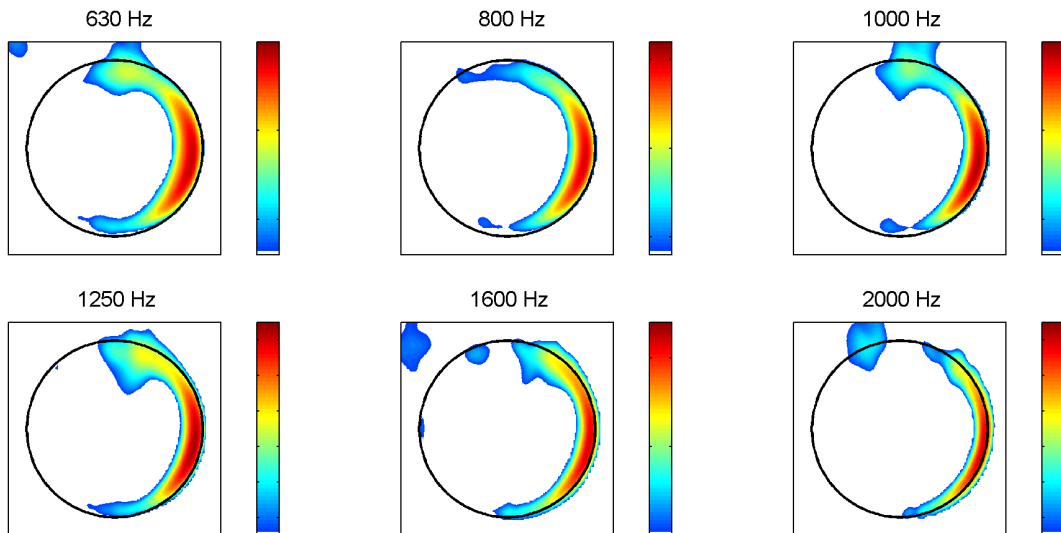


Figure 6-12: Predicted source maps for Turbine 2.

In general good qualitative agreement is observed between experiments and simulations. As in the experiments, the simulated source maps show dominant noise radiation from the outer part of the blades, during their downward movement. This asymmetric source pattern, which is due to trailing edge noise directivity and convective amplification, causes the swishing noise during the passage of the blades. Note that for an observer on the ground, due to the time delay between emission and perception of the sound, the swish may *seem* to be generated when the blades are close to the tower (depending on RPM and distance to the turbine).

Similar to the experiments, the predicted source maximum shifts to a higher radius for increasing frequency, which can be attributed to the higher flow speed and thinner trailing edge boundary layer. In some cases even the minor side-lobes (for example between 10 and 12 o'clock for 400-630 Hz in the Turbine 1 results), which are an artefact of the array method, are reproduced in the simulations. Obviously, the minor experimental noise sources at the nacelle and the tower are not reproduced in the simulation, because these are not simulated in the trailing edge noise prediction model. The nature of the 'tower source', which occurs at higher frequencies for both turbines, is hard to assess on the basis of the present data, but it could originate from (1) reflection of blade noise on the tower, (2) impingement of blade tip vortices on the tower, and/or (3) the upstream influence of the tower on the flow field around the blade. At high frequencies, Turbine 1 also shows a minor tip noise source during the upward movement of the blades, which is not modeled in the present prediction model.

Whereas the previous results concern misalignment angles around  $0^\circ$ , for Turbine 1 experimental data are also available for large misalignment angles. The measured and predicted source maps for these angles are shown in Figure 6-13.

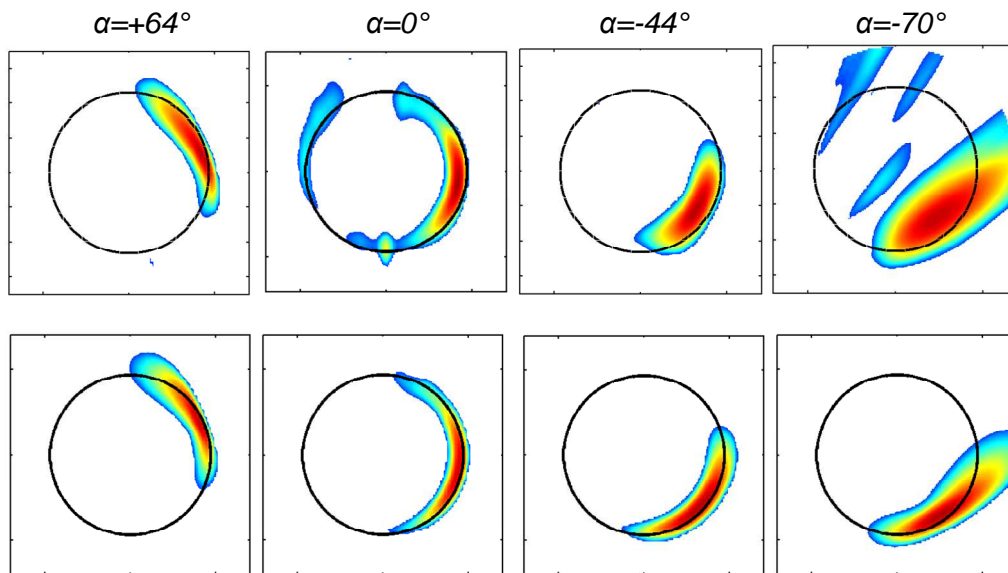


Figure 6-13: Measured (upper row) and predicted (lower row) source maps for Turbine 1 at different misalignment angles (800 Hz).

It can be seen that the location of the source region shifts upward or downward when the right- or left-hand side of the rotor plane is turned towards the array, respectively. This can be qualitatively explained by the change in the component of the blade velocity in the direction of the array, which results in a change in convective amplification (Section 6.3.3). At high misalignment angles the array resolution decreases due to the oblique view angle. Again a good qualitative agreement between simulation and experiment is found, indicating that the changes in source pattern are well captured by the trailing edge noise prediction method.

#### 6.4.2 Rotor noise spectra

As explained in Section 6.2.2, the source maps are quantified using a power integration method. Before comparing the predictions to the measured rotor noise spectra, first some intermediate results from the predictions are discussed. As an example, Figure 6-14 shows

three rotor noise spectra from the simulations for Turbine 1: the source strength spectrum (output of Section 6.3.2), the rotor spectrum after including directivity and convective effects (Section 6.3.3), and the integrated rotor spectrum from the array simulation (Section 6.3.4).

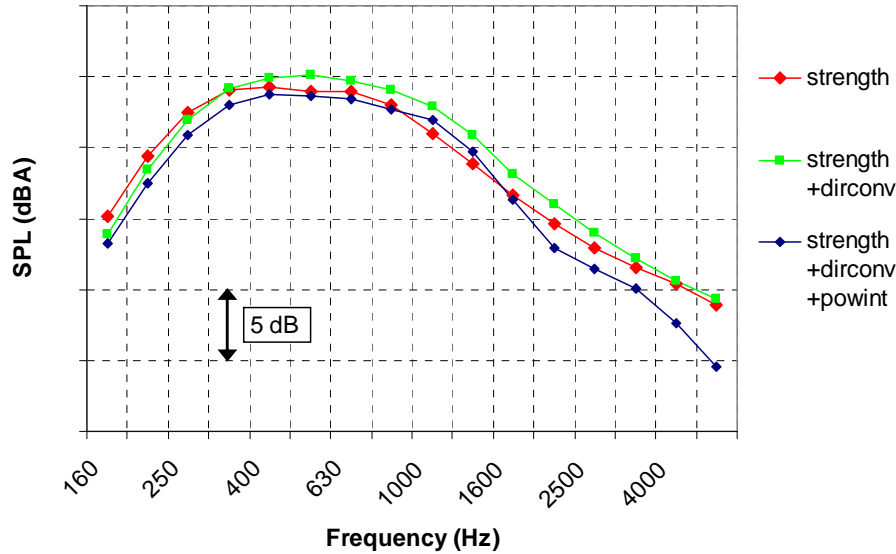


Figure 6-14: Intermediate rotor noise spectra from the prediction for Turbine 1.

By comparing the first two lines, it can be seen that directivity and convection result in a small shift of the spectrum to higher frequencies, because the blades are moving towards the observer on the ground when they produce most of their noise. Interestingly, the noise *level* is hardly affected: although directivity and convection yield a large asymmetry in the noise source distribution, the effect is rather small when averaged over all rotor azimuths (for the upwind array position). By comparing the second and third line, it can be seen that the power integration method results in an underestimation of the actual rotor noise level. The difference is small at low frequencies, but increases to almost 5 dB at the highest frequency. As mentioned in Section 6.2.2, this deviation is probably due to certain assumptions and simplifications in the power integration method [42]. As a result of the deviation, the power integration method underestimates the actual overall rotor source level by 1.4 dB for the present simulation. Note that this effect occurs both for the simulated and the measured integrated rotor noise spectra.

The measured and simulated integrated rotor noise spectra for both turbines are shown in Figures 6-15 and 6-16. These spectra correspond to the source maps presented in Figures 6-9 to 6-12. As mentioned before, the experimental results are averaged over all measurements, and the simulations are done for turbine conditions close to the average experimental conditions. For Turbine 2 the experimental spectrum is corrected on the basis of the individual blade noise spectra [36], to obtain the spectrum of a 'clean' rotor. For the measured source maps the hub region is excluded from the integration. For both turbines a good agreement between predicted and measured peak frequencies is observed, and the fair prediction of the spectral shape confirms that our model for trailing edge noise is adequate. A quantitative assessment of the predicted overall sound levels is given in the next section.



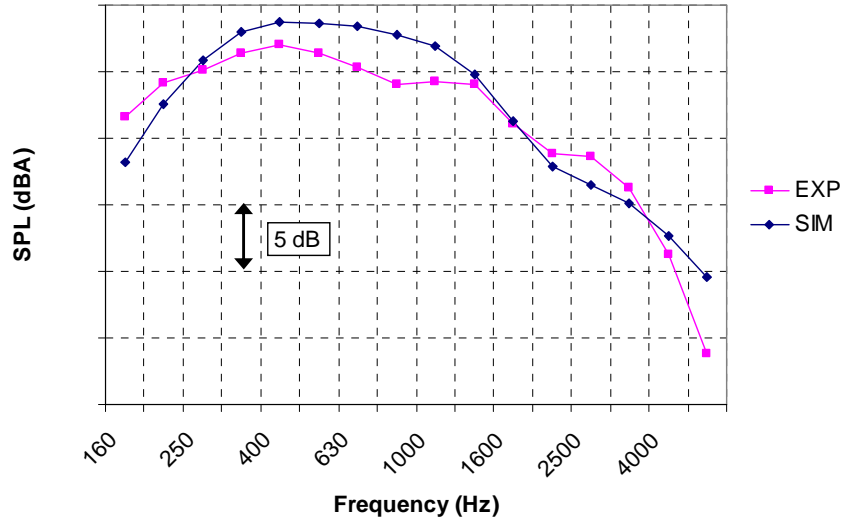


Figure 6-15: Measured and predicted rotor noise spectra for Turbine 1.

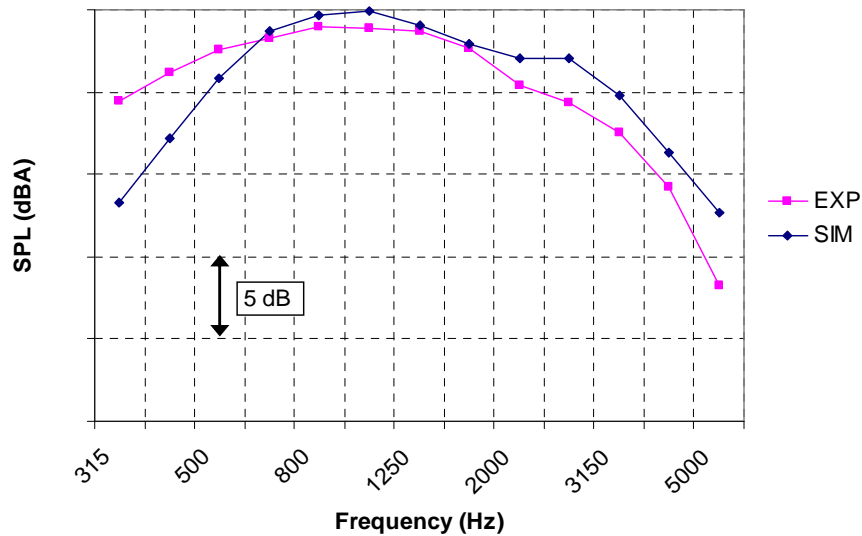


Figure 6-16: Measured and predicted rotor noise spectra for Turbine 2.

#### 6.4.3 Overall sound level as function of rotor power

The results of the previous section show that the average experimental spectra for both turbines correspond well to the predictions for the average experimental wind speed. Next, it is investigated if the predictions also accurately capture the dependence of the turbine noise on wind speed. Calculations are done for a range of wind speeds and the overall sound level was determined as the sum of the predicted rotor source distribution (i.e. without array processing, see Section 6.3.4). The experimental sound level is determined from the integrated rotor spectrum for all measurements, to which 2 dB is added for both turbines to account for the underestimation by the power integration method and coherence loss effects (Section 6.2.2). In addition, 1.5 dB is subtracted from the overall levels of Turbine 2, to

account for the fact that the rotor has a tripped and an untreated blade, while the simulations are for a clean rotor. This 1.5 dB correction is based on the differences in overall sound level between the three blades, which are practically independent of rotor power [36]. As mentioned in Section 6.3.1, we focus on the clean rotor since this is considered to be most representative for normal operation. In order to avoid disturbing effects from the uncertainty in the measured nacelle wind speed for Turbine 2, the sound levels are plotted as a function of the rotor power.

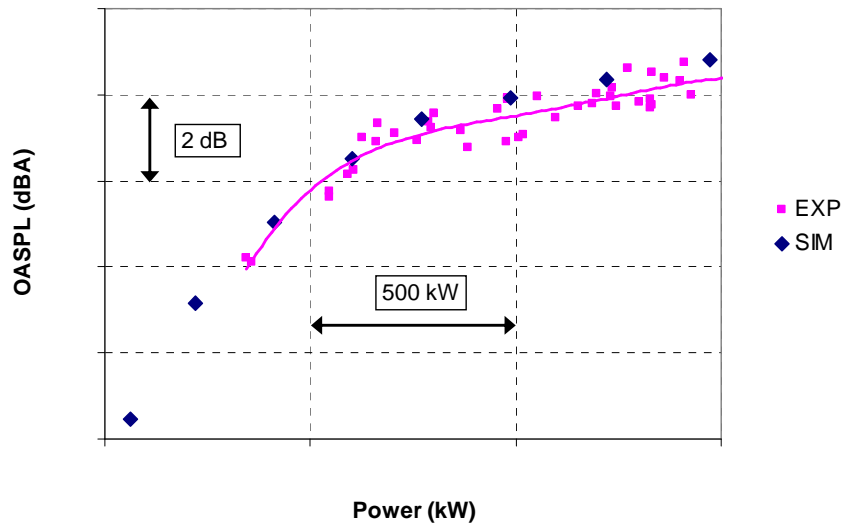


Figure 6-17: Measured and predicted overall rotor noise levels for Turbine 1.

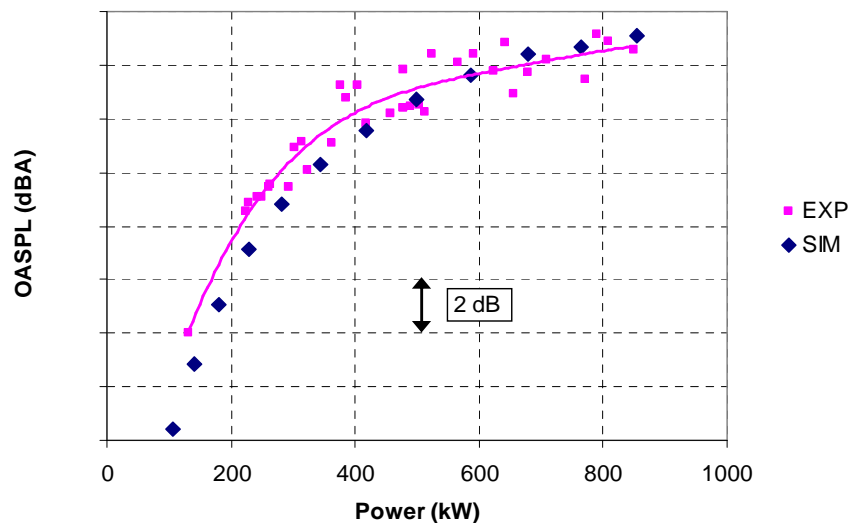


Figure 6-18: Measured and predicted overall rotor noise levels for Turbine 2.

Figures 6-17 and 6-18 show that for both turbines a good agreement is obtained between the predicted and measured overall levels. The dependence on rotor power is also well reproduced, although Turbine 2 shows a systematic deviation of 1-2 dB below 500 kW, for

which no explanation is available yet. Nevertheless, for both turbines the difference between measurement and prediction is less than 1-2 dB, which is smaller than the scatter in the experimental data. This accuracy is considered satisfactory for the present semi-empirical prediction model.

#### 6.4.4 Directivity and swish

For Turbine 1, far field measurements were performed with eight ground microphones on a 240-m diameter circle around the turbine (Figure 6-2 and Table 6-1). To determine the directivity of the turbine noise, the average level on each microphone is plotted as a function of microphone angle  $\xi$  for each 30 s measurement (Figure 6-19).

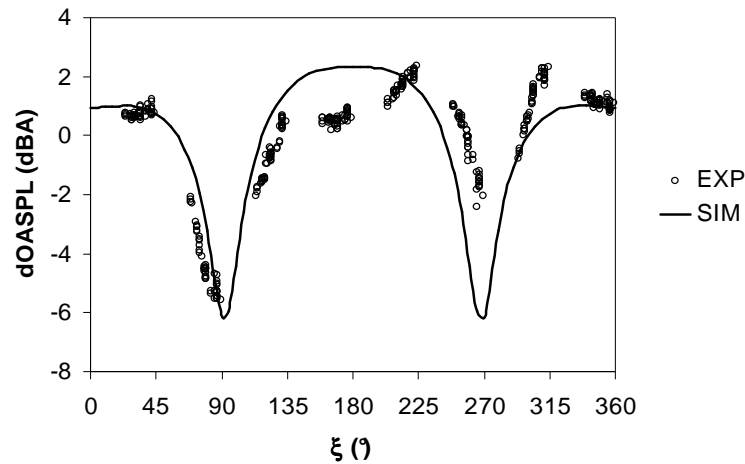


Figure 6-19: Measured and predicted directivity for Turbine 1.

In order to focus on the dominant trailing edge noise, and exclude possible low-frequency wind noise or high-frequency tip noise, the overall A-weighted levels are summed between 250 and 800 Hz. In order to account for variations in the absolute sound level (due to variations in weather and turbine operating conditions), the levels for each measurement are normalized using the average level on the eight microphones. The average misalignment angle  $\alpha$  for the ground microphone measurements is  $-11^\circ$ , and the variation in  $\alpha$  is  $20^\circ$ , which explains the eight 'traces' in Figure 6-19. The most distinct feature in the measured directivity pattern are the two 'dips' in the crosswind direction. A similar decrease in noise level close to the rotor plane was also found in [26,29]. Figure 6-19 also shows the *predicted* directivity on a 240-m diameter circle around the turbine, for a wind speed close to the average experimental wind speed. It can be seen that the predicted curve follows the measured curve within 1-2 dB, with two 6 dB dips in the cross-wind direction. These dips can be understood from the reduced levels of the trailing edge noise directivity function close to the plane of blade (Figure 6-8B). The predicted upwind sound levels are slightly higher than the downwind levels, which is mainly due to the convective factor in Eq. (6.1), because around  $\psi = 90^\circ$  the inverted blade flow velocity vector points slightly upwind.

Next, the *variation* in noise level due to the revolution of the blades (swish) is considered for the different directions. In order to exclude variations due to varying weather or turbine conditions, the overall level on each ground microphone is plotted as a function of the rotor

azimuth angle and averaged over all measurements (Figure 6-20, left). For each ground microphone three practically identical humps are found, corresponding to the passage of the blades. The predicted graphs are shown in the same figure.

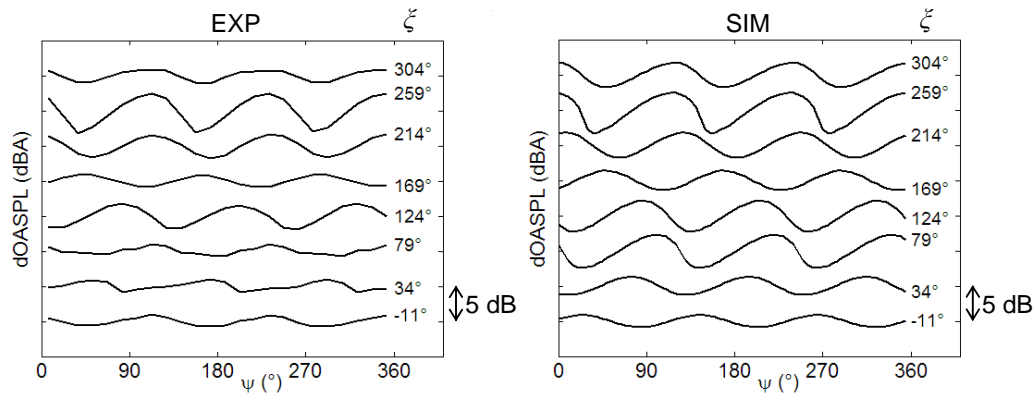


Figure 6-20: Measured and predicted sound level variation as a function of rotor azimuth  $\psi$ , for different far field positions  $\xi$ .

For the upwind measurement positions ( $90^\circ < \xi < 270^\circ$ ), both the amplitude and the phase of the humps match quite well with the measurements. However, for the downwind microphones the measured amplitude is lower than predicted. Since the signal-to-noise ratio (i.e. the minimum sound level in Figure 6-20 minus the background noise level with stopped rotor) is generally higher than 9 dB, this does not explain the reduced swish amplitude. However, comparison of the graphs for the individual 30-s measurements (not shown) indicates that slight variations in the phase of the humps reduce the amplitude of the averaged graphs. Due to propagation of the sound through the rotor wake, this effect can be expected to be stronger for the downwind microphones. Thus, in order to obtain a reliable experimental value of the swish, rather than taking the amplitude from the averaged graphs in Figure 6-20, the amplitude is determined for each individual 30-s measurement, and then averaged over all measurements. The resulting experimental swish amplitudes are shown together with the predicted values in Figure 6-21.

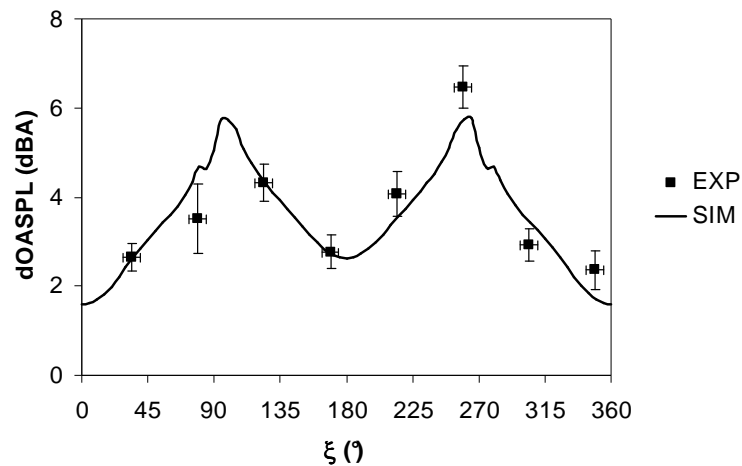


Figure 6-21: Measured and predicted swish amplitude as a function of far field position  $\xi$ .

The error bars indicate the standard deviation in swish amplitude and far field position. It can be seen that the swish amplitude is predicted within 1 dB for all directions. The relatively low swish amplitude for  $\xi = 79^\circ$  may be partly explained by shielding of the tower [33,39]. Note that the predicted swish amplitude is closely related to the variation in level along the microphone 'trajectories' (Figure 6-6) on the trailing edge noise directivity function in Figure 6-8B.

### 6.5 Application: prediction of noise and swish footprints

The previous section provides an extensive validation of the prediction model against the experimental results, in terms of the noise source distribution, rotor noise spectra, wind speed dependence, directivity and swish. The measurements are limited to the array position and a 240-m diameter circle around the turbine. However, since the measurements on the circle cover almost the complete trailing edge noise directivity function (Figure 6-6), the prediction method can also be applied to calculate the noise at larger distances. Figure 6-22 shows instantaneous turbine noise footprints (top view) for four different rotor azimuth angles, up to a distance of ten times the rotor diameter. Details of the calculation are provided in Section 6.3.4. The turbine is located at the center of the footprint, and the wind goes from left to right. The rotor azimuth at observer time is indicated in the upper right corner of each footprint. In order to limit the range of the dB scale, the levels are normalized using the horizontal distance  $r_h$  to the turbine:  $SPL_{norm} = SPL + 20 \log r_h$ . In this way the levels at a given distance can be directly compared. Note that atmospheric attenuation and sound refraction due to wind shear are not included in the predictions. Refraction may in practice reduce the upwind sound levels.

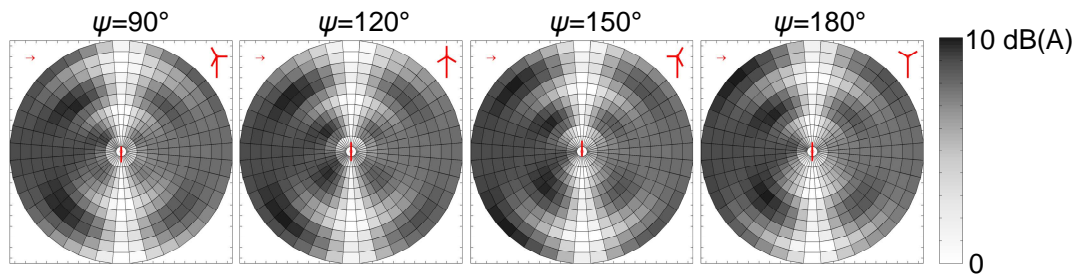


Figure 6-22: Predicted instantaneous noise footprints for increasing rotor azimuth angle, up to a distance of 10 times the rotor diameter. The wind goes from left to right.

The footprints show two 'waves' of increased sound level, one in each cross-wind direction, which start close to the turbine at  $\psi = 90^\circ$  and propagate outward with the speed of sound. The wave on the side of the down-going blade is generated when the blade is around  $\psi = 30^\circ$ , while the wave on the side of the upgoing blade is generated when the blade is around  $\psi = 180^\circ$ . After  $\psi = 180^\circ$  the cycle repeats and both waves can be seen to propagate further to the edge of the footprints. The distance between two successive waves is about 5 rotor diameters, which is consistent with the time period of 1.33 s between the passage of two blades (the RPM is 15) and a speed of sound of 340 m/s. Due to the passage of these sound waves from the blades, the noise levels in the crosswind directions vary significantly, while in the up- and downwind directions the levels are quite constant at large distances. This is

illustrated in Figure 6-23, which shows the average and swish (level variation) footprints for a complete revolution. It can be seen that both footprints do not change significantly beyond a distance of a few rotor diameters. For both cross-wind directions, the *average* level is lower than in the up- and downwind directions, but the *variation* in level is larger. Even at a large distance, trailing edge noise directivity and convective amplification may cause swish amplitudes up to more than 5 dB in the cross-wind directions. This may be an explanation for the increased amplitude modulation reported in [33-35,39], although it should be noted that at large distances (beyond several rotor diameters) variations in atmospheric conditions, which are not modeled here, may also cause fluctuations in the perceived noise level. Note that at small distance to the turbine (one rotor diameter) substantial swish is observed in *all* directions, which is consistent with the measurements.

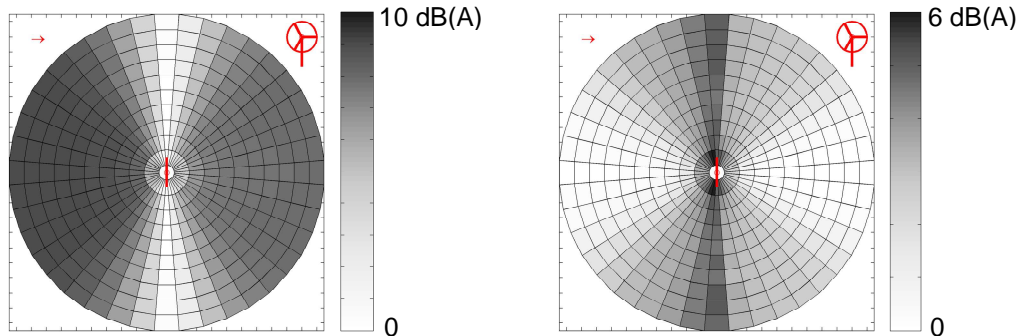


Figure 6-23: Predicted average footprint (left) and swish footprint (right) for a complete revolution.

## 6.6 Conclusions

A semi-empirical prediction method for trailing edge noise has been applied to calculate the noise from two modern large wind turbines. The prediction code only needs the blade geometry and the turbine operating conditions as input. Using detailed acoustic array and directivity measurements, a thorough validation of the predictions has been carried out. The predicted noise source distribution in the rotor plane (as a function of frequency and observer position) shows the same characteristics as in the experiments: due to trailing edge noise directivity and convective amplification, practically all noise (emitted to the ground) is produced during the downward movement of the blades, causing a swishing noise during the passage of the blades. Good agreement is also found between the measured and predicted spectra, in terms of levels and spectral shape. For both turbines, the deviation between predicted and measured overall sound levels (as a function of rotor power) is less than 1-2 dB, which is smaller than the scatter in the experimental data. Using a smoothed analytical trailing edge noise directivity function, the turbine noise directivity is predicted within 1-2 dB, and the swish amplitude in different directions within 1 dB. This semi-empirical directivity function shows similar characteristics as the theoretical directivity function for a flat plate, except for regions close to the plane of the blade. The validated prediction code is then applied to calculate noise footprints of the wind turbine as a function of rotor azimuth. These footprints show that for cross-wind directions the average level is lower than in the up- and downwind directions, but the variation in level is larger. Even at large distance, swish amplitudes up to 5 dB can be expected for cross-wind directions.

## Acknowledgments

The authors would like to thank the colleagues from GAMESA, GE, and the University of Stuttgart for their valuable contributions to the definition of the field tests and the interpretation of the results. The comments from A. Hirschberg (University of Twente) during the preparation of this paper are highly appreciated. The experiments were performed in the framework of the European SIROCCO project, funded partly by the European Commission and partly by the Netherlands Organisation for Energy and the Environment (NOVEM).

## References

- [1] F. van den Berg, E. Pedersen, J. Bouma, R. Bakker, WINDFARM perception: Visual and acoustic impact of wind turbine farms on residents - Final report, 2008.
- [2] S. Wagner, R. Bareiss, G. Guidati, *Wind Turbine Noise*. Springer Verlag, 1996.
- [3] G. Guidati, J. Ostertag, S. Wagner, Prediction and reduction of wind turbine noise: an overview of research activities in Europe, AIAA paper 2000-0042, 2000.
- [4] J.E. Ffowcs Williams, L.H. Hall, Aerodynamic sound generation by turbulent flow in the vicinity of a scattering half plane, *Journal of Fluid Mechanics* 40 (1970), 657-670.
- [5] R.K. Amiet, Noise due to turbulent flow past a trailing edge. *Journal of Sound and Vibration* 47 (1976) 387-393.
- [6] M.S. Howe, A review of the theory of trailing edge noise. *Journal of Sound and Vibration* 61 (1978) 437-465.
- [7] R.H. Schlinker, R.K. Amiet, *Helicopter rotor trailing edge noise*, NASA CR-3470, 1981.
- [8] W.K. Blake, *Mechanics of Flow-Induced Sound and Vibration*, Academic Press, 1986.
- [9] T.F. Brooks, D.S. Pope, M.A. Marcolini, *Airfoil Self-Noise and Prediction*. NASA Reference Publication 1218, 1989.
- [10] T. Dassen, R. Parchen, G. Guidati, S. Wagner, S. Kang, A.E. Khodak, Comparison of measured and predicted airfoil self-noise with application to wind turbine noise reduction, *Proceedings of the European Wind Energy Conference*, Dublin, October 1997.
- [11] G. Guidati, R. Bareiss, S. Wagner, T. Dassen, R. Parchen, Simulation and measurement of inflow-turbulence noise on airfoils, AIAA paper 97-1698, 1997.
- [12] M.S. Howe, Edge-source acoustic Green's function for an airfoil of arbitrary chord with application to trailing-edge noise, *The Quarterly Journal of Mechanics and Applied Mathematics* 54, 2001.
- [13] A.A. Oberai, F. Roknaldin, T.J.R. Hughes, Computation of Trailing-Edge Noise Due to Turbulent Flow over an Airfoil, AIAA Journal, Vol. 40, No. 11, 2002.
- [14] F.V. Huthcheson, T.F. Brooks, Effects of angle of attack and velocity on trailing edge noise, AIAA paper 2004-1031, 2004.
- [15] S. Oerlemans, P. Migliore, Aeroacoustic wind tunnel tests of wind turbine airfoils, AIAA paper 2004-3042, 2004.
- [16] S. Moreau, M. Roger, Competing broadband noise mechanisms in low speed axial fans, AIAA paper 2004-3039, 2004.
- [17] M. Herr, W. Dobrzynski, Experimental investigations in low noise trailing edge design, AIAA paper 2004-2804, 2004.
- [18] M. Roger, S. Moreau, Back-scattering correction and further extensions of Amiet's trailing-edge noise model. Part 1: theory, *Journal of Sound and Vibration* 286 (2005) 477-506.
- [19] P.J. Moriarty, G. Guidati, P. Migliore, Prediction of turbulent inflow and trailing-edge noise for wind turbines, AIAA paper 2005-2881, 2005.
- [20] T. Lutz, A. Herrig, W. Würz, M. Kamruzzaman, E. Krämer, Design and wind tunnel verification of low noise airfoils for wind turbines, *American Institute of Aeronautics and Astronautics Journal*, Vol 45, No. 4, 2007, pp 779-792.
- [21] S. Glegg, B. Morin, O. Atassi, R. Reba, Using RANS Calculations of Turbulent Kinetic Energy to Provide Predictions of Trailing Edge Noise, AIAA paper 2008-2993, 2008.
- [22] R.D. Sandberg, N.D. Sandham, Direct numerical simulation of turbulent flow past a trailing edge and the associated noise generation, *Journal of Fluid Mechanics* 596 (2008), 353-385.

- [23] A. de Bruijn, W.J. Stam, W.B. de Wolf, Determination of the acoustic source power levels of wind turbines, *Proceedings of the European Wind Energy Conference*, Hamburg, October 1984.
- [24] F.W. Grosveld, Prediction of broadband noise from large horizontal axis wind turbine generators, AIAA paper 84-2357, 1984.
- [25] S.A.L. Glegg, S.M. Baxter, A.G. Glendinning, The prediction of broadband noise from wind turbines, *Journal of Sound and Vibration* 118 (1987) 217-239.
- [26] H.H. Hubbard, K.P. Shepherd, Aeroacoustics of large wind turbines, *Journal of the Acoustical Society of America* 89 (1991) 2495-2508.
- [27] M.V. Lowson, Theory and experiment for wind turbine noise, AIAA paper 94-0119, 1994.
- [28] P. Fuglsang, H.A. Madsen, Implementation and verification of an aeroacoustic noise prediction model for wind turbines, Risø-R-867(EN), Risø National Laboratory, 1996.
- [29] M.V. Lowson, J.V. Lowson, A.J. Bullmore, Wind turbine noise: analysis of results from a new measurement technique, AIAA paper 98-0037, 1998.
- [30] P. Moriarty, P. Migliore, *Semi-empirical aeroacoustic noise prediction code for wind turbines*. NREL/TP-500-34478, National Renewable Energy Laboratory, Golden, CO, 2003.
- [31] W.J. Zhu, N. Heilskov, W.Z. Shen, J.N. Sørensen, Modeling of aerodynamically generated noise from wind turbines, *Journal of Solar Energy Engineering* (2005), Vol. 127, 517-528.
- [32] G. Leloudas, W.J. Zhu, J.N. Sørensen, W.Z. Shen, S. Hjort, Prediction and reduction of noise from a 2.3 MW wind turbine, *Proceedings of The Science of Making Torque from Wind*, Journal of Physics: Conference Series 75 (2007).
- [33] P. Dunbabin, An investigation of blade swish from wind turbines, *Proceedings of Internoise 96*, 463-469, 1996.
- [34] G.P. van den Berg, Effects of the wind profile at night on wind turbine sound, *Journal of Sound and Vibration* 277, 2004.
- [35] A. Moorhouse, M. Hayes, S. von Hünerbein, B. Piper, M. Adams, Research into aerodynamic modulation of wind turbine noise: final report, University of Salford, July 2007.
- [36] S. Oerlemans, P. Sijtsma, B. Méndez López, Location and quantification of noise sources on a wind turbine, *Journal of Sound and Vibration* 299, 2007.
- [37] S. Oerlemans, J.G. Schepers, Prediction of wind turbine noise and comparison to experiment, *Proceedings of the Second International Meeting on Wind Turbine Noise*, Lyon, France, September 2007.
- [38] S. Oerlemans, M. Fisher, T. Maeder, K. Kögler, Reduction of wind turbine noise using optimized airfoils and trailing-edge serrations, AIAA paper 2008-2819, 2008.
- [39] D. Bowdler, Amplitude modulation of wind turbine noise, *Acoustics Bulletin of the Institute of Acoustics (UK)*, Vol. 33, No. 4, July/August 2008.
- [40] IEC norm 61400-11, Wind turbine generator systems – Acoustic noise measurement techniques, 2002.
- [41] D.H. Johnson, D.E. Dudgeon, *Array Signal Processing*, Prentice Hall, 1993.
- [42] S. Oerlemans, L. Broersma, P. Sijtsma, Quantification of airframe noise using microphone arrays in open and closed wind tunnels, *International Journal of Aeroacoustics*, Vol. 6, Nr. 4, 2007.
- [43] P. Sijtsma, S. Oerlemans, H. Holthusen, Location of rotating sources by phased array measurements, AIAA paper 2001-2167, 2001.
- [44] P. Sijtsma, R.W. Stoker, Determination of Absolute Contributions of Aircraft Noise Components using Fly-Over Array Measurements, AIAA paper 2004-2958, 2004.
- [45] B.H. Bulder, S.A.M. Barhorst, J.G. Schepers, F. Hagg, Theory and user's manual BLADOPT, ECN-C-01-011, Energy Research Centre of the Netherlands ECN, 2001.
- [46] B. Montgomerie, A. Brand, J. Bosschers, R. van Rooij, Three-dimensional effects in stall, ECN-C-96-079, Energy Research Center of the Netherlands ECN, 1997.
- [47] M. Drela, XFOIL: An analysis and design system for low Reynolds number airfoils, *Low Reynolds number aerodynamics*, T. J. Mueller, Ed., University of Notre Dame, Paris, 1989.
- [48] E.T.G. Bot, Aerodynamische Tabel Generator (in Dutch), ECN-C-01-077, Energy Research Centre of the Netherlands ECN, 2001.
- [49] M.R. Fink, Noise component method for airframe noise, *AIAA Journal of Aircraft* 17 (10), 1979.
- [50] T.F. Brooks, C.L. Burley, Rotor broadband noise prediction with comparison to model data, AIAA paper 2001-2210, 2001.
- [51] A.P. Dowling and J.E. Ffowcs Williams, *Sound and sources of sound*, Ellis Horwood Ltd., 1983.



## Chapter 7

### Aeroacoustic wind tunnel tests of wind turbine airfoils

*Published as: P. Migliore and S. Oerlemans, Wind tunnel aeroacoustic tests of six airfoils for use on small wind turbines, Journal of Solar Energy Engineering Vol. 126, 2004 (reprinted with permission).*

#### **Abstract**

Aeroacoustic tests of seven airfoils were performed in an open jet anechoic wind tunnel. Six of the airfoils are candidates for use on small wind turbines operating at low Reynolds numbers. One airfoil was tested for comparison to benchmark data. Tests were conducted with and without boundary layer tripping. In some cases, a turbulence grid was placed upstream in the test section to investigate inflow turbulence noise. An array of 48 microphones was used to locate noise sources and separate airfoil noise from extraneous tunnel noise. Trailing-edge noise was dominant for all airfoils in clean tunnel flow. With the boundary layer untripped, several airfoils exhibited pure tones that disappeared after proper tripping was applied. In the presence of inflow turbulence, leading-edge noise was dominant for all airfoils.

## 7.1 Introduction

The U.S. Department of Energy, working through its National Renewable Energy Laboratory (NREL), is engaged in a comprehensive research effort to improve the understanding of wind turbine aeroacoustics. The research is motivated by the desire to make use of the large expanse of low wind speed sites that tend to be closer to U.S. load centers. Quiet wind turbines are an inducement to widespread deployment, so the goal of NREL's aeroacoustic research is to develop tools for use by U.S. industry in developing highly efficient, quiet wind turbines for deployment at these low wind speed sites. NREL's National Wind Technology Center (NWTC) is implementing a multi-faceted research approach that includes wind tunnel tests, field tests, and theoretical analyses in direct support of low wind speed turbine development by its industry partners. NWTC researchers are working hand-in-hand with industry engineers to ensure that research findings are available to support ongoing design decisions.

The work described herein focuses on the experimental aeroacoustic analysis of six airfoils that are candidates for use on small wind turbines having rated power of approximately 20 kW or less. However, without knowledge of both the aerodynamic and aeroacoustic performance of airfoils, engineers are frustrated in making decisions on new blade designs. This is particularly true for small wind turbines, which operate at low Reynolds numbers of 1 million or less, at which airfoil aerodynamic characteristics are both sensitive and difficult to predict. Thus, the present work must be considered in the context of the broader research effort that includes wind tunnel *aerodynamic* and *aeroacoustic* tests. The aerodynamic tests were conducted at the University of Illinois at Urbana-Champaign, and the aeroacoustic tests were conducted at the Netherlands National Aerospace Laboratory (NLR) in Emmeloord. The results, which are documented in published NREL reports [1,2], provide a valuable airfoil database for designers who wish to consider the tested airfoils and for researchers who wish to use the results in code validation efforts.

The primary factor that determines wind turbine blade noise is tip speed, as most noise sources scale with tip speed to the fifth or sixth power. There is a limit, however, to the use of tip speed reduction as a design tool for decreasing noise. One consideration, particularly for small wind turbines, is that low tip speeds imply low Reynolds numbers, which imply diminished aerodynamic efficiency. Furthermore, in optimizing life cycle cost of energy, lower tip speeds typically result in larger blade twist and chord, along with increased tower thrust and drive train torque loads. These factors lead to costlier components. Therefore, although low tip speed is a prerequisite for low-noise turbines, it also makes good sense to begin the rotor-optimization process with the quietest airfoils available. This assumes, of course, that airfoils can be identified that are both quiet and aerodynamically efficient.

For the aeroacoustic tests described in this paper, the two-dimensional airfoil models were mounted between two acoustically treated endplates and tested with and without boundary layer trips and a turbulence grid, at three angles of attack and five wind tunnel speeds corresponding to Reynolds numbers from 0.2 to 1.0 million. Approximately 500 configurations were tested. Results were obtained in the form of 1/3-octave band acoustic 'source plots' using conventional beamforming, which allows separation of source and background noise. Further processing provided noise spectra and overall sound pressure levels. The principal objective was to obtain a relative comparison of the prominent noise sources for the tested airfoils and conditions. Significant results are presented as a comparison

of noise emissions for the various airfoils, the influence of inflow turbulence on leading-edge noise, and the effect of boundary layer tripping. Because this paper is a significant condensation of the larger NREL report [2], many details have been omitted.

## 7.2 Sources of wind turbine blade noise

We consider six sources that independently generate aeroacoustic emissions [3,4]: inflow turbulence, turbulent boundary layer trailing-edge interaction, separated flow, laminar boundary layer vortex shedding, trailing-edge bluntness (von Karman) vortex shedding, and tip vortex formation. These sources are superimposed to form the total noise spectrum from a wind turbine blade. The spectra are often summed to calculate an overall sound power level.

Inflow turbulence noise is caused by the interaction of atmospheric (or synthesized wind tunnel) turbulence with the airfoil surface. In some cases, as the data will show, it can be a dominant source radiating from the airfoil leading edge. In previous wind tunnel tests [5], Hagg, et al. observed that airfoil thickness had a large influence on inflow turbulence noise, while camber and angle of attack appeared to be unimportant. The effect of leading-edge radius was not conclusively demonstrated because that parameter was not varied independently. Subsequently, Guidati, et al. [6] confirmed that increased airfoil thickness leads to a reduction of inflow turbulence noise and demonstrated that a reduction could be obtained by appropriately changing airfoil shape without increasing thickness.

The other sources of noise are collectively called airfoil self noise because they are caused by the airfoil interacting with its own boundary layer and near wake. If the trailing-edge thickness of the airfoil is very thin relative to the boundary layer thickness, as was the case for the models tested, trailing-edge bluntness noise will not be an important source. In addition, two-dimensional airfoil models tested between endplates do not have a tip vortex or any associated noise, although interaction between the endplate boundary layer and model-endplate juncture may cause extraneous noise.

Turbulent boundary layer trailing-edge noise is generally considered the most important source of airfoil self noise for modern wind turbine blades. It is caused by the interaction of turbulent eddies in the boundary layer with the trailing edge, with radiation enhancement due to scattering. As the angle of attack increases, the thickness of the turbulent boundary layer increases and large-scale unsteady structures can cause noise production from the trailing edge. Fully separated flow (deep stall) causes radiation from the chord as a whole [7].

Laminar boundary layer vortex shedding noise is created by a feedback loop between vortices being shed at the trailing edge and instability waves in the laminar boundary layer upstream. This source of noise can occur on the suction or pressure side of the airfoil and it can be particularly annoying because it is often manifested in pure tones resulting from feedback amplification. It is not likely to be important for large turbines operating at high Reynolds numbers, but it may be significant for small wind turbines.

## 7.3 Airfoil models

Tests were conducted on seven airfoil models, each having a 22.86-cm chord and a 0.51-m span. Six of the airfoils are either being used or considered for use on small wind turbine blades. These are the FX 63-137, S822, S834, (Selig-Donovan) SD2030, (Selig-Giguere) SG6043, and (Selig-Hanley) SH3055. The models are shown in Figure 7-1 along with a

NACA 0012 profile (center of photograph) used as a benchmark for comparison to previous results obtained by the National Aeronautics and Space Administration (NASA) [7].

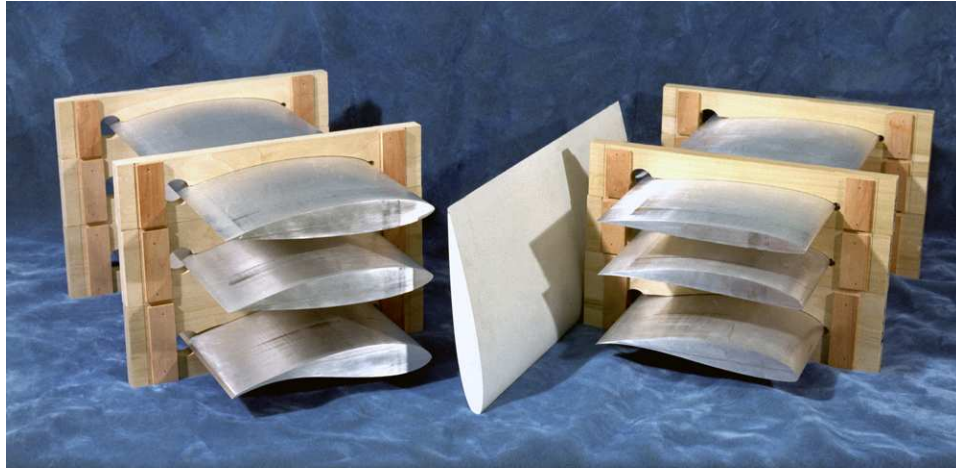


Figure 7-1: Wind tunnel airfoil models.

The airfoil models were built to exacting tolerances, in which the difference between the specified and as-built surface was required to be within 0.05% of the model chord, or 0.1143 mm. Trailing-edge thickness was to be no greater than 0.375 mm with 0.1875 mm as a preferred upper limit. A coordinate-measuring machine was used to verify the final dimensions, and in every case, the model geometry was within the specified tolerances. Figure 7-2 shows a typical result. The noticeable deviation at the trailing edge occurs because the airfoil coordinates prescribe a trailing-edge thickness of zero, which is impossible to fabricate.

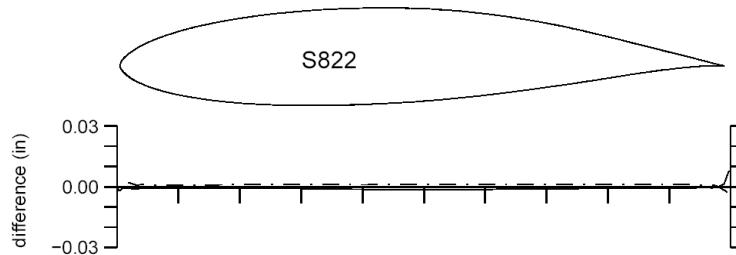


Figure 7-2: S822 airfoil model accuracy (difference between specified and measured coordinates).

The NACA 0012 model was constructed of carbon-fiber fabric pre-impregnated with epoxy resin and cured at room temperature. Although the accuracy of this model was acceptable, we decided to construct the remaining models of solid aluminum to accelerate the fabrication process.

For tests with a fully turbulent boundary layer, tripping was initiated using zigzag tape of width = 5% chord over the entire model span at 2% and 5% chord on the suction and pressure sides of the airfoil, respectively. The standard trip thickness was 0.25 mm, but for some conditions, trips of up to 0.5 mm were used. In some cases, a stethoscope was employed to verify whether the trips induced the desired boundary layer transition. The stethoscope was

attached to an L-shaped total-pressure tube, which was traversed manually over the surface of the model. Transition from a laminar to a turbulent boundary layer was observed by listening.

Airfoil efficiency, as indicated by lift-to-drag ratio, is expected to suffer with boundary layer tripping. For example, the maximum lift-to-drag ratio of the FX 63-137 airfoil degrades from approximately 88 untripped to approximately 56 tripped at a Reynolds number of 350,000 [1]. This situation emulates the real world of wind turbine blades, which are often soiled by dirt, sand, rain, snow, or bugs. Designers accommodate this reality by evaluating rotor performance both clean and dirty (boundary layer untripped and tripped). This is why it was important to obtain airfoil aerodynamic and aeroacoustic data for both untripped and tripped boundary layers.

#### 7.4 Measurements and data analyses

The aeroacoustic tests were conducted in NLR's Small Anechoic Wind Tunnel KAT (Figure 7-3). This open-circuit wind tunnel, the test section of which is surrounded by an anechoic room completely covered with foam wedges, yields more than 99% sound absorption above 500 Hz. Horizontal endplates are mounted to the upper and lower sides of a rectangular 0.38 m x 0.51 m nozzle, providing a semi-open test section for airfoil noise measurements. To suppress reflections, the endplates are acoustically lined with layers of sound-absorbing foam covered by perforated plates. For inflow turbulence measurements, a turbulence grid consisting of diagonally oriented, cylindrical 12 mm bars with a mesh width of 60 mm is installed in the nozzle. Although the tunnel is equipped with a force balance, that information was not used in these tests.



Figure 7-3: NLR anechoic wind tunnel set up with acoustically lined endplates and microphone array.

#### 7.4.1 Test Section Calibration

To verify acceptable flow quality, a calibration study was performed using hot-wire anemometers in the empty test section. Cross hot-wires were used to measure the turbulence intensity and flow angularity with and without the turbulence grid. Hot-wire traverses were made in both cross flow directions for two Mach numbers,  $M=0.12$  and  $M=0.18$ , at two axial locations roughly corresponding to the position of the leading and trailing edge of the tested models.

The test section calibration resulted in profiles of axial velocity, axial turbulence intensity, lateral turbulence intensity, and flow angularity. Without the turbulence grid, the central part of the test section had turbulence levels of 1% or less. With the turbulence grid, the levels increased to 9% and 5% at locations corresponding to the model leading and trailing edges, respectively. Although the flow angularity increased slightly with increasing speed and turbulence level, it always remained within  $1^\circ$  in the central area of the test section.

#### 7.4.2 Microphone Array

Sound pressure level data were acquired using an acoustic array consisting of 48 ½-inch LinearX M51 microphones mounted in an open grid. The microphone sensitivities at 1 kHz were determined prior to the tests using a pistonphone, and the frequency response of the individual array microphones was taken from calibration sheets. No corrections were applied for microphone directivity because this effect is the same for all airfoils and less than 2 dB for angles up to  $45^\circ$  and frequencies up to 15 kHz. Phase matching of the microphones was checked prior to the test using a calibration source at a known position. Acoustic data from the array microphones were synchronously measured at a sample frequency of 51.2 kHz and a measurement time of 30 s. A 500-Hz high-pass filter was used to enhance the dynamic range.

To obtain high resolution at low frequencies, the array dimensions need to be rather large ( $0.8 \text{ m} \times 0.6 \text{ m}^2$ ). The microphone pattern was designed for maximum side lobe suppression at frequencies between 1 kHz and 20 kHz. The array was placed outside the tunnel flow 0.6 m from the tunnel axis, either on the suction or pressure side of the model as dictated by the test matrix. The relatively small distance between the array and the model was chosen to obtain a maximum signal-to-noise ratio. The center of the array was placed at the same height as the tunnel axis. Thus, the levels measured by the array represent airfoil noise levels radiated in the average direction of the array microphones.

There is experimental evidence that source directivity is approximately the same for all airfoils, as was shown by Brooks and Hutcheson [8] for trailing-edge noise of symmetric and cambered airfoils. We made this assumption in comparing noise from different airfoils at a single measurement position. The directivity measurements of the current experiment, performed by moving the array from the suction to the pressure side, were consistent with this assumption.

#### 7.4.3 Test Program

Array measurements were made on the suction side of the six candidate airfoils, with and without tripping and turbulence grid for three angles of attack. Tests were conducted at tunnel speeds of 22.4, 32.0, 47.9, and 63.9 m/s corresponding to Reynolds numbers of 350,000; 500,000; 750,000; and 1,000,000, respectively. The NACA 0012 airfoil was tested for the same conditions as in Ref. [7]: with and without trip, without turbulence grid, for four

Reynolds numbers and five angles of attack. An overview of the suction-side test matrix is shown in Table 7–1. For a number of conditions, pressure-side array measurements were also made to determine directivity effects. Some measurements were repeated with thicker zigzag tape to assess its effectiveness in tripping the boundary layer.

*Table 7–1: Test matrix showing measured Reynolds numbers (in millions) with the array on the suction side of the model. For the six small-wind-turbine airfoils, all Reynolds numbers were tested at geometrical angles of attack of  $0^\circ$ ,  $10^\circ$  and  $18^\circ$ , except the shaded boxes (tested at  $0^\circ$ ,  $5^\circ$  and  $10^\circ$ ). The NACA 0012 airfoil was tested at geometrical angles of attack of  $0^\circ$ ,  $4.5^\circ$ ,  $9.0^\circ$ ,  $12.0^\circ$  and  $16.5^\circ$  to obtain the same effective angles of attack ( $0^\circ$ ,  $2^\circ$ ,  $4^\circ$ ,  $5.3^\circ$  and  $7.3^\circ$ ) as in Ref. [7].*

Airfoil	Turbulence grid off		Turbulence grid on	
	Trip	No trip	Trip	No trip
S822	0.20/ 0.35/ 0.50/ 0.75/ 1.0	0.20/ 0.35/ 0.50/ 0.75/ 1.0	0.20/ 0.35/ 0.50/ 0.75/ 1.0	0.20/ 0.35/ 0.50/ 0.75/ 1.0
S834	0.20/ 0.35/ 0.50/ 0.75	0.20/ 0.35/ 0.50/ 0.75	0.20/ 0.35/ 0.50/ 0.75	0.20/ 0.35/ 0.50/ 0.75
FX63-137	0.20/ 0.35/ 0.50/ 0.75	0.20/ 0.35/ 0.50/ 0.75	0.20/ 0.35/ 0.50/ 0.75	0.20/ 0.35/ 0.50/ 0.75
SG6043	0.11/ 0.20/ 0.35/ 0.50	0.11/ 0.20/ 0.35/ 0.50	0.11/ 0.20/ 0.35/ 0.50	0.5
SH3055	0.50/ 0.75/ 1.0	0.50/ 0.75/ 1.0	0.50/ 1.0	0.50/ 1.0
SD2030	0.20/ 0.35/ 0.50	0.20/ 0.35/ 0.50	0.20/ 0.50	0.20/ 0.50
NACA0012	0.50/ 0.62/ 0.87/ 1.12	0.50/ 0.62/ 0.87/ 1.12	0.50/ 0.62/ 0.87/ 1.12	0.50/ 0.62/ 0.87/ 1.12

Using methods (based on lifting surface theory) applied by Brooks, et al. [7] in NASA open jet tests of NACA 0012 airfoils, the model angles of attack ( $\alpha$ ) set in the wind tunnel were corrected to account for flow curvature and downwash deflection. For the specific geometry of our NLR tunnel tests, the effective angle of attack ( $\alpha_{\text{eff}}$ ) was equal to the geometric angle of attack ( $\alpha$ ) divided by 2.26. The nominal, effective angles of attack defining the test matrix were  $0^\circ$ ,  $4^\circ$ , and  $8^\circ$ .

In reporting open-jet tests of a NACA 63-215 airfoil, Brooks and Hutcheson [8] note that more accurate angle of attack corrections, which include camber effects, are available. However, it was not clear to them how an increased refinement with camber effects would be properly utilized. Therefore, they took a heuristic approach to determine input angles, and the same correction formulas were used as for symmetrical airfoils. This same approach was taken in the NLR tests reported here.

Although these angle-of-attack corrections address the integral effect of the jet deflection, the surface pressure distribution may differ somewhat from that over the airfoil in a closed tunnel or in the atmosphere [9]. Consequently, boundary layer development over the tested airfoils and the resulting sound emissions may be somewhat different than for airfoils in free flow (or for that matter, a wind turbine blade operating in the atmosphere). This dilemma is repeatedly confronted by researchers contemplating aeroacoustic tests in open-jet tunnels instead of closed-wall tunnels, which have their own vexing problems.

We chose to test at specific angles of attack, rather than lift coefficients, to compare the airfoils' acoustic emissions at the likely operating points near their maximum lift-to-drag ratios. Wind turbine blades, which are sometimes clean and sometimes dirty, operate in unsteady flow conditions. Thus, rather than operating at a constant angle of attack, they operate in an angle-of-attack range near the optimum. Table 7–2 contains airfoil aerodynamic data at  $Re = 350,000$  showing that the optimum angle of attack for the S822, S834, and

SD2030 is around  $8^\circ$ , while the optimum angle of attack for the FX 63-137, SH3055, and SG6043 is closer to  $4^\circ$ . Thus, it is of little use to compare the S822 to the FX 63-137, for example, at a particular lift coefficient; but it is meaningful to compare the S822 at  $8^\circ$  to the FX 63-137 at  $4^\circ$ . For consistency in presenting results, and to simplify the test matrix, all the airfoils were tested at the same three angles of attack.

*Table 7-2: Aerodynamic characteristics from Ref. [1] for tested airfoils with tripped boundary layers at Reynolds number = 350,000. Airfoil thickness, chord, and angle of attack =  $t$ ,  $c$ , and  $\alpha$ , respectively.  $C_l$  = lift coefficient;  $l/d$  = lift to drag ratio. An asterisk (\*) indicates that details may not be published because of restrictions on the release of intellectual property data.*

Airfoil	$t/c$ (%)	Camber (%)	$\alpha^\circ$ @ $c_l = 0$	$c_{l,max}$	$\alpha^\circ$ @ $c_{l,max}$	$l/d_{max}$	$\alpha^\circ$ @ $l/d_{max}$	$c_l$ @ $l/d_{max}$	$\alpha^\circ$ range $l/d_{max}$
SH3055	16.5	*	-6.5	1.57	15	55	3	1.1	2 - 4
S822	16.0	*	-2.0	1.15	15	45	8	0.9	6 - 9
S834	15.0	*	-2.0	1.07	13	43	8	0.8	6 - 9
FX63-137	13.6	5.94	-7.0	1.53	14	56	3	1.1	2 - 4
SG6043	10.0	5.50	-5.6	1.42	14	46	3	0.9	2 - 4
SD2030	8.6	2.25	-2.2	1.17	12	56	8	1.0	7 - 9

#### 7.4.4 Data Processing

Processing methods and computer programs are referenced in the test report [2], but details are not discussed there and cannot be discussed here because of their proprietary nature. Conventional beamforming was applied to obtain acoustic source plots, such as the one presented in Figure 7-4. The effect of sound refraction by the tunnel shear layer was corrected using the Amiet method [10], and the array scan plane was placed in the plane of the model and rotated in accordance with the angle of attack. Using these source plots, noise originating from the model was separated from background noise.

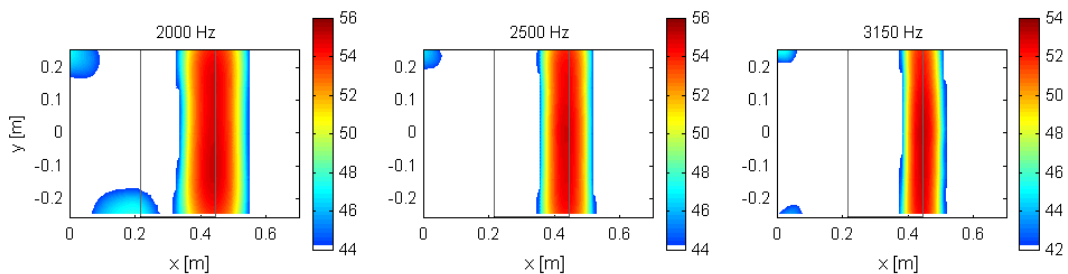


*Figure 7-4: Acoustic source plots for the untripped NACA 0012 airfoil at 39.6 m/s and  $\alpha=0^\circ$  (array on pressure side) illustrating prominent trailing-edge emissions. Flow direction is from left to right.  $x$  [m] and  $y$  [m] are distances from the nozzle exit and the model centerline, respectively, in meters. The dynamic range is shown on the vertical scale in dB. Figures 7-5, 7-6 and 7-9 are similarly labeled.*

Special measures were taken in the beamforming process. First, the main diagonal in the cross power matrix (auto powers) was discarded to suppress the influence of tunnel background noise. Second, a spatial window was applied to the microphone signals to reduce effective array aperture with increasing frequency and reduce coherence loss effects.

For quantitative comparison of different airfoils and conditions, the array results were processed to obtain narrowband or 1/3-octave-band spectra for specific source regions (again,



the main diagonal in the cross power matrix was discarded). The acoustic data were processed using a block size of 2048, yielding a narrowband frequency resolution of 25 Hz. By defining an integration contour around the mid-span of the model, extraneous noise sources at junctions of the model and end plates were suppressed. A preliminary review of the test results showed that for measurements without the turbulence grid, noise was radiated from the trailing edge of the model. Therefore, in those cases, the mid-span integration area was centered on the trailing edge. This process is illustrated in Figure 7-5. For measurements with the turbulence grid, the dominant noise source was observed to be located at the leading edge of the model. In those cases, the integration contour was centered on the leading edge.

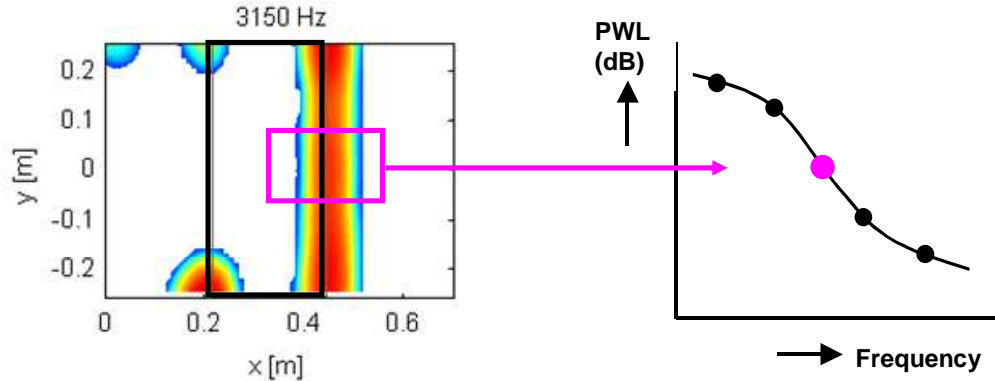


Figure 7-5: Acoustic source plot (left) indicating noise source locations in the plane of the model. The model contour is indicated by the (black) vertical rectangle. Flow moves from left to right. The (pink) horizontal rectangle indicates the trailing-edge integration contour used to translate acoustic source plots to airfoil noise spectra. For measurements with the turbulence grid, a leading-edge integration contour was used.

Because the integration area cuts through the line source region at the leading or trailing edge, 'leakage' from sources outside the integration area into the integration contour, and vice versa, will occur. The magnitude of this effect depends on array resolution, and therefore on frequency. To account for this effect, a 'line source correction' was applied using simulations similar to those described by Oerlemans and Sijtsma [11]. The resulting spectral levels are Sound Power Levels produced by 10 cm of span. This procedure was validated by comparing the trailing-edge noise spectrum from array measurements to the sound levels at the central array microphone for a noisy trailing-edge case [12]. It was found that the *absolute* levels agreed within approximately 2 dB. The *relative* accuracy of the sound levels, determined from repeat measurements on the same airfoil, was approximately 0.5 dB.

#### 7.4.5 Extraneous Noise Sources

In some cases, the airfoil noise levels were so low that, despite the procedures described above, the spectra were dominated by extraneous wind tunnel noise sources. To facilitate rapid judgment of the validity of the measured levels, procedures were developed to indicate the importance of tunnel noise in the spectra.

For a significant number of conditions, the trailing-edge noise levels were influenced by extraneous sources at the model-endplate junctions. These 'corner sources' are illustrated in Figure 7-6. A routine was developed to determine the importance of these corner sources and, in cases in which their influence on the trailing-edge noise level is more than 1 dB, to

calculate an upper limit for the trailing-edge noise level. In graphs of the trailing-edge noise spectra, these upper limits are indicated by the absence of a marker (plotting symbol) at that specific frequency. If significant corner sources are absent, calculated noise levels are assumed absolute, and a marker is placed at that specific frequency on the spectral plots. These data processing methods were successful in isolating the corner sources and mitigating their influence on calculated noise levels. Furthermore, toward the end of the test program, a technique was identified for physically reducing the corner sources [2]. A treatment of porous foam in the small spaces between the model and the endplates resulted in a drastic reduction (up to 10 dB) in broadband noise of the corner sources. In future tests, this technique will enable the detection of very low trailing-edge noise levels [12].

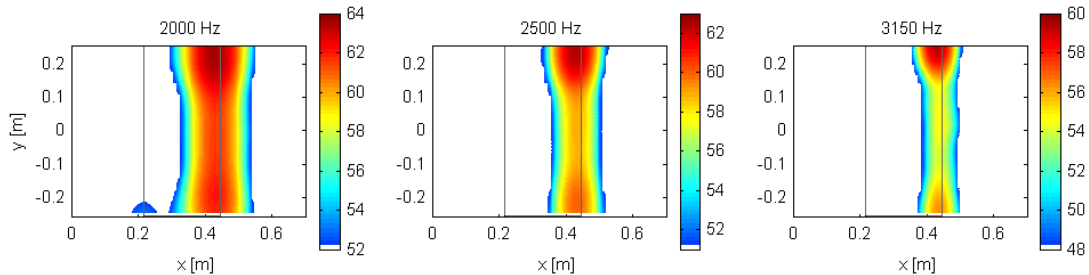


Figure 7-6: Acoustic source plots for tripped S822 airfoil at 47.9 m/s and  $\alpha=0^\circ$  (array on suction side). Note the extraneous 'corner sources' in contrast to the uniform sources shown in Figure 7-4.

For measurements with the turbulence grid in place, background noise from the grid itself, rather than corner sources, often obscured the leading-edge noise levels. In those cases, leading-edge noise levels were compared to those obtained in the empty test section (with turbulence grid) for the same speed. If the leading-edge noise level was at least 6 dB higher than the background noise level, a marker is placed at that specific frequency on the spectral plots. Absence of a marker indicates that the spectral level was influenced by grid noise.

## 7.5 Results

A large amount of data was acquired and analyzed in the experiments, but only a small amount can be presented in this paper. The reader may wish to obtain the full NREL report [2], which includes graphical presentations and narrative discussion of the following topics:

- Test section calibration data
- Sound power level *trailing-edge* noise spectra for the six small wind turbine airfoils tested, including the effect of boundary layer tripping
- Comparison of trailing-edge noise data to benchmark NACA 0012 data [7]
- Sound power level *leading-edge* noise spectra for the six small wind turbine airfoils tested, including the effect of boundary layer tripping
- Normalized leading and trailing-edge noise spectra illustrating collapse of data for different speeds
- Emission of pure tones for several airfoils, including suppression by aggressive boundary layer trips

- Directivity tests with the microphone array on both pressure and suction sides of the model
- Leading- and trailing-edge noise comparisons for all airfoils at 32 m/s and several angles of attack
- Discovery of techniques to significantly reduce extraneous corner source noise.

### 7.5.1 Trailing-edge Noise Spectra

Figure 7-7 illustrates typical trailing-edge noise spectra obtained from acoustic source plots such as those shown in Figure 7-4. Results for the tripped boundary layer exhibit smooth broadband spectra typically associated with trailing-edge noise. Results for the untripped boundary layer show some significant peaks that can be associated with laminar boundary layer vortex shedding [7]. The frequency of the peaks increases with speed at the angle of attack shown.

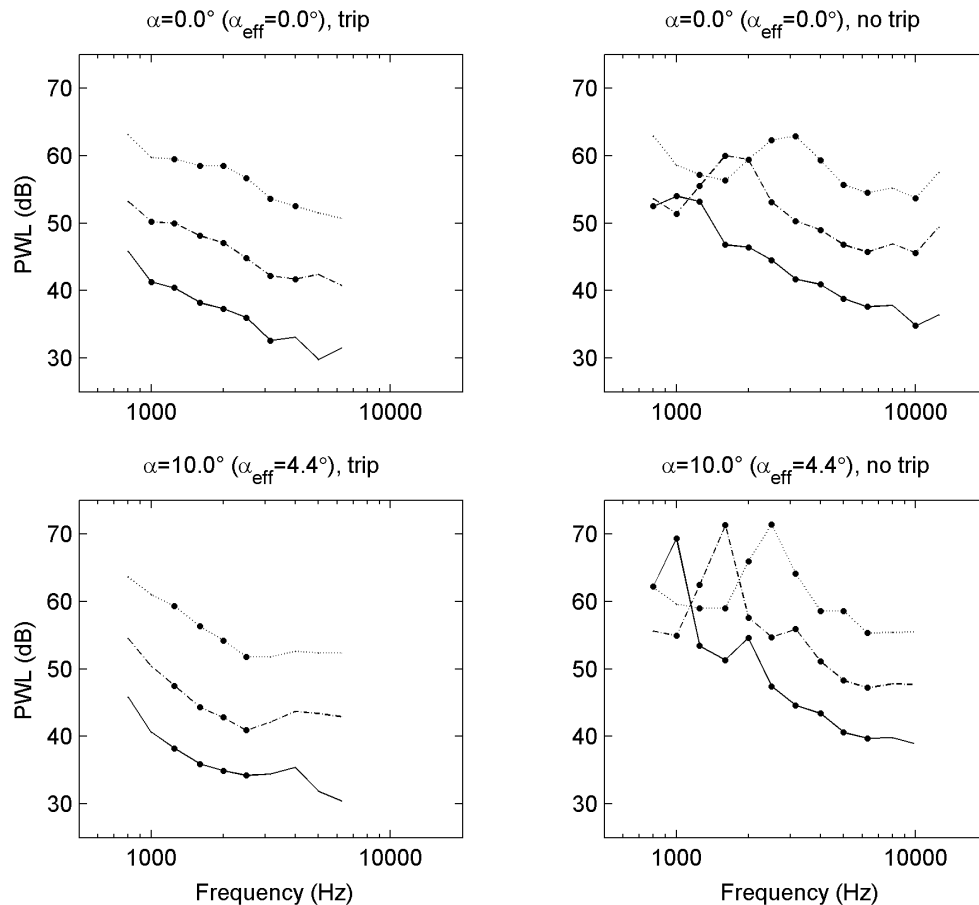


Figure 7-7: Trailing-edge noise spectra for the S834 airfoil (array on suction side) plotted versus frequency in Hz. — 22.4 m/s; - - 32.0 m/s; ... 47.9 m/s. As explained in Section 7.4.5, upper limits are indicated by the absence of a plotting symbol. Symbols indicate absolute noise levels.

We investigated the directivity of trailing-edge noise by conducting certain tests with the array first on the suction side and then on the pressure side. The directivity was found to be

symmetrical about the chord, as demonstrated by Figure 7-8. Speed dependence, occurrence of tones, and comparison between different airfoils will be discussed in subsequent sections.

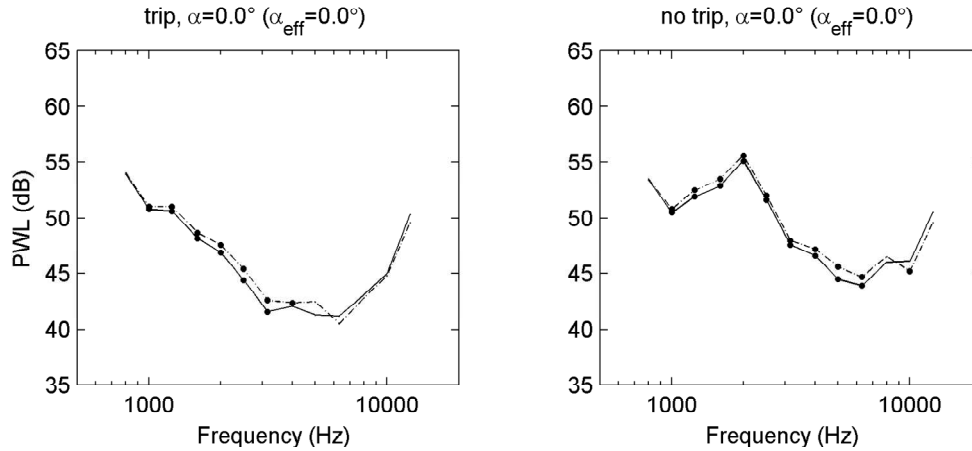


Figure 7-8: Trailing-edge noise spectra for S822 airfoil at 32 m/s.  $\text{---}$  array on pressure side;  $\text{- -}$  array on suction side. Note the symmetry about the chord, suggesting uniform directivity.

### 7.5.2 Leading-edge Noise Spectra

When the airfoils were tested with the turbulence grid installed in the tunnel, inflow turbulence noise (indicated by a source at the leading edge) became dominant for all airfoils. This was clearly indicated in the source plots (Figure 7-9), which reveal no prominent trailing-edge emissions. The peak levels in the source plots do not exactly coincide with the model leading edge, probably because the deflection of the open jet is not taken into account in the array processing. However, using an integration contour (Figure 7-5), the peak is captured anyway. The dynamic range of the source plots was 12 dB, which implies that the leading-edge source was much stronger than the trailing-edge source. For example, at 47.9 m/s and  $\alpha=10^\circ$ , the peak *leading-edge* noise level for the S834 airfoil (Figure 7-10) with the turbulence grid was approximately 83 dB compared to a peak *trailing-edge* noise level (Figure 7-7, trip) of 59 dB without the grid. With the turbulence grid, tripped and untripped results were identical, and leading-edge noise directivity was found to be symmetrical around the chord.

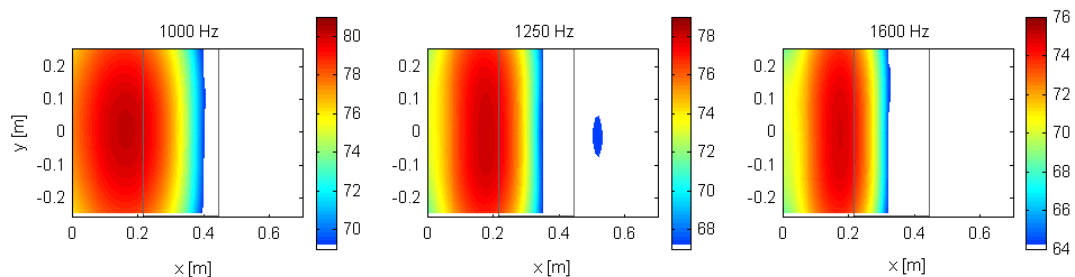


Figure 7-9: Leading-edge noise from SD2030 airfoil with trip, with turbulence grid, at a tunnel speed of 32.0 m/s and  $\alpha=18^\circ$  (array on suction side). Note the dominance of the leading-edge sources.

It is important to note that the level of turbulence in the tunnel was much greater than that which is usually experienced in the atmosphere at typical rotor speeds. Therefore, it should not be concluded from these experiments that in the presence of atmospheric turbulence, leading-edge noise would dominate wind turbine aeroacoustic emissions, at least on the A-weighted scale. To the authors' knowledge, the many analytical and empirical studies reported in the literature do not conclusively demonstrate a relationship between ingested turbulence characteristics and inflow turbulence noise. Additional research is needed to better understand this matter.

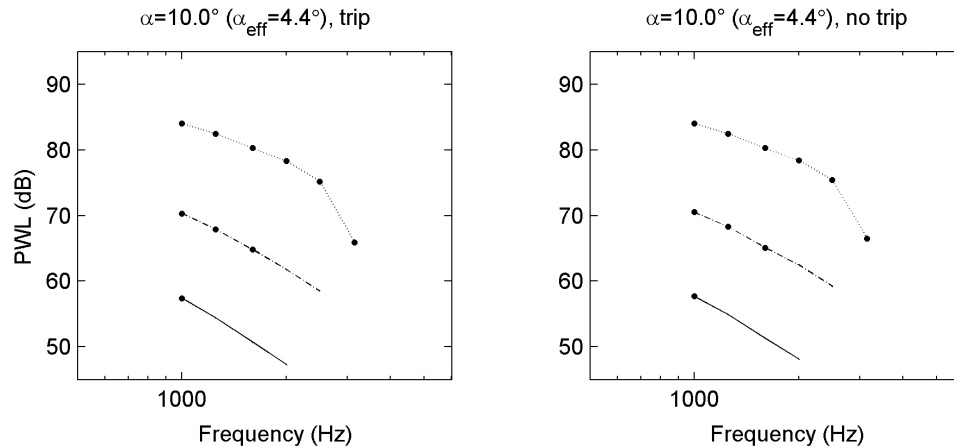


Figure 7-10: Leading-edge noise spectra for S834 airfoil (array on suction side). — 22.4 m/s; - - 32.0 m/s; ... 47.9 m/s. Note that the levels are much higher than the trailing-edge noise spectra shown in Figure 7-7.

### 7.5.3 Normalized Noise Spectra

To investigate the speed dependence of the airfoil noise levels, it is useful to normalize the noise spectra (Figure 7-11). Here, the normalized sound power level is given by  $PWL_{norm} = PWL - 10 \log U^m$ .  $PWL$  is the airfoil sound power level determined from array measurements, and the exponent  $m$  denotes the speed dependence of airfoil noise levels.  $PWL_{norm}$  is plotted against Strouhal number  $fc/U$ , where  $f$  is the acoustic frequency and  $c$  is the model chord. Typically, Strouhal scaling is based on boundary layer thickness, but because that information was not available, the model chord was used.

The best data collapse was obtained for a value of the exponent  $m = 4.5$  determined iteratively. The S834 airfoil data in Figure 7-11 is provided for illustration, but review of the spectra for all airfoils showed very good data collapse for trailing-edge noise in *tripped* conditions. For a given angle of attack, the trailing-edge noise levels at different speeds coincided within 1-2 dB. Because normalization in terms of  $St$  and  $PWL_{norm}$  works well for the turbulent boundary layer trailing-edge noise, experimental results for one speed can be extrapolated to other speeds within the range of frequencies investigated.

The optimum value of  $m = 4.5$  is slightly lower than the value of  $m = 5.0$  that was found in earlier studies [4] and is generally expected. A reason for this discrepancy could be that despite several measures taken to reduce coherence loss, this effect still plays a role, resulting in lower levels at high wind speeds. On the other hand, several studies [13,14] of slat noise,

which may be regarded as a trailing-edge noise mechanism, also find a value of  $m = 4.5$ . This may be an indication that some physical basis exists for scaling at this exponent.

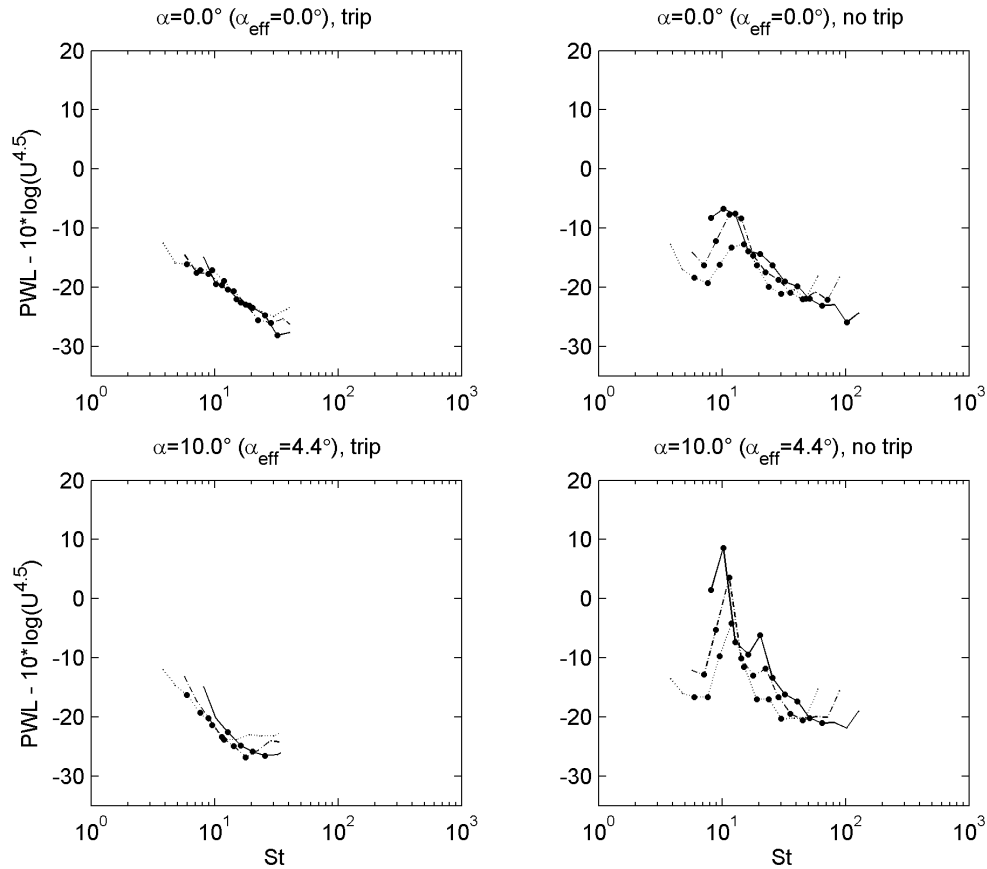


Figure 7-11: Normalized trailing-edge noise spectra for the S834 airfoil (array on suction side) plotted versus Strouhal number,  $St = fc/U$ . — 22.4 m/s; - - 32.0 m/s; ... 47.9 m/s.

For *untripped* conditions, peak Strouhal numbers for different speeds were found to coincide within about 30%. A slight increase in  $St$  with increasing speed suggests that a better collapse of peak frequencies could be obtained by using the boundary layer thickness as the length scale in  $St$ , rather than chord [7], because boundary layer thickness at the trailing edge will decrease with increasing Reynolds number.

The spectral levels for the *untripped* results did not collapse as well as for the *tripped* data. Other values of the exponent  $m$  did not significantly improve the collapse. This illustrates that the normalization in terms of  $St$  and  $PWL_{norm}$  was not very successful for the complex feedback mechanism associated with laminar boundary layer vortex shedding noise, which is an important source for untripped airfoils at low Reynolds numbers.

We also normalized the leading-edge (inflow turbulence) noise spectra in a manner similar to that described for trailing-edge noise. The best collapse of data was obtained for the exponent  $m = 6$ , which is in good agreement with theoretical predictions for low frequency inflow turbulence noise [4]. Figure 7-12 provides an example for the S822 airfoil.

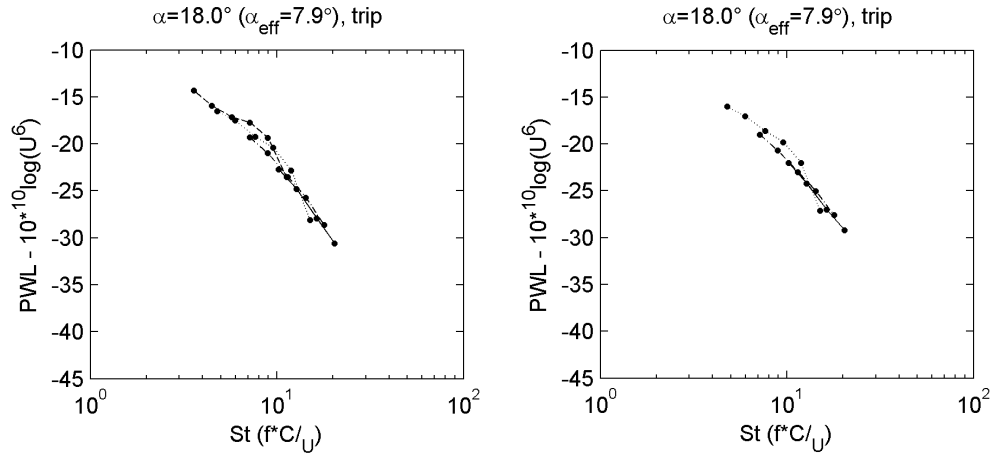


Figure 7-12: Normalized leading-edge noise spectra for tripped S822 (left) and S834 (right) airfoils (array on suction side). — 22.4 m/s; - - 32.0 m/s; ... 47.9 m/s; - · - 63.9 m/s.

#### 7.5.4 Comparison to Benchmark

Acoustic measurements on the NACA 0012 airfoil enabled direct comparison to benchmark data from NASA [7]. The tested airfoil shapes and chords were identical, and in both studies, the model was mounted between endplates attached to opposite sides of a rectangular tunnel nozzle. There were some differences in the manner of boundary layer tripping, but the NLR measurements were performed at the same tunnel speeds and effective angles of attack as the NASA study.

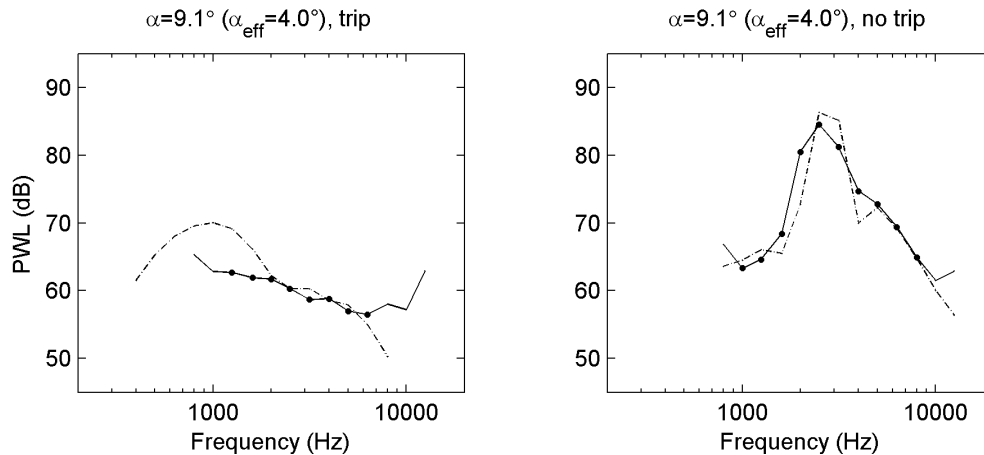


Figure 7-13: Trailing-edge noise spectra for the NACA 0012 airfoil at 55.5 m/s. — NLR data (array on suction side); - - NASA data [7].

Detailed comparisons of the test results are beyond the scope of this paper, but in general, the spectral characteristics (Figure 7-13) agreed. Broadband spectra for the tripped cases and spectral humps (tones) for a number of untripped cases were reproduced. The *tripped* results revealed an interesting difference between the NASA and NLR data. Although the sound power levels compared well for intermediate frequencies, the NASA data consistently exhibited a hump around 1 kHz that did not appear in the NLR data. Possible explanations for

this behavior are the topic of continuing dialogue among NLR, NASA, and NREL researchers. Issues include differences in the manner of boundary layer tripping (NASA trips were more severe) and differences in measurement technique (NASA used a 2-microphone correlation method and NLR used a 48-microphone array).

### 7.5.5 Pure Tones

One of the most interesting observations of the test campaign was the presence of intense, narrowband peaks in the trailing-edge noise spectra for several airfoils at different operating conditions. These are called 'pure tones' and are perceived as such by a listener. They are illustrated in Figure 7-14 for the trailing-edge noise spectra of the untripped S834 ( $\alpha=10^\circ$ ), SG6043 ( $\alpha=0^\circ$ ), and SD2030 ( $\alpha=0^\circ$ ) airfoils. The nature of these tones was investigated in more detail at 22.4 m/s because they were most pronounced at this tunnel speed. The spectra for these cases show peaks at around 1 kHz and 2 kHz for all three airfoils. The angle of attack range for which these tones occurred was estimated by listening in the test section during a sweep of angle of attack. This gave the following ranges:  $7.5^\circ < \alpha < 13^\circ$  for S834,  $-8^\circ < \alpha < 2^\circ$  for SG6043, and  $-10^\circ < \alpha < 4^\circ$  for SD2030.

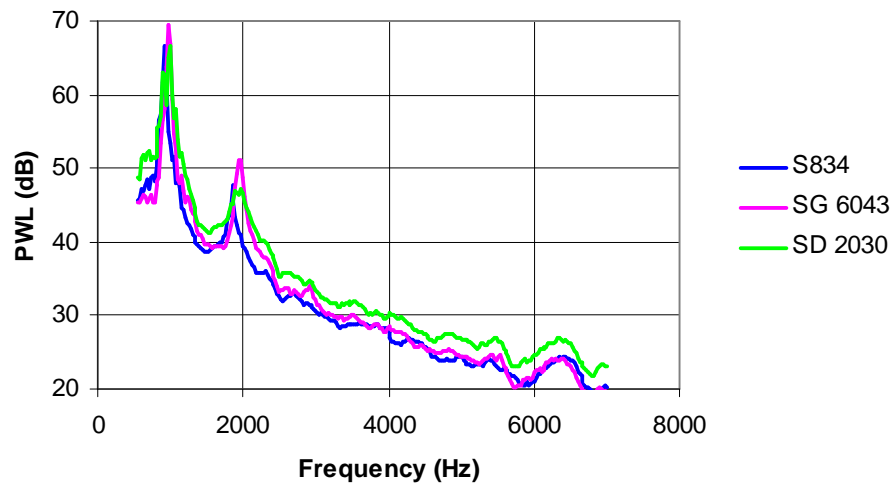


Figure 7-14: Narrowband trailing-edge noise spectra for three untripped airfoils that showed intense tones ( $U=22.4$  m/s;  $\alpha=10^\circ$  for S834,  $\alpha=0^\circ$  for SG6043 and SD2030).

Although such tones sometimes result from blunt-trailing-edge vortex shedding, the extremely thin trailing edges of the models made this unlikely. Calculations of the Strouhal number ( $St$ ), which is approximately 0.2 for von Karman vortex shedding, confirmed this was not the cause. We hypothesized, therefore, that laminar boundary layer vortex shedding caused the tones. To investigate this hypothesis, we applied a different thickness of zigzag tape and observed the effects. By tripping one side of the airfoil at a time, we could determine where the tones originated. For the S834 and SD2030 airfoils, the tones originated from the pressure side; whereas for the SG6043 airfoil, the tones originated from the suction side. Stethoscope measurements on the pressure side of the untripped S834 model indicated a laminar boundary layer up to about 80% chord. With tripping, transition to a turbulent boundary layer occurred directly behind the trip at 5% chord. This observation supported the hypothesis that the tones were due to laminar boundary layer vortex shedding.



The sensitivity of the tones to trip thickness was investigated in more detail for the S834 airfoil, with results shown in Figure 7-15. The untripped case shows the narrowband peak at 925 Hz and the harmonic at 1850 Hz. It can be seen that the standard trip thickness of 0.25 mm on both sides of the airfoil was not effective. In fact, the level of the tones increased slightly with respect to the untripped case, and a harmonic appears at 2775 Hz. Application of a slightly thicker trip (0.30 mm) on the pressure side caused the spectral level to decrease dramatically and the 925 Hz and 1850 Hz tones to vanish completely. Interestingly, the broadband level decreased even further after the addition of a 0.30 mm trip on the suction side.

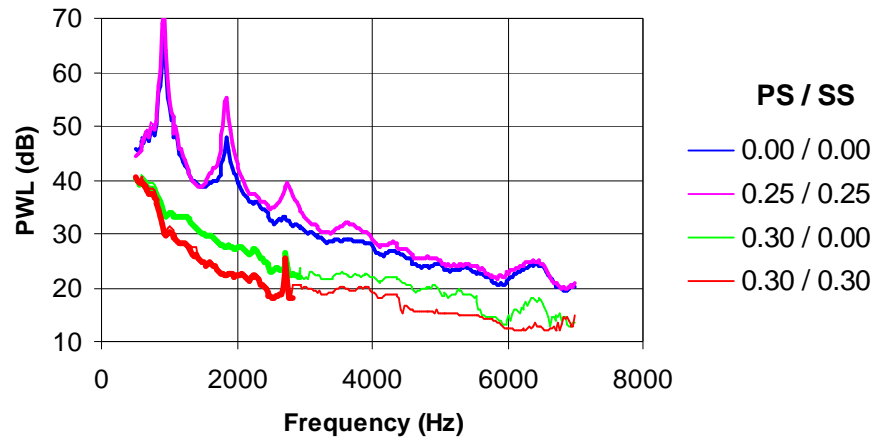


Figure 7-15: Narrowband trailing-edge noise spectra for S834 airfoil at 22.4 m/s and  $\alpha=10^\circ$  as a function of trip thickness on pressure side (PS) and suction side (SS). A thin line indicates that these spectral values are an upper limit for the trailing-edge noise level.

Another interesting observation was that the tones disappeared in the presence of upstream turbulence. Observation of the source plots with and without the turbulence grid showed that the inflow turbulence removed the trailing-edge tones, and the grid noise became dominant. Although direct evidence of boundary layer transition was not obtained, the inflow turbulence evidently interrupted the feedback mechanism responsible for the tones.

#### 7.5.6 Comparison of Airfoils

An important objective of the wind tunnel tests was to observe the noise levels of the different airfoils. A common point for comparing all models exists at 32 m/s and angles of attack of  $0^\circ$ ,  $10^\circ$ , and  $18^\circ$ . (The NACA 0012 data were taken at a slightly different speed of 31.7 m/s and angles of attack of  $0^\circ$ ,  $9.5^\circ$ , and  $16.5^\circ$ .)

The NREL report [2] compares the trailing-edge noise spectra of the different airfoils. For the untripped condition, the noisiest airfoils were the SD2030 and SG6043 at  $0^\circ$  and the NACA 0012 and S834 at  $10^\circ$ . For the tripped condition, pure tones were eliminated and noise levels were reduced for most airfoils. Figure 7-7, in which tripped and untripped spectra are displayed side-by-side, illustrates this trend. Although the comparison among airfoils was obscured by the fact that for many frequencies only upper limits are available (see Section 7.4.5 above), it appeared that, for the tripped case, the FX 63-137 and SH3055 airfoils were somewhat noisier than the others. These observations are reflected in Figure 7-16, which

shows the A-weighted overall sound power level obtained by summing the 1/3-octave band sound pressure levels between 0.8 kHz and 12.5 kHz. These overall sound power levels are an *upper limit* for the actual two-dimensional trailing-edge noise.

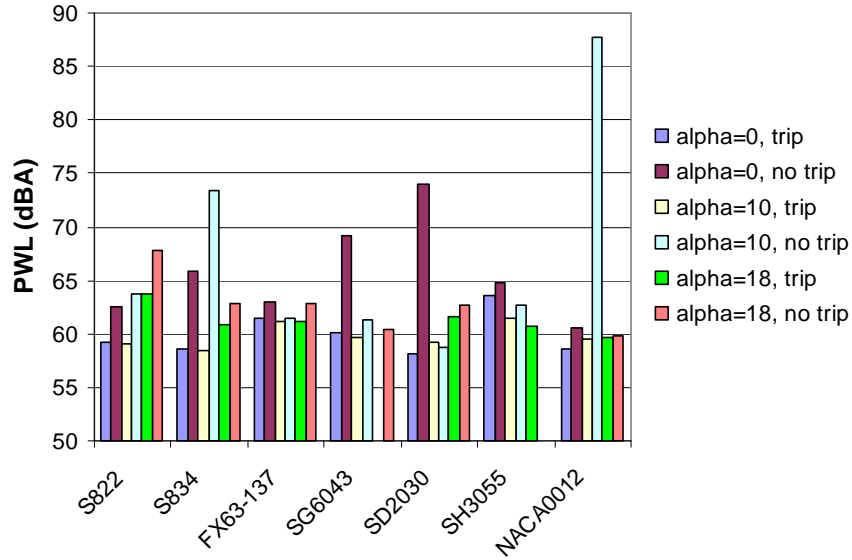


Figure 7-16: A-weighted overall trailing-edge noise levels at 32 m/s.

We also compared the inflow turbulence noise spectra for the airfoils. Because the results were unchanged for tripped and untripped conditions, only tripped data were examined. Differences in leading-edge noise of 8 dB were observed between the quietest and noisiest airfoils. By examining these results in relationship to the airfoil shapes, we observed a general trend: the thinner the airfoil, the higher the inflow turbulence noise. This trend is demonstrated in Figure 7-17, which plots the A-weighted overall noise levels for three angles of attack. These were obtained by summing the 1/3-octave band levels between 1 kHz and 2.5 kHz, where airfoil noise is attributed to inflow turbulence. Data in Figure 7-17 are presented from left to right in the order of decreasing airfoil thickness.

It is important to note that comparing airfoil noise data at the *same* angle of attack can be misleading because the airfoils may operate at *different* angles of attack. For example, peak aerodynamic efficiency for the FX 63-137 occurs around  $\alpha = 4^\circ$ , while the S822 is best around  $\alpha = 8^\circ$  [1]. Therefore, to estimate which airfoil will be quieter, we must compare at their respective design points (angle of attack, Reynolds number, surface condition, and tip speed). Following this logic, Figure 7-16 suggests that if trailing-edge noise is dominant, the FX 63-137 ( $\alpha_{\text{eff}}=4.4^\circ$ ,  $\alpha=10^\circ$ ) is likely to be quieter than the S822 ( $\alpha_{\text{eff}}=7.9^\circ$ ,  $\alpha=18^\circ$ ). However, the S822 trailing-edge noise spectra in Ref. [2] had a sharp peak between 1 kHz and 2 kHz, indicating laminar boundary layer vortex shedding and a boundary layer that was not fully tripped. This demonstrates that simply comparing data at the same Reynolds number is insufficient. The *character* of the boundary layer, in particular the extent of laminar flow, must also be simulated. In fact, the data showed that the tripped FX 63-137 and S822 had no tones and that the S822 was actually quieter than the FX 63-137.

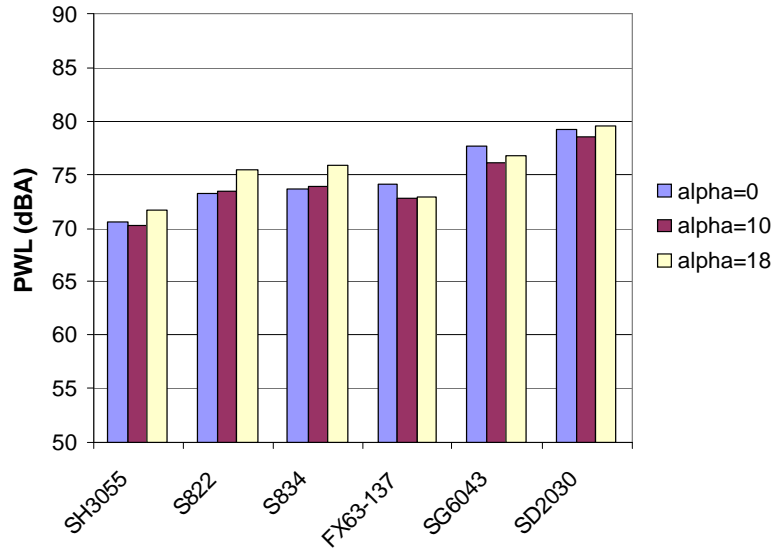


Figure 7-17: A-weighted overall leading-edge noise levels at 32 m/s. Airfoils are presented from left to right in the order of decreasing thickness (and increasing inflow turbulence noise at  $\alpha=0^\circ$ ).

## 7.6 Summary

Large amounts of high quality data were obtained for the airfoils tested in this project. This is attributed to precise models and rigorous test methods. One consequence of this precision was that trailing-edge-bluntness vortex shedding noise did not materialize, owing to the extremely thin trailing edge of the models. We believe model precision also contributed to the good agreement obtained with the NASA data for the spectral characteristics of the NACA 0012 airfoil, although a discrepancy in sound power level at below 2 kHz is still being investigated.

In quiescent inflow, trailing-edge noise was dominant. Test results suggest that untripped airfoils operating at low Reynolds numbers ( $< 1$  million) can be expected to exhibit pure tones at some angles of attack. For example, it was common to observe tones of 10 – 15 dB above the broadband level. This was attributed to laminar boundary layer vortex shedding. It was also observed that proper tripping eliminated pure tones and reduced broadband noise. Even those airfoils that did not exhibit pure tones experienced a reduction in sound power level of up to 3 dB(A) when tripped. In highly turbulent inflow, pure tones disappeared, probably due to the suppression of the laminar boundary layer and/or disruption of the feedback mechanism responsible for laminar boundary layer vortex shedding noise.

In considering the sound emissions of different wind turbine airfoils, it is not appropriate to compare at the same lift coefficient. It is more important to compare at the angle of attack expected at the design condition, which may vary significantly from one airfoil to another. By this criterion, the tested airfoils exhibited notably different turbulent boundary layer trailing-edge noise levels. This source, which is likely to be dominant for typical wind turbines, differed by as much as 6 dB(A) among the airfoils tested.

Leading-edge inflow turbulence noise became the dominant source, masking trailing-edge noise, in the presence of severe upstream turbulence. A trend was observed of increasing inflow turbulence noise with decreasing airfoil thickness. Whether this is attributable to *thickness* or to *sharpness* is unclear because, as in previous research [5,6], leading-edge radius

was not independent of airfoil thickness in our tests. This may be a moot point because there is a strong correlation between the two geometrical attributes.

### Acknowledgements

A lengthy and ambitious project such as this has many contributors. In our case, credit must first be given to the extraordinary craftsmanship of Yvan Tinel of Northbrook, Illinois, who fabricated the airfoil models to exacting specifications. Michael Selig of the University of Illinois at Urbana-Champaign performed the coordinate measurements and plotting. The test engineers and technicians at NLR deserve special mention. They operate a superb facility and exhibit great professionalism and a commitment to quality. We also thank the technical reviewers, whose meticulous scrutiny compelled us to tidy up some important details of the paper.

### References

- [1] Selig, M. and McGranahan, B., 2004, Wind Tunnel Aerodynamic Tests of Six Airfoils for Use on Small Wind Turbines, NREL SR-500-34515.
- [2] Oerlemans, S., 2004, Wind Tunnel Aeroacoustic Tests of Six Airfoils for Use on Small Wind Turbines, NREL SR-500-35339.
- [3] Moriarty, P. and Migliore, P., 2003, Semi-empirical Aeroacoustic Noise Prediction Code for Wind Turbines, NREL TP-500-34478.
- [4] Wagner, S., Bareiß, R. and Guidati, G., 1996, Wind Turbine Noise, Springer-Verlag, Berlin, pp. 14-21.
- [5] Hagg, F., Dassen, A., Parchen, R., and Bruggeman, 1996, Influence of the Airfoil Shape and Thickness on the Emission of Turbulence Inflow Noise as Measured in the Wind Tunnel, 1996 European Wind Energy Conference, Göteborg, Sweden.
- [6] Guidati, G., Bareiß, R., Wagner, S., Dassen, T., and Parchen, R., 1997, *Simulation and Measurement of Inflow-Turbulence Noise on Airfoils*, AIAA-97-1698-CP.
- [7] Brooks, T., Pope, D. and Marcolini, M., 1989, *Airfoil Self-Noise and Prediction*, NASA Reference Publication 1218.
- [8] Brooks, T. and Hutcheson, F., 2004, Effects of Angle of Attack and Velocity on Trailing-edge Noise, AIAA-2004-1031.
- [9] Moreau, S., Henner, M., Iaccarino, G., Wang, M., and Roger, M., 2003, *Analysis of Flow Conditions in Free Jet Experiments for Studying Airfoil Self-Noise*, AIAA Journal 41 (10).
- [10] Amiet, R., 1978, Refraction of Sound by a Shear Layer, *Journal of Sound and Vibration*, Vol. 58, No. 2, pp 467-482.
- [11] Oerlemans, S. and Sijtsma, P., 2002, Determination of Absolute Levels from Phased Array Measurements Using Spatial Source Coherence, AIAA-2002-2464.
- [12] Oerlemans, S. and Migliore, P., 2004, *Aeroacoustic Wind Tunnel Tests of Wind Turbine Airfoils*, AIAA-2004-3042.
- [13] Pott-Pollenske, M., Dobrzynski, W., Buchholz, H., Gehlar, B., and Walle, F., 2002, Validation of a Semi empirical Airframe Noise Prediction Method through Dedicated A319 Flyover Noise Measurements, AIAA 2002-2470.
- [14] Pott-Pollenske, M., Alvarez-Gonzalez, J., and Dobrzynski, W., Effect of Slat Gap on Far Field Radiated Noise and Correlation with Local Flow Characteristics, AIAA-2003-3228.

## Chapter 8

### Reduction of wind turbine noise using optimized airfoils and trailing edge serrations

*Published as: S. Oerlemans, M. Fisher, T. Maeder, K. Kögler, Reduction of wind turbine noise using optimized airfoils and trailing-edge serrations, AIAA Journal 47(6), 2009 (reprinted with permission).*

#### **Abstract**

Acoustic field measurements were carried out on a 94-m diameter three-bladed wind turbine, with one standard blade, one blade with trailing edge serrations, and one blade with an optimized airfoil shape. A large horizontal microphone array, positioned at a distance of about one rotor diameter from the turbine, was used to locate and quantify the noise sources in the rotor plane and on the individual blades. The acoustic source maps show that, for an observer at the array position, the dominant source for the baseline blade is trailing edge noise from the blade outboard region. Due to convective amplification and directivity, practically all of this noise is produced during the downward movement of the blade, which causes the typical swishing noise during the passage of the blades. Both modified blades show a significant trailing edge noise reduction at low frequencies, which is more prominent for the serrated blade. However, the modified blades also show tip noise at high frequencies, which is mainly radiated during the upward part of the revolution, and is most important at low wind speeds due to high tip loading. Nevertheless, average overall noise reductions of 0.5 dB and 3.2 dB are obtained for the optimized blade and the serrated blade, respectively.

## Nomenclature

$D$	Trailing edge noise directivity function
$f$	Frequency
$M$	Local blade inflow Mach number
$N$	Number of measurements
$P$	Rotor power
$St$	Strouhal number ( $f\delta^*/U$ )
$U$	Local blade inflow velocity
$U10$	Wind speed at 10 m height
$\alpha$	Misalignment angle between array and wind turbine
$\delta^*$	Trailing edge boundary layer displacement thickness
$\varepsilon$	Standard deviation of the mean (standard error) ( $\sigma/\sqrt{N}$ )
$\theta$	Angle between blade chord line and source-observer line
$\zeta$	Angle between blade flow velocity and source-observer line
$\sigma$	Standard deviation
$\varphi$	Angle between blade plane and plane containing chord line and observer
$\psi$	Blade azimuth angle

### 8.1 Introduction

Wind turbine noise is one of the major issues for the widespread use of wind energy. For a modern large wind turbine, aerodynamic noise from the blades is generally considered to be the dominant noise source, provided that mechanical noise is adequately treated [1]. The sources of aerodynamic noise can be divided into airfoil self-noise and inflow-turbulence noise. Airfoil self-noise is the noise produced by the blade in an undisturbed inflow, and is caused by the interaction between the boundary layer and the trailing edge of the blade. Self-noise can be tonal or broadband in character, and may be caused by several mechanisms, such as turbulent boundary layer trailing edge interaction noise (subsequently denoted as trailing edge noise), laminar boundary layer vortex shedding noise, trailing edge bluntness noise, or blade tip noise. Inflow-turbulence noise is caused by the interaction of upstream atmospheric turbulence with the blade, and depends on the atmospheric conditions. It is an open issue to what extent inflow-turbulence noise contributes to the overall sound level of a wind turbine [2].

Due to the large number of applications (e.g. wind turbines, airplanes, helicopters, fans), the characteristics of airfoil noise have been investigated extensively in both experimental and theoretical studies [3-13]. Both inflow-turbulence and self-noise mechanisms were considered and the dependence on parameters such as flow speed, angle-of-attack, radiation direction, and airfoil shape was characterized. These studies formed the basis of several semi-empirical wind turbine noise prediction models, which were validated by comparison to field measurements [14-20]. Since the field results only provided the overall sound level of the turbine, the relative importance of the different mechanisms was determined mainly on the basis of the predictions. In some studies inflow-turbulence noise was regarded to be the dominant source [11,14-16,18], while others considered trailing edge noise to be dominant [17]. In another case, the turbine noise in different frequency ranges was attributed to mechanical noise, trailing edge noise, tip noise, and inflow-turbulence noise [19].

In a few studies, source location measurements were performed to provide more direct information on the source mechanisms [21-25]. The results from [21-23] were obtained using an acoustic parabola or a linear array of microphones, and focused only on the horizontal (downward) blade position ( $\psi=90^\circ$ ). In [24,25], a large two-dimensional microphone array, positioned on the ground about one rotor diameter upwind of the turbine, was used to localize the noise sources in the complete rotor plane and on the individual blades, for two different wind turbines. It was shown that practically all recorded noise was produced during the downward movement of the blades. This strongly asymmetric source pattern, which causes the typical swishing noise during the passage of the blades, was explained by convective amplification and trailing edge noise directivity. The following directivity function for trailing edge noise was used [26]:

$$D = \frac{2 \sin^2(\theta/2) \sin^2 \phi}{(1 - M \cos \xi)^4}, \quad (8.1)$$

where  $\theta$  is the angle between the blade chord line and the source-observer line,  $\phi$  is the angle between the plane of the blade and the plane containing the chord line and the observer,  $\xi$  is the angle between the (inverted) local blade inflow velocity and the source-observer line, and  $M$  is the local blade inflow Mach number (see Figure 8-1 for definition of angles).

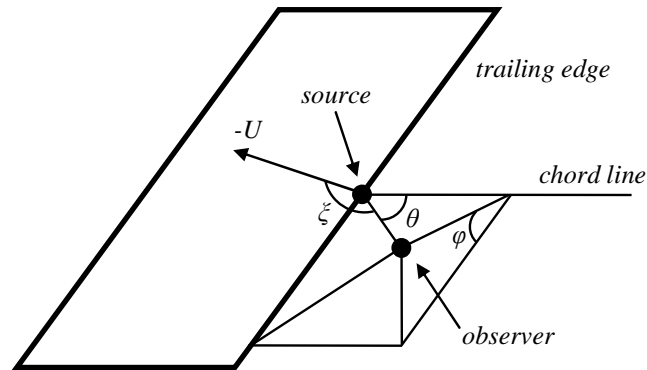


Figure 8-1: Definition of angles for trailing edge noise source.

The numerator in Eq. (8.1) describes the directivity of high-frequency trailing edge noise, and indicates that most of the noise is radiated in the direction of the airfoil leading edge. It was analytically derived for edge noise from a semi-infinite flat plate [6,27], but was also found to be valid for finite airfoils [9], provided that the angle  $\theta$  is not too close to  $180^\circ$ . In the limit for low-frequency dipole noise, where the acoustic wavelength is much larger than the airfoil chord, the  $\sin^2(\theta/2)$  term changes into  $\sin^2 \theta$  [5,26]. Nevertheless, in [24] Eq. (8.1) was found to be valid for the whole tested frequency range, including the low frequencies where the acoustic wavelength was of the same order as the blade chord. The denominator in Eq. (8.1) represents the 4<sup>th</sup> power convective amplification factor for trailing edge noise [28], and indicates that the noise source becomes louder when it is moving towards the observer.

Many studies have addressed the reduction of airfoil or wind turbine noise. Since inflow turbulence noise and trailing edge noise both scale with approximately the 5<sup>th</sup> power of the local blade inflow velocity [5,6,24], an obvious means for noise reduction is to reduce the

rotor RPM or rotor diameter. However, these measures also reduce the power output of the turbine [1]. The same holds for increasing the blade pitch angle (i.e. turning the blade leading edge against the wind): this reduces the local angle of attack and therefore the noise, but due to the reduced lift also the power production. Thus, the challenge is to achieve a noise reduction without a reduction in power output. With regard to tip noise, which depends on the characteristics of the tip vortex, it has been demonstrated in several studies that the tip shape can have a significant influence on the noise from a wind turbine [1,6]. The importance of inflow-turbulence noise depends on the structure of the atmospheric turbulence and on the shape of the blades. It has been shown both experimentally and numerically that inflow turbulence noise levels increase with increasing 'sharpness' of the airfoil leading edge [10,13].

With regard to trailing edge noise, a number of reduction concepts have been investigated. After it had been shown theoretically that the acoustic radiation efficiency of a trailing edge can be reduced by serrations [29] (see Figure 8-2), this concept was investigated in a number of experimental studies on 2-D airfoils [30], model wind turbines [31,32], and a full-scale wind turbine [23]. In [31], serrations were applied to a 16-m diameter model wind turbine, and depending on the flow conditions overall noise reductions of up to 3.5 dB were obtained. In order to prevent increased noise at high frequencies, it was found to be critical to align the plane of the serrations with the trailing edge flow. In [23], serrations were applied to a 1 MW wind turbine, and an overall noise reduction of 2-3 dB was obtained, despite increased noise at high frequencies. It should be noted that the measurements in [31,23] only focused on the horizontal (downward) blade position ( $\psi=90^\circ$ ), which may give an incomplete picture.



Figure 8-2: Climber removing trips from serrated blade.



An alternative concept for trailing edge noise reduction is the application of flexible trailing edge brushes. The brushes align automatically with the trailing edge flow and have shown significant noise reduction potential in wind tunnel tests on flat plates and on a 2-D airfoil [12,33]. However, a first attempt to apply this concept to a full-scale wind turbine yielded a reduction of only 0.5 dB [34], possibly because the improvised brushes were too short. Finally, it has been shown in calculations and wind tunnel tests on 2-D airfoils that trailing edge noise can be reduced by a modification of the airfoil shape, without a loss in aerodynamic performance [35]. Note that in the case of an acoustically optimized airfoil shape, trailing edge noise is reduced by changing the structure of the boundary layer turbulence, whereas serrations or brushes are meant to affect only the scattering at the trailing edge. Thus, the effects of an optimized airfoil shape and brushes or serrations are expected to supplement each other.

The present study concerns acoustic field measurements on a 2.3 MW, 94-m diameter wind turbine with one standard (baseline) blade, one blade with an acoustically optimized airfoil shape and one standard blade with trailing edge serrations. The tests were performed in the framework of the European SIROCCO (Silent Rotors by Acoustic Optimisation) project [34]. Building on the results from earlier wind tunnel studies on a model rotor [32], the subject of the project was the design, testing, and full-scale validation of quiet wind turbine blades, without a loss in power performance. In an earlier stage of the project, acoustic field measurements on the baseline turbine [25] indicated that trailing edge noise from the outer 25% of the blades was the dominant noise source for this turbine, and that the three blades produced practically the same sound pressure levels: the average overall sound pressure level (OASPL) for the three blades differed by less than 0.15 dB, and for the two standard blades that were used again in the present campaign less than 0.05 dB.

Subsequently, optimized airfoil shapes were designed and assessed through aerodynamic and acoustic wind tunnel tests on 2-D airfoils [34-36]. The principle of the airfoil design was to reduce the dominant low-frequency (<1 kHz) trailing edge noise peak in the spectrum (which is due to the thick suction side boundary layer), by reducing the loading of the suction side, at the expense of an increased pressure side loading (which causes a slightly higher noise level at less important medium frequencies of 1-3 kHz) [35]. The wind-tunnel tests showed 2-3 dB reduction in OASPL (depending on lift coefficient) [34], and an improved aerodynamic performance for the newly designed airfoils, even though severe geometric and aerodynamic constraints had to be considered in the design (to enable implementation in the existing blade structure). The new airfoil was then incorporated in the design of the outer part of the optimized blade (subsequently denoted as the SIROCCO blade). The twist distribution of the SIROCCO blade was modified such that the lift distribution was approximately the same as for the baseline blade.

In addition to the new blade design, the third rotor blade was used to test a second noise reduction concept, trailing edge serrations. The serrated blade had the same nominal geometry as the baseline blade (including the twist distribution). From power and loads measurements on the baseline and modified rotor, it was found that the in-plane and out-of-plane blade loads on the serrated blade (and, to a lesser extent, also on the SIROCCO blade) were slightly higher than on the baseline blade, causing the aerodynamic performance of the modified blades to be similar or slightly better than the baseline blade [34].

The main goal of the present test campaign was to assess the acoustic performance of the two modified blades versus the baseline blade. In order to assess the effect of blade roughness

due to dirt or insects, the blades were tested in both clean and tripped conditions. A large horizontal microphone array, positioned at a distance of about one rotor diameter from the turbine, was used to measure the distribution of the noise sources in the rotor plane and on the individual blades. Since the array position was fixed and the wind direction varied, both up- and downwind measurements were performed. In the present paper the acoustic array results are presented and analyzed. The noise characteristics for the three blades are investigated as a function of wind speed, rotor azimuth angle, and observer position (upwind or downwind), for clean and tripped conditions. Section 8.2 describes the test set-up, test program, and the array processing methods. In Section 8.3 the results are presented and discussed. The conclusions of this study are summarized in Section 8.4.

## 8.2 Experimental Method

### 8.2.1 Test set-up

The measurements were carried out in March/April 2007 on the same General Electric 2.3 MW prototype test wind turbine that was used in the baseline test campaign in 2005. It had a rotor diameter of 94 m, a tower height of 100 m, and was located on the Netherlands Energy Research Foundation test site in the Wieringermeer (The Netherlands). The turbine control system adjusted the RPM and blade pitch angle depending on the wind speed measured at the nacelle: for higher wind speeds the pitch angle was increased, reducing the local angle of attack and thus the blade loading. The RPM increased up to a certain wind speed, after which it remained constant. The turbine had a yaw mechanism which automatically turned the rotor against the wind. In order to compare the blade performance for identical weather and turbine conditions, the rotor consisted of one standard (baseline) blade, one standard blade with trailing edge serrations, and one SIROCCO blade. The SIROCCO blade was nominally identical to the baseline blade, except for the outer ~30%, where it had a new airfoil. The serrated blade had the same nominal geometry as the baseline blade. The aluminum serrations, with a thickness of 2 mm, were mounted to the outer 12.5 m of the blade, on the pressure side. The 2 mm step was smoothed using filler material over a few centimeters of chord. Similar to [32], the length of the serrations was about 20% of the local chord, and varied as a function of radius: the tooth length was about 10 cm at the tip and about 30 cm at the most inboard position. A picture of the serrated blade is shown in Figure 8-2. Using templates for different radial stations, the plane of the serrations was aligned with the flow direction at the blade trailing edge (as determined from flow calculations). This trailing edge flow direction is constant in the variable RPM region of the turbine. By aligning the serrations with the flow it was attempted to minimize their aerodynamic impact and prevent increased high frequency noise by flow through the teeth. Before the acoustic measurements, all blades were cleaned. In order to assess the effect of blade roughness due to dirt or insects, the blades were tested with and without trips: in State 1 all blades were tripped and in State 2 all blades were clean. The 2-D trips, with a thickness of about 0.4 mm and a width of 4 mm, were installed close to the leading edge on both sides of the blade, from the very tip to about half the blade span. The (variable) blade pitch angle was the same for the three blades.

An acoustic array was used to locate and quantify the noise sources on the rotor and on the individual blades. The acoustic array consisted of 148 Panasonic WM-61 microphones,

mounted on a horizontal wooden platform of  $16 \times 18 \text{ m}^2$ , which was positioned at a distance of about one rotor diameter from the turbine (Figure 8-3).

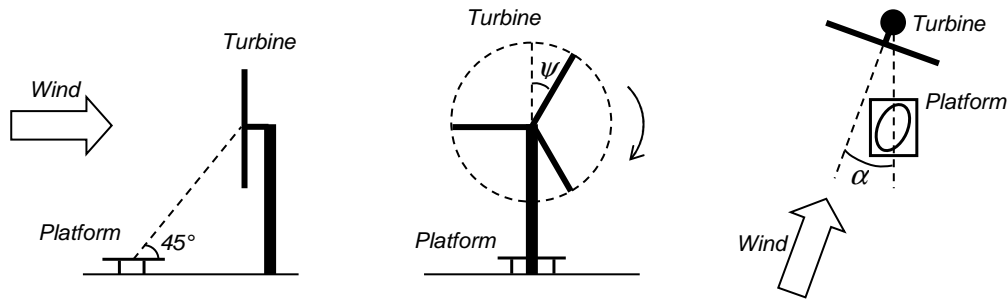


Figure 8-3: Side view (left), front view (middle), and top view (right) of test set-up. The array microphones were mounted on the platform in an elliptic shape for optimum resolution.

Since the array position was fixed and the wind direction varied, both up- and downwind measurements were performed. The Panasonic microphones were mounted flush to the surface of the platform, with the membrane parallel to the platform, and were equipped with wind screens. As a reference, two calibrated LinearX M51 microphones equipped with hemisphere wind screens were mounted on the platform as well. To correct for the view angle of about  $45^\circ$  (Figure 8-3), the microphone array had an elliptic shape (Figure 8-4) rather than the conventional round array design.

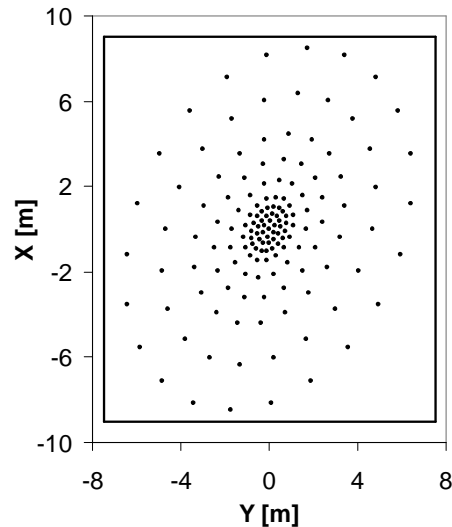


Figure 8-4: Layout of array microphones. The rectangle indicates the platform dimensions.

In this way the effective array shape, as seen from the rotor, is round, so that the resolution with which the noise sources in the rotor plane are localized is approximately the same in the horizontal and vertical directions. The ellipse was slightly tilted to the right-hand side of the rotor plane, to obtain maximum resolution on the side where the blades move downward (for the standard array position, i.e. upwind of the turbine) and where maximum noise radiation was observed in the 2005 campaign. The array had a high microphone density in the center to ensure low side-lobe levels at high frequencies, and a low-density outer part to obtain a good resolution at low frequencies [37]. The distance and orientation of the array with respect to the turbine were determined using a laser distance meter and a compass.

### 8.2.2 Data acquisition

Acoustic data from the array microphones were synchronously measured using the VIPER multi-channel data-acquisition system [38], at a sample frequency of 30.7 kHz and a measurement time of 30 s. The acoustic data were processed using FFT blocks of 1024 samples with a Hanning window and 50% overlap, yielding 1800 averages and a narrowband frequency resolution of 30 Hz. A second-order 500 Hz high-pass filter (-12 dB/octave [38]) was used to suppress high-amplitude pressure fluctuations at low frequencies, and thus to extend the dynamic range of the A/D converter, so that low pressure amplitudes at high frequencies are included. The sound levels were corrected for the filter response and for pressure doubling due to reflections at the platform. Prior to the measurements, the sensitivity at 1 kHz was determined for all array microphones using a calibrated pistonphone. The frequency response of the Panasonic microphones was taken from previous calibration measurements. The frequency response of the M51 microphones was taken from calibration sheets. No corrections were applied for microphone directivity, since calibration measurements showed that these effects amounted to less than 2 dB up to 20 kHz, for angles smaller than 75° with respect to the microphone axis. Phase matching of the microphones was checked using a calibration source at known positions. A trigger signal from the turbine (one pulse per revolution) was recorded synchronously with the acoustic data, in order to determine the location of the blades as a function of time for the source localization on the individual blades (Section 8.2.4).

In parallel to the acoustic measurements, several parameters from the turbine and two nearby meteorological masts were continuously measured at a sample rate of 4 Hz or higher. These data included wind speed, wind direction, temperature, power production, turbine orientation (misalignment angle  $\alpha$ ), RPM, and blade pitch angle.

### 8.2.3 Test program

During the 4-week test campaign, in total more than 600 measurements were taken. Following the IEC norm for wind turbine noise measurements [39], it was attempted to obtain measurements at wind speeds (at 10 m height) between 6 and 10 m/s. The wind speed at 10 m height was calculated by multiplying the average wind speed measured at the nacelle by 0.70 (according to the standard wind profile from [39]). Since the array position was fixed and the wind direction varied, both up- and downwind measurements were performed. Measurements with a large misalignment angle  $\alpha$  (see Figure 8-3) were excluded from the analysis, because for very oblique view angles the array resolution becomes poor. On the basis of the turbine operational data, the most stable measurements (i.e. small variation in wind speed, RPM, pitch angle, and turbine orientation) were selected for further analysis.

*Table 8–1: Number of selected measurements per wind speed bin for each rotor state.*

	6 m/s	7 m/s	8 m/s	9 m/s	10 m/s
State 1 (tripped rotor; array downwind)	8	8	8	0	0
State 2a (clean rotor; array upwind)	7	8	8	8	6
State 2b (clean rotor; array downwind)	8	8	8	0	0

An overview of the selected measurements is given in Table 8–1. Due to unpredictable weather conditions, it was not possible to obtain measurements in each wind speed bin, and for State 1 only downwind measurements were done. Since the clean rotor is considered to be

most representative for the rotor during normal operation, and since the upwind measurements covered all relevant wind speeds, the focus of this paper will be on State 2a.

The average turbine and weather conditions for the different rotor states are listed in Table 8–2 (equal weights per wind speed bin). As mentioned in Section 8.2.1, the blade pitch angle (not to be confused with the twist distribution) is zero at low wind speeds and increases for higher wind speeds. In order to give an impression of the variation of the parameters within each state, this table also shows the standard deviation for each value, defined as

$$\sigma = \sqrt{\frac{1}{N-1} \sum_{i=1}^N (x_i - \bar{x})^2}, \quad \text{with} \quad \bar{x} = \frac{1}{N} \sum_{i=1}^N x_i. \quad (8.2)$$

Note that the power, RPM, and blade pitch angle are not randomly distributed around the mean value, but depend on the wind speed according to the turbine control system. Therefore, the standard deviations for these parameters are based on linear curve fits through the measured data as a function of wind speed. Since the turbine had an automatic yaw system, the yaw angle (i.e. the difference between the wind direction and the turbine orientation) was assumed to be zero.

*Table 8–2: Average weather and turbine parameters for each rotor state. The standard deviation  $\sigma$  is indicated between parentheses.*

	$U10$ (m/s)	$P$ (MW)	RPM	$\alpha$ (°)	blade pitch (°)
State 1	6.9	1.6 (0.1)	14.5 (0.2)	-204 (12)	0.0 (0.1)
State 2a	8.1	2.1 (0.1)	14.9 (0.0)	-2 (4.4)	5.1 (0.6)
State 2b	6.9	1.6 (0.1)	14.6 (0.1)	-183 (2.4)	0.0 (0.0)

#### 8.2.4 Phased array processing

The microphone array data were processed using two different methods. With the first (stationary) method, noise sources in the complete rotor plane were localized using conventional beamforming [40]. Thus, noise from the rotor hub can be separated from blade noise, and it can be seen where in the rotor plane the blade noise is produced. The method shows the integrated effect of the three blades, averaged over the complete measurement time of 30 s (i.e. several revolutions). The first step of this processing involves the calculation of an averaged cross-spectral matrix which contains the cross-powers of all microphone pairs in the array. To improve the resolution and to suppress background noise (e.g. wind-induced pressure fluctuations on the microphones), the main diagonal of the cross-power matrix (i.e. the auto-powers) was discarded. A spatial window was applied to the microphone signals, which reduced the effective array size with increasing frequency, and which corrected for the variation in microphone density over the surface of the array [37]. In this way, the array resolution at low frequencies was improved, and coherence loss effects at high frequencies (due to propagation of the sound through the atmospheric boundary layer) were suppressed.

Acoustic source maps of the rotor plane were produced by electronically steering the array to a set of grid points, and calculating the noise radiated from each of them. The scan grid, with a diameter of 140 m and a mesh width of 2 m, was placed in the rotor plane and rotated in accordance with the orientation of the turbine (depending on wind direction). The 4° tilt angle between the rotor axis and the horizontal plane was also accounted for. The effect

of sound convection in the atmospheric boundary layer was taken into account by assuming a constant wind speed between the scan location and the microphones. This constant wind speed was calculated as the average wind speed between the rotor hub and the array center, as determined from the standard wind velocity profile in [39].

The narrowband acoustic source maps were summed to 1/3-octave bands, and the source levels were normalized to a constant reference distance. The noise sources in the rotor plane were quantified using a source power integration method [37]. This technique sums the source powers in (part of) the measured source map, and corrects the results with a scaling factor obtained by performing a simulation for a monopole source at the centre of the integration region. The thus obtained integrated sound pressure level of the turbine, as measured at the array position, is similar to the 'apparent sound power level' defined in [39]. All spectra presented in this paper are in 1/3-octave bands. The accuracy of the integration method is discussed in the next section.

The second processing method employed three rotating scan planes to localize the (de-dopplerized) noise sources on the three individual blades [ROTating Source Identifier (ROSI)] [41]. This enabled a comparison of the noise from the different blades. The start position of the scan planes was determined using a trigger signal from the turbine that was recorded synchronously with the acoustic data. Acoustic source maps of the different blades were produced by electronically steering the array to a set of rotating grid points, and calculating the noise radiated from each of them. The three scan grids were placed in the rotor plane at azimuthal positions corresponding to the three blades. The blade grids ran from 15 to 60 m in radial direction, had a chordwise extent of 30 m, and had a mesh width of 1 m.

Similar to the first processing method, the narrowband acoustic source maps were summed to 1/3-octave bands, and the source levels were normalized to a constant reference distance. The ROSI results show the noise sources on the individual blades, averaged over a specified part of the revolution. In order to distinguish between the noise production during the down- and upward movement of the blades, separate ROSI scans were done for blade azimuth angles  $\psi$  from  $0^\circ$  to  $180^\circ$  and from  $180^\circ$  to  $360^\circ$  (with  $0^\circ$  the upper vertical blade position). In order to limit processing time, only the first rotor revolution after the start of each acoustic measurement was processed. The noise from the blades was quantified using a power integration method for moving sound sources [42], which is similar to the aforementioned integration method for the stationary rotor plane. The thus-obtained integrated sound levels represent the contribution of the different blades to the overall sound pressure level of the turbine, as measured at the array position.

### 8.2.5 Accuracy of source localization and quantification

The relative position and orientation of the acoustic array and the wind turbine were determined using a laser distance meter and a compass. Nevertheless, there are a number of uncertainties in the localization method, which may cause a deviation between the measured and actual source position. First, the blades are not located exactly in the rotor plane: the  $4^\circ$  rotor tilt angle is accounted for but the rotor cone angle and the bending of the blades outside the plane not. Second, sound refraction by wind shear and sound convection by wind gusts are not accounted for; a constant wind speed is assumed. Third, the rotor RPM is assumed to be constant within one revolution. Therefore, the accuracy of the source localization technique was assessed by attaching for a short period of time a whistle to one of the blades, at a

position unknown to the acoustic test team. After determining to which blade the whistle was mounted, the ROSI source maps were used to estimate the exact whistle position (Figure 8-5). The thus-obtained source radius was found to deviate only 0.5 m from the actual radius, which is considered to be accurate enough for these tests. Figure 8-5 also illustrates that the scan resolution is sufficiently high to determine accurate integrated blade noise levels: from numerical simulations [43] it was found that as long as the distance between adjacent scan points is smaller than the main lobe width (i.e. the width at 3 dB below the peak level), the integrated levels are accurate.

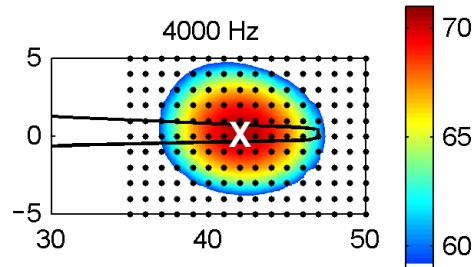


Figure 8-5: Acoustic source map for whistle measurement. The black dots indicate the scan grid and the cross indicates the actual whistle position.

The acoustic source maps were quantified using the power integration method described in the previous section. The accuracy of this method in terms of *absolute* sound pressure levels was verified by comparing the integrated rotor source maps to the measured sound pressure levels at the array microphones. If all the noise measured by the array microphones is due to the turbine rotor, these spectra should coincide. Figure 8-6 shows the spectra measured by the array microphones ('array') and the reference microphone at the center of the array ('refmic'), versus the integrated spectra for the rotor ('powint') and the three blades ('ROSI'). These spectra were averaged over all measurements in State 2a, were corrected for pressure doubling by the array surface, and were normalized to the same reference distance. It can be seen that the average spectrum of the array microphones is practically equal to that on the reference microphone. The small difference at low and high frequencies may be due to wind noise on the array microphones at the edge of the platform.

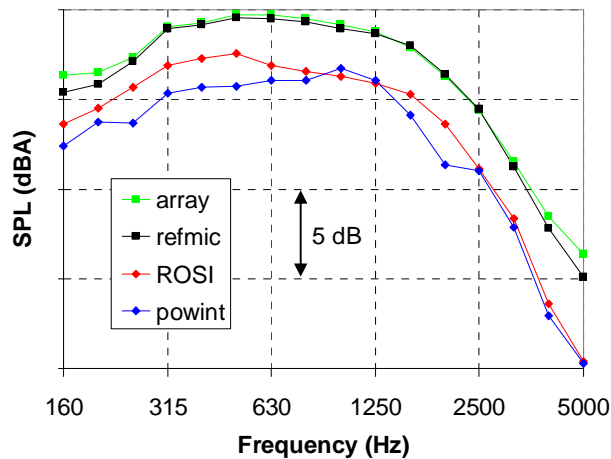


Figure 8-6: Verification of power integrated method.

Figure 8-6 also shows that the integrated spectra for the rotor and the blades have the same shape as the reference spectrum, but are about 3 dB lower over the whole frequency range. This discrepancy cannot be explained by the fact that the array method is applied to incoherent extended sources, since simulations for an incoherent line source yielded accurate integrated levels [37]. However, in addition to the above-mentioned possible deviation between the rotor plane and the actual blade position, the observed difference may be partly explained by certain assumptions and simplifications in the integration method, such as the use of a single monopole source at the centre of the integration region to determine the scaling factor for the source powers. For a simulated, realistic wind turbine rotor noise source distribution, the difference between the actual and integrated overall rotor noise level was about 1 dB [25]. The difference may also be partly attributed to coherence loss at the array microphones, due to propagation of the sound through the turbulent atmospheric boundary layer. A similar effect has also been observed in open jet wind tunnel tests [37]. However, coherence loss effects typically increase with frequency, while here a more or less constant offset is found. Furthermore, coherence loss effects would be expected to increase with increasing wind speed, while here the difference between the integrated rotor noise level and the level of the reference microphone remained constant (within about 0.5 dB) for increasing wind speed. An alternative explanation for the lower integrated levels could be that the reference and array microphones pick up some background noise (e.g. from the wind over the platform), which is not present in the integrated rotor noise spectra (no background noise measurements with stopped rotor were performed in the present test campaign).

The difference between the two integrated spectra may be due to the fact that the ROSI spectrum is dedopplerized and the rotor spectrum is not. For the down-going blade, dedopplerization results in reduced frequencies and reduced sound levels (due to convective amplification, see Section 8.1), and conversely for the up-going blade. Furthermore, the different integration regions (complete rotor versus outer part of the blades) will result in different scaling factors (depending on e.g. the sidelobe behaviour [37]) which may lead to differences in the integrated spectra.

For the evaluation of the noise reduction concepts in the present study, the accuracy of the *relative* sound levels (i.e. level differences between the different blades) was most important. This accuracy was assessed in the baseline test campaign by comparing the individual blade noise spectra for two consecutive revolutions: for each blade the overall sound pressure level (averaged over all selected measurements) reproduced within 0.06 dB for the two consecutive revolutions, and the differences between the blades reproduced within 0.03 dB. It should be noted that due to the small difference in the out-of-plane blade loads (see Section 8.1), the bending may be different for the three blades. Since the scan planes for all three blades are placed in the rotor plane, this may affect the measured noise differences between the blades. However, since the difference in bending between the blades can be estimated to be quite small (less than 0.25 m) on the basis of the load measurements, and the spatial array resolution perpendicular to the rotor plane is limited, the systematic error in the noise difference can be determined to be less than about 0.05 dB (from array simulations). This means that the average level differences between the blades can be considered to be accurate within 0.1 dB, for the given weather conditions, turbine operation parameters, and misalignment angle.



### 8.3 Results and discussion

In this section the results of the acoustic array measurements are presented and discussed. First, the noise source distribution in the rotor plane is analyzed for the up- and downwind array position. Next, the noise sources on the individual blades are investigated, to assess the performance of the SIROCCO blade and the serrations, as a function of array position, wind speed, and rotor azimuth angle. Since the clean rotor is considered to be most representative for the rotor during normal operation, and since the upwind measurements covered all relevant wind speeds, the focus will be on State 2a.

#### 8.3.1 Noise sources in the rotor plane

Each 30 s measurement resulted in acoustic source maps, showing the noise sources in the rotor plane as a function of frequency. In order to show the general trends, these maps were averaged over all selected measurements in the respective rotor state (Figures 8-7 to 8-9). Thus, these maps show the average effect of all three blades over all revolutions. The black circle indicates the 94-m rotor diameter and the X indicates the center of the rotor plane. The range of the color scale is always 12 dB and the maximum is adjusted for each frequency band and each rotor state. The purpose of these source maps is to show the qualitative source characteristics; a quantitative comparison between the different rotor states will be made in Section 8.3.2. The rotation direction is clockwise; note that the source maps in Figures 8-7 and 8-9 are mirrored to allow easy comparison to the upwind measurements (i.e., an observer at the array position would see the rotor turn in counter-clockwise direction).

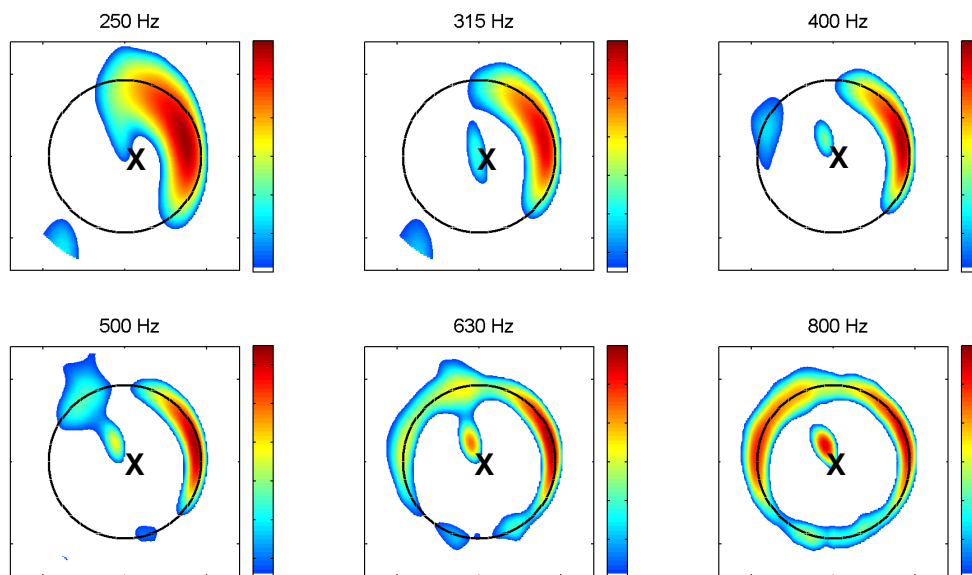


Figure 8-7: Average stationary source maps for State 1 (tripped rotor, downwind array position). The range of the color scale is 12 dB and the maximum is adjusted for each frequency band.

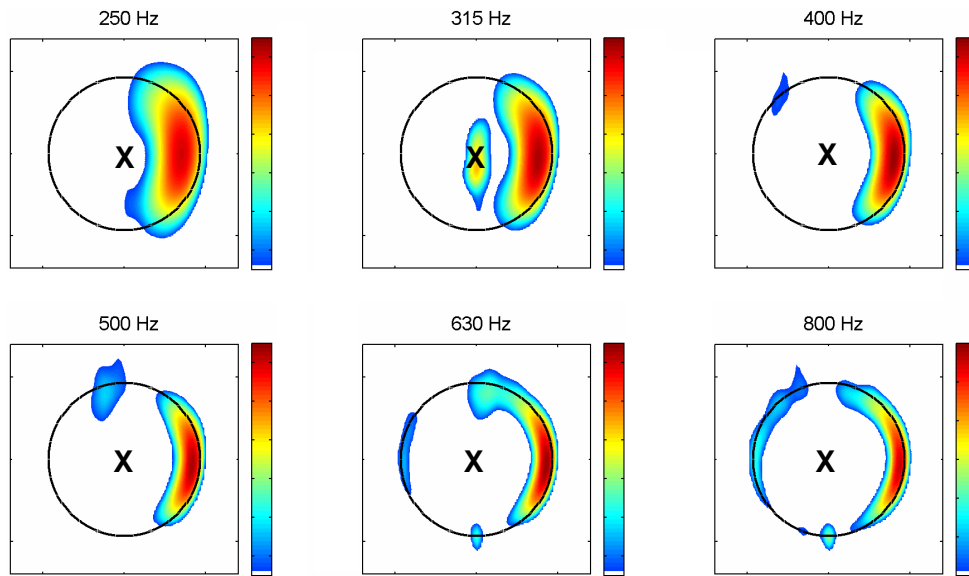


Figure 8-8: Average stationary source maps for State 2a (clean rotor, upwind array position). The range of the color scale is 12 dB and the maximum is adjusted for each frequency band.

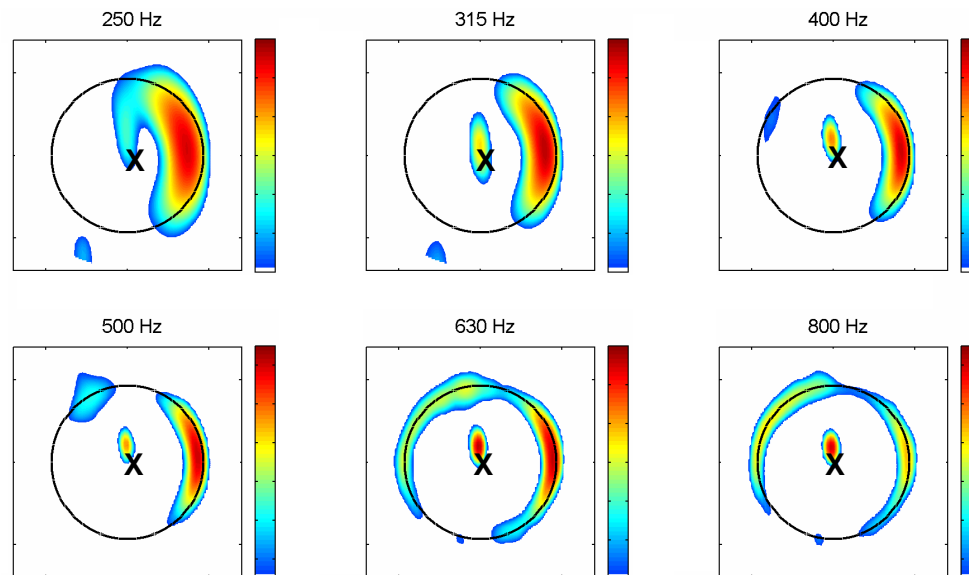


Figure 8-9: Average stationary source maps for State 2b (clean rotor, downwind array position). The range of the color scale is 12 dB and the maximum is adjusted for each frequency band.

Similar to the previous results on the baseline turbine [25], the upwind measurements (Figure 8-8) indicate that, for an observer at the array position, most of the noise is produced by the outer 25% of the blades, during their downward movement. This effect, which causes the typical swishing noise during the passage of the blades, can be explained by convective amplification and trailing edge noise directivity [24], as described in Eq. (8.1). For the higher frequencies, minor noise sources can also be observed at the tip of the up-going blades, and at the location where the blades pass the tower. The nature of this tower source is hard to assess on the basis of the present data, but it could originate from (1) reflection of blade noise on the tower, (2) impingement of blade tip vortices on the tower, and/or (3) the upstream influence of the tower on the flow field around the blade.

For the *downwind* measurements (Figures 8-7 and 8-9), nacelle noise appears to be more pronounced than for the upwind array position. In these plots the nacelle source appears off-centre because it is located in front of the scan plane, which coincides with the rotor plane. Only about 2.5 dB of the observed difference between the up- and downwind nacelle noise level can be explained by the smaller distance to the array and the distance between the source and the scan plane. The remaining difference may be explained by a combination of two factors: first, mechanical noise generated inside the nacelle is radiated mainly in the downwind direction, because the ventilation opening is on the rear side of the nacelle. The relative nacelle noise level in State 1 is lower than in State 2*b*, probably because of the misalignment angle of  $-204^\circ$  (i.e. a deviation of  $24^\circ$  with respect to  $-180^\circ$ ) in State 1 (see Table 8-2). Second, on the basis of the  $\xi$ -dependence in Eq. (8.1), the trailing edge noise from the blades is expected to be slightly higher on the upwind side than on the downwind side (due to the wind speed and rotor tilt angle). This was confirmed by comparison of the blade noise spectra in states 2*a* and 2*b* for the same wind speed bins (see Section 8.3.2.5). Despite the (relatively) increased nacelle noise, the overall turbine noise is still dominated by the noise from the blades. Note that in Figure 8-7 the source maximum for the down-going blade has shifted anti-clockwise (relative to the State 2 plots), which can be explained by the convective amplification factor in Eq. (8.1) for the average misalignment angle of  $-204^\circ$  in this rotor state [25]. Also note that in the downwind source maps the noise source at the tip of the up-going blades is more prominent than in the upwind maps. In the next section it will be shown that, besides a small directivity effect, this difference is mainly due to the lower average wind speed for these measurements (Table 8-2), which leads to a lower pitch angle and higher tip loading (see also Section 8.2.1).

### 8.3.2 Noise sources on the individual blades

As mentioned in Section 8.1, acoustic field measurements on the baseline turbine [25] showed that the average OASPL for the two standard blades that were used again in the present campaign (i.e. the baseline and serrated blade) differed by less than 0.05 dB. Furthermore, it was argued in Section 8.2.5 that the average level differences between the blades, as measured with the microphone array, are accurate within 0.1 dB. Thus, with the present test set-up it is well possible to assess the acoustic performance of the serrations and the new airfoil. In this section, first the possibilities and limitations of acoustic measurements with a single microphone are shortly discussed. Then, the array results are used to study the average blade noise characteristics, and the dependence on rotor azimuth, wind speed, observer position (upwind versus downwind), and rotor state (tripped versus clean blades).

### 8.3.2.1 Single-microphone analysis

In this section the acoustic results of a single microphone are analyzed, to demonstrate the possibilities and limitations of such measurements, and to illustrate subjective on-site observations. During the field tests, the three different blades could be clearly distinguished by the difference in swishing noise produced during the passage of each blade. This can be illustrated by plotting the OASPL measured on a single microphone (i.e. the reference microphone at the center of the array) as a function of rotor azimuth angle (Figure 8-10). The overall levels in this figure were summed between 250 Hz and 800 Hz to focus on the low-frequency noise of the down-going blade. The result is A-weighted. Furthermore, the levels were averaged over all measurements and all revolutions in State 2a (synchronization was done using the trigger signal from the turbine). As a reference, the result for the test campaign on the baseline turbine (2005) is shown as well. Note that the results from the baseline rotor cannot be compared directly to those from the modified rotor, due to the different meteorological conditions. However, the *variation* in noise level between the three blades can be compared for the two test campaigns.

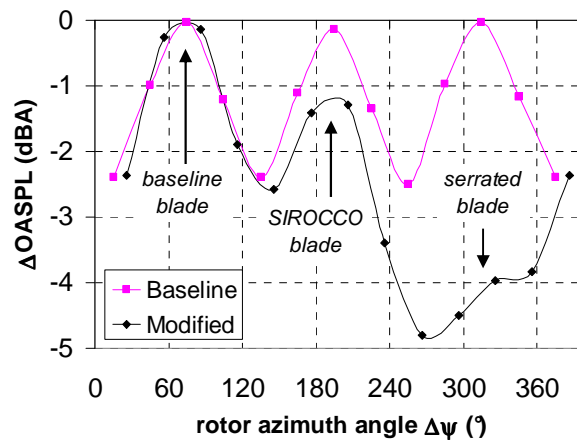


Figure 8-10: Average sound pressure level on central array microphone as a function of rotor azimuth, for baseline rotor (2005) and rotor with modified blades (State 2a).

For the baseline rotor, clearly three humps are observed, representing the swishing noise which is observed when the three blades pass the 3 o'clock position (see also Figure 8-8). The three blades are practically equally noisy, and the amplitude variation (or swish) during the passage of the blades is about 2.5 dB. For the modified rotor, three humps with different amplitude are observed, which can be associated to the baseline blade, the SIROCCO blade, and the serrated blade respectively. Thus, it can be estimated that the SIROCCO blade yields a reduction of more than 1 dB, while the serrated blade is about 4 dB quieter than the baseline blade. However, it should be noted that these values only pertain to the low-frequency noise radiated from around the 3 o'clock position, whereas the blades may also produce significant noise during the other part of the revolution, as will be seen below. Moreover, at each moment the single microphone picks up the noise from all three blades, so that the contribution of each blade cannot be extracted from the single-microphone results. Thus, although Figure 8-10 confirms subjective on-site observations, a dedicated array processing method (as described in Section 8.2.4) is required to obtain a clear picture of the noise radiated by each individual blade during the complete revolution.

### 8.3.2.2 Average blade noise characteristics

The source maps for the individual blades, averaged over one complete revolution and over all measurements in State 2a, are shown in Figure 8-11. The source maps run from 15 m to 60 m in radial direction, and have a chordwise extent of 30 m. The black line indicates the outer 32 m of the blade (trailing edge on upper side). The range of the color scale is 12 dB and the maximum is adjusted for each frequency band, so that the colors within one row can be compared directly.

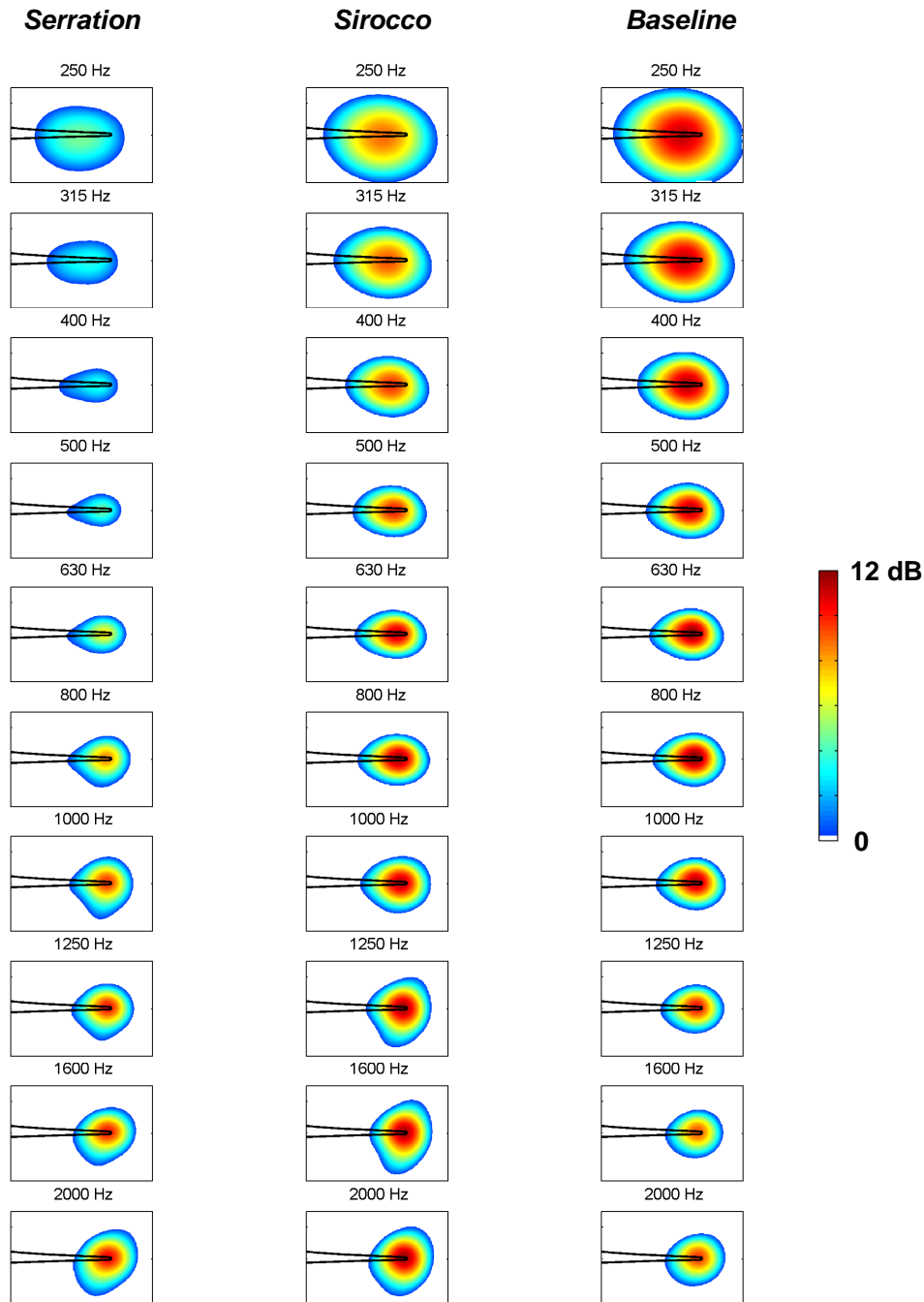


Figure 8-11: Average rotating source maps for individual blades in State 2a, as a function of frequency. The range of the color scale is 12 dB and the maximum is the same within each row.

First, the source maps show that the differences in source *position* for the three blades are small. The source radial position, defined as the radius at which the maximum level in the source map occurs, is shown in Figure 8-12 as a function of frequency for the three blades. Since the mesh size of the scan grid was 1 m (Section 8.2.4), these source radial positions are multiples of 1 m. For all blades the source radial position increases with frequency, which can be understood using the relation  $St = f \delta^* / U = const.$  for the trailing edge noise peak [6,33]: for increasing radius the local blade inflow velocity  $U$  increases and the boundary layer displacement thickness  $\delta^*$  decreases, so that the produced frequencies are higher [24,25]. Except for the lowest frequencies, where the modified blades have a lower source radius, the differences in average source radial positions between the different blades are small.

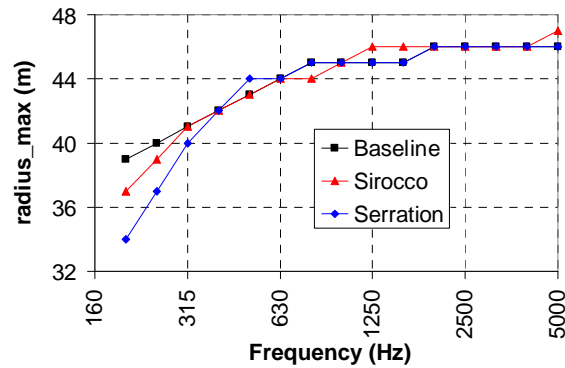


Figure 8-12: Average source radial position as a function of frequency for the three blades in State 2a.

More importantly, the source maps in Figure 8-11 show that for low frequencies both modified blades are significantly quieter than the baseline blade, especially the serrated blade. For high frequencies however, both modified blades are noisier than the baseline blade, especially the SIROCCO blade. These trends are illustrated in Figure 8-13, which shows the average integrated spectra for the three blades. These spectra were obtained by averaging the integrated spectra for all measurements in State 2a, with equal weights per wind speed bin. As mentioned in Section 8.2.4, these sound levels represent the contribution of the different blades to the overall sound pressure level of the turbine, as measured at the array position.

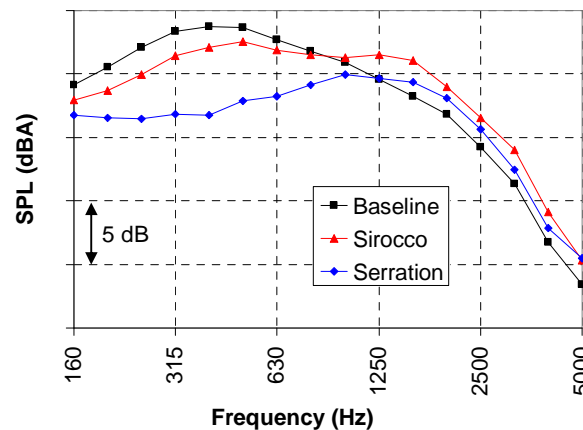


Figure 8-13: Average blade noise spectra for State 2a.

The integrated spectra confirm the low-frequency noise reduction and high-frequency noise increase for the modified blades. For the serrated blade the A-weighted sound pressure level at high frequencies is even higher than at low frequencies. The reasons for the increased noise level of the modified blades at high frequencies will be discussed in subsequent sections.

Based on these average spectra, for the upwind measurements on the clean rotor (i.e., State 2a), which are considered most representative for normal operation and which cover all relevant wind speeds, average overall noise reductions of 0.5 dB and 3.2 dB were obtained for the SIROCCO and serrated blades, respectively. For the other two rotor states, which covered only the lower wind speeds, average noise reductions of 0.0 dB and 1.6 dB (State 1) and 0.2 dB and 1.2 dB (State 2b) were found for the SIROCCO and serrated blades, respectively. The reasons for the lower noise reduction in these states will be discussed in subsequent sections. The measurement uncertainty of the above-mentioned average noise reductions will be discussed below in Section 8.3.2.4.

### 8.3.2.3 Dependence of blade noise on rotor azimuth

In order to better understand the acoustic behavior of the modified blades, it is interesting to look at the dependence of the blade noise on the rotor azimuth angle (Figure 8-15, next page). This figure shows the overall source maps for the different blades for 12 rotor azimuth intervals of  $30^\circ$ , starting at  $\psi=0^\circ$  (12 o'clock). These overall source maps (averaged over all measurements in State 2a) were obtained by summing the source maps between 160 Hz and 5 kHz, after applying A-weighting and a correction for array resolution (which depends on frequency and blade position) to the levels. Thus, the OASPL of the blade is equal to the sum of all scan levels in a given source map. Similar to the previous blade source maps, the black line indicates the outer 32 m of the blade. The range of the color scale is 12 dB and the maximum is the same for all maps, so that the colors can be compared directly. This figure shows that during the *downward* movement of the blades, both modified blades are substantially quieter than the baseline blade. However, during the *upward* movement both modified blades are noisier. These observations are illustrated in Figure 8-14, which shows the integrated blade spectra for the down- and upward half of the revolution separately.

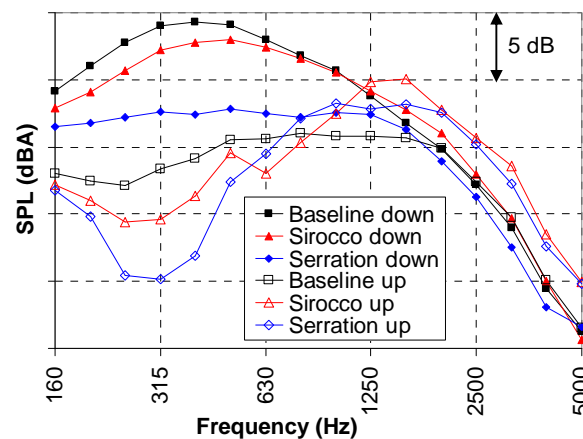


Figure 8-14: Average blade noise spectra for the upward and downward part of the revolution in State 2a.

The high-frequency noise increase for the modified blades occurs mainly during the upward part of the revolution, and for the serrated blade, the increased noise of the up-going blade even dominates the overall average spectrum.

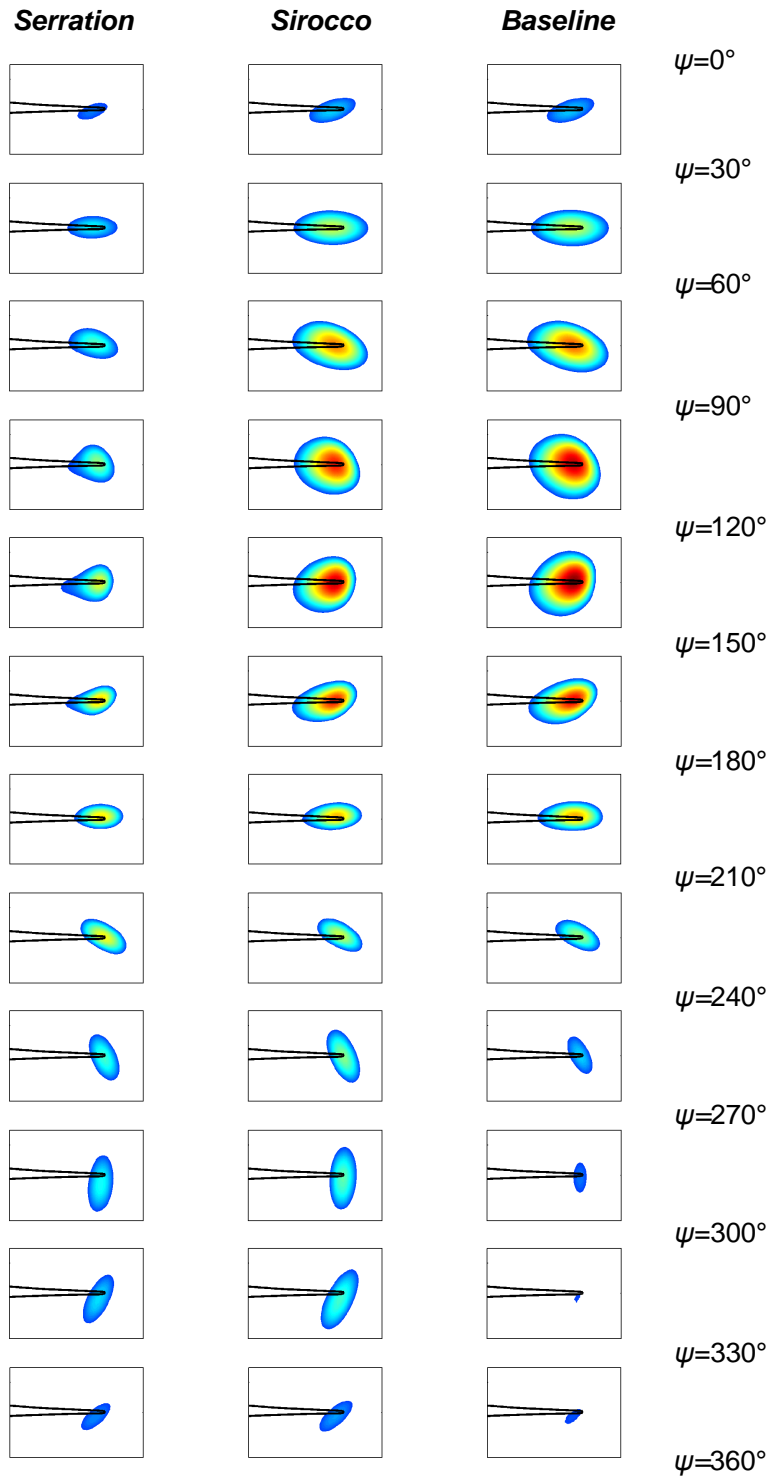


Figure 8-15: Average overall source maps for individual blades in State 2a, as a function of rotor azimuth. The range of the color scale is 12 dB and the maximum is the same for all maps.



### 8.3.2.4 Dependence of blade noise on wind speed

In addition to the rotor azimuth, the blade noise characteristics were also found to depend strongly on the wind speed. This is illustrated in Figures 8-16 and 8-17, which show the integrated blade noise spectra for the 7 m/s and 10 m/s bins of State 2a, respectively (the State 2b spectra in Figure 8-16 will be discussed below in Section 8.3.2.5). The 7 m/s blade spectra show a high-frequency hump around 1250-1600 Hz, which is absent in the 10 m/s spectra. As seen in the previous section, this high-frequency noise is mainly produced during the upward movement, and originates from the very tip of the blade (Figures 8-11 to 8-15). Because the average blade pitch angle was  $0^\circ$  in the 7 m/s bin and higher in the 10 m/s bin, this suggests that the high-frequency noise at low wind speeds can be associated with the increased tip loading as a result of the lower pitch angle (see Section 8.2.1 for turbine operation details). This also explains the fact that the up-going blades were noisier in States 1 and 2b than in State 2a (Figures 8-7 to 8-9), since the average blade pitch angle was lower than in State 2a (Table 8-2). Apparently this tip noise does not follow the trailing edge noise directivity function described in Eq. (8.1), since it is mainly radiated during the upward movement of the blades.

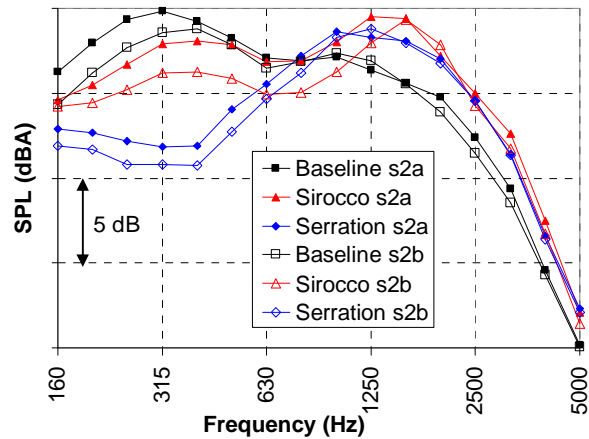


Figure 8-16: Average blade noise spectra for the 7 m/s wind speed bin of States 2a and 2b.

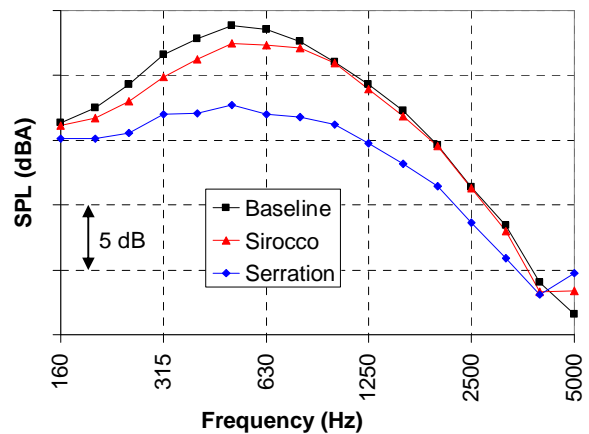


Figure 8-17: Average blade noise spectra for the 10 m/s wind speed bin of State 2a.

Figure 8-16 also shows that the tip noise is much more prominent for the modified blades than for the baseline blade, which is always dominated by trailing edge noise. Thus, the adapted pressure distribution on the modified blades, possibly in combination with the slightly increased blade loading (Section 8.1), changes the tip vortex characteristics such that tip noise increases.

For the baseline and SIROCCO blades the frequency of the low-frequency trailing edge noise peak is higher at 10 m/s than at 7 m/s, which can be explained by the lower blade loading (due to the higher pitch angle), which leads to a thinner suction side boundary layer. This is confirmed in Figure 8-18, which shows the source radial positions for both blades in these two wind speed bins: for a given radius, the trailing edge boundary layer thickness decreases for the higher wind speed, so that the produced frequencies are higher. For both bins the source radial position of the SIROCCO blade is slightly lower than for the baseline blade, which is consistent with the higher trailing edge noise peak frequency, and which suggests that the main objective of the airfoil design, i.e. to obtain a thinner suction side boundary layer (see Section 8.1), has succeeded.

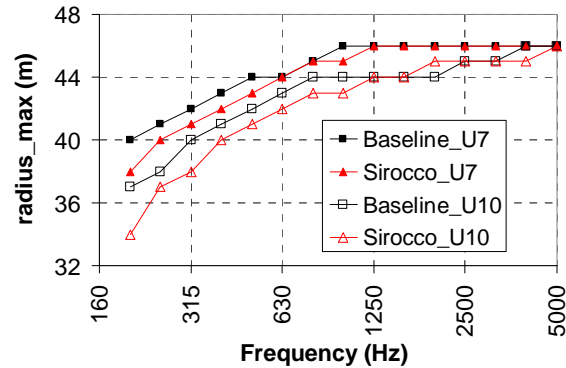


Figure 8-18: Source radial position as a function of frequency for the baseline and SIROCCO blades in the 7 m/s and 10 m/s wind speed bins of State 2a.

If we suppress the spectral influence of tip noise by considering only the downward part of the revolution (Figure 8-14), a slight trailing edge noise increase is observed between 1 and 3 kHz for the SIROCCO blade, which, similar to the wind tunnel results, can be attributed to the increased pressure side boundary layer thickness [35]. However, even if we consider only the downward part of the revolution, the average reduction in OASPL for the SIROCCO blade in State 2a is only 1.0 dB, which is lower than the 2-3 dB found in the wind tunnel tests. The reasons for this discrepancy between wind tunnel and field results are not fully clear yet. Apart from blade quality, a possible explanation could be that instationary inflow conditions in the field lead to lift fluctuations well beyond the prescribed design lift range [34].

In terms of A-weighted overall sound pressure levels (summed between 160 Hz and 5 kHz), both modified blades were found to reach maximum noise levels at a wind speed  $U_{10}$  of about 7 m/s, where the tip loading and therefore the tip noise are highest (the blade pitch angle only starts to increase significantly for wind speeds higher than 7 m/s). The noise from the baseline blade, which is dominated by trailing edge noise, also peaks around 7 m/s. The corresponding noise reductions (Figure 8-19) are lowest around 7 m/s and increase for higher wind speeds, for both the serrated and SIROCCO blades. Thus, the results indicate that at high wind speeds the noise from the three blades is dominated by trailing edge noise, which is

effectively reduced by the new airfoil shape and the serrations. However, at lower wind speeds (increased tip loading due to lower pitch angle), significant high-frequency tip noise is generated by both modified blades during their upward movement, which partly cancels the trailing edge noise reduction. As a result, the average noise reductions obtained in States 1 and 2*b*, which had lower wind speeds and therefore lower average blade pitch angles (Table 8–2), were lower than the 3.2 dB and 0.5 dB found in State 2*a* for the serrated and SIROCCO blades, respectively.

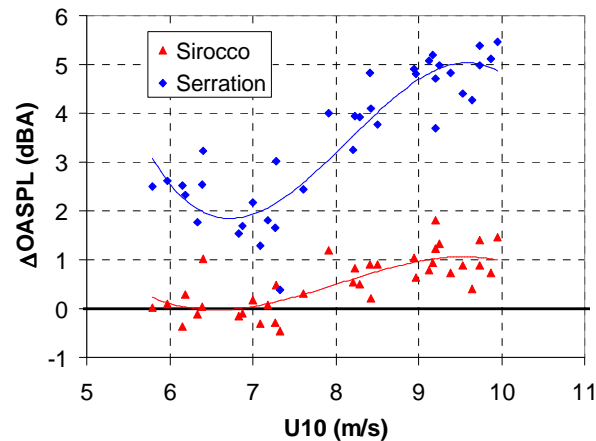


Figure 8-19: Overall blade noise reduction as a function of wind speed for State 2*a*. The solid lines are third-order least-squares fits through the measured data.

In order to evaluate these average noise reductions it is important to understand the uncertainty levels associated with the measurement method employed during this study. As argued in Section 8.2.5, for the weather conditions and turbine operation parameters in State 2*a*, the measurement uncertainty of the average noise reductions is smaller than 0.1 dB. For *different* turbine and meteorological conditions (within the tested range), the uncertainty in the noise reduction can be assessed from the scatter in Figure 8-19: for the serrated and SIROCCO blade, standard deviations  $\sigma$  of 0.6 dB and 0.4 dB were found, which leads to standard deviations of the mean ( $\varepsilon$ ) for the *average* noise reductions of 0.10 dB and 0.06 dB, respectively. Since these  $\varepsilon$ -values are smaller than the average noise reductions of 3.2 dB and 0.5 dB, the average reductions are significant for the tested range of turbine and meteorological conditions.

### 8.3.2.5 Upwind versus downwind measurements

In order to assess the effect of observer location (i.e. upwind versus downwind array position), Figure 8-16 compares the blade noise spectra for the 7 m/s bin in States 2*a* and 2*b*. The meteorological and turbine parameters were similar for both cases. It can be seen that for all three blades the level of the low-frequency trailing edge noise hump is lower on the downwind side. A partial explanation for this could be that the downwind integrated blade noise levels suffer from increased coherence loss (see also Section 8.2.5), because the blade noise propagates through the rotor wake. Indeed, the difference between the integrated rotor noise level and the level of the reference microphone was about 1 dB higher for the downwind measurements than for the upwind measurements in the 7 m/s bin. In addition, the

reduced downwind trailing edge noise levels may be explained by the  $\xi$ -dependence in Eq. (8.1), due to the wind speed and rotor tilt angle (see also Section 8.3.1). In contrast to the low-frequency noise, the high-frequency tip noise peak has approximately the same level for the up- and downwind measurements, which means that the *relative* importance of tip noise is higher on the downwind side. In addition to the tip loading effect discussed in the previous section, this increased importance of tip noise on the downwind side is an additional explanation for the lower noise reductions obtained in States 1 and 2*b* (as compared to State 2*a*), and for the fact that the up-going blades are noisier in States 1 and 2*b* than in State 2*a* (Figures 8-7 to 8-9).

### 8.3.2.6 Baseline blade noise for different rotor states

Figure 8-20 shows the baseline blade noise spectra for the three different rotor states. With regard to the clean rotor, a number of differences can be observed between states 2*a* and 2*b*: first, the low-frequency trailing edge noise peak for State 2*a* has a higher frequency and higher level than State 2*b*. This can be explained respectively by the higher wind speed (i.e., lower blade loading and thinner boundary layer) in State 2*a*, and the difference in directivity for the up- and downwind observer position (see Sections 8.3.2.4 and 8.3.2.5 above). Second, the State 2*b* spectrum shows a high frequency tip noise peak, which is almost absent in State 2*a*. As mentioned before, this can be explained by the lower average wind speed (and thus higher tip loading) in State 2*b* (Section 8.3.2.4), and by the increased importance of tip noise on the downwind side (Section 8.3.2.5). Thus, to assess the influence of tripping on blade noise, State 1 should be compared to State 2*b*. The average conditions for these two states are practically the same, except for the misalignment angle (Table 8-2). Figure 8-20 shows that the low-frequency trailing edge noise peak for State 1 has a higher level and lower frequency than in State 2*b*. This suggests that the trip has increased the trailing edge boundary layer thickness. Furthermore, the high-frequency tip noise peak is slightly lower for the tripped case. Thus, the results do indicate a small effect of tripping (0.6 dB increase in OASPL for the present conditions), but for a conclusive answer measurements should be done with a clean and a tripped blade on one rotor.

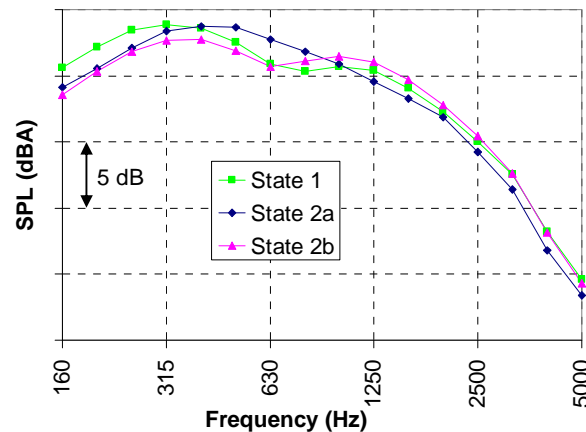


Figure 8-20: Average baseline blade noise spectra for different rotor states.

#### 8.4 Conclusions

Acoustic field measurements were carried out on a 94-m diameter wind turbine, with one standard blade, one blade with an optimized airfoil shape, and one standard blade with trailing edge serrations. The blade modifications had no adverse effect on their aerodynamic performance. In order to assess the effect of blade roughness due to dirt or insects, the blades were tested in both clean and tripped conditions. A large horizontal microphone array, positioned at a distance of about one rotor diameter from the turbine, was used to locate and quantify the noise sources in the rotor plane and on the individual blades. Since the array position was fixed and the wind direction varied, both up- and downwind measurements were performed.

The acoustic source maps for the baseline blade showed that, for an observer at the array position, the dominant source was trailing edge noise from the outer 25% of the blade. Due to convective amplification and directivity, practically all noise was produced during the downward movement of the blade, which caused the typical swishing noise during the passage of the blades. Both modified blades showed a significant trailing edge noise reduction at low frequencies, which was more prominent for the serrated blade. However, the modified blades also showed a noise increase at high frequencies, which could be associated with the blade tips. This high-frequency tip noise was mainly radiated during the upward part of the revolution, and was most important at low wind speeds (i.e. high tip loading) and for the downwind array position. Nevertheless, for the upwind measurements on the clean rotor, which were considered most representative for normal operation and covered all relevant wind speeds, average overall noise reductions of 0.5 dB and 3.2 dB were obtained for the optimized blade and the serrated blade, respectively. For both blades the noise reduction increased with increasing wind speed. The downwind measurements on the clean and tripped rotors only covered the lower wind speeds, and showed less noise reduction. Comparison of the noise from the baseline blade for clean and tripped conditions suggested a noise increase of 0.6 dB due to tripping.

#### Acknowledgments

The authors would like to thank the colleagues from the University of Stuttgart and from the Netherlands Energy Research Foundation (ECN) for their valuable contributions to the definition of the tests and the interpretation of the results. Financial support for this research was given in part by the European Commission's Fifth Framework Programme, project reference: SIROCCO, Silent Rotors by Acoustic Optimisation (ENK5-CT-2002-00702). Financial support was also given by the Netherlands Organisation for Energy and the Environment (NOVEM).

#### References

- [1] Wagner, S., Bareiss, R., Guidati, G., *Wind Turbine Noise*, Springer Verlag, 1996.
- [2] Guidati, G., Ostertag, J., Wagner, S., "Prediction and reduction of wind turbine noise: an overview of research activities in Europe", AIAA Paper 2000-0042, 2000.
- [3] Amiet, R., "Acoustic Radiation from an Airfoil in a Turbulent Stream", *Journal of Sound and Vibration* 41, 1975.
- [4] Howe, M.S., "A review of the theory of trailing edge noise", *Journal of Sound and Vibration* 61, 1978.

- [5] Blake, W.K., *Mechanics of Flow-Induced Sound and Vibration*, Academic Press, 1986.
- [6] Brooks, T.F., Pope, D.S., Marcolini, M.A., "Airfoil Self-Noise and Prediction", NASA Reference Publication 1218, 1989.
- [7] Dassen, T., Parchen, R., Guidati, G., Wagner, S., Kang, S., Khodak, A.E., "Comparison of measured and predicted airfoil self-noise with application to wind turbine noise reduction", *Proceedings of the European Wind Energy Conference*, Dublin, October 1997.
- [8] Guidati, G., Bareiss, R., Wagner, S., Dassen, T., Parchen, R., "Simulation and measurement of inflow-turbulence noise on airfoils", AIAA Paper 97-1698, 1997.
- [9] Hutcheson, F.V., Brooks, T.F., "Effects of angle of attack and velocity on trailing edge noise", AIAA Paper 2004-1031, 2004.
- [10] Oerlemans, S., Migliore, P., "Aeroacoustic wind tunnel tests of wind turbine airfoils", AIAA Paper 2004-3042, 2004.
- [11] Moreau, S., Roger, M., "Competing broadband noise mechanisms in low speed axial fans", AIAA Paper 2004-3039, 2004.
- [12] Herr, M., Dobrzynski, W., "Experimental investigations in low noise trailing edge design", AIAA Paper 2004-2804, 2004.
- [13] Moriarty, P.J., Guidati, G., Migliore, P., "Prediction of turbulent inflow and trailing-edge noise for wind turbines", AIAA Paper 2005-2881, 2005.
- [14] Grosveld, F.W., "Prediction of broadband noise from large horizontal axis wind turbine generators", AIAA Paper 84-2357, 1984.
- [15] Glegg, S.A.L., Baxter, S.M., Glendinning, A.G., "The prediction of broadband noise from wind turbines", *Journal of Sound and Vibration* 118, 1987.
- [16] Hubbard, H.H., Shepherd, K.P., "Aeroacoustics of large wind turbines", *Journal of the Acoustical Society of America* 89, 1991.
- [17] Lawson, M.V., "Theory and experiment for wind turbine noise", AIAA Paper 94-0119, 1994.
- [18] Fuglsang, P., Madsen, H.A., "Implementation and verification of an aeroacoustic noise prediction model for wind turbines", Risø-R-867(EN), Risø National Laboratory, 1996.
- [19] Lawson, M.V., Lawson, J.V., Bullmore, A.J., "Wind turbine noise: analysis of results from a new measurement technique", AIAA Paper 98-0037, 1998.
- [20] Moriarty, P., Migliore, P., "Semi-empirical aeroacoustic noise prediction code for wind turbines", NREL/TP-500-34478, National Renewable Energy Laboratory, Golden, CO, 2003.
- [21] de Bruijn, A., Stam, W.J., de Wolf, W.B., "Determination of the acoustic source power levels of wind turbines", *Proceedings of the European Wind Energy Conference*, Hamburg, October 1984.
- [22] van der Borg, N.J.C.M., Vink, P.W., "Acoustic noise production of wind turbines in practice", *Proceedings of the European Wind Energy Conference*, Thessaloniki, October 1994.
- [23] Hagg, F., van Kuik, G.A.M., Parchen, R., van der Borg, N.J.C.M., "Noise reduction on a 1 MW sized wind turbine with a serrated trailing edge", *Proceedings of the European Wind Energy Conference*, Dublin, October 1997.
- [24] Oerlemans, S., Sijtsma, P., Méndez López, B., "Location and quantification of noise sources on a wind turbine", *Journal of Sound and Vibration* 299, 2007.
- [25] Oerlemans S., Schepers, J.G., "Prediction of wind turbine noise and comparison to experiment", *Proceedings of the Second International Meeting on Wind Turbine Noise*, Lyon, France, September 2007.
- [26] Brooks, T.F., Burley, C.L., "Rotor broadband noise prediction with comparison to model data", AIAA Paper 2001-2210, 2001.
- [27] Schlinker, R.H., Amiet, R.K., "Helicopter rotor trailing edge noise", NASA CR-3470, 1981.
- [28] Dowling A.P., Ffowcs Williams, J.E., *Sound and sources of sound*, Ellis Horwood Limited, 1983.
- [29] Howe, M.S., "Noise produced by a sawtooth trailing edge", *The Journal of the Acoustic Society of America* 90, 1991.
- [30] Dassen, T., Parchen, R., Bruggeman, J., Hagg, F., "Results of a wind tunnel study on the reduction of airfoil self-noise by the application of serrated blade trailing edges", *Proceedings of the European Wind Energy Conference*, Göteborg, 1996.
- [31] Braun, K.A., van der Borg, N., Dassen, A., Doorenspleet, F., Gordner, A., Ocker, J., Parchen, R., "Serrated Trailing Edge Noise (STENO)", *Proceedings of the European Wind Energy Conference*, Nice, October 1999.

- [32] Oerlemans, S., Schepers, J.G., Guidati, G., Wagner S., "Experimental demonstration of wind turbine noise reduction through optimized airfoil shape and trailing-edge serrations", *Proceedings of the European Wind Energy Conference*, Copenhagen, July 2001.
- [33] Herr, M., "Design criteria for low-noise trailing edges", AIAA paper 2007-3470, 2007.
- [34] Schepers, J.G., Curvers, A., Oerlemans, S., Braun, K., Lutz, T., Herrig, A., Wuerz, W., Matesanz, A., Garcillán, L., Fisher, M., Koegler, K., Maeder, T., "SIROCCO: Silent rotors by acoustic optimisation", *Proceedings of the Second International Meeting on Wind Turbine Noise*, Lyon, France, September 2007.
- [35] Lutz, T., Herrig, A., Würz, W., Kamruzzaman, M., Krämer, E., "Design and wind tunnel verification of low noise airfoils for wind turbines", *AIAA Journal*, Vol 45, No. 4, 2007, pp 779-792.
- [36] Herrig A., Würz W., Lutz T., Krämer E.: "Trailing-Edge Noise Measurements Using a Hot-Wire Based Coherent Particle Velocity Method", *Proceedings of the 24th AIAA Applied Aerodynamics Conference*, San Francisco, California, June 5-8, 2006.
- [37] Oerlemans, S., Broersma, L., Sijtsma, P., "Quantification of airframe noise using microphone arrays in open and closed wind tunnels", *International Journal of Aeroacoustics*, Vol. 6, Nr. 4, 2007.
- [38] Holthusen, H., Smit, H., "A new data-acquisition system for microphone array measurements in wind tunnels", AIAA paper 2001-2169, 2001.
- [39] IEC norm 61400-11, Wind turbine generator systems – Acoustic noise measurement techniques, 2002.
- [40] Johnson, D.H., and Dudgeon, D.E., *Array Signal Processing*, Prentice Hall, 1993.
- [41] Sijtsma, P., Oerlemans, S., and Holthusen, H., "Location of rotating sources by phased array measurements", AIAA Paper 2001-2167, 2001.
- [42] Sijtsma, P., and Stoker, R.W., "Determination of Absolute Contributions of Aircraft Noise Components using Fly-Over Array Measurements", AIAA Paper 2004-2958, 2004.
- [43] Broersma, L., "Acoustic Array Measurements - Airframe Noise and Wind Turbine Noise", Master's Thesis, University of Twente, The Netherlands, January 2006.





## Chapter 9

### Conclusions

This thesis deals with the detection of aeroacoustic sound sources on aircraft and wind turbines using phased microphone arrays. The main conclusions are described in the following.

First, the reliability of the phased array technique for quantifying flow-induced sound is assessed using airframe noise measurements in open and closed wind tunnels (Chapter 4). For both tunnels it is shown that diagonal removal (i.e. elimination of the main diagonal of the cross-power matrix) must be applied to obtain meaningful results. The results for the open jet show that, although the absolute integrated array level can be too low by more than 10 dB due to coherence loss, the relative sound levels (i.e. differences between configurations) are accurate within 0.5 dB. Since coherence loss depends on wind speed, one should be careful to compare integrated spectra for different wind speeds. For the closed test section, the absolute array levels are accurate within 3 dB, and the relative levels within 1 dB. This means that phased arrays enable reliable quantitative airframe noise measurements in closed wind tunnels, which usually have better aerodynamic properties than open jets.

Next, the phased array technique is used to characterize the noise sources on two modern large wind turbines (Chapters 5 and 6). For both turbines it is demonstrated that, besides a minor source at the nacelle, practically all noise emitted to the ground is produced by the outer part of the blades during their downward movement. This asymmetric source pattern, which causes the typical swishing noise during the passage of the blades, can be explained by trailing edge noise directivity and convective amplification. The blade noise is found to scale with the fifth power of the local flow speed, and a narrowband analysis of the dedopplerized spectra indicates that tonal blunt trailing edge noise is not important. Applying a roughness strip to the blade (to simulate dirt or insects) can significantly increase the noise level. All in all, the test results convincingly show that broadband trailing edge noise is the dominant sound source for both turbines.

Having determined the dominant source mechanism, a prediction method is developed for the noise from large wind turbines (Chapter 6). First, the acoustic source strength of each blade segment is calculated using a semi-empirical prediction code for trailing edge noise from wing sections. Then, the effects of source motion and directivity, which depend on observer position, are included. The simulations are validated extensively against the experimental data from both wind turbines. The predicted noise source distribution in the rotor plane (as a function of frequency and observer position) shows the same characteristics as in the experiments. Good agreement is also found between the measured and predicted spectra, in terms of levels and spectral shape. For both turbines the predicted overall sound levels (as a function of rotor power) are accurate within 1-2 dB. The turbine noise directivity is also predicted within 1-2 dB, and the swish amplitude (in different directions) within 1 dB.

Moreover, it is shown that the experimental data can be used to assess the theoretical trailing edge noise directivity function. Finally, the validated prediction method is applied to calculate so-called noise footprints of the wind turbine. These footprints show that swish amplitudes up to 5 dB can be expected for cross-wind directions, even at large distance.

The influence of airfoil shape on blade noise is investigated through acoustic wind tunnel tests on a series of candidate airfoils for small wind turbines (Chapter 7). In quiescent inflow, trailing edge noise is dominant for all airfoils. At low Reynolds numbers (below 1 million), several airfoils exhibit pure tones that can be attributed to laminar boundary layer vortex shedding. Proper boundary layer tripping eliminates the tones and reduces broadband noise. The level of broadband trailing edge noise is found to differ substantially among the tested airfoils. In the presence of severe upstream turbulence, leading edge noise is dominant for all airfoils. The inflow turbulence noise level increases with decreasing airfoil thickness (or increasing sharpness).

Finally, two noise reduction concepts are tested on a large wind turbine: acoustically optimized airfoils and trailing edge serrations (Chapter 8). Both blade modifications yield a significant trailing edge noise reduction at low frequencies, which is more prominent for the serrated blade. However, the modified blades also exhibit increased tip noise at high frequencies, which is mainly radiated during the upward part of the revolution, and which is most important at low wind speeds due to high tip loading. Nevertheless, average overall noise reductions of 0.5 dB and 3.2 dB are obtained for the optimized blade and for the serrated blade, respectively. Thus, it is demonstrated that wind turbine noise can be halved without adverse effects on the aerodynamic performance.

## Appendix

### Signal processing

In order to obtain a complete description of a random pressure signal  $p(t)$ , we would have to measure it continuously for an infinite time. Since this is not practical, we measure it only for a limited period of time and assume that the signal is statistically stationary. Moreover, to enable digital processing, the signal is sampled at some sample interval  $\Delta t_s$ , where each sample is stored in a given number of bits (typically 16). Thus, the sampled signal  $p(w\Delta t_s)$ , with integer  $w$ , is obtained. The *sample frequency*  $f_s$  is defined as  $1/\Delta t_s$ . The frequency content of the signal can be analyzed by applying the Discrete Fourier Transform (DFT) to a block of  $W$  samples:

$$P(f_j) = \frac{2}{W} \sum_{w=0}^{W-1} p(w\Delta t_s) e^{-i\omega_j w\Delta t_s}, \quad (\text{A.1})$$

where  $P$  is the complex pressure amplitude at frequency  $f_j$  and  $\omega_j = 2\pi f_j$ . Since the DFT implicitly assumes that the time signal is periodic with period  $W\Delta t_s$ , the spectrum is discrete and is only evaluated at multiples  $j$  of the fundamental frequency:  $f_j = j/(W\Delta t_s)$ . Conversely, since the time signal is discrete, the spectrum is also periodic, with a period equal to the sample frequency  $f_s$  (Figure A-1).

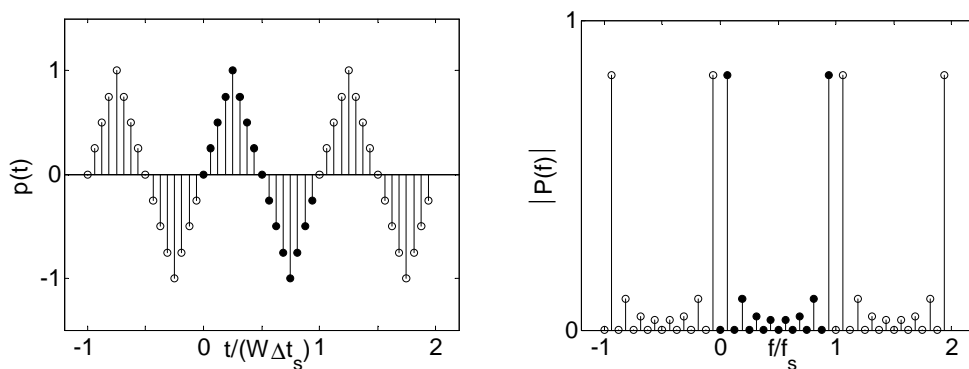


Figure A-1: Example of discrete time signal (left) and its spectrum (right), for  $W=16$ .

The sampled time signal can be reconstructed from the complex spectrum using the Inverse Discrete Fourier Transform:

$$p(w\Delta t_s) = \frac{1}{2} \sum_{j=0}^{W-1} P(f_j) e^{i\omega_j w\Delta t_s} = \sum_{j=1}^{W/2-1} P(f_j) e^{i\omega_j w\Delta t_s}. \quad (\text{A.2})$$

In the second equality it is assumed that  $W$  is even and that the time signal has zero mean. Moreover, use is made of the property  $P(f_j) = P^*(f_s - f_j)$ , where the asterisk denotes complex conjugation. This property shows that signal components with a frequency higher than the *Nyquist frequency* of  $f_s/2$  will contribute to the spectrum at lower frequencies, i.e. a signal with frequency  $f_s - f_j$  cannot be distinguished from a signal with frequency  $f_j$  (Figure A-2).

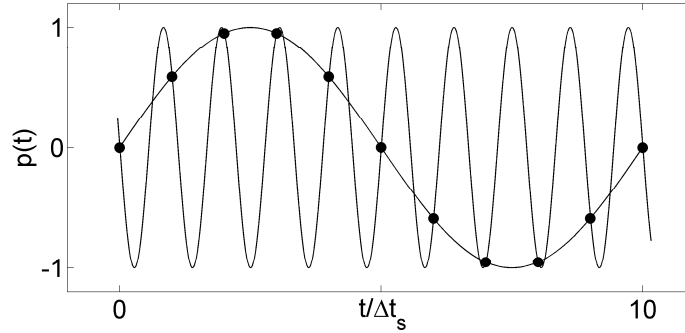


Figure A-2: Aliasing for two signals with frequencies of  $0.1 \cdot f_s$  and  $0.9 \cdot f_s$ .

This undesired phenomenon is called *aliasing* and can be avoided by passing the signal through a low-pass filter that removes all frequencies above the Nyquist frequency, before entering the analogue/digital (A/D) converter. Thus, the relevant number of frequency lines (between zero and  $f_s/2$ ) is equal to  $W/2 - 1$ , as illustrated in Figure A-1. If the block size  $W$  is chosen such that  $W$  is a power of 2, the so-called Fast Fourier Transform (FFT) can be applied to evaluate Eq. (A.1) in a computationally efficient way. Typical practical values for  $W$  are 1024, 2048, or 4096. Using Parseval's theorem, the mean square of the time signal  $p(t)$  can be written as the sum over the squared complex amplitudes  $P(f_j)$ :

$$\overline{p^2} \equiv \frac{1}{W} \sum_{w=0}^{W-1} |p(w\Delta t_s)|^2 = \frac{1}{2} \sum_{j=1}^{W/2-1} |P(f_j)|^2, \quad (\text{A.3})$$

so that  $\frac{1}{2}|P(f_j)|^2$  can be regarded as the acoustic energy in the frequency band

$$\frac{j - \frac{1}{2}}{W\Delta t_s} < f < \frac{j + \frac{1}{2}}{W\Delta t_s}. \quad (\text{A.4})$$

Since the implicit DFT assumption of a periodic time signal is generally not true for broadband noise, the reconstructed periodic time signal will show discontinuities at the edges of each period  $W\Delta t_s$ . As a result the DFT spectrum will be distorted by frequency side lobes or *leakage*. This phenomenon can be reduced by applying a *window* to the time signal, which forces the signal to zero at the edges of the block of samples. In this thesis generally the so-called Hanning window is used, which has a sine-squared shape and whose amplitude is scaled such that acoustic energy is conserved. If the signal is *stationary* (i.e. statistical

properties are independent of time), statistical variations can be averaged out by averaging the (frequency-dependent) *autopowers*  $\frac{1}{2}PP^* = \frac{1}{2}|P|^2$  over many blocks of samples (note that averaging the complex pressure  $P$  itself results in a value of zero, since the phase in each block is random). If the relation between two signals  $P_1$  and  $P_2$  is considered, the *cross-powers*  $\frac{1}{2}P_1P_2^*$  can be averaged in the same way. The number of averages lies typically between 1000 and 3000.

The sound spectrum calculated according to Eq. (A.1) provides the distribution of acoustic energy as a function of frequency in *narrow bands*. These frequency bands, defined in Eq. (A.4), have a fixed width of  $(W\Delta t_s)^{-1}$ . A spectrum can also be represented in terms of *proportional* frequency bands, whose width is proportional to the frequency. In this thesis generally 1/3-octave bands are used, with center frequencies of 100 Hz, 125 Hz, 160 Hz, 200 Hz, etc. The sound level in a proportional frequency band is obtained by summing the spectral values in the corresponding narrow bands. The *overall* sound pressure level represents the total acoustic energy, and is obtained by summing the spectral values over the whole frequency range. As indicated in Eq. (A.3), the total acoustic energy is equal to the mean square of the time signal. In order to account for the sensitivity of the human ear, sound levels can be corrected by frequency-dependent weight factors. The most commonly used frequency weighting is *A-weighting*. The resulting sound levels are expressed in dB(A).



## Acknowledgements

It has been a privilege to work in the field of aeroacoustics for more than ten years at the National Aerospace Laboratory NLR. During the last years many people have contributed in various ways to the work presented in this thesis. In particular I would like to mention the following persons.

In the first place, I would like to thank Pieter Sijtsma, who is the brain behind the array technique at NLR. He came up with many useful suggestions and was always open for new ideas and discussions about the method. I am also very grateful to professor Mico Hirschberg, who stimulated me to perform this doctoral research and learned me a lot about aeroacoustics. Furthermore, I want to thank my (former) colleagues at NLR, especially those from the Aeroacoustics Group, for their advice and dedicated support in many projects during the last years. In particular, I would like to mention Corné Boons, Marko Beenders, Onno Stallinga, Arjan Hanema, and Floor Pieters, who participated in the sometimes demanding field tests, and sacrificed many weekends and holidays because the weather conditions happened to be good for measurements.

The development of the array technique at NLR was initiated by my predecessor Ton Dassen, in collaboration with DNW and TNO. Over the years, many important contributions were made by the people from DNW, especially Hermann Holthusen. They kindly lended us their data acquisition systems, even after we returned them filled with Spanish sand. I also want to thank Liekele Broersma, who joined a rainy test campaign in the muddy Wieringermeer polder, and whose master's thesis was the basis for Chapter 4. This work would not have been possible without the support of NLR. In particular I would like to mention my managers Harry Brouwer and Christophe Hermans, who enabled me to spend time on this doctoral research besides my normal work. The assistance and advice of the NLR publishing department in producing this thesis, in particular Isabel Puts, is very much appreciated.

Much of the work in this thesis was carried out in close cooperation with various project partners. The contribution of the people from DLR and Airbus to the airframe noise measurements in the DNW wind tunnel is greatly appreciated. I would also like to thank Paul Migliore for setting up the fruitful cooperation between NREL and NLR, and for his valuable contributions to the performance and analysis of the airfoil tests. The early field tests on the GAMESA wind turbine were only possible thanks to the efforts of Beatriz Méndez López, who also acted as a tour guide in Madrid and even arranged tickets for Real Madrid. The preparation, execution and analysis of the measurements on the GE turbine were tremendously supported by many people from GE, including Rainer Arelt, Murray Fisher, Klaus Kögler, Thierry Maeder, Kevin Kinzie and Laurent Bonnet. Without their efforts to obtain approval for publishing our nice results, this thesis would not have been possible. The people from the University of Stuttgart, especially Andreas Herrig, Kurt Braun, Werner Würz, and Thorsten Lutz, provided many useful suggestions with regard to the field tests. Special thanks go to ECN, in particular Gerard Schepers and Toine Curvers, who were involved in most of the field tests and contributed to the calculations in Chapter 6.

I am grateful to my friends and family for their support and interest. Last, but not least, I want to thank my favorite waste of time, Anna, for adding random fluctuations to my life during the last thirteen years. And above all for her love.





## Curriculum Vitae

- 24 March 1974 Born in Geffen, The Netherlands.
- 1986-1992 Gymnasium B, Titus Brandsma Lyceum, Oss.
- 1992-1998 Applied Physics, Eindhoven University of Technology, The Netherlands
- Master's thesis at Philips Research Laboratories: 'Turbulent two-phase jets: An experimental and numerical study into the physical properties of free steam jets in air' (Prof. M.E.H. van Dongen)
  - Internship University of New South Wales (Sydney, Australia) on surface reactions of a semiconductor (Dr. N.K. Singh)
  - Internship Eindhoven University of Technology on surface reactions of catalysts (Prof. H.H. Brongersma)
- 1998-present Research engineer aeroacoustics, National Aerospace Laboratory NLR, The Netherlands. Several national and international research projects on flow-induced sound from aircraft, wind turbines, and helicopters.

### Selected publications

- S. Oerlemans and A. de Bruin, Reduction of landing gear noise using an air curtain, AIAA paper 2009-3156, 2009.
- S. Oerlemans and J.G. Schepers, Prediction of wind turbine noise and validation against experiment, accepted for International Journal of Aeroacoustics.
- S. Oerlemans, M. Fisher, T. Maeder, K. Kögler, Reduction of wind turbine noise using optimized airfoils and trailing-edge serrations, AIAA Journal 47(6), 2009.
- J. Yin, B.G. van der Wall, S. Oerlemans, Acoustic Wind Tunnel Tests on Helicopter Tail Rotor Noise (HeliNOVI), Journal of the American Helicopter Society 53(3), 2008.
- S. Oerlemans, L. Broersma, P. Sijtsma, Quantification of airframe noise using microphone arrays in open and closed wind tunnels, International Journal of Aeroacoustics 6(4), 2007.
- S. Oerlemans, P. Sijtsma, B. Méndez López, Location and quantification of noise sources on a wind turbine, Journal of Sound and Vibration 299(4-5), 2007.
- P. Migliore and S. Oerlemans, Wind tunnel aeroacoustic tests of six airfoils for use on small wind turbines, Journal of Solar Energy Engineering 126, 2004.
- S. Oerlemans and M. Pott-Pollenske, An experimental study of gear wake/flap interaction noise, AIAA paper 2004-2886, 2004.
- S. Oerlemans and P. Sijtsma, Acoustic array measurements of a 1:10.6 scaled Airbus A340 model, AIAA paper 2004-2924, 2004.
- S. Oerlemans and P. Sijtsma, Determination of absolute levels from phased array measurements using spatial source coherence, AIAA paper 2002-2464, 2002.
- S. Oerlemans, J.G. Schepers, G. Guidati, S. Wagner, Experimental demonstration of wind turbine noise reduction through optimized airfoil shape and trailing-edge serrations, European Wind Energy Conference, Copenhagen, 2001.
- P. Sijtsma, S. Oerlemans, H. Holthusen, Location of rotating sources by phased array measurements, AIAA paper 2001-2167, 2001.
- S. Oerlemans, R. Badie, M. E. H. Van Dongen, An experimental and numerical study into turbulent condensing steam jets in air, Experiments in Fluids 31, 2001.
- S. Oerlemans and P. Sijtsma, Effects of wind tunnel side-plates on airframe noise measurements with phased arrays, AIAA paper 2000-1938, 2000.